REFERENCES

[1]   DTI, "UK Energy in Brief", National Statistics, UK Govt., (2006).

[2]   DNV and RISO, *Guidelines for Design of Wind Turbines*, Scanprint, Denmark, 2nd Edition, (2002).

[3]   C. Berggreen, K. Branner, J. F. Jensen and J. P. Schultz, "Application and analysis of sandwich elements in the primary structure of large wind turbine blades", *Journal of Sandwich Structures and Materials*, 9, 525-552 (2007).

[4]   L. G. Brazier, "On the flexure of thin cylindrical shells and other "thin" sections", *Royal Society -- Proceedings*, 116, 104-114 (1927).

[5]   K. Branner, F. M. Jensen, P. Berring, A. Puri, A. Morris and J.P. Dear, "Effect of Sandwich Core Properties on Ultimate Strength of a Wind Turbine Blade", *8th International Conference on Sandwich Structures*, (2008).

[6]   GOM mbH, *ARAMIS user manual*, GOM mbH, Revision A, (2005).

[7]   M. Sjodahl, "Accuracy in electronic speckle photography", *Applied Optics*, 36, 2875-85 (1997).

[8]   GOM mbH, "ARAMIS", GOM mbH,

[9]   ASTM International, "ASTM C393 Standard Test Method for Core Shear Properties of Sandwich Constructions by Beam Flexure", (2000).

[10] J. B. Sha, T. H. Yip and S. K. M. Wong, "In situ surface displacement analysis of fracture and fatigue behaviour under bending conditions of sandwich beam consisting of aluminium foam core and metallic face sheets", *Materials Science and Technology*, 22, 51-60 (2006).

[11] M. R. Wisnom, "3-D finite element analysis of curved beams in bending", *Journal of Composite Materials*, 30, 1178-90 (1996).

[12] D. Zenkert, *An introduction to sandwich construction*, Engineering Materials Advisory Services Ltd, (1995).

[13] C. E. Glenn and M. W. Hyer, "Bending behavior of low-cost sandwich plates", *Composites Part A: Applied Science and Manufacturing*, 36, 1449-1465 (2005).

[14] K. E. Evans, "Design of doubly curved sandwich panels with honeycomb cores", *Composite Structures*, 17, 95-111 (1991).

[15] L. Nicolaou, "DIC and FEA of Composite Wind Turbine Blade Structures: Final Year MEng Project", Mechanical Engineering, Imperial College London, (2007).

FAILURE MODES AND STRENGTH OF GLASS/VINYL ESTER FACE SHEET-ECO-CORE SANDWICH PANEL

Kunigal Shivakumar and Huanchun Chen

Center for Composite Materials Research
Department of Mechanical and Chemical Engineering
North Carolina A&T State University
Greensboro, NC 27411, USA
e-mail: kunigal@ncat.edu, web page: http://www.ncat.edu/~ccmradm/ccmr/

Chris Ibeh

Center for Nanocomposites and Multifunctional Materials
Plastics Engineering Technology
Pittsburg State University
Pittsburg, KS 66762, USA
e-mail: cibeh@pittstate.edu, web page: http://www.cncmm.org/ibeh.html

Key words: Sandwich structures, Glass/Vinyl Ester Composite, Eco-Core, Failure Mode, Strength

Summary. *Eco-Core material was developed under the US Navy (ONR program). It offers exceptional fire and toxicity properties and very good mechanical properties compared to other core materials such as balsa and PVC. Structural performance of Eco-Core sandwich panel which used a composite face sheet was tested through a design of test specimen to simulate different failures that occur in similar sandwich structures. The design exercise demonstrated that Eco-Core sandwich panels are highly unlikely to fail by face sheet wrinkling. The potential failure modes are core shear, core fracture by flexure, core shear crimping, face sheet yielding and face sheet buckling. Many of these failures were simulated by short beam shear, 4-point bend flexure and edgewise compression tests. Predicted failure loads for short beam shear and edgewise compression agreed very well with the experimental data (with the accepted data scatter). Furthermore, through-width delaminated panel failed as expected by buckling of delaminated sublaminate. The predicted load agreed very well with the test data. Four-point bend flexure tests were not successful because of test fixture limitation. This test and others will be repeated to generate data of statistical significance.*

1 INTRODUCTION

It has been known and realized for a long time that sandwich structures are highly efficient in carrying flexural loads. Structural efficiency and rigidity of sandwich structures are second to

Kunigal Shivakumar, Huanchun Chen and Chris Ibeh

none compare to other types of structural configurations, such as, I, Z and T sections. Sandwich structures with composite face sheet and PVC or balsa core materials are used in marine applications. US and European navy are using or considering to use composite sandwich construction in building ships for example mine sweepers, coastal protection, destroyers, etc. The fiber reinforced plastic (FRP) composite material is structurally highly efficient, fatigue insensitive and corrosion proof but its composition of 50% by weight of resin makes it highly susceptible to fire. Norwegian mine sweeper accident in 2002 was a prime example of danger in composite ships. Like resin, the PVC cores offer no resistance to fire. On the other hand balsa tolerates or inhibits the growth of fire but it suffers from non-uniform density (depends on the source and life time seasonal variation) and large moisture ingression, which leads to delamination failures. Recent studies [1] have shown about 800% density change and 35% volume change in balsa in the presence of water. To mitigate fire Shivakumar and his team [2, 3, 4] developed a core material called "Eco-Core" using the floater type of fly ash and phenolic binder. The novelty of this technology is that it uses little binder and large volume of ceramic hollow microbubbles (fly ash), together press molded to any size and shape. The eco-core has superior mechanical properties, excellent fire resistant properties (passed Mil Spec 2031 up to 75 kW/m^2) and is non toxic. The research focuses on the evaluation of structural performance of the Eco-Core sandwich panels and the comparison with that of PVC and balsa core panels. This paper is the first part of the research that involves design of test specimen for various types of failure under shear, flexure and edgewise compression loading; verification of the design by experiments; identification of failure modes in the sandwich structures. The face sheet used is FGI 1854 E-glass/vinyl ester composite. The core material is Eco-Core that was manufactured at CCMR with a nominal density of 31 lb/ft^3 (0.5 g/cc). Design of specimens, fabrication of panels, testing and test results are discussed.

2 DESIGN OF TEST SPECIMENS

Sandwich structures consist of a lightweight core material which is covered by face sheets on both sides. Figure 1 is the schematic diagram of the sandwich cross section. The nomenclature used in the design of test specimens is defined: t_c is the core thickness, t_f is the face sheet thickness and d is the sandwich thickness which is the distance between two centroids of the face sheets ($d=t_c+t_f$). The width of the panel is represented by b. Strength, elastic modulus, shear strength and shear modulus of the core are σ_c, E_c, τ_c and G_c, respectively. Strength and elastic modulus of the face sheet are σ_f and E_f, respectively.

$$\text{Face sheet, } \sigma_f, E_f$$

$$d = t_c + t_f \qquad d$$

$$\text{Core, } \sigma_c, E_c, \tau_c, G_c \qquad t_c$$

$$t_f$$

$$D = 2D_f + D_0 + D_c$$

$$D_f = \frac{1}{12} E_f t_f^{\,3}$$

$$D_0 = \frac{E_f t_f d^2}{2}$$

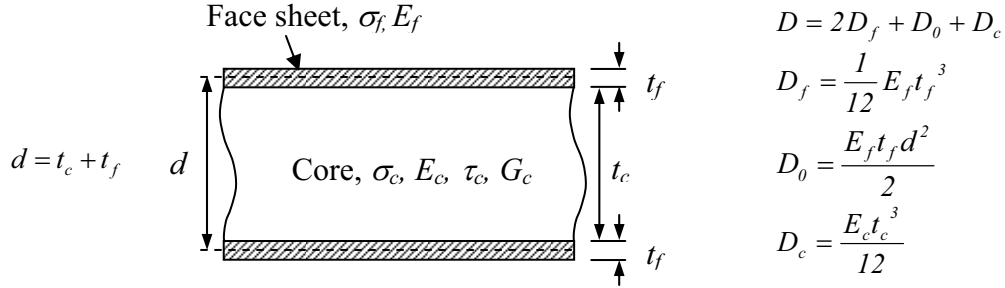$$D_c = \frac{E_c t_c^{\,3}}{12}$$

Figure 1: Schematic diagram of the sandwich cross section and nomenclature

The face sheet considered is FGI 1854 glass/Derakane 510A-40 vinyl ester composite. The core materials considered are Eco-Core, Balteck SB100 and PVC foam core Divinycell H100. Table 1 lists the mechanical properties of the face sheet [5] and core materials [2, 6, 7]. The nominal core and face sheet thicknesses are 1 in and 0.05 in, respectively.

The test specimens were designed to simulate typical failures of core shear, face yielding, face wrinkling, shear crimping and general buckling that occur in sandwich panels as in references 8 and 9. These failures can be simulated by short beam shear, flexure (4-point bend), and edgewise compression tests. Test specimens were designed for the above failures using the equations given in References 8 and 9.

Table 1: Material properties of core and face sheet materials

Material	Density lb/ft^3	Tensile Modulus msi	Tensile Strength psi	Compressive Modulus msi	Compressive Strength psi	Shear Modulus msi	Shear Strength psi
FGI 1854/Derakane 510A-40 [5]	-	4.23	74,313	4.63	52,693	0.58	11,180
Eco-Core [2]	31.21	0.37	937	0.17	3,168	0.14	668
Baltek SB100 [6]	9.43	0.51	1,885	0.57	1,837	0.02	426
Divinycell H100 [7]	6.24	0.02	508	0.02	290	0.01	232

2.1 Short Beam Shear Test Specimen

The short beam shear test was designed to measure shear strength of the core material. Four-point and 3-point bend loaded testing are commonly used. Here we chose 4-point bend with quarter point loading. Figure 2(a) shows the schematic of the short beam shear test. *S* is the support of the span and *S/2* is the load span.
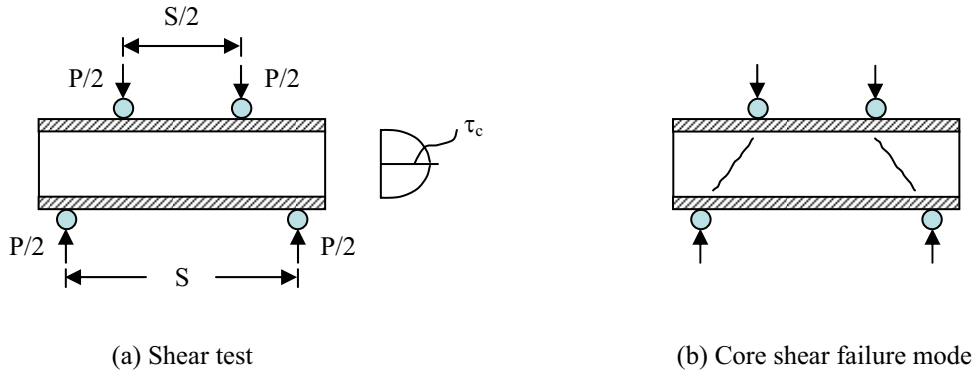
(a) Shear test   (b) Core shear failure mode

Figure 2: Schematic of short beam shear test and failure mode

The critical load at failure is P_s, which is related to core shear strength and test specimen geometry:

$$P_s = \frac{4}{3}\tau_c db \tag{1}$$

The typical failure mode in short beam shear test is core shear as illustrated in Figure 2(b).
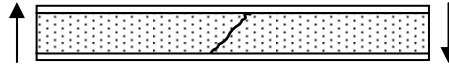
2.2 4-Point Bend Flexure Test Specimen

Figure 3(a) shows the schematic of 4-point bend flexure test. Under flexure loading, sandwich beam can fail by three different modes [8, 9], namely, face yielding, core shear and face wrinkling, depending on span to depth and face sheet-core thickness ratios and properties of face sheet and core materials. Figure 3(b) illustrates the potential failure modes. The failure loads for each of the modes are calculated using the equations given in References 8 and 9.
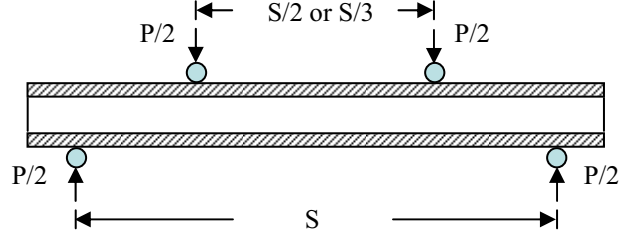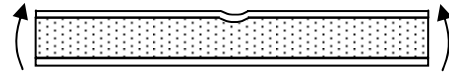
(a) Schematic of 4-point bend flexure loading
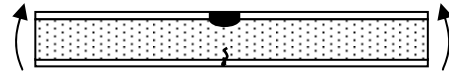
(a) Face yielding

(b) Core shear

(c) Face wrinkling

(d) Face wrinkling

(b) Failure modes under flexure loading

Figure 3: Schematic of 4-point bend flexure test and potential failure modes

(a) Face yielding

When face yielding occurs, the stress in the face sheet exceeds the compressive yield strength of the face sheet. The failure load P_f can be calculated using the beam equation [8, 9]:

$$P_f = \frac{16 D_0 \sigma_f b}{SdE_f}$$

(2)

Where D_0 is the flexural rigidity of the face sheet, $D_0 = \frac{E_f t_f d^2}{2}$.

(b) Core shear

Assuming parabolic distribution of shear stress in the core, the failure load for core shear failure is

$$P_f = \frac{4}{3}\tau_c db \tag{3}$$

(c) Face wrinkling

When face wrinkling occurs, the stress in the face sheet σ_f exceeds or equals to the critical wrinkling strength σ_{cr} of the sandwich, which is given by:

$$\sigma_{cr} = 0.5\left(E_f E_c G_c\right)^{1/3} \tag{4}$$

The failure load for face wrinkling is:

$$P_f = \frac{16 D_0 \left(E_f E_c G_c\right)^{1/3}}{S d E_f} b \tag{5}$$

Based on Eqs (2), (3) and (5), the failure load P_f under quarter point loading for the three different failure modes were calculated for glass/vinyl ester composite face sheet and three core materials and were plotted as a function of the span S in Figure 4.

   Because the face sheet yielding involves only face sheet properties, there is one curve for all three core materials. For Eco-Core and Balsa cores, face wrinkling occurs at very high load and/or large span, therefore this failure is difficult to simulate. Furthermore, before wrinkling occurs, the specimen fails by face sheet yielding. Face yielding and core shear are the possible failure modes that can be simulated by 4-point bend flexure test. The failure mode is core shear for span less than 24 in and 37 in for Eco-Core and balsa, respectively. The failure mode is face compressive yielding for spans greater than the above limits. The test span can be reduced to lower limits if the load points are moved to third point (See Figure 5). The span limits are 18 in and 28 in for Eco-Core and balsa, respectively. For PVC core, the failure load required for face yielding is higher than that for face wrinkling. Therefore core shear and face wrinkling are the possible failure modes. The failure mode is core shear if the span is less than 78 in and is face

wrinkling if the span is greater than that value. For third point loading, that limits reduced to 40 in.
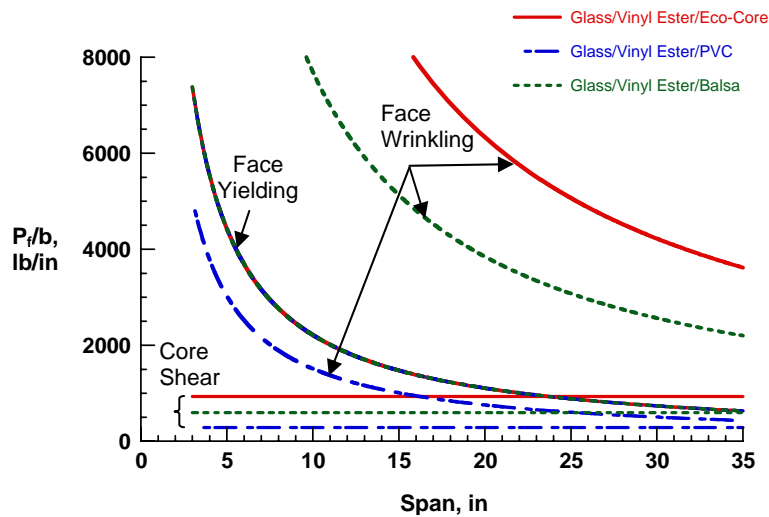

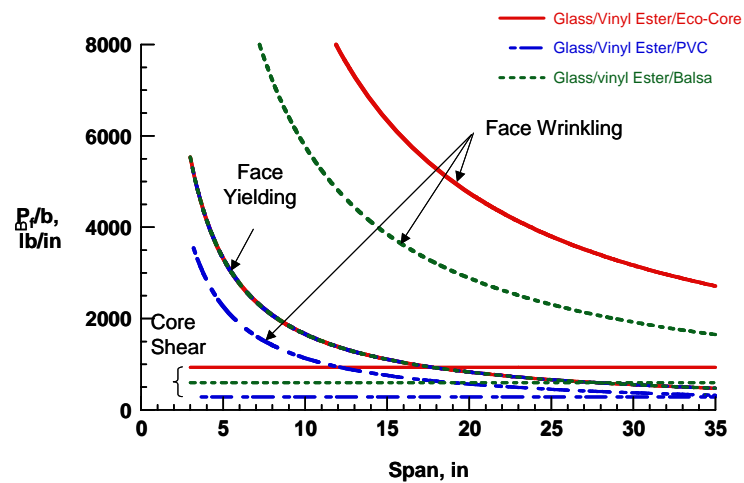Figure 4: Design plot for different core materials under quarter point flexure loading

Figure 5: Design plot for different core materials under third point flexure loading

2.3 Edgewise Compression Test Specimen

Under edgewise compression, (See Figure 6(a)), the possible failure modes were identified by many researchers [9] and are shown in Figure 6(b). The failure modes are general buckling, shear crimping, face wrinkling and face dimpling. There are two modes of face wrinkling: symmetrical and anti-symmetrical. Dimpling is a symmetrical mode of face wrinkling.
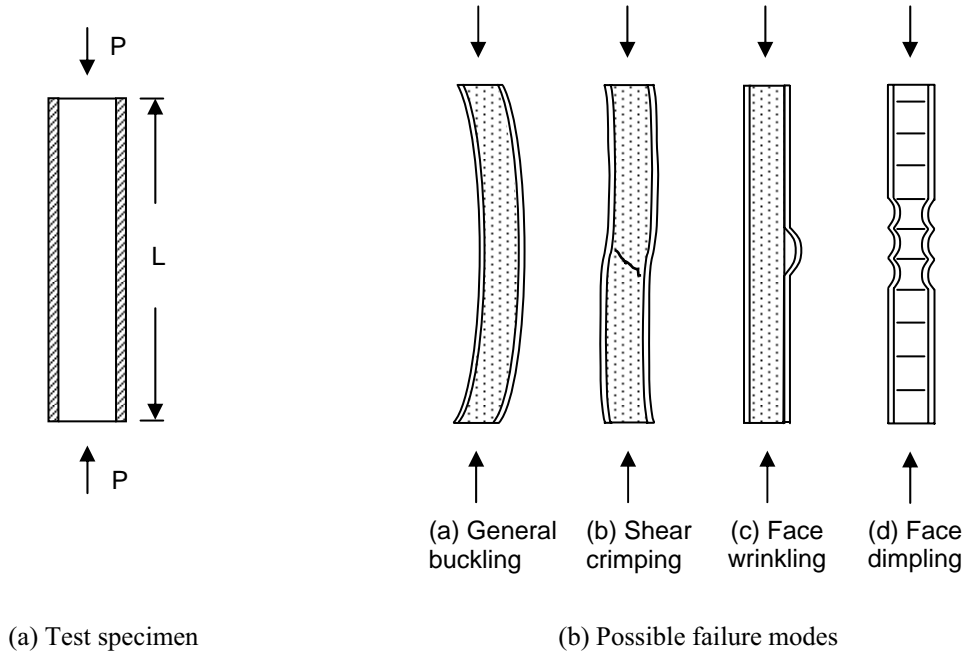

(a) General buckling   (b) Shear crimping   (c) Face wrinkling   (d) Face dimpling

(a) Test specimen   (b) Possible failure modes

Figure 6: Schematic of edgewise compression test and possible failure modes

(a) General Buckling

It is an Euler buckling of the specimen including shear deformation effect. The buckling load $P_{buckling}$ is given by:

$$P_{buckling} = \frac{\pi^2 D}{\left\{ L^2 + \frac{\pi^2 D t_c}{G_c d^2} \right\}} b \qquad (6)$$

The flexural stiffness D and the expression for its components are given in Figure 1.

Equation 6 simplifies to Eq. 7 for thin face sheet sandwich beam, Eq. 8 for thick face sheet and Eq. 9 for soft core.

$$P_{thin} = \frac{\pi^2 D}{\left\{ L^2 + \dfrac{\pi^2 D t_c}{G_c d^2} \right\}} b \qquad (7)$$

$$P_{thick} = \frac{\left\{ \dfrac{2\pi^2 D_f D_0}{L^4} + \dfrac{\pi^2 D G_c d^2}{L^2 t_c} \right\}}{\left\{ \dfrac{n^2 \pi^2 D_0}{L^2} + \dfrac{G_c d^2}{t_c} \right\}} b \qquad (8)$$

$$P_{soft} = \frac{2\pi^2 D_f}{L^2} b \qquad (9)$$

(b) Shear crimping load

Shear crimping is a failure of core due to low shear modulus of the core (G_c). The shear crimping failure load P_s is given by:

$$P_s = \frac{G_c d^2}{t_c} b \qquad (10)$$

(c) Wrinkling failure load

There are two types of wrinkling instability; symmetrical and anti-symmetrical modes of buckling of face sheets. The failure load for symmetrical wrinkling is:

$$\sigma_{cr} = 0.91 \left(E_f E_c G_c \right)^{1/3} \quad \text{for } h < t_c/2 \qquad (11)$$

$$\sigma_{cr} = 0.817 \sqrt{\frac{E_f E_c t_f}{t_c}} + 0.166 G_c \left(\frac{t_c}{t_f} \right) \quad \text{for } h \geq t_c/2 \qquad (12)$$

where h is the depth over which the core is affected by the wrinkling of the face sheet.

Failure load for anti-symmetrical mode of face sheet buckling is

$$\sigma_{cr} = 0.51\left(E_f E_c G_c\right)^{1/3} + 0.33 G_c\left(\frac{t_c}{t_f}\right) \quad \text{for } h < t_c/2 \tag{13}$$

$$\sigma_{cr} = 0.59\sqrt{\frac{E_f E_c t_f}{t_c}} + 0.387 G_c\left(\frac{t_c}{t_f}\right) \quad \text{for } h \geq t_c/2 \tag{14}$$

The critical stresses for all four possible failures are shown in Figure 7 for FGI 1854/Derakan 510A-40/Eco-Core sandwich. The minimum stress, that is, $\sigma_{cr} = 0.91\left(E_f E_c G_c\right)^{1/3}$ is used to predict the failure load. Therefore the wrinkling load is:

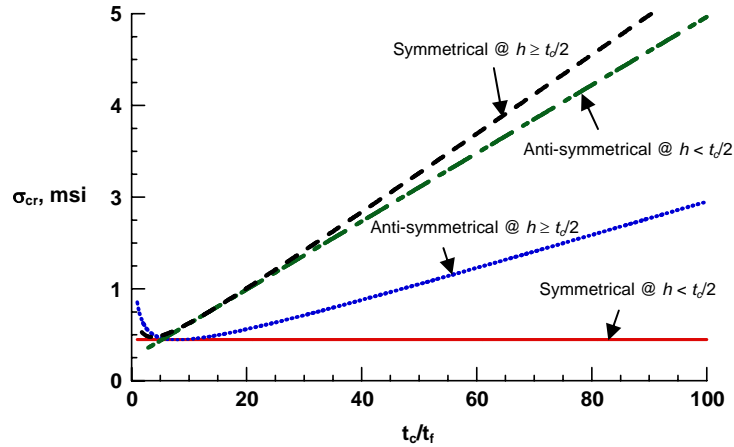$$P_w = 0.91 t_f\left(E_f E_c G_c\right)^{1/3} b \tag{15}$$

Figure 7: Critical wrinkling stress as a function of t_c/t_f

Figure 8 is the plot of critical load P_{cr}/b against specimen length L for FGI 1854/Derakane 510A-40/Eco-Core illustrating different failure modes under edgewise compression loading. Of the three failures, only the sandwich beam buckling and shear crimping are important. These

failure modes are considered to assess the failure of balsa and PVC along with Eco-Core in Figure 9. For short specimens, both shear crimpling and general buckling are equally probable. For length, L, greater than 3, 10 and 15 in, the failure is by buckling for Eco-Core, balsa and PVC cores, respectively. Therefore, the test specimen must be longer than the above values to simulate the buckling failure.
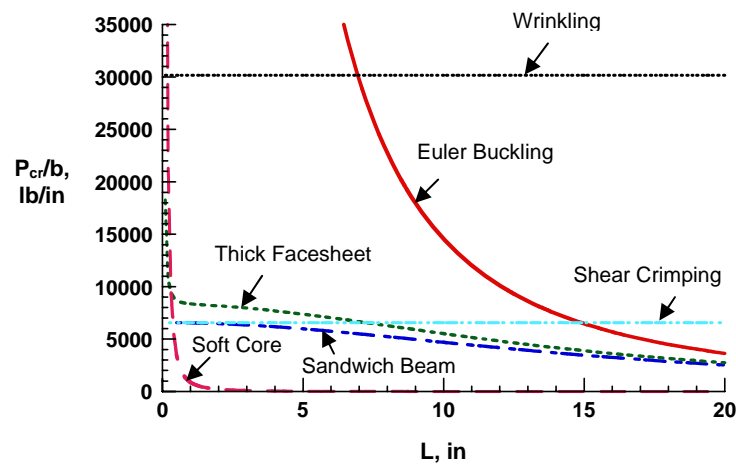
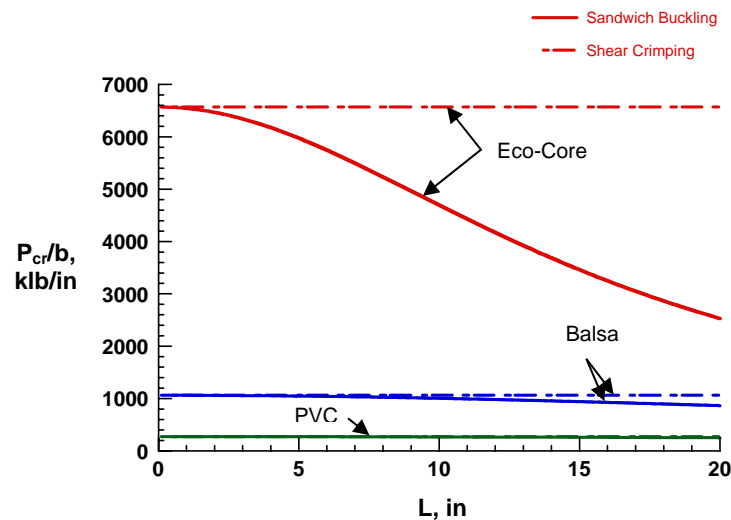Figure 8: Critical load as a function of specimen length

Figure 9: Critical load as a function of specimen length for different core materials

In summary, for Eco-Core sandwich panel test specimen span (*S*) and width (*b*) are:
1.   Short beam shear (Core shear failure): $S = 4$ in; $b = 2$ in
2.   4-point bend flexure: $S = 15.5$ in; b = 2 in
3.   Edgewise compression: $L = 8$ in; $b = 1$ in

The nominal thickness of the core and the face sheet selected are 1.0 in and 0.05 in, respectively.

3   FABRICATION OF SANDWICH PANEL AND SPECIMEN

The sandwich face sheets were unidirectional 3-ply FGI 1854 glass/Derakane 510A-40 vinyl ester composite fabricated by Vacuum Assisted Resin Transfer Media (VARTM) process [10]. The thickness of face sheet achieved was 0.55 in. The core material used was Eco-Core. The properties of the face sheet and the core material are listed in Table 1. The manufacturing process of Eco-Core is described in Reference 2. Eco-Core panels of 14"×14"×1" were made and adhesively bonded to the face sheets. The adhesive used was Loctite Hysol E-90FL epoxy adhesive. It is a toughened and medium viscosity adhesive with tensile strength of 1,900 psi, lap shear strength of 810 psi and elongation of 64%. Vacuum bag was used for the bonding and the pressure applied was 20 inHg (9.8 psi). The sandwich panel was kept in vacuum bag at room temperature for 8 hours for the adhesive to be cured.   Figure 10 shows the bonding interface morphology. The adhesive layer was about 100 μm thick. Noticed that a penetration layer existed next to the adhesive layer in which the adhesive filled the microballons of the core. The thickness of the penetration layer was about 700 μm. After fabrication, the sandwich panel was cut into specimens for short beam shear, 4-pt bend flexure and edgewise compression tests. Table 2 lists the specimen nominal geometries for different tests.
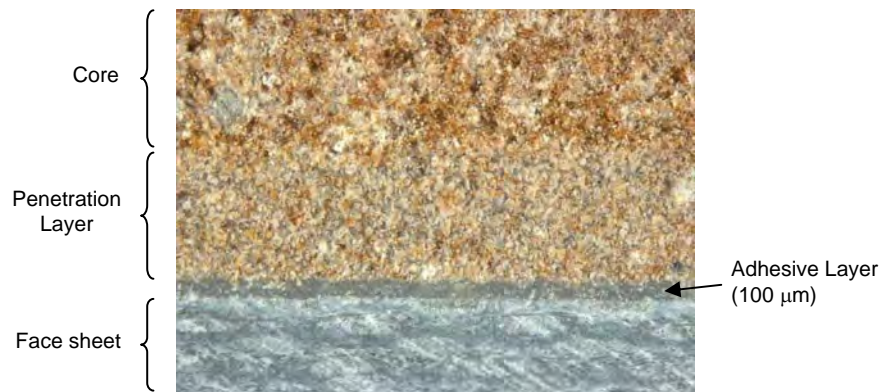

Figure 10: Morphology of the facesheet-Eco-Core bonding region

Table 2: Specimen nominal geometry

Specimen Geometry	Test		
	Short Beam Shear	4-pt Bend Flexure	Edgewise Compression
Lenth, L, in	6.0	20.0	8.0
Width, b, in	2.0	2.0	1.0
Thickness, d, in	1.1	1.1	1.1
Span Length, S, in	4.0	15.5	-

4   Testing

Short beam shear, 4-point bend flexure and edgewise compression tests were conducted on the FGI 1854 glass/Derakane 510A-40 face sheet-EcoCore sandwich specimens to verify the design theories described in the Design of Test Specimens section. The tests were conducted in an Instron 4202 testing machine with a 10 kip load cell. During each of the tests, load and displacement were recorded continuously by data acquisition system and the specimen was monitored visually as well as recorded on a digital camcorder.

4.1 Short Beam Shear Test

The 4-point short beam shear test was conducted in accordance with ASTM standard C393-00. The specimens were 6 in long, 2 in wide and 1 in thick. Quarter point loading was applied. The supporting span length was 4 in and the upper loading span was 2 in. Figure 11 shows the test setup. The specimens were loaded at a cross-head speed of 0.02 in/min.   The test was repeated on three specimens.

Figure 11: Short beam shear test setup

4.2 4-point Bend Flexure Test

The 4-point bend flexure test was conducted in accordance with ASTM standard C393-00. The specimens were 19.5 in long, 2 in wide and 1 in thick. Third point loading was used. The supporting span length was 15.5 in.   The loading span was 5.2 in. Figure 12 shows the test setup. The specimens were loaded at a cross-head speed of 0.05 in/min.
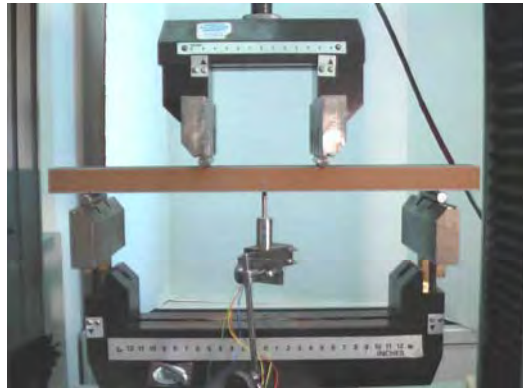

Figure 12: 4-pt bend flexure test setup

4.3 Edgewise Compression Test

Edgewise compression test was conducted in accordance with ASTM standard C364-00. The specimen ends were supported by two clamps made of rectangular steel bars fastened together to prevent the specimen from slipping from the fixture. The specimen was 8 in long, 1 in wide and 1 in thick. The unsupported length (L') was 7 in. The test was performed at the cross-head speed of 0.02 in/min. As previously stated, load and displacement were continuously recorded and the specimen was monitored by a digital camcorder. Figure 13 shows the test setup.
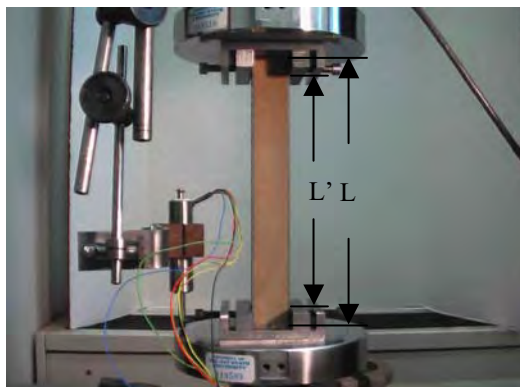

Figure 13: Edgewise compression test setup

5   Test Results and Discussion

5.1 Short Beam Shear Test

The specimen geometry and the failure loads were summarized in Table 3. Figure 14 shows the load-displacement responses of three tests. Each curve shows two load drops indicating two shear crack formation during the test. At the first load drop, one crack initiated at one upper loading point just below the face sheet and propagated across the core at 45° reaching the bottom face sheet. Figure 15(a) demonstrates the appearance of the first crack. After the first load drop, the load started to increase again until reaching the second peak. At the second load drop, another crack appeared symmetrically on the opposite side. Figure 15(b) shows the two cracks demonstrating typical shear failure of the core. Once the crack reached the bottom face sheet, it continued to grow at the interface between the penetration layer and core. Based on Eq. 1, the predicted critical load is 1,882 lb. The experimental data give an average 2,712 lb of three tests. The experimental failure load is higher than the predicted value possibly because the core was confined between the face sheets that would have strengthened the core.

Table 3: Specimen geometry and failure loads of short beam shear test

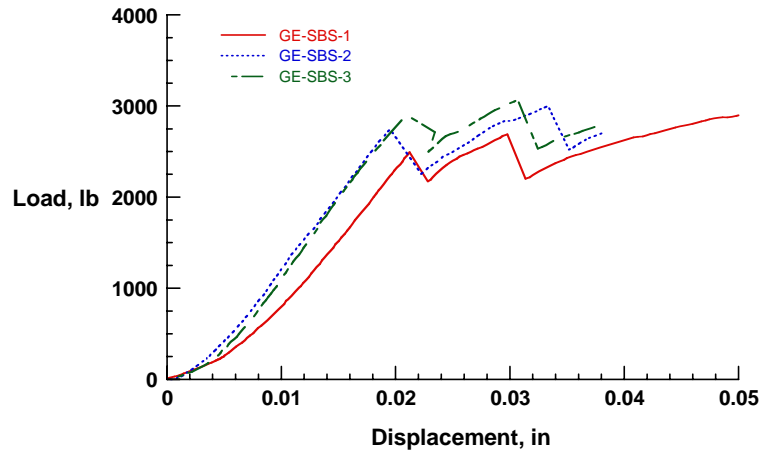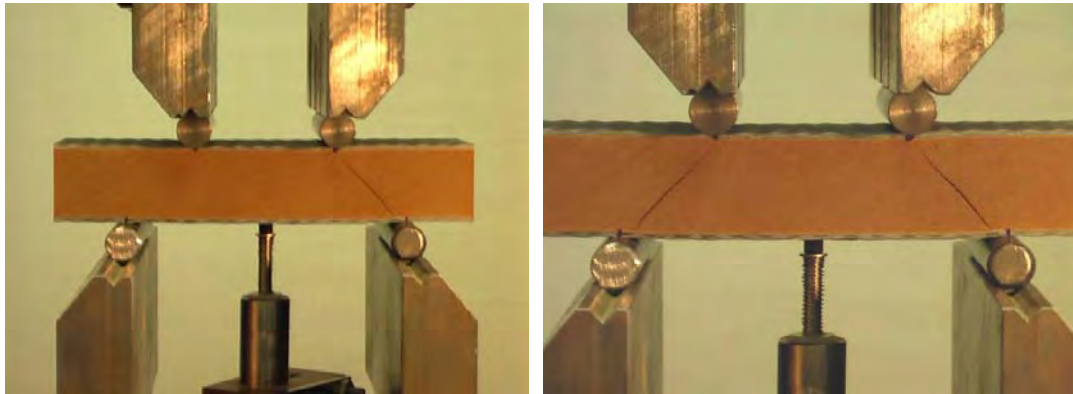| Specimen#	Length (L), in	Width (b), in	Thickness (d), in	Failure Load (P_f), lb
GE-SBS-1	5.90	2.00	1.07	2,492
GE-SBS-2	5.90	1.99	1.07	2,744
GE-SBS-3	6.01	2.07	1.07	2,900

Figure 14: Load-displacement response of short beam shear test

(a) The first crack on the right side   (b) The second crack on the left side

Figure 15: Shear failure of short beam shear test

5.2 4-point Bend Flexure Test

One of the limitations of this test was test fixture span. The fixture we had has about 15.5 in instead of minimum 18 in span for third point loading in order to simulate face yielding. Therefore, only two tests were conducted. One is loading at one-third point and the other is 3-point bend loading. The load deflection responses of the two tests are shown in Figure 16. Both

specimens failed by core shear followed by core-face sheet interfacial debonding (See Figure 17). The failure mode and crack initiation and propagation were similar to that of the short beam shear test. The experimental failure load was compared with the design plot as shown in Figure 18. The predicted shear failure load is 1,882 lb while the experimental failure initiation load is 819 lb. A further study was conducted to explore the reasons for the premature failure. The specimen was analyzed for flexural compression and tension failure in the core.
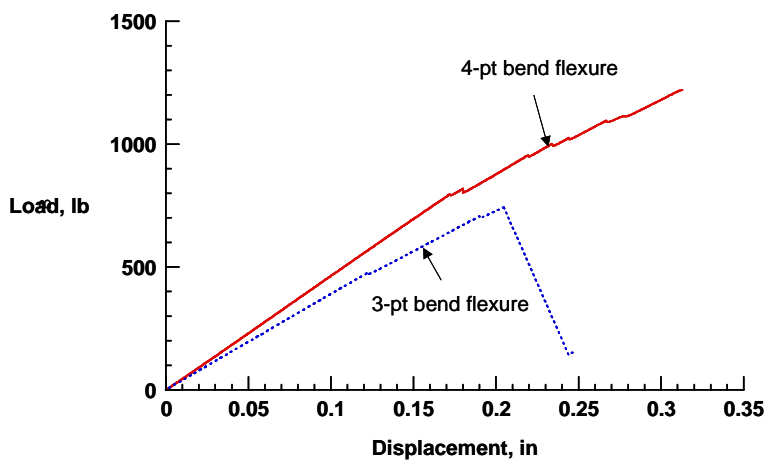

Figure 16: Load-displacement response of 4-pt bend and 3-pt bend flexure tests
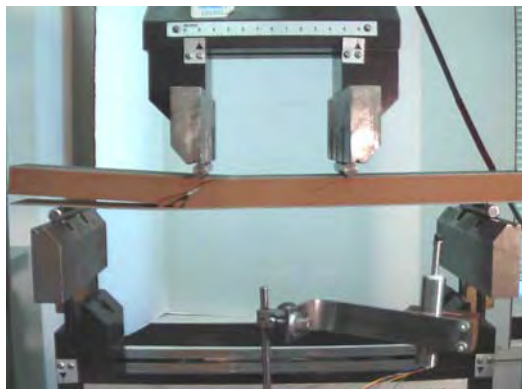

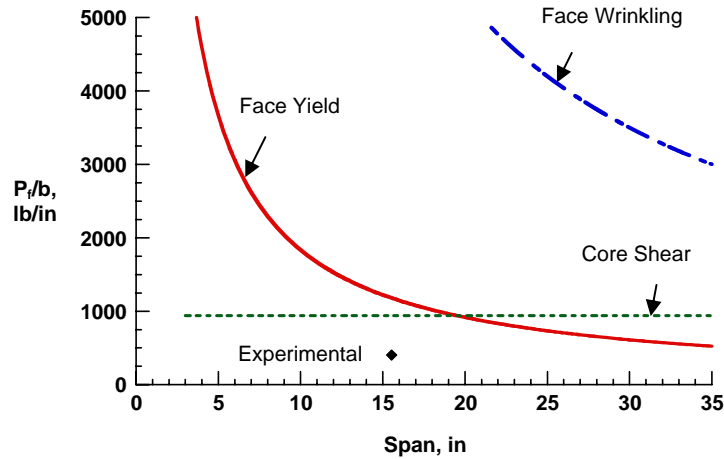Figure 17: Post failure picture of 4-pt bend flexure test

Figure 18: Comparison of design and experimental results for 4-point bend flexure test

5.3 Edgewise Compression Test

Table 4 summarizes the specimen geometry and the failure loads of three edgewise compression tests. Figure 19 shows the load-displacement plots of three tests. The load-displacement plot of specimen GE-EC-1, which is represented by the solid line in Figure 19, shows two load drops. The load first dropped at 6,579 lb resulting in one face sheet buckling which is illustrated in Figure 20(a). The second load drop occurred at 6,560 lb. This time the other face sheet buckled and separated from the core (See Figure 20(b)). Specimens GE-EC-2 and GE-EC-3 showed simultaneous face sheet buckling on both sides. Figure 21 compares the predicted and experimental critical buckling loads. The predicted critical buckling load is 5,496 lb while the experimental critical load is 6,356 lb. Note that the debonding initiated and propagated along the face sheet-adhesive interface rather than in the adhesive impregnated layer or in the core which is considered to be a weak region.

Kunigal Shivakumar, Huanchun Chen and Chris Ibeh

Table 4: Specimen geometry and failure loads of the edgewise compression test

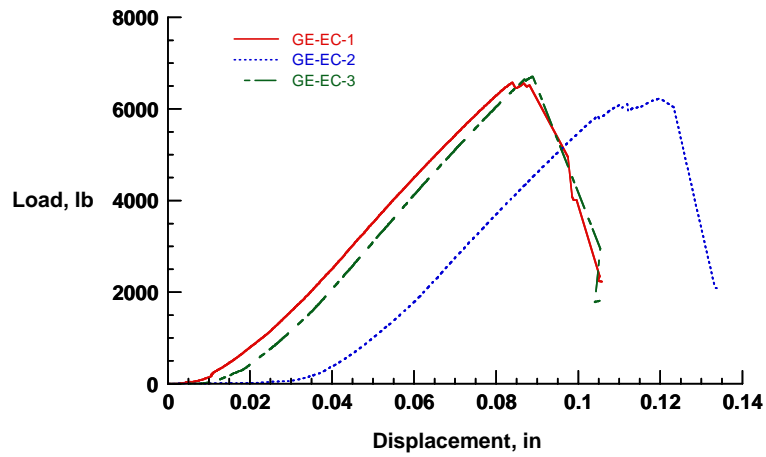| Specimen#	Length (L), in	Unsupported Length (L'), in	Width (b), in	Thickness (d), in	Initial Failure Load $(P_{cr)}$, lb
GE-EC-1	7.98	6.98	1.00	1.07	6,579
GE-EC-2	7.98	6.98	0.95	1.07	5,848
GE-EC-3	7.98	6.98	1.00	1.07	6,642

Figure 19: Load-displacement response of edgewise compression test
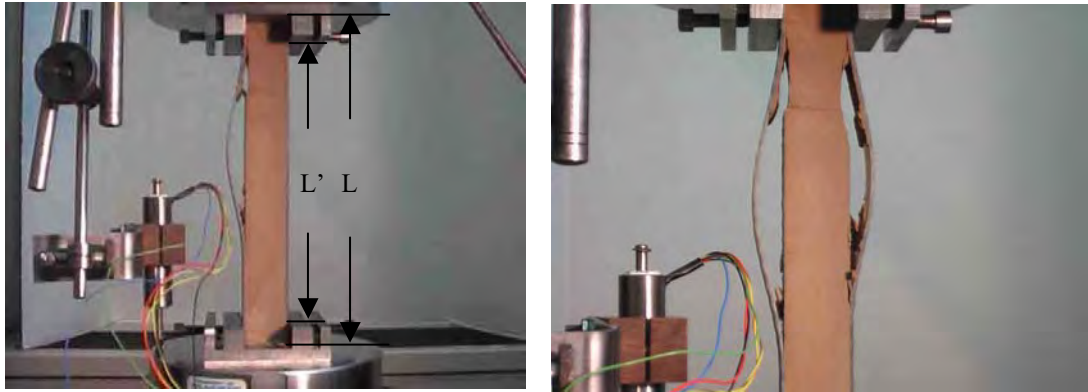
(a) Face sheet buckling on one side   (b) Face sheet buckling on both sides

Figure 20 Failure modes of edgewise compression test
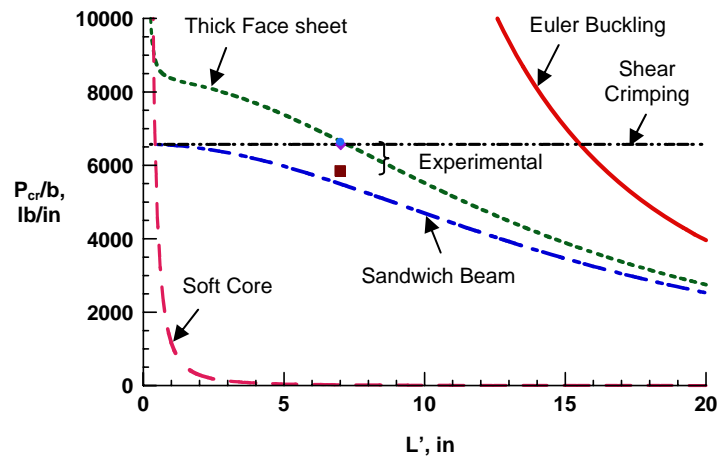
Figure 21: Comparison of prediction and experimental data of edgewise compression failure

5.4 Edgewise Compression with Delamination

In order to understand the delamination stability and propagation in sandwich structure, a through-width delamination test was conducted on the specimen with a 1-in long interfacial delamination created below the face sheet-core bonding line parallel to the face sheet in the

middle of specimen (See Figure 22). Figure 23 shows the load-displacement plots of three tests. Table 5 summarizes the specimen geometry and the buckling loads of the three tests. The failure occurred first by buckling of the delaminated face sheet that was followed by delamination growth. Final fracture was delamination on both sides. Figure 24 presents the initiation and final fracture of the test specimen. The median value of buckling load is 4,319 lb with a range of 574 lb. This load compares very well with the predicted buckling load ($P_{cr}=2\pi^2 D/a^2$) of 4,814 lb for clamped-clamped strip.
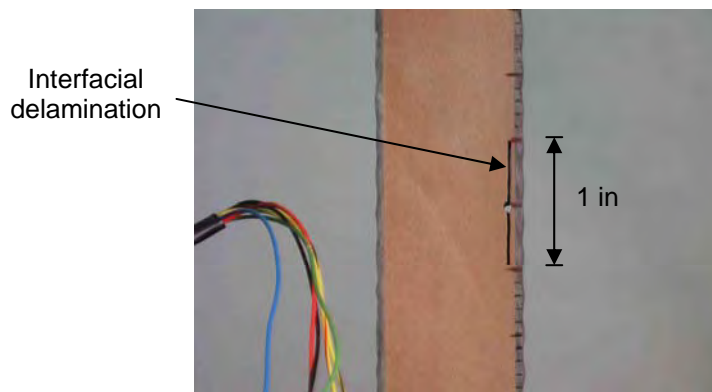
Figure 22: Delaminated edgewise compression specimen

Table 5: Specimen geometry and failure loads of delaminated edgewise compression test

| Specimen#	Length (L), in	Usupported Length (L'), in	Width (b), in	Delamination Length (2a), in	Thickness (d), in	Failure Load (P_{cr}), in
GE-EC-delam-1	7.98	6.98	1.01	0.99	1.07	4,032
GE-EC-delam-2	7.98	6.98	0.96	0.97	1.07	4,343
GE-EC-delam-3	7.98	6.98	0.94	0.97	1.07	4,606
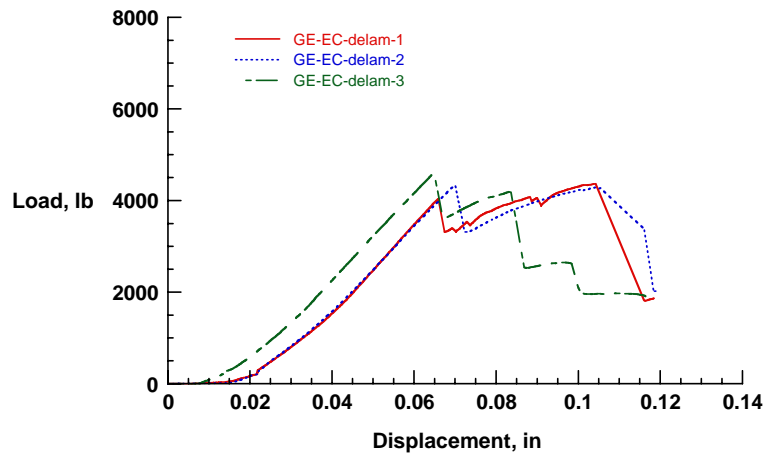
Figure 23: Load-displacement plot of delaminated edgewise compression test

(a) Face sheet buckling on one side (b) Final face sheet buckling on both sides
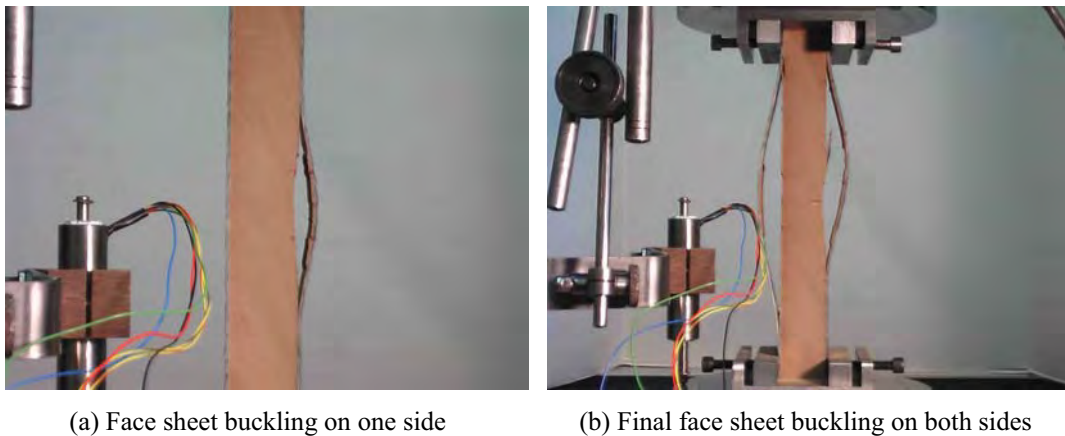
Figure 24: Failure modes of delaminated edgewise compression test

6 CONCLUSIONS

Eco-Core material was developed under the US Navy (ONR program). It offers exceptional fire and toxicity properties and very good mechanical properties compared to other core materials such as balsa and PVC. Structural performance of Eco-Core sandwich panel which used a composite face sheet was tested through a design of test specimen to simulate different failures that occur in similar sandwich structures. The design exercise demonstrated that Eco-Core

sandwich panels are highly unlikely to fail by face sheet wrinkling. The potential failure modes are core shear, core fracture by flexure, core shear crimping, face sheet yielding and face sheet buckling. Many of these failures were simulated by short beam shear, 4-point bend flexure and edgewise compression tests. Predicted failure loads for short beam shear and edgewise compression agreed very well with the experimental data (with the accepted data scatter). Furthermore, through-width delaminated panel failed as expected by buckling of delaminated sublaminate. The predicted load agreed very well with test data. Four-point bend flexure tests were not successful because of test fixture limitation. This test and others will be repeated to generate data of statistical significance.

7   ACKNOWLEDGEMENT

8   REFERENCES

[1]   R. L. Sadler, M. M. Sharpe and K. N. Shivakumar, "Water Immersion Of Eco-Core and Two Other Sandwich Core Materials," SAMPE 2008.

[2]   K. N. Shivakumar, S. D. Argade, R. L. Sadler, M. M. Sharpe, L. Dunn, G. Swaminathan, and U. Sorathia, "Processing and Properties of a Lightweight Fire Resistant Core Material for Sandwich Structures, Journal of Advanced Materials, Vol. 38, No. 1, 2006, pp. 32-38.

[3]   S. Argade, K. Shivakumar, R. Sadler, M. Sharpe, G. Swaminathan and U. Sorathia, "Mechanical Fire Resistance properties of a Core Material," SAMPE 2004, May 16-20, 2004 Long Beach Convention Center, Long Beach, CA.

[4]   K. N. Shivakumar, M. Sharpe, and U. Sorathia, "Modification of Eco-Core to Enhance Toughness and Fire Resistance", SAMPE-2005, Long Beach, CA.

[5]   G. Swaminathan, K. N. Shivakumar and M. Sharpe, "Material Property Characterization of Glass and Carbon/Vinyl Ester Composites," Composites Science and Technology, Vol. 66, No. 10, pp. 1399-1408.

[6]   http://www.baltek.com.

[7]   http://www.diabgroup.com/americas/u_products/u_divinycell_h.html.

[8]   H. G. Allen, Analysis and Design of Structural Sandwich Panels, Pergamon Press, Oxford, 1969.

[9]   D. Zenkert, An Introduction to Sandwich Construction, Chameleon Press, London, UK, 1997.

[10]   R. L. Sadler, K. N. Shivakumar, and M. M. Sharpe, "Interlaminar Fracture Properties of Split Angle-Ply Composites," SAMPE 2002, Long Beach, CA.

JACK VINSON'S SESSIONS

ON ELASTICA RESPONSE OF SANDWICH PANELS WITH A COMPLIANT CORE

Y. Frostig[1]

Technion-Israel Institute of Technology
Faculty of Civil and Environmental Engineering
Haifa 32000, Israel
e-mail: cvrfros@techunix.technion.ac.il

Key words: elastica, sandwich panels, soft core, buckling, post-buckling, wrinkling.

Summary. *The elastica behavior of a sandwich panel with a "soft" core when subjected to in-plane compressive loads is presented and it is compared with the elastica response of its equivalent single layer (ESL) with shear deformations. The field equations are described for the sandwich and the ESL panels. They have been derived using the High-Order Sandwich Panel (HSAPT) approach that takes into account the vertical flexibility of the core. The governing equations include the effects of the extension of the mid-surface rather then the classical elastica approach that assumes that the mid-plane of the panel does not extend as well as the shear deformations of the face sheets. The results of the elastica response of a simply-supported sandwich panel and its equivalent panel with shear deformations when subjected to in-plane compressive loads are presented and compared. The results reveal that the ESL behavior differs significantly then that of the sandwich panel.*

1 INTRODUCTION

Modern sandwich panels are used in a large variety of applications within the aerospace, naval and transportation industries as main and secondary carrying structural components. In order to exploit their potential and to define their safety the non-linear response that consist of large displacements and large rotations, i.e. elastica, is more then required. A typical sandwich panel is actually a layered structure that consists of two face sheets made of metal or laminated composite and a core that is made of either metallic or low strength honeycomb or foam. In modern sandwich panel this core is usually compliant, low strength and compressible. As a result, its shape is not preserved under deformation as well as distortions in the section of the pane.

In general, two major approaches are considered for the analysis. In the first one the actual layered panel is replaced by an equivalent one that consist of a single layer, denoted by ESL (equivalent single layer) with equivalent properties, see for example Mindlin first-order theory [1], and Reddy's high-order theories [2], while in the second one a layered configuration is considered. The classical approaches to the layered sandwich panel assume

---

[1] Professor of Structural Engineering, Ashtrom Engineering Company Chair in Civil Engineering

that the core is incompressible and is infinitely stiff in the vertical direction, see text books by Allen [3], Plantema [4], Zenkert [5] and Vinson [6]. A different approach where the flexibility of the core is considered along with the localized effects involved has been taken by the author and many others using the High-Order Sandwich Panel Theory (HSAPT) approach, see Frostig *et. al* [7]. It has been applied successfully to a large number of linear and no-linear analyses such as: buckling of sandwich panels, see Frostig and Baruch [8], and Frostig [9], non-linear behavior of sandwich panels with rigid and non-rigid interfaces including branching behavior, see Sokolinsky and Frostig [10] and many more.

Elastica of inextensible bars and beams made of a solid section, had attracted many researchers for many years starting with the pioneering works of Euler and Lagrange, see Dym and Shames [11], using closed-form solutions with the aid of elliptic integrals. The elastica of bars with various sections, particular type of loadings and boundary conditions has been studied by many researchers that use analytical or numerical approaches, and to mention a few: Wang [12] dealt with elastic of a clamped-simply-supported beam using perturbation, asymptotic and numerical method; Chucheepsakul and Huang [13] used the FE approach to analyze a beam with a point load between the supports and many more In general, the analyses of the elastica of the rods, mentioned above, use the equilibrium of the deformed shape of a differential segment of the rod to derive the equilibrium equations.

A variational approach that uses Reissners' kinematic relations, see Reissner [14], has been considered by Flajs *et al* [15] that used Lagrange multiplier to impose the kinematic relations as constraints; and similarly Pak and Stauffer [16].

The problem of large deflections of unidirectional sandwich panels has been considered by very few researchers assuming that the layered panel can be described by an equivalent single layer with shear deformation, see Huang and Kardomateas [17] and Bazant and Beghini [18].

The brief literature survey reveals that the elastica response of sandwich panels made of two face sheets and a compliant core where the vertical flexibility of the core is considered is missing. The approach used here is based on the HSAPT model along with the variational approach. The assumptions adopted follow the "classical" assumptions for sandwich structures with compliant cores: the face sheets possess in-plane and bending rigidities; the face sheets and the core material are assumed be linear elastic; the face sheets include shear deformations assuming that a plane remains plane after deformation but not perpendicular to its deformed centroidal line, and they undergo large displacements and large rotations with small strains; the core is considered as a 2D linear elastic continuum that undergoes large rigid displacements (due to its bond to the adjacent face sheets), but with kinematic relations that correspond to small deformations, where the core height may change during deformation, and section planes do not remain plane after deformation; the core possesses only shear and vertical normal stiffness, whereas the in-plane (longitudinal) normal stiffness is assumed to be nil; full bond is assumed between the face sheets and the core; and the mechanical loads are applied to the face sheets only.

The paper consists of a mathematical formulation and a numerical part. In the mathematical formulation the governing equations of a sandwich panel and the equivalent single layer panel (ESL) are described briefly. In the numerical part a comparison between the two panels are presented. Finally a summary is included and conclusions are drawn.

2 MATHEMATICAL FORMULATION

The formulation chapter consists of two parts. The first one deals with a real sandwich panel using the HSAPT approach while the second part defines the equations for an equivalent single layer sandwich panel with shear deformations.
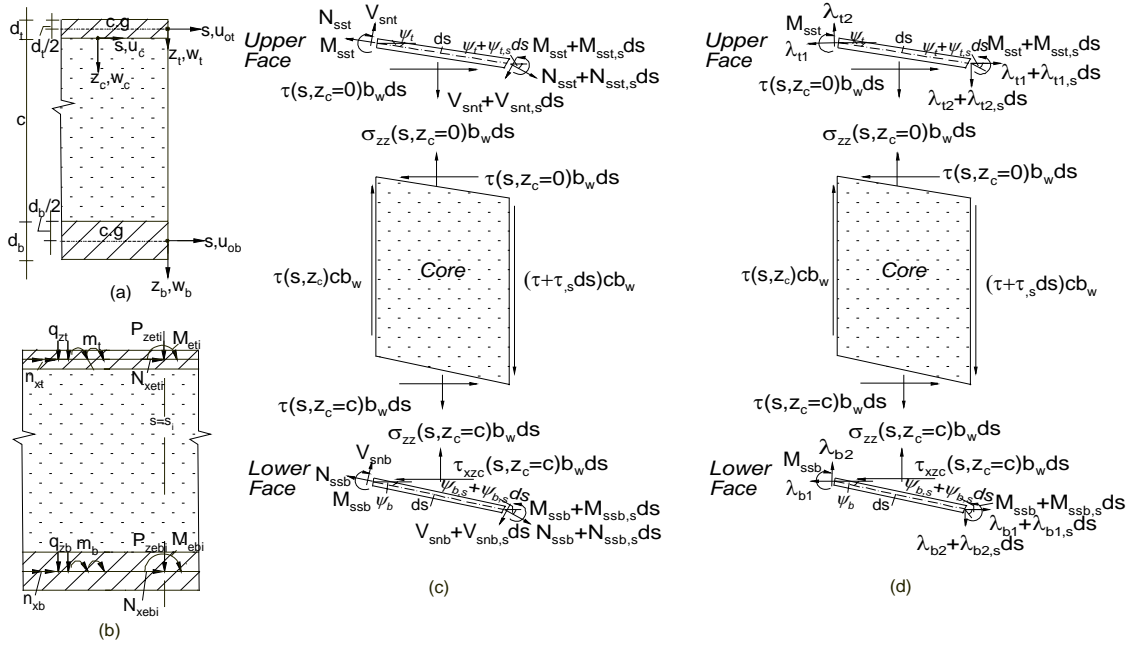

Figure 1: Dimensions and signs conventions of a typical sandwich panel: (a) geometry; (b) loads at face sheets; (c) internal stress resultants in local coordinate directions; (d) internal stress resultants in global directions.

2.1 Sandwich Panel – HSAPT model

The governing equations of the three layered sandwich panel are derived based the variational principles of extremum of the total potential energy. The external potential energy consists of the contribution of the distributed and concentrated loads applied at the face sheets, see Fig. 1b. The internal potential energy include the contribution of the normal and shear stresses in the face sheets and the vertical normal stresses and shear stresses in the core in addition to the contribution of the Lagrange multipliers, λ_{j1} and λ_{j2}, $(j=t,b)$, (see Fig. 1d), of the special kinematic relation due to the large displacements and rotations (see Reissner[14]) that read:

$$
\begin{aligned}
\frac{d}{ds} u_{oj}(s) &= \left(1 + \varepsilon_{oj}(s)\right) \cos\left(\psi_j(s)\right) - \gamma_j(s) \sin\left(\psi_j(s)\right) \\
\frac{d}{ds} w_j(s) &= \left(1 + \varepsilon_{oj}(s)\right) \sin\left(\psi_j(s)\right) + \gamma_j(s) \cos\left(\psi_j(s)\right)
\end{aligned}
\tag{1}
$$

where $u_{oj}(s)$ and $w_j(s)$ are the in-plane and vertical displacements respectively, in the global coordinates, of the face sheets; $\psi_j(s)$ is the rotation angle of the section plane of the face

sheets, $\varepsilon_{oj}(s)$ is the mid-plane strain of the face sheets; $\gamma_j(s)$ is the shear angle of the various face sheets; and s is the longitudinal coordinate, see Fig. 1 for geometry, coordinates, loads and stress resultant in local and global coordinates directions.

The governing equations of the sandwich panel are derived assuming that: the face sheets follow Navier assumption, linear isotropic, bonded to the adjacent face sheets; the core is isotropic linear and follows the results of the HSAPT model, see Frostig et al [7], that consist of a uniform shear distribution, linear vertical normal stresses, quadratic vertical normal stresses and cubic in-plane displacements. Hence after some algebraic manipulations they read:

$$\frac{d}{ds}\lambda_{j1}(s) = -\alpha\,\tau(s)\,b_w - n_{xj}(s) \tag{2}$$

$$\frac{d}{ds}\lambda_{j2}(s) = -\alpha\left(\left(-\frac{w_t(x)}{c} + \frac{w_b(x)(x)}{c}\right)E_{zc} + \frac{1}{2}\,\alpha\,c\left(\frac{d}{dx}\tau(x)\right)\right)b_w - q_{zj}(s) \tag{3}$$

$$\frac{d}{ds}M_{ss_j}(s) = \left(-\frac{\cos(\psi_j(s))\sin(\psi_j(s))}{EA_j} + \frac{\cos(\psi_j(s))\sin(\psi_j(s))}{k_j\,GA_j}\right)\lambda_{j1}(s)^2 + \left(\left(\right.\right.$$
$$-\frac{\sin(\psi_j(s))^2}{EA_j} - \frac{\cos(\psi_j(s))^2}{k_j\,GA_j} + \frac{\cos(\psi_j(s))^2}{EA_j} + \frac{\sin(\psi_j(s))^2}{k_j\,GA_j}\right)\lambda_{j2}(s)$$
$$\left.- \sin(\psi_j(s))\right)\lambda_{j1}(s) + \left(\frac{\cos(\psi_j(s))\sin(\psi_j(s))}{EA_j} - \frac{\cos(\psi_j(s))\sin(\psi_j(s))}{k_j\,GA_j}\right)\lambda_{j2}(s)^2$$
$$+ \lambda_{j2}(s)\cos(\psi_j(s)) - \frac{1}{2}\tau(s)\,b_w\,d_j + m_j(s) \tag{4}$$

$$\frac{d}{ds}\psi_j(s) = -\frac{M_{ss_j}(s)}{EI_j} \tag{5}$$

$$-\frac{1}{12}\frac{c^3\left(\frac{d^2}{ds^2}\tau(s)\right)}{E_{zc}} + \left(-\frac{1}{2}d_t - \frac{1}{2}c\right)\psi_t(s) + \frac{c\,\tau(s)}{G_{xzc}} + \left(-\frac{1}{2}c - \frac{1}{2}d_b\right)\psi_b(s)$$
$$+ u_{ot}(s) - u_{ob}(s) = 0 \tag{6}$$

where $\tau(s)$ is the shear stress in the core; $\alpha=1$ when $j=t$ and -1 when $j=b$; N_{ssj}, V_{snj} and M_{ssj} $(j=t,b)$ are the in-plane, shear and bending moments stress resultants of the upper and the lower face sheets respectively, see Fig. 1c; EA_j, GA_j and EI_j $(j=t,b)$ are the axial, shear and the flexural rigidity of each face sheet, respectively and k_j is the shear correction coefficient of the face sheet, d_j $(j=t,b)$ are the thicknesses of the face sheets, c is the thickness of the core; b_w is the width of the panel; and n_{xj}, q_{zj} and m_j $(j=t,b)$ are the in-plane and vertical distributed loads (in the global coordinates) and the bending moment distributed loads respectively.
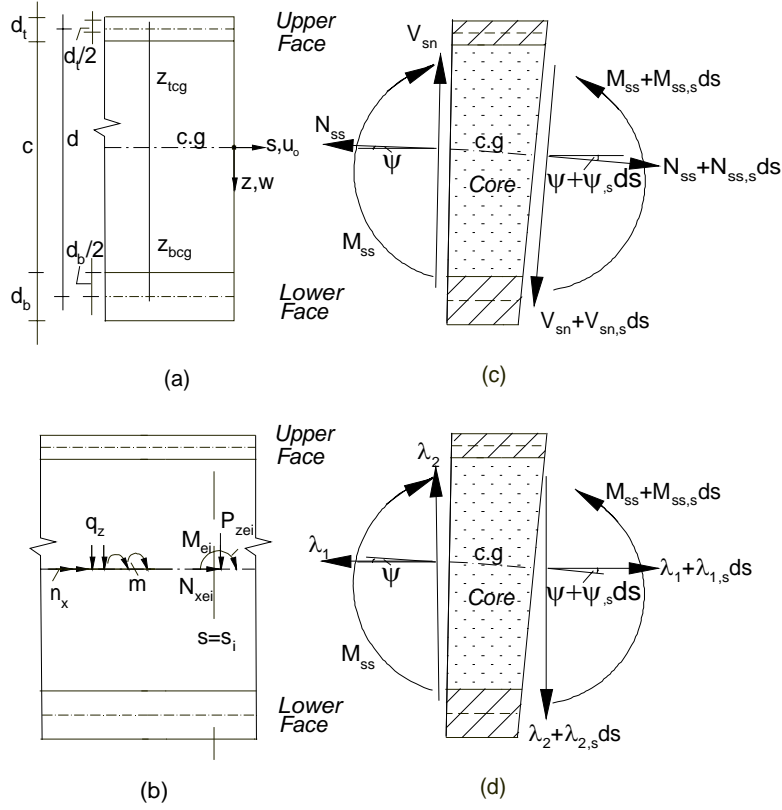
Figure 2: Dimensions and signs conventions of an Equivalent Single Layer (ESL) sandwich panel: (a) geometry; (b) loads at face sheets; (c) internal stress resultants in local coordinate directions; (d) Internal stress resultants in global directions.

2.2 Equivalent Single Layer (ESL) Sandwich Panel

The ESL approach replaces the actual layered unidirectional sandwich panel with an equivalent single layer panel that has the same rigidities and follows the well known first-order shear deformable model (FOSDT) model, see Mindlin [1]. Thus, the axial and the flexural rigidity of the equivalent panel corresponds to that of the face sheet only while the equivalent shear rigidity is that of the core only, see Fig. 2, and they yield the following constitutive relations:

$$N_{ss}(s) = EA_g \, \varepsilon(s), \, V_{sn}(s) = k_g \, GA_g \, \gamma(s), \, M_{ss}(s) = -EI_g \left(\frac{\mathrm{d}}{\mathrm{d}s} \, \psi(s) \right) \tag{7}$$

where $\varepsilon(s)$ and $\gamma(s)$ are the mid-plane strains and the shear angle of the equivalent panel; EA_g, EI_g and $k_g GA_g$ are the equivalent axial, flexural and shear rigidity of the ESL model and they are related to the rigidities of the sandwich panel through the following relations:

$$\begin{aligned} EA_g &= EA_t + EA_b \\ EI_g &= EI_t + EI_b + EA_t \, z_{cgt}^2 + EA_b \, z_{cgb}^2 \end{aligned} \tag{8}$$

$$k_g \, GA_g = G_c \, b_w \left(c + \frac{1}{2} \, d_t + \frac{1}{2} \, d_b \right), k_g = 1.0$$

where z_{cgj} ($j=t,b$) denotes the distance between the centroid of the sandwich panel and the centroid of the upper and the lower face sheet respectively, see Fig. 2a.

The elastica response of the sandwich panel that uses the HSAPT approach takes into account the shear deformations of the face sheets using the FOSDT model, see Eqs. (2) to (5). Hence, the governing equations of the ESL model correspond to those of the face sheets of the sandwich panel, in previous section, with some modifications as a result of the stress free upper and lower surfaces of the equivalent panel. Hence the governing equations of the equivalent panel read:

$$-\left(\frac{d}{ds} \, \lambda_1(s) \right) - n_x(s) = 0 \tag{9}$$

$$-\left(\frac{d}{ds} \, \lambda_2(s) \right) - q_z(s) = 0 \tag{10}$$

$$
\begin{aligned}
\frac{d}{ds} \, M_{ss}(s) = {}& \left(-\frac{\cos(\psi(s)) \, \sin(\psi(s))}{EA} + \frac{\cos(\psi(s)) \, \sin(\psi(s))}{k \, GA} \right) \lambda_1(s)^2 + \Bigg(\Bigg(\\
& -\frac{\sin(\psi(s))^2}{EA} - \frac{\cos(\psi(s))^2}{k \, GA} + \frac{\cos(\psi(s))^2}{EA} + \frac{\sin(\psi(s))^2}{k \, GA} \Bigg) \lambda_2(s) - \sin(\psi(s)) \Bigg) \\
& \lambda_1(s) + \left(\frac{\cos(\psi(s)) \, \sin(\psi(s))}{EA} - \frac{\cos(\psi(s)) \, \sin(\psi(s))}{k \, GA} \right) \lambda_2(s)^2 \\
& + \lambda_2(s) \, \cos(\psi(s)) + m(s)
\end{aligned} \tag{11}
$$

$$\frac{d}{ds} \, \psi(s) = -\frac{M_{ss}(s)}{EI} \tag{12}$$

where λ_1, λ_2 and M_{ss} and the projections of the stress resultants in the longitudinal and vertical global coordinate direction and the bending moment of the equivalent panel, respectively, see Fig. 2c and 2d.

The elastica response is described through the numerical solution of the non-linear set of differential equations that is solved using numerical schemes such as the multiple-shooting points method, see Stoer and Bulirsch [19], or the finite-difference approach using trapezoid or mid-point methods with Richardson extrapolation or deferred corrections, see Ascher and Petzold [20], as implemented in Maple, see Char *et al.* [21], along with parametric or arc-length continuation methods, see Keller [22].

3 NUMERICAL STUDY

The numerical study presents the elastica response of a sandwich panel with a "soft" core when subjected to in-plane compressive loads and compares it with the response of an equivalent single layer (ESL) model with shear deformation. The results include description of the response along the panel and deformed shape at various load levels and equilibrium curves of load versus extreme values of some structural quantities.

The panel consists of two face sheets made of Kevlar with an equivalent modulus of elasticity of *27.4 GPa* and a shear modulus of *10.55 GPa*, and a lightweight, low strength core

of *Rohacell 50* with $E_{zc}=70.0$ *MPa* and $G_{xzc}=19.0$ *MPa* where the shear deformations of the face sheets has been neglected. The edges of the sandwich panel are simply-supported with immovable conditions and they have been reinforced with edge beams to make it comparable with the conditions of the ESL model. The in-plane compressive load, applied at the right edge of the panel, has been induced through a controlled end-shortening displacement (horizontal movement), denoted by u_{oe}, of the right pinned support, see Fig. 3. The geometry, material properties and boundary conditions of the sandwich panel appear in Fig. 3a and the ESL one in Fig. 3b. Notice that the ESL model is described by the centroidal line of the core, denoted by *c.g.esl*, see Fig. 3a. In order to achieve a non-trivial solution, at the bifurcation load, an imperfection of a small distributed load has been applied to the face sheets of $q_{zt}=q_{zb}=0.01N/mm$. In the case of the ESL model the imperfection load is much smaller and equals *0.00001 N/mm*.
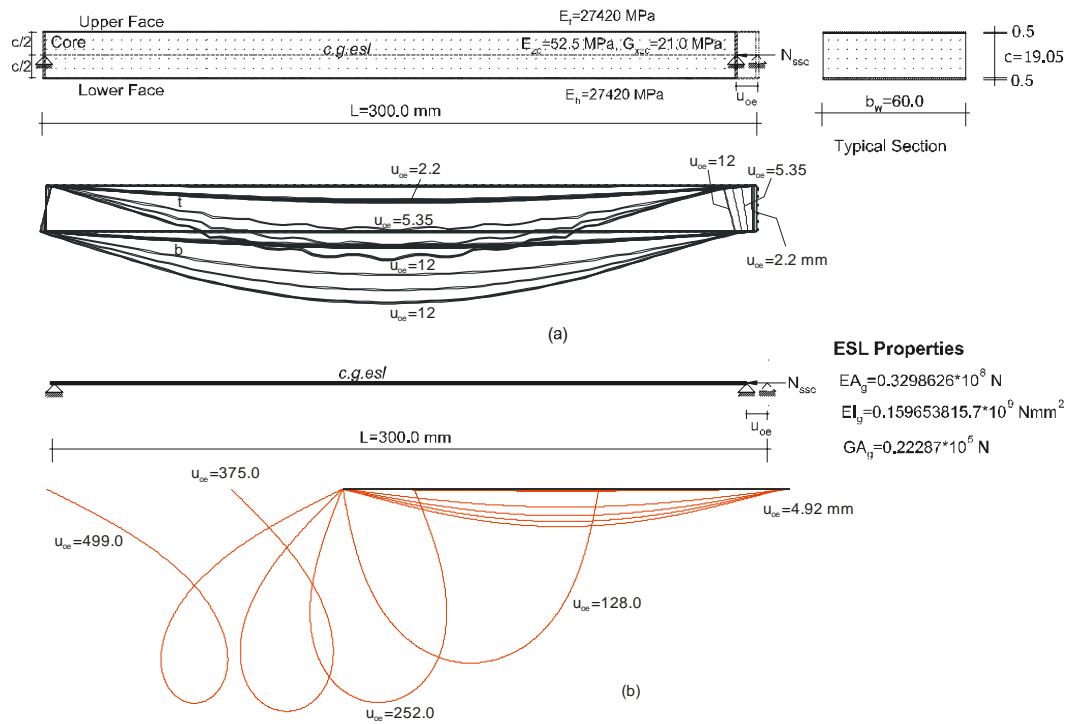

Figure 3: Geometry, mechanical properties and deformed shape of: (a) sandwich panel; (b) equivalent single layer panel.

The results of the sandwich panel correspond to a maximum end-shortening of $u_{oe}=12.0$ *mm* due to numerical difficulties while with the ESL model there is no limit and the maximum end-shortening considered reached a value of *499 mm*. The numerical difficulties of the solution of the sandwich panel stem from the fact that a mixed mode of overall and wrinkling buckling deformations has been observed as the end-shortening displacement increases. In additions, as the end-shortening of the sandwich panel increases the corresponding compressive load decreases while in the case of the ESL the compressive load increases as the

end-shortening increases. Numerically, the elastica problem of the sandwich panel is totally different and is much more sensitive as compared with that of the ESL model.

The deformed shape of the two panels appears in Fig. 3. The deformed shape of the sandwich panel appears in Fig. 3a and it describes the deformed shape of the panel at various compressive load levels that correspond to small (u_{oe}=2.2mm) and large (u_{oe}=12.0 mm) end-shortening. At the low load levels the panel exhibits overall buckling, see curve of u_{oe}=2.2 mm where the two face sheets almost move the same. As the load increases, the upper face sheet wrinkles in addition to an overall buckling, see curves of u_{oe}=5.35-12 .0 mm while the lower face sheet maintain a smooth curve with mild wrinkles. The deformed shape of the ESL model appears in Fig. 3b and it exhibits overall buckling which is totally different then that of the corresponding sandwich panel. The ESL model exhibits overall buckling with large deformations and large end-shortening displacements, u_{oe}=4.92–499 mm,.
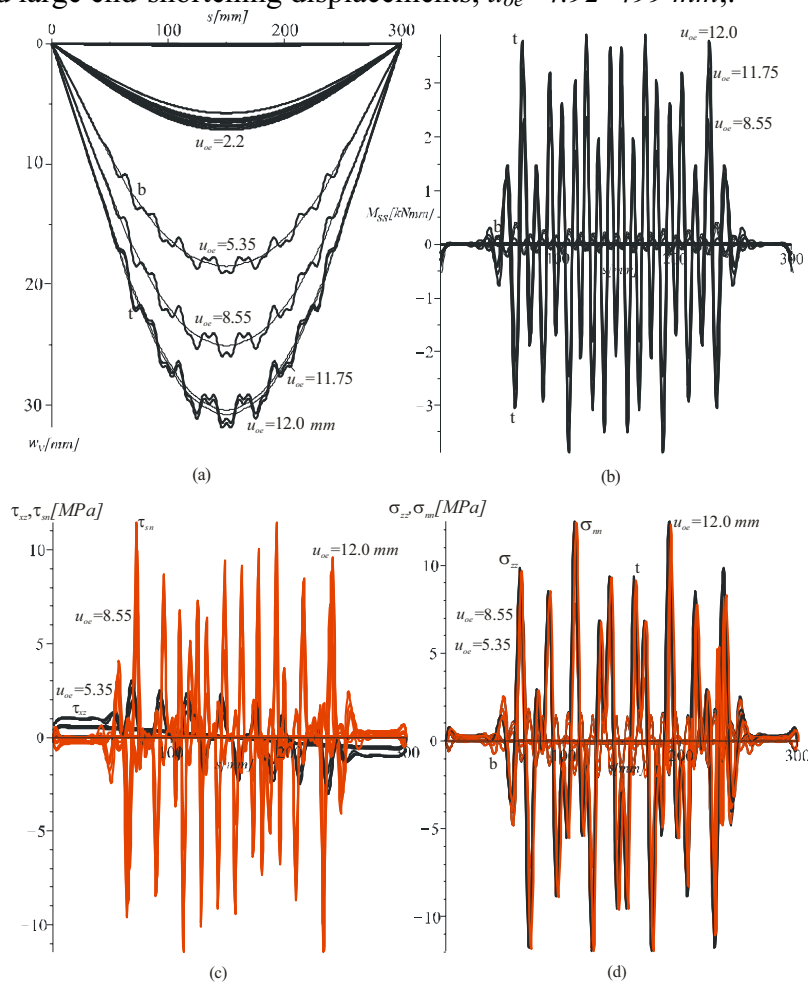
Figure 4: Sandwich panel results along panel in global and local coordinate directions. At upper and lower face sheets: (a) vertical displacements; (b) bending moments; and in core: (c) shear stress; (d) interfacial vertical stresses at face-core interfaces. Legend: _____ (thick) upper face/interface, _____ (thin) lower face/interface, black – global direction, red – local direction.

The results along the sandwich panel appear in Fig. 4 at various end-shortening levels. The vertical displacement appears in Fig. 4a and it reveals that at low end-shortening displacements overall buckling is observed and as these prescribed displacement increase wrinkling of the upper face sheet in addition to the overall buckling is observed. Notice, that also the lower face sheet has wrinkles but with small magnitude. The bending moment at each of the face sheets, see Fig. 4b, reveal extremely high values at the upper face sheet and small ones at the lower one at the large end-shortening displacements. Notice that for smaller end-shortening the bending moments are quite small. The effect of the wrinkling of the upper face sheet on the shear stresses of the core (in the global and local direction), see Fig. 4c, is significant and is associated with extremely large values. Finally the interfacial normal stresses at the upper and the lower face sheets in the global and the local vertical directions appear in Fig. 4d. Notice that also here the effects of the wrinkling of the upper face sheets are extremely large and yields an erratic behavior along the panel with large values.
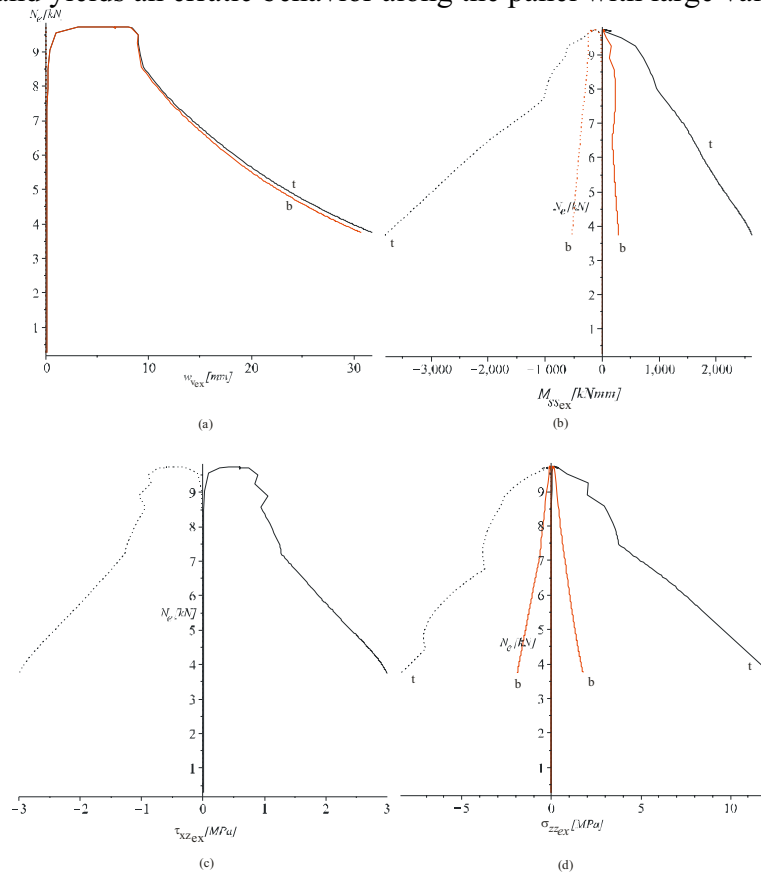
Figure 5: Equilibrium curves of a sandwich pane of load versus extreme values along panel of: (a) vertical displacements of faces sheets; (b) bending moments in faces; (c) shear stress in core; (d) interfacial vertical stresses at face-core interfaces. Legend: _____ positive value, ……. negative value, black – upper face sheet, red – lower face sheet.

The equilibrium curves of compressive load that is induced at the supports as a result of the prescribed end-shortening for various structural quantities appear in Fig. 5. Load versus the

extreme vertical displacement along the panel appears in Fig. 5a. The curves reveal that up to the buckling load there is an abrupt jump in the load with very small vertical displacements. In the post-buckling range there is a minor increase in the load as the vertical displacement increase and then it starts to drop as the displacement increases and then at a vertical displacement of about 10 mm there is a drastic drop in the load which proceeds with a steep continuous decline with an increase of the displacement. Hence, the post-buckling behavior of this panel is more that of a shell type rather then that of a beam. The same trends are observed for the extreme bending moment in the face sheets, see Fig 5b, the shear stress in the core in the global vertical direction and in the vertical interfacial stresses, see Fig. 5c and the core vertical normal stresses at the upper and the lower face-core interfaces, see Fig. 5d. Notice that the curves of the bending moments and the interfacial normal stress, immediately beyond the bifurcation point, exhibit continuous decline with the load.

The purpose of using an ESL model is to simulate the complicated behavior of the sandwich panel with a simple model. Hence, the question of to what extent is the ESL model actually described the behavior of the sandwich panel is discussed. This comparison is presented through the equilibrium curves of the sandwich panel, the bifurcations load of a sandwich panel, see Frostig and Baruch [7], denoted by HSAPT and the ESL model of load versus extreme vertical displacement that appear in Fig. 6. The curves reveal that the bifurcation load of the sandwich panel is smaller and nearly coincide with that of the HSAPT load, see [7], then that of the ESL one and the post-buckling curve are totally different. The post-buckling response of the sandwich panel is associated with a drop in the load as the vertical displacement increases while the ESL described a beam behavior where the load remains constant while vertical displacement increases. Hence, the ESL elastica behavior is totally different then that of the sandwich panel and it should be used with great cautious when simulating the real behavior of the sandwich panel.
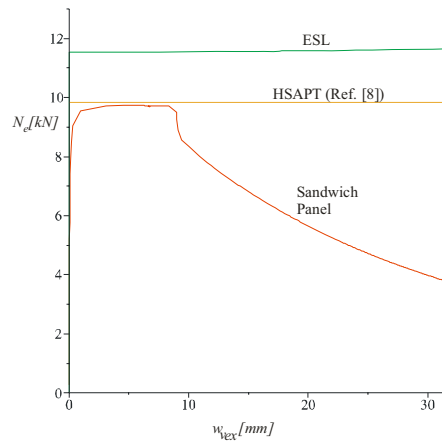

Figure 6: Load versus extreme vertical displacement of sandwich panel and ESL model.

4 SUMMARY AND CONCLUSIONS

The elastica behavior of a sandwich panel with a soft/compliant core is presented. The

analysis considers the shear deformations in the face sheets using the first-order shear deformation approach in addition to the flexural ones and takes into account the extension of the centroid lines of the face sheets. The kinematic relations adopted, Reissner's strains, are based on large displacements and large rotations. The mathematical formulation is based on a variational approach and uses Lagrange multipliers to impose the special kinematic relations.

In many applications the complex behavior of the sandwich panel is simulated using an equivalent single layer (ESL) panel. Hence, the elastica behavior of a single layer panel (ESL model) with shear deformations is presented for comparison.

The numerical study presents the results of a sandwich panel with edge beam constraints and its equivalent one where the shear deformation of the core is considered while that of the face sheets is neglected. The numerical results are described in terms of deformed shapes, structural quantities along the panel, and equilibrium curves of load versus extreme structural quantities along the panel.

The numerical investigation reveals that the sandwich panel reaches a bifurcation point in a global buckling mode and wrinkles in addition to the global buckling as it goes deep into the post-buckling range. This wrinkling phenomenon is associated with a drop in the load as the imposed end-shortening increases. Thus, a shell buckling behavior with a snap-through may occur when a load control test is conducted. The wrinkling waves are also associated with extremely large stresses and deformations. In addition, a numerical instability has been observed as a result of the loss of stability deep in the post-buckling range that is associated with a reduction of the load as the displacement increases.

The ESL results follow the well known results of elastica of slender beams with an overall buckling. The numerical solution is much more stable due to the fact that the overall response is stable and as the load increases also the displacement increases. The bifurcation load in this case is higher then that of the sandwich panel.

The comparison between the elastica response of the sandwich panel and that of the ESL model reveal a totally different behavior. Hence, the use of an ESL model to simulate the real behavior of a sandwich panel may be quite inaccurate. Finally, in order to detect the real failure patterns of sandwich panels which exceed large deformations the proposed elastica formulation must be used.

6 REFERENCES

1. Mindlin, R. D, "Influence of Transverse Shear Deformation on the Bending of Classical Plates", Transaction of ASME, Journal of Applied Mechanic, 8, pp. 18-31, 1951.
2. Reddy, J. N. *Energy and variational Methods in Applied Mechanics*, John Wiley and Sons, Inc., New York, 1984.
3. Allen, H.G. *Analysis and Design of Structural Sandwich Panels*, London, Pergamon Press, 1969.
4. Plantema, F.J. *Sandwich Construction,* New York, John Wiley and Sons, 1966.
5. Zenkert, D. *An Introduction to Sandwich Construction*, Chameleon Press Ltd., London, 1995.

6. Vinson JR. *The behavior of Sandwich Structures of Isotropic and Composite Materials*, Lancaster, Technomic Publishing Co. Inc, 1999.

7. Frostig, Y., Baruch, M., Vilnay, O. and Sheinman, I. "A High Order Theory for the Bending of Sandwich Beams with a Flexible Core", *Journal off ASCE, EM Division*, 118(5), May, pp. 1026-1043, 1992.

8. Frostig, Y., Baruch, M. "Buckling of Simply-Supported Sandwich Beams with Transversely Flexible Core - A High Order Theory", *Journal of ASCE, EM Division*, 119(3), March, pp. 476-495, 1993.

9. Frostig, Y. "Buckling of Sandwich Panels with a Transversely Flexible Core - High-Order Theory", *International Journal of SOLIDS and STRUCTURES*, 35(3-4), pp. 183-204, 1998.

10. Sokolinsky V., Frostig, Y. "Branching Behavior in the Non-Linear Response of Sandwich panels with a transversely Flexible Core", *International Journal of Solids and Structures,* 37, November 2000, pp. 5745-5772, 2000

11. Dym C.L. and Shames I.H. *Solid Mechanics, A variational Approach,* McGraw-Hill Kogakusha, 1973.

12. Wang C.Y. "Post-buckling of a clamped-simply-supported elastica", *Int. J. of Non-Linear Mechanics*, Vol. 32, No. 6, pp. 1115-1122, 1997.

13. Chucheepsakul S. and Huang, T. "Finite-Element Solution of Variable-Arc-Length Beams under a point load", *J. of Structural Engineering ASCE*, Vol. 123, No. 7, July pp. 968-970, 1997.

14. Reissner E. "On One-Dimensional Finite Strain Beam Theory: the Plane Problem", *Journal of Applied mathematics and Physics (ZAMP)*, Vol. 23, pp. 795-804, 1972.

15. Flajs R., Saje M. and Zakrajsek E. (), "On the existence and Uniqueness of the Generalized Solution of Reissner's Elastica", *Mathematical and Mechanics of Solids,* Vol. 8, pp. 3-19, 2003.

16. Pak R. Y. S. and Stauffer E. J. "Non-Linear Finite Deformation Analysis of Beam and Columns", *Journal of Engineering Mechanics, ASCE,* Vo. 120, No. 10, October, pp. 2136-2153, 1993.

17. Huang H. and Kardomateas G.A. (), "Buckling and Initial Post-Buckling Behavior of Sandwich Beams including Transverse Shear", *AIAA Journal,* Vo. 40, No. 11, November, pp. 2331-2335, 2002.

18. Bazant, Z.P. and Beghini A. "Stability and finite strain of homogenized structure soft in shear: Sandwich or fiber composites and layered bodies", *International Journal of Solids and Structures,* Vol. 43, pp. 1571-1593, 2006.

19. Stoer J, Bulirsch R. *Introduction to Numerical Analysis*, Springer, New York, 1980.

20. Ascher UM, and Petzold L, *Computer Methods for Ordinary Differential Equations and Differential-Algebraic Equations*, SIAM, Philadelphia,1998.

21. Char BW, Gedddes KO, Gonnet GH, Leong BL, Monagan MB, Watt SM, *Maple V Library Reference Manual,* Springer-Verlag, New-York, 1991.

22. Keller H.B. *Numerical Methods For Two-Point Boundary Value Problems*, Dover Publications, New York, 1992.

SIMPLIFIED RULE OF MIXTURES APPROACH FOR THE ACCURATE ESTIMATION OF THE ELASTIC PROPERTIES OF GRID-SCORED POLYMER FOAM CORE SANDWICH PLATES

Ole Thybo Thomsen and Jesper Larsen

Department of Mechanical Engineering, Aalborg University
Pontoppidanstræde 101, DK-9220 Aalborg East, Denmark
e-mail: ott@ime.aau.dk, web page: http://www.me.aau.dk

Key words: Sandwich plates, Grid-scored core, Estimation of elastic properties, Rule of mixtures.

Summary. *The paper presents a simple closed-form rule of mixtures approach for the accurate estimation of the elastic properties of grid-scored polymer foam or balsa cored sandwich plates. The analytical approach is based on a "homogenization" technique for the core material, such that equivalent orthotropic elastic plate properties are assumed corresponding to a first-order shear deformation plate theory. The analytical predictions are compared with predictions based on finite element analyses as well as a closed-form analytical solution based on a first order shear deformation theory, and an excellent match is found overall.*

1 INTRODUCTION

Sandwich structures are used in an increasing number of products, ranging from relatively low-tech everyday goods to advanced aerospace structures. The reasons for utilizing sandwich structures for many applications include high specific stiffness, high specific strength, thermal insulation, sound absorption, to mention a few [1], [2]. For a variety of applications, such as ship hulls and ship superstructures, control surfaces on aircraft structures, primary load carrying space craft structures in satellites and launch vehicles, train body structures and last but not the least wind turbine blades, high specific stiffness and strength are design parameters of primary importance.

Very often the requirements for structures as mentioned above dictate that they should have a doubly curved geometry, which implies that the sandwich structure needs to be draped in order to follow the geometry. This is usually not a problem for the faces, since these are made of thin layers of fibres of UD, multi-directional, woven or NCF constitution. Polymeric foam sandwich core materials made from thermoset bulk polymers (usually PVC or PMI) or balsa cores are used for a large variety of modern sandwich structures, and for such materials

thermoforming is not feasible. Thus, the core materials, which are usually delivered as plates, are cut in small blocks attached to a thin carrier fabric, which can then be draped. If the manufacturing is based on vacuum infusion, resin material passes through these cuts, thus creating a resin grid within the lightweight core. Since the resin material is much stiffer than the foam material, the presence of the grid will often significantly affect the stiffness and load transfer of the core material.

The present paper presents a simple analytical rule of mixtures approach for the accurate estimation of the elastic properties of grid-scored polymer foam or balsa cored sandwich plates. The work was done as part of a M.Sc. thesis work [3]. The motivation for this analysis is to obtain a method of estimating the elastic stiffnesses of the sandwich plate analytically, but also to gain an explicit understanding of the parameters which govern the plate stiffnesses. A somewhat similar attempt has been reported in [4] for sandwich beams. The analytical approach is based on a "homogenization" technique for the core material, such that equivalent orthotropic elastic plate properties are assumed corresponding to a first-order shear deformation plate theory [1]. The analytical predictions are compared with predictions based on finite element analyses as well as a closed-form analytical solution based on a first order shear deformation theory.

2 ANALYTICAL APPROACH

As mentioned above, the 3 dimensional grid and foam structure is reduced to a 2 dimensional plate, which effectively rids the system of the extensional stiffness in the thickness direction, and hence the two Poisson ratios ν_{yz} and ν_{xz}. However, the contribution to the stiffness in the thickness direction due the grid geometry is of interest, and will be included in the analysis. The transverse shear stiffnesses are usually also neglected in thin plate analysis [1], [2]. However transverse shear stress resultants can cause significant deformations in sandwich plates due to the combination of a thick and compliant core material with stiff and thin face sheets [1], [2]. In order to estimate these stiffnesses all independent and homogenized elastic constants of the core must be determined. The procedure for acquiring these constants is based on a simple "mechanics of materials approach" [5], which is applied to a unit-cell of the core. The chosen unit cell geometry is defined in Figure 1.

Since the objective of the analysis is to evaluate the stiffnesses of a sandwich plate due the grid-foam composition of the core, the stiffness contribution of the face layers are of less interest. The face layers are therefore assumed to be isotropic.

Neglecting the Poisson ratios ν_{yz} and ν_{xz}, leaves seven elastic constants to be found. These constants are the Young's moduli in the x, y, z directions, E_x, E_y and E_z, the in-plane Poisson ratio ν_{xy}, the in-plane shear modulus G_{xy}, and the out-of-plane shear moduli G_{zx} and G_{zy} (see

Figure 1). The determination of the Poisson´s ratio based on the simple rules of mixture approach cannot be expected to provide sufficiently accurate results [5], and only the estimation of the Young´s and Shear moduli will therefore be treated herein.
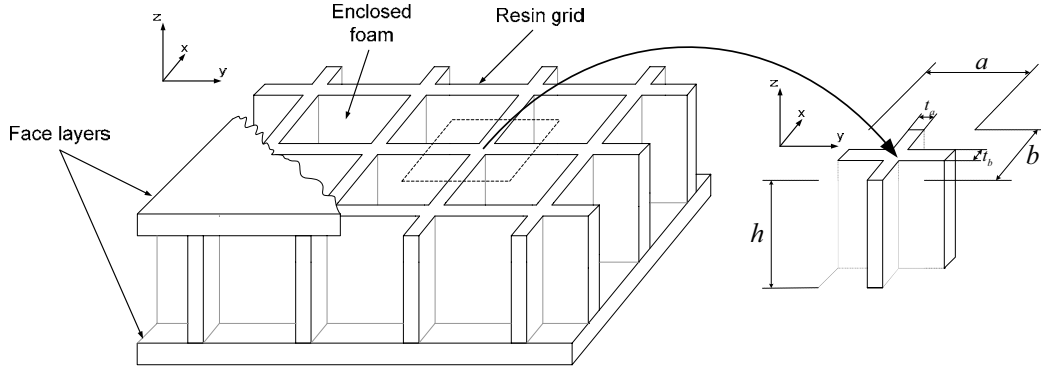

Figure 1: Cut-out of the sandwich plate, with a "unit-cell" extracted from the core.

2.1 Estimation of the Young´s moduli

Assuming perfect bonding between the resin grid and the foam and by looking at a top view of the unit-cell, the Young's modulus in the y-direction can be estimated by assuming sections of the cell to be springs in parallel and in series. See Figure 2.
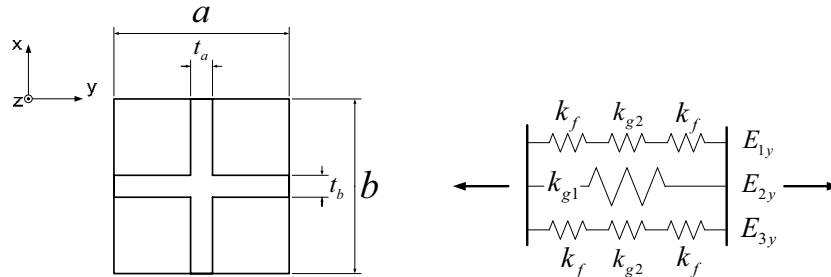

Figure 2: Left: top view of the unit-cell. Right: spring analogy of the individual stiffnesses of sub-sections of the cell.

E_{1y}, which is equal to E_{3y}, can be found by the following relation

$$E_{1y} = E_{3y} = \frac{E_f E_g}{V_g E_f + V_f E_g} \tag{1}$$

E_f and E_g are the Young's moduli of the foam and the resin, respectively, and V_f and V_g are the volume fractions of the foam and grid, respectively. E_{2y} is simply the same as E_g.

The equivalent Young's modulus E_y can now be found by

$$E_y = E_{1y} V_{1y} + E_{2y} V_{2y} + E_{3y} V_{3y} \tag{2}$$

Inserting equation (1) into (2) and expressing the E_y in terms of the dimensions of the unit-cell yields

$$E_y = \tfrac{t_b}{b} E_g + \left(1 - \tfrac{t_b}{b}\right) \frac{E_g E_f}{\left(1 - \tfrac{t_a}{a}\right) E_g + \tfrac{t_a}{a} E_f} \tag{3}$$

The above approach can be applied in the same manner for the x-direction. Accordingly, the Young's modulus in this direction can therefore be expressed as

$$E_x = \tfrac{t_a}{a} E_g + \left(1 - \tfrac{t_a}{a}\right) \frac{E_g E_f}{\left(1 - \tfrac{t_b}{b}\right) E_g + \tfrac{t_b}{b} E_f} \tag{4}$$

Plotting the Young's moduli as functions of the rib thicknesses gives an impression of the stiffness contribution of the ribs in both directions as shown in Figure 3. The Young's modulus in both of the 3D plots shown in Figure 3 are the relative Young's moduli of the resin and foam, meaning that $E_i=0$ (i=x,y) equals the Young's modulus of pure foam and $E_i=1$ (i=x,y) equals the Young's modulus of pure resin.
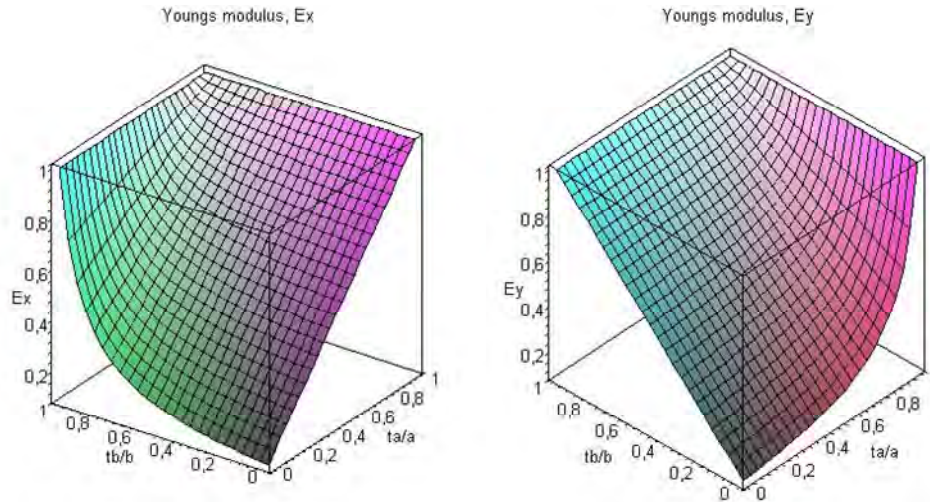

Figure 3: Relative in-plane Young's moduli plotted as a function of the rib thicknesses

The shape of the plots shows that the Young's moduli are linearly dependent on the rib thickness along the primary direction, and nonlinearly dependent of the rib thickness transverse to this direction.

The Young's modulus in the through-thickness direction (z) is obtained by simply adding the volume fractions of the foam and resin. E_z can be expressed similar to E_y in equation (2):

$$E_z = V_g E_g + V_f E_f \tag{5}$$

where the volume fraction of the resin grid, V_g, can be written as

$$V_g = \frac{t_a}{a} + \frac{t_b}{b} - \frac{t_a}{a}\frac{t_b}{b} \tag{6}$$

Inserting (2) into (5) yields

$$E_z = \left(E_f - E_g\right)\frac{t_a}{a}\left(\frac{t_b}{b} - 1\right) + \left(-E_f + E_g\right)\frac{t_b}{b} + E_f \tag{7}$$

Plotting this function shows that the through-thickness Young's modulus E_z depends linearly on both rib thicknesses as can be seen from Figure 4.
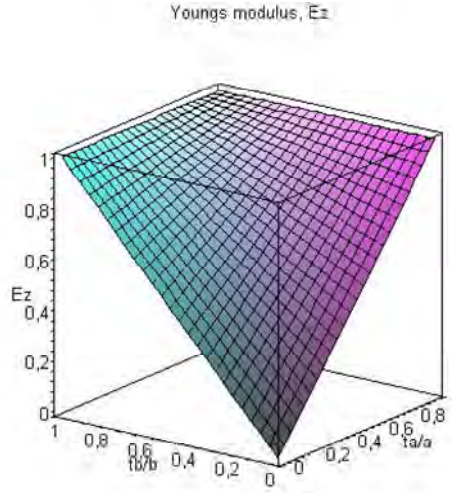

Figure 4: Relative through-thickness Young's modulus plotted as a function of the rib thicknesses.

2.2 Estimation of the Shear moduli

To determine the Shear moduli, it is again necessary to divide the unit-cell into sections, and estimate equivalent stiffnesses of these. The equivalent stiffnesses are then used for estimating the Shear moduli of the entire unit-cell. The adopted unit-cell for the case of the through-thickness shear modulus G_{yz}, is shown in Figure 5.

The deformations in volume 1 and 3 are equal since the shear stress is assumed constant in the x-direction, and the dimensions and composition of materials in these volumes are the same. Volume 2 consists of pure resin and the shear modulus in this volume is therefore known. The deformations of volumes 1 and 3 are more complex than the deformation of volume 2, which implies that it is not readily possible to average the through-thickness shear moduli of the 3 volumes. Finding an equivalent shear modulus for volumes 1 and 3 is therefore necessary, in order to find the total equivalent Shear modulus for the unit-cell. The equivalent Shear modulus for the unit-cell can be expressed in terms of volume fractions:

$$G_{yz} = V_{Vol1}G_{yz,Vol1} + V_{Vol2}G_{yz,Vol2} + V_{Vol3}G_{yz,Vol3} \tag{8}$$
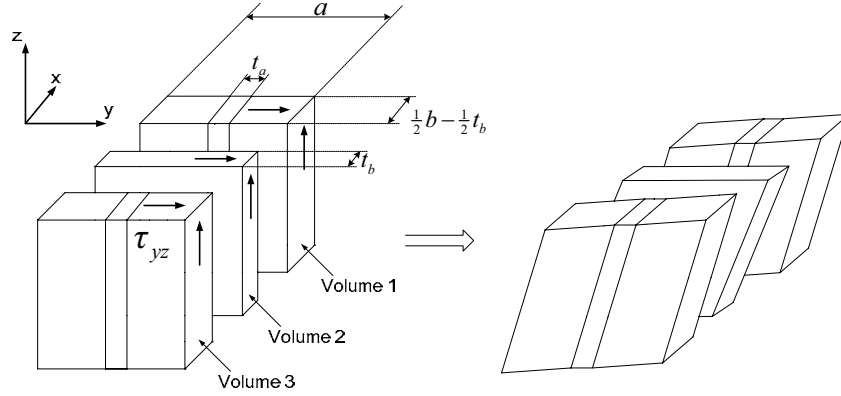
Figure 5: Left: The unit-cell divided into 3 volumes. Right: The deformations of each of the volumes due to out-of-plane shear..

The Shear modulus for volumes 1 and 3 can be expressed as [5]:

$$G_{yz,Vol1} = G_{yz,Vol3} = \frac{G_g G_f}{V_g G_f + V_f G_g} \tag{9}$$

Inserting the dimensions of the unit-cell in equation (9) yields the estimate for G_{yz}:

$$G_{yz} = \frac{t_b}{b} G_g + \left(1 - \frac{t_b}{b}\right) \frac{G_g G_f}{\left(1 - \frac{t_a}{a}\right) G_g + \frac{t_a}{a} G_f} \tag{10}$$

in which G_g and G_f are the Shear moduli for the resin and the foam respectively. Similarly, the estimate for G_{xz} is obtained as:

$$G_{xz} = \frac{t_a}{a} G_g + \left(1 - \frac{t_a}{a}\right) \frac{G_g G_f}{\left(1 - \frac{t_b}{b}\right) G_g + \frac{t_b}{b} G_f} \tag{11}$$

It is seen that the expressions for the transverse Shear moduli are similar to those of the Young's moduli. Accordingly, plotting the relative Shear moduli (defined as the relative Young´s moduli in section 2.1) as functions of the rib thicknesses produces the same plots as shown in Figure 3.

An expression for the in-plane Shear modulus G_{xy} is obtained in a similar manner as the out-of-plane Shear moduli, i.e. the unit-cell is divided into three volumes. The only difference is that the equation for total Shear modulus is not the same as equation (8), but can instead be expressed as:

$$G_{xy} = \frac{G_{xy,Vol1} G_{xy,Vol2} G_{xy,Vol3}}{V_{Vol1} G_{xy,Vol2} G_{xy,Vol3} + V_{Vol2} G_{xy,Vol1} G_{xy,Vol3} + V_{Vol3} G_{xy,Vol1} G_{xy,Vol2}} \tag{12}$$

The terms in equation (12) become evident when looking at the in-plane shear stress in each of the three volumes in the unit-cell, see Figure 6.

The equivalent in-plane Shear moduli of volumes 1 and 3 can be written as

$$G_{xy,Vol1} = G_{xy,Vol3} = \frac{G_g G_f}{V_f G_g + V_g G_f} \qquad (13)$$
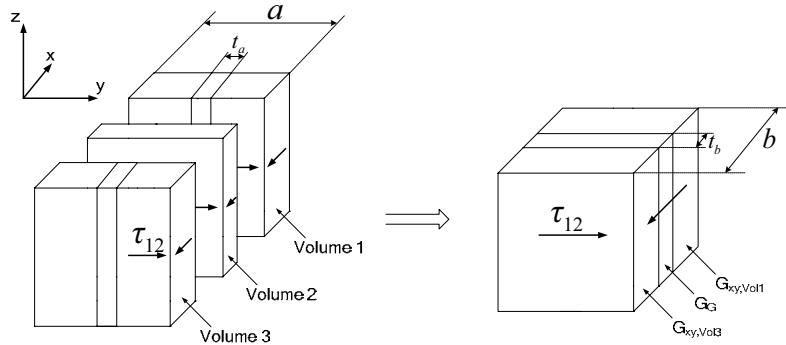

Figure 6: In-plane shear stresses depicted in the 3 volumes of the unit-cell. The equivalent Shear modulus is calculated for volume 1 and 3, in order to obtain an equivalent unit-cell (Right).

Inserting equation (13) into equation (12) yields the estimate of the in-plane Shear modulus

$$G_{xy} = \frac{G_f G_g ab}{a\left(bG_g + \left(G_f - G_g\right)t_b\right) + \left(b - t_b\right)\left(G_f - G_g\right)t_a} \qquad (14)$$

Naturally, equations (10), (11) and (14) can also be obtained by dividing the unit-cell along the y-direction instead of the x-direction. This, however, can be proven to yield the exact same result. Plotting the relative in-plane Shear modulus (defined as the relative Youngs´s muduli in section 2.1) vs. the rib thicknesses yields Figure 7. From Figure 7 it is clear that the "cross" made up by two perpendicular resin-ribs does not contribute much to the in-plane shear stiffness, unless the ribs are considerably thick.

2.3 Remarks on the adopted mechanics of materials approach

In order to decrease the complexity of the analytical approach, several assumptions have been made. For example, it is assumed that the uniformly applied stresses cause uniform strains in both resin and foam, which is clearly not possible due to the differences between the Young´s moduli of the materials. Furthermore, Poisson ratio effects, when estimating the Young's moduli, are also completely neglected, which tend to produce a more flexible structure.
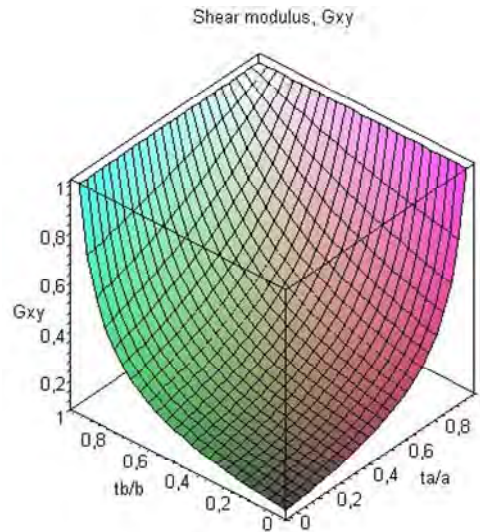
Figure 7: Relative in-plane Shear modulus plotted as a function of the rib thicknesses. On the z-axis "1" represents the Shear modulus of pure resin, and "0" represents the Shear modulus of pure foam.

3   EVALUATION OF STIFFNESS ESTIMATES USING FE ANALYSIS

To evaluate the accuracy of the proposed analytical estimates for the Young´s and Shear moduli, it is appropriate to compare the load-response predictions of various structural models in which the homogenized core properties are adopted, or where the core/resin-grid is modelled, respectively.

3.1 Model definition

The following plate models have been used: In the present work the load-response of a square sandwich plate simply supported along all four edges was assessed using the following plate models:

- Analytical model based on Mindlin-Reissner First Order Shear Deformation Theory (FSDT) using homogenised core properties derived using the analytical models proposed herein. The load-response modelling was conducted using the software ESAComp [6]. Many suggestions for deriving the shear correction factors for sandwich plates have been proposed, see [7], but in the present work the shear correction factor used is based on equalling the strain energy and the work done by the external forces (see [6]).
- Finite element analysis using 3-D solid elements and where the core/resin-grid is modelled exactly. This model will represent the reference for evaluation of the predictions of the other models, and will be referred to as the "exact FE model".
- Finite element analysis using 3-D solid elements, but with homogenised core properties calculated using the analytical models proposed herein ("homogenised core FE model").

To assess the accuracy of the analytical models proposed herein, as well as to compare the predictions of the 3 sandwich plate models, it is necessary to assign material properties, geometry and external loading conditions. For simplicity, the face layers were chosen to be aluminium, with a Young's modulus E=70 GPa and a Poisson ratio v=0,3. The foam core and resin materials were assumed to be linearly elastic, isotropic and homogeneous. The Young's moduli and the Poisson ratios were chosen to be E_F = 100MPa (corresponding roughly to H100 PVC foam core material), E_G = 1.5 GPa (corresponding to polyester or epoxy resin) and v_F = 0,25, v_G = 0,25 for the foam (subscript F=Foam), and resin grid (subscript G=Grid), respectively.

Five different grid configurations were chosen (A-E), such that the thickness of the ribs in the first principal material direction can attain five different thickness values, and the rib-thickness in the second principal material direction is kept constant. The rib thicknesses and the elastic constants of the homogenized cores of the five grid configurations are listed in Table 1.

Grid configurations	E_x [MPa]	E_y [MPa]	G_{xy} [MPa]	v_{xy}	G_{xz} [MPa]	G_{yz} [MPa]
Core A: $\left[\frac{t_a}{a} = \frac{1}{5} \quad, \frac{t_b}{b} = \frac{1}{20}\right]$	383	192	53	0.25	155	77
Core B: $\left[\frac{t_a}{a} = \frac{1}{10} \quad, \frac{t_b}{b} = \frac{1}{20}\right]$	244	180	46	0.25	99	72
Core C: $\left[\frac{t_a}{a} = \frac{1}{20} \quad, \frac{t_b}{b} = \frac{1}{20}\right]$	175	175	44	0.25	70,3	70,3
Core D: $\left[\frac{t_a}{a} = \frac{1}{30} \quad, \frac{t_b}{b} = \frac{1}{20}\right]$	151	173	43	0.25	61	70
Core E: $\left[\frac{t_a}{a} = \frac{1}{40} \quad, \frac{t_b}{b} = \frac{1}{20}\right]$	140	172	43	0.25	56	69

Table 1: Rib thicknesses and homogenized elastic constants of the five different grid configurations.
The elastic constants of a pure foam core, Core F, are also shown.

The sandwich plates considered are assumed to be of square plate simply supported along all four edges, with plan form 400×400 mm, core thickness 10 mm, face layer thickness 1 mm and subjected to a uniformly distributed load q=0.1 MPa. See Figure 8. The unit-cell size was 20×20 mm, and the grid configurations and homogenized core properties correspond to those of Table 1. Both of the finite element analyses were geometrically linear. The bottom edge of the lower face layer is constrained in the z-direction, and both finite element analyses utilize the symmetric constitution of the plate, which means that only a quarter of the plate is being analyzed. The deflection is measured in both the x-direction and the y-direction, since the core is orthotropic.

The FE-models used were based on 3D solid elements, and the FE meshing was conducted 10-node tetrahedral elements for all parts in the assembly (ANSYS 10.0). A rather fine FE

mesh was used, and Figure 9 shows side view of the top part of the sandwich plate at the yz symmetry plane meshed with 10-node tetrahedrals. The element side length was 0. 5mm, and the number of elements through the thickness was 26. The total number of elements was about 18,000 with approximately 340,000 nodes each with 3 DOF.
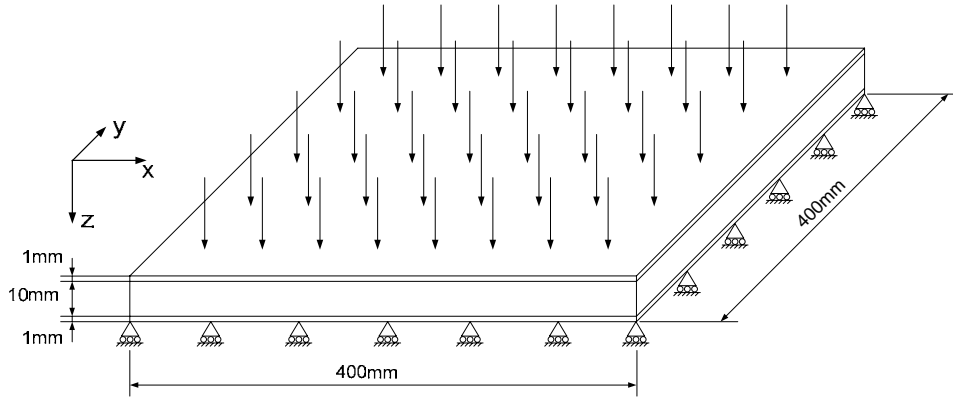

Figure 8: Sandwich plate investigated numerically using 3 different models.
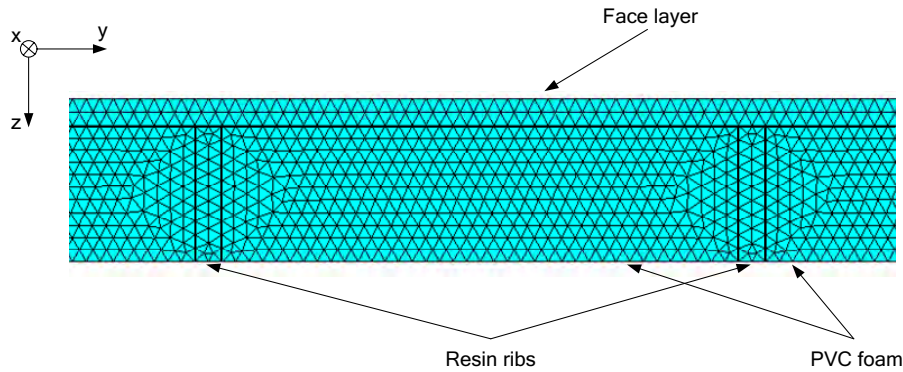The uniformly distributed load is set to 0.1 MPa.

Figure 9: Side view of the top part of the sandwich plate (with core/resin grid) meshed with 10-node tetrahedrals (yz symmetry plane). The element side length is 0.5mm and the number of elements through the thickness is 26.

3.2 Numerical results

The comparison of the predictions of the 3 models is based on comparing the deflection of the middle of the sandwich plates A-F defined from Table 1 in both the x and y directions, i.e. from y = 200mm and throughout the length (x-direction), and from x=200mm and throughout the width (y-direction), see Figure 8. Since the bending stiffnesses of the sandwich plates vary only marginally for the different core configurations, the differences in deflection are almost entirely due the differences in the transverse shear stiffnesses for the 2 FE models, and the accuracy of the transverse shear correction factor for the analytical plate model.

Figures 10, 11, 12, 13 and 14 show the predicted deflection profiles along the xz and yz symmetry planes. An excellent match is observed between the predicted deflections of the "exact" and "homogenised core" FE models. This indicates that the analytical estimates of the homogenised core stiffness parameters (Young´s moduli and in particular the Shear moduli) proposed herein are very accurate, especially the homogenised transverse shear stiffnesses. It is further observed that the poorest match between the "exact" and "homogenised core" FE models is obtained for configuration A, whereas an almost identical match is obtained for configurations C, D and E. This is no surprise as the stiff resin grid is much thicker for configuration A ($t_a/a=1/3$, $t_b/b=1/20$ – see Figure 1 and Table 1) than for the other configurations. In other words, the homogenisation procedure proposed herein provides the most accurate stiffness predictions for smaller volume fractions of resin/grid material.
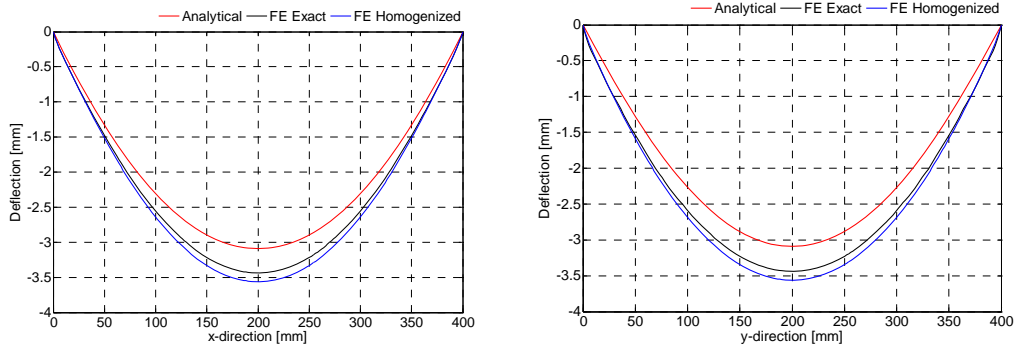

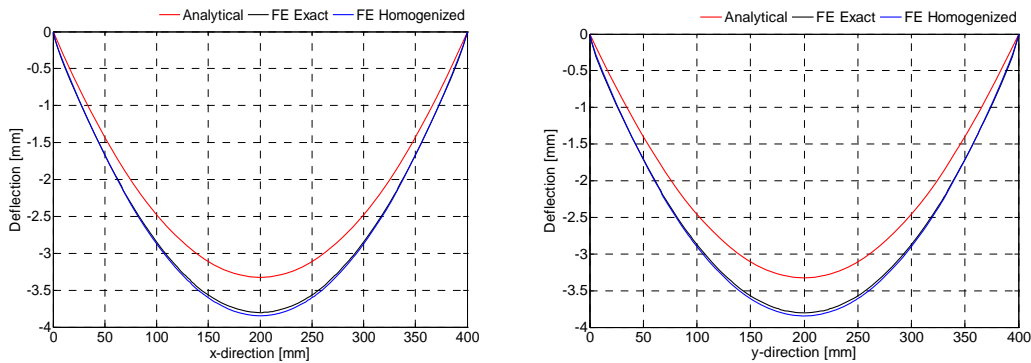Figure 10: Deflection curves of sandwich plate A (see Table 1) along symmetry planes xz and yz.

Figure 11: Deflection curves of sandwich plate B (see Table 1) along symmetry planes xz and yz.

With respect to the predictions of the closed-form FSDT model, it is observed that it overestimated the plate stiffnesses by 15-20% for the considered sandwich plate configurations (A-E, Table 1).
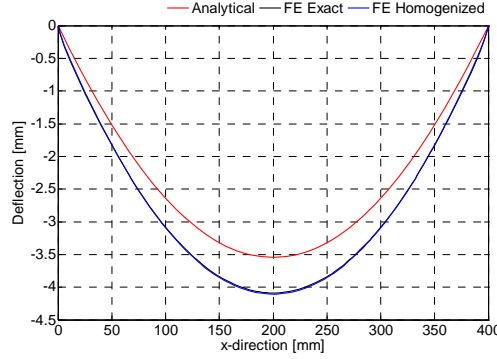
Ole Thybo Thomsen and Jesper Larsen.

Figure 12: Deflection curves of sandwich plate C (see Table 1) along symmetry planes xz and yz. Since plate C is quasi-isotropic the deflection in both in-plane directions are identical and only the deflection curve in the x-direction is therefore shown.
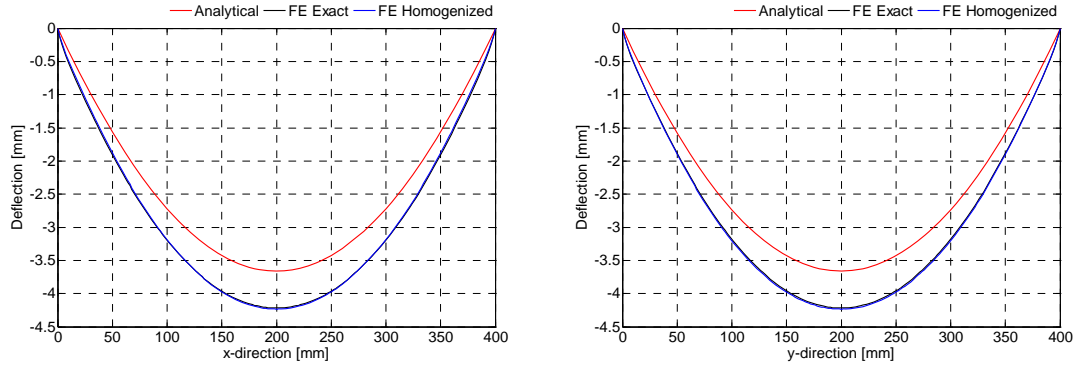
Figure 13: Deflection curves of sandwich plate D (see Table 1) along symmetry planes xz and yz.

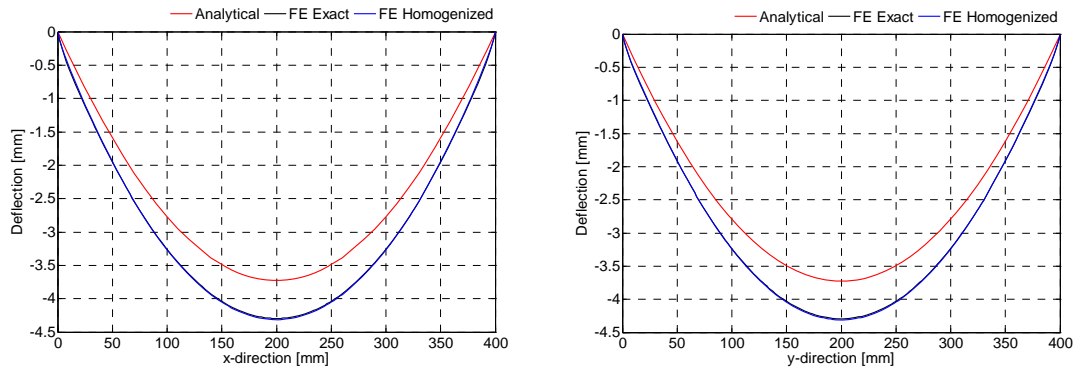

Figure 14: Deflection curves of sandwich plate E (see Table 1) along symmetry planes xz and yz.

The main reason for this is the shear correction factor adopted in this work, which stems from the ESAComp software code. The predictions of the FSDT plate model could have been improved by adopting another shear correction factor approach, but as no analytical method

has proven superior for estimating the "correct" value of the shear correction factor for sandwich structures [7], the FSDT approach has not been pursued further in this work. Instead the shear correction factor issue is considered an inherent and general problem of the FSDT approach to the accurate modelling of the load-response of laminated sandwich structures.

4 CONCLUSIONS

A simple method of estimating the homogenised elastic constants of grid scored sandwich cores has been proposed. The modelling is based on a "mechanics of materials" approach applied to a unit-cell of the grid/core. The method has been applied to different resin-grid/foam core sandwich plate configurations in order to assess the accuracy of the predicted homogenised core stiffnesses. The load-response was modelled using 3 different approaches. The first model used a first order shear deformation plate theory, which requires the adoption of a shear correction factor. Secondly, the load-response was modelled using FE analysis based on 3D solid modelling. One FE model included the "exact" grid/foam configuration, whereas the other was based on homogenised core properties.

An excellent match was found between the predictions of the "exact" and "homogenised core" FE models. Thus, it has been shown hat the proposed analytical homogenisation procedure provides accurate estimates of the homogenised grid-core stiffness coefficients.

The analytical FSDT model overestimated the plate stiffness by 15-20% for the considered sandwich plate configurations (A-E, Table 1). The main reason for this is the shear correction factor adopted in this work.

REFERENCES

[1] Vinson, J.R., *The Behavior of Sandwich Structures of Isotropic and Composite Materials*. Technomic Publishing Co. (1999).

[2] Zenkert, D., *An Introduction to Sandwich Construction*. EMAS Publishing. (1995).

[3] Larsen, J., *A Study of the Strength and Stiffness of Sandwich Structures Made with Grid Scored Core*, M.Sc. thesis, Department of Mechanical Engineering, Aalborg University, Denmark (February 2007).

[4] Wikström, N., *A Study of the Effect of Different Infusion Techniques on Sandwich Beam Properties*. M.Sc. thesis, Department of Aeronautics, Royal Institute of Technology, Sweden (2002).

[5] Jones, R.M., *Mechanics of Composite Materials*, 2nd Edition, Taylor & Francis (1999).

[6] ESAComp®, Composites analysis and design software, Web link: http://www.componeering.com/esacomp/index.html (2008).

[7] Birman, V. and Bert, C.W., "On the Choice of Shear Correction Factor in Sandwich Structures", *Journal of Sandwich Structures and Materials*, Vol. 4, No. 1, pp. 83-95 (2002).

THE COMPRESSIVE AND SHEAR RESPONSES OF CORRUGATED HIERARCHICAL AND FOAM FILLED SANDWICH STRUCTURES

S. Kazemahvazi[*] and D. Zenkert[*]

[*] Kungliga Tekniska Högskolan, KTH
100 44 Stockholm, Sweden
e-mail: sohrabk@kth.se and danz@kth.se, web page: http://www.kth.se

Key words: Corrugated cores, Smart structures, Hierarchical structures, Foam filled cores.

Summary. *The mechanical behaviour of two types of corrugated sandwich cores are investigated experimentally and modelled analytically; (i) Corrugation with monolithic composite elements and (ii) a hierarchical sandwich structure (with sandwich core elements). An additional core design, foam filled corrugation, is investigated experimentally and compared to the aforementioned designs. Results show that the hierarchical structure has significantly higher specific strength than the monolithic and foam filled core designs.*

1 INTRODUCTION

Sandwich structures with cellular cores have proven superior weight specific stiffness and strength properties compared to its monolithic counterpart. Polymer foams and hexagonal honeycomb structures are commonly used as core materials. During the past years, many core designs with improved quasi-static and dynamic performance have been proposed. These comprise aluminium foams and various metallic core topologies such as truss- and plate-like configurations [1]. Numerous metallic truss configurations have been proposed with competitive quasi-static properties [2] and dynamic properties [3]. The metallic plate configurations include various honeycomb cores (square, hexagonal, triangular) [4] and prismatic cores (diamond lattice and corrugations) [5]. Further, Kooistra *et al* [6] have analysed the behaviour of corrugated hierarchical metal sandwich panel concepts. Their results show that the second order structure has significantly higher weight specific strength performance than its first order counterpart while the weight specific stiffness tend to decrease with increasing structural hierarchy.

Using fibre composite materials to manufacture the aforementioned core topologies increases the design space additionally and consequently further optimisation of the structure can be done; this due to the anisotropic nature of the composite materials. Composite corrugation cores introduce other failure modes compared to that of metallic structures. As an example, material rupture occurs instead of plastic buckling when the core members are subjected to large bending deformations. In addition to the differences in failure modes, it is also necessary to know in which lamina failure occurs. In order to predict such failure

mechanisms, knowledge of the stress distribution over the entire core members is necessary.

Recently, Kazemahvazi and Zenkert [7] developed models suitable for predicting stiffness and strength of all composite corrugated sandwich cores. The strength model is based on the stress distribution prediction over each core member when the sandwich core is subjected to a shear or compressive load condition. The strength model also accounts for initial imperfections that may arise during the manufacturing process.

Within this work, the previously mentioned model is extended to account for shear deformations in addition to bending and stretching deformations. The model is used to predict the compressive and shear strength of an all composite hierarchical sandwich structure, see figure 1c. Further, an experimental programme is conducted in order to compare the compressive and shear response of three different all composite corrugated core designs. The different core designs are: (i) A corrugation where each core element is a monolithic composite shell, see figure 1(a), (ii) a foam filled version of (i), see figure 1(b), and (iii) each core element is a sandwich plate (hierarchical sandwich structure), see figure 1(c).

The outline of the paper is as follows. First manufacturing methods and the experimental programme are described. Second, we briefly review the analytical model for strength prediction of corrugated monolithic cores. A strength model for the hierarchical sandwich structure is then described and failure mechanism maps are used to discuss appropriate core designs. Finally, we compare the properties of the three corrugation cores and summarise the experimental findings.

(a)   (b)   (c)
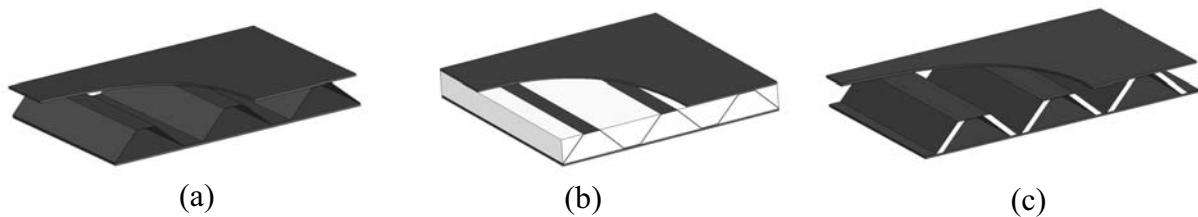
Figure 1: Three different sandwich cores. (a) Monolithic composite core elements, (b) foam filled composite corrugation and (c) composite sandwich core elements (hierarchical sandwich structure).

2   MANUFACTURING ROUTES AND EXPERIMENTAL PROTOCOL

The monolithic corrugated core was manufactured using a machined aluminium mould. Prepreg laminae were stacked to obtain the desired thickness and the laminate was cured for 1 hour in 120ºC under vacuum pressure, see figure 2a. The hierarchical corrugation core was manufactured in the same way as the monolithic corrugation with the addition of PMI foam (Rohacell) in the core members, see figure 2b. The foam filled corrugated cores were manufactured as shown in figure 2c. The foam was cut into trapezoid shapes and bonded to a pre-cured monolithic corrugation using structural adhesives. A summary of the tested corrugation configurations is found in table 1. At least two specimens of each corrugation configuration were tested and all results are presented as mean values of the conducted experiments.

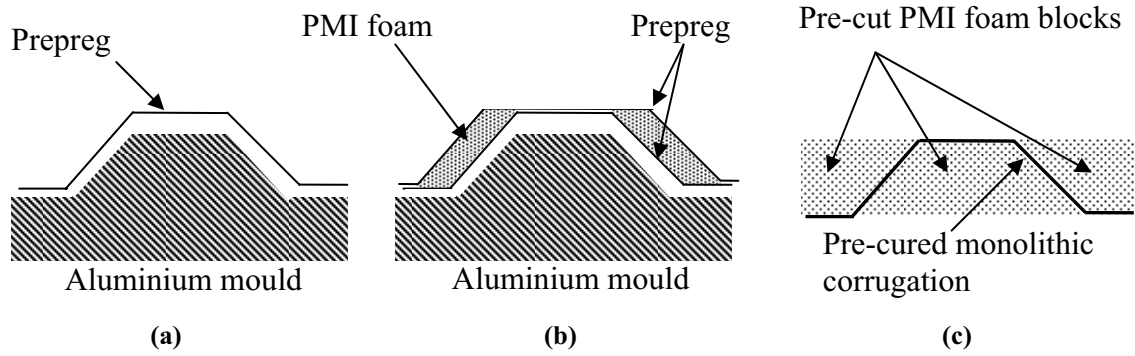Figure 2: Manufacturing route of (a) monolithic corrugation, (b) hierarchical corrugation structures and (c) foam filled corrugation structure.

	Core member length, l_1	Web/face thickness, t, t_f	Core member core thickness, t_{cweb}	Core member core/filling density, ρ_{cweb}	Core density ρ_c
Monolithic 1	35.16 mm	0.4 mm	--	--	34 kgm^{-3}
Monolithic 2	35.16 mm	1.2 mm	--	--	100 kgm^{-3}
Hierarchical 1	35.16 mm	0.2 mm	5.1 mm	32 kgm^{-3}	42 kgm^{-3}
Hierarchical 2	35.16 mm	0.2 mm	5.1 mm	110 kgm^{-3}	58 kgm^{-3}
Foam filled 1	35.16 mm	0.4 mm	--	32 kgm^{-3}	65 kgm^{-3}
Foam filled 2	35.16 mm	0.4 mm	--	51 kgm^{-3}	85 kgm^{-3}

Table 1: Corrugation configurations tested in the experimental programme. The geometrical variables are shown in figure 4.

2.1 Constitutive material

The corrugations were made of unidirectional carbon fibre SE-84LV prepreg system supplied by Gurit. All corrugations were made using unidirectional laminates with the fibre direction along the corrugation. Material properties for a unidirectional lamina are presented in table 2.

E_1 [GPa]	140
E_2 [GPa]	7.45
G_{12} [GPa]	3.85
$\hat{\sigma}_{1t}$ [MPa]	1950
$\hat{\sigma}_{1c}$ [MPa]	858
$\hat{\sigma}_{2t}$ [MPa]	26.6

Table 2: Material properties of unidirectional SE-84LV carbon fibre prepreg. E is the Young's modulus, G the shear modulus and $\hat{\sigma}$ the ultimate strength. The notations 1 and 2 refer to the direction of the load where 1 is along the fibres and 2 is transverse the fibres. The notations t and c refers to tensile or compressive loading.

2.2 Test method

Single-block shear tests were conducted according to ASTM C273-00. Two unit cells of the corrugation were bonded to rigid steel blocks and tensile loading was applied at the ends of the rigid plates, see figure 3(a). Deflections were measured using extensometers and digital calipers. Compression tests were conducted on a unit cell of the corrugation mounted between two stiff steel plates, see figure 3(b). All experiments were conducted in a screw-driven 30kN test machine at a quasi-static strain rate.
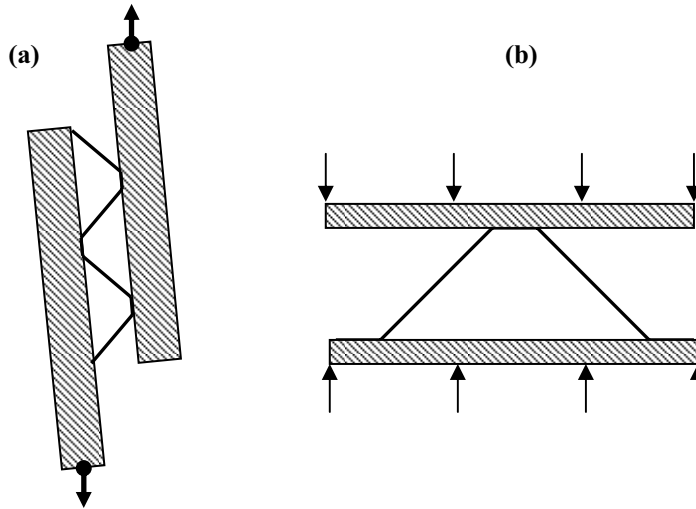
Figure 3: (a) Testing of the core shear properties and (b) testing of the out-of-plane properties of the core.

3   BRIEF SUMMARY OF ANALYTICAL MODELS

3.1 Compressive and shear response of a monolithic core

Consider a unit cell of a corrugated core with geometrical quantities as specified in figure 4. Assume that each core member is built-in to the face sheets so that the ends of the members have clamped boundary conditions. The equivalent shear and compressive modulus of the core is given by equation 1 and equation 2, respectively [7]. D_{11} is the bending stiffness of the core member, S_1 is the shear stiffness and A_{11} is the extensional stiffness component. For isotropic materials A_{11} reduces to Et, where E is the Young's modulus of the material and t is the thickness.

$$G_{xz} = \frac{\tau_{xz}}{\gamma_{xz}} = \frac{\sin\omega}{(l_1\cos\omega + l_2)}\left[A_{11}\cos^2\omega + \frac{\sin^2\omega}{\frac{l_1^2}{12D_{11}} + \frac{1}{S_1}}\right] \tag{1}$$

$$E_{zz} = \frac{\sigma_{zz}}{\varepsilon_{zz}} = \frac{\sin\omega}{(l_1\cos\omega + l_2)}\left[A_{11}\sin^2\omega + \frac{\cos^2\omega}{\dfrac{l_1^2}{12D_{11}} + \dfrac{1}{S_1}} \right] \qquad (2)$$
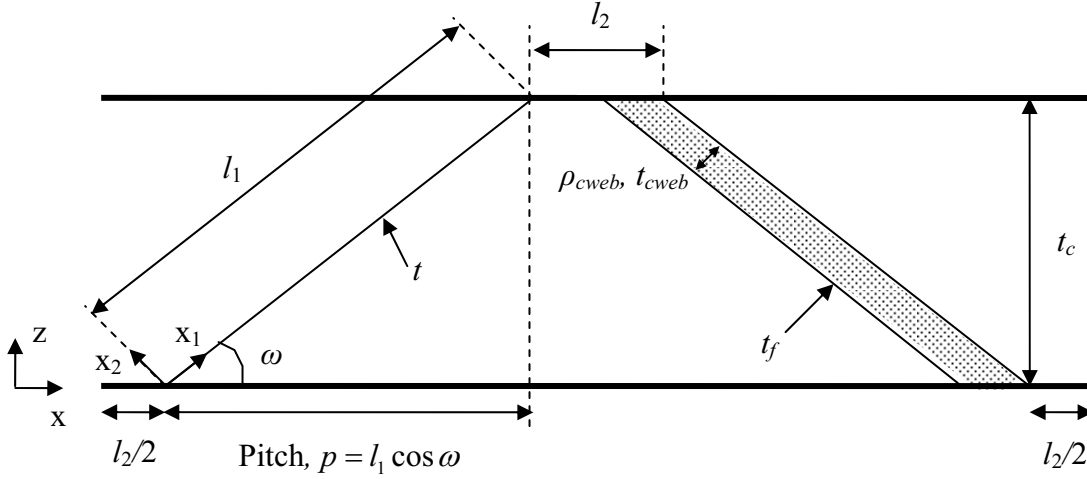
Figure 4: Unit cell of a corrugated core. The left core member shows a monolithic version and the right core member shows a sandwich version.

Consider the compression loaded part of a unit cell as described in figure 5. Due to the clamped end condition of the core members they will undergo both stretching and bending deformation. Due to the presence of bending deformations, the in-plane stretching force (N_1) causes additional bending deformation that must be taken into account in order to capture elastic instability phenomena. Further, each core member is assumed to have an initial imperfection in the shape of the first buckling mode of a clamped strut.

Figure 5: Beam problem that corresponds to a unit deformation of a core web.

For slender monolithic core members shear deformations are assumed to be negligible. The in-plane stretching force (N_1) is assumed to be constant over the entire core member and the transverse force T_1 is chosen so that the bending deformation at the end of the beam equals a

unit deflection δ_b. The ordinary differential equation that describes the deformation of the core member is solved analytically and a closed form 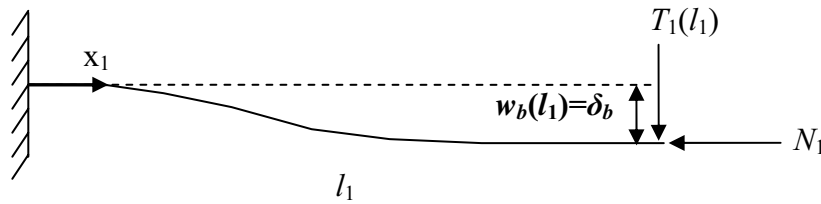solution for the bending deformation $w_b(x_1)$ is obtained. Consequently, the bending moment $M(x_1)$ and the transverse force $T(x_1)$ distributions are obtained. A simple strength model can now be employed based on the strength of the material. Failure of the core is assumed when, (i) the applied load is within 2 percent of the critical buckling load or (ii) the compressive stresses exceed the compressive strength of the laminate or (iii) the tensile stresses exceed the tensile strength of the laminate.

3.2 Compressive and shear response of a core with sandwich core members

The model described in section 3.1 is now extended to account for shear deformation in addition to the bending and stretching deformation. The initial imperfections of the core members are however neglected in this analysis. The same solution method, as for the model described in section 3.1, is used to obtain the closed form solution of the deformation of a sandwich core member. Again, the bending moments $M(x_1)$ and the transverse forces $T(x_1)$ are obtained explicitly. A strength model based on five competing failure modes is now employed. The different failure modes are shown schematically in figure 6 and the failure criteria are described in subsequent sections.
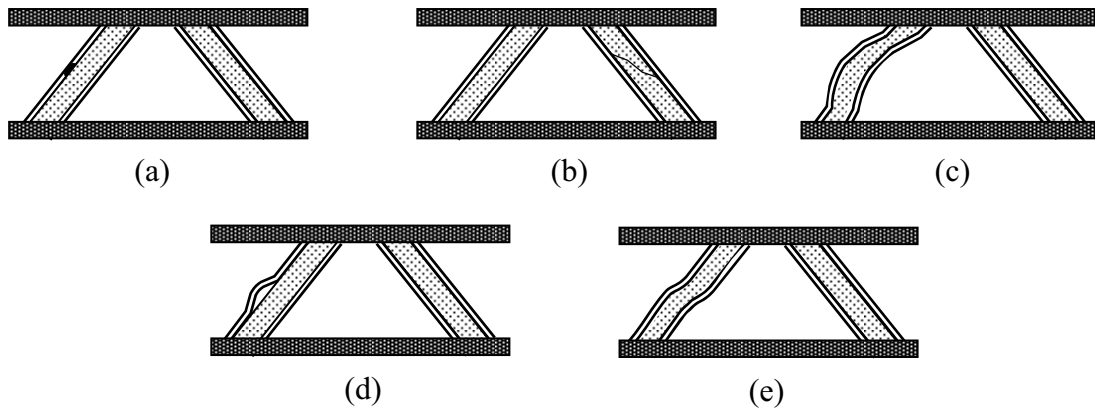
Figure 6: Failure modes of composite corrugation with sandwich core members. (a) Face fracture, (b) core shear failure, (c) general buckling, (d) local buckling/wrinkling and (e) shear buckling.

3.2.1 Face fracture

Face fracture (figure 6a) is assumed to occur when the compressive stress in a face reaches the ultimate compressive strength of the material, $\hat{\sigma}_f$. This is given by,

$$\sigma_f = \frac{M_1^{\max} d}{2D_{11}} E_f + \frac{N_1}{t_f} \geq \hat{\sigma}_f \tag{3}$$

where t_f is the core member face thickness, t_{cweb} the core member core thickness, $d = t_{cweb} + t_f$ and E_f the modulus of the core member face sheet.

3.2.2 Core shear failure

Shear failure of the core elements (figure 6b) is assumed to occur when the shear stress in the core reaches the ultimate shear strength of the core material, $\hat{\tau}_{12}$. This is given by,

$$\tau_{12} = \frac{T_1^{max}}{d} \geq \hat{\tau}_{12} \tag{4}$$

3.2.3 General Buckling

The mode I symmetrical buckling load (figure 6c) of a clamped sandwich column is given by equation 5 [8]. General buckling is thus assumed to occur when the compressive force acting on the core member reaches this critical value.

$$N \geq N_{cr} = \frac{\dfrac{4\pi^2 D_{11}}{l_1^2}}{1 + \dfrac{4\pi^2 D_{11}}{l_1^2 S_1}} \tag{5}$$

3.2.4 Face wrinkling/local buckling

Hoff's method [9] has been used as a failure criterion for local buckling, see figure 6d. Local buckling is assumed to occur when the compressive stress in a face reaches the critical local buckling stress as specified in equation 6.

$$\sigma_f \geq \sigma_{cr}^{Localbuckling} = 0.5\sqrt[3]{E_f E_c G_c} \tag{6}$$

where E_c is the modulus and G_c the shear modulus of the core material.

3.2.5 Shear buckling

The shear buckling of a core member (figure 6e) is set by its shear stiffness, S_1, as discussed in [8]. Shear buckling is thus assumed to occur when,

$$N_1 \geq S_1. \tag{7}$$

3.2.6 Failure mechanisms

In order to validate the analytical model for a range of configurations and failure modes, failure mechanism maps were created. Using these maps different core member configurations with different failure modes could be chosen for the experimental programme. Figure 7 shows a failure mechanism map for a 45-degree corrugation with sandwich core members loaded in out-of-plane compression or shear. The face thickness and the length of the core members are fixed while the core density (ρ_{cweb}) and core thickness (t_{cweb}) of the core

members are altered. For a core thickness of 5 mm three different failure modes can occur depending on the core density. For low core density, <45 kgm^{-3}, the core members are predicted to fail in general buckling. For intermediate core densities, 45 kgm^{-3}-170 kgm^{-3}, the core member is predicted to fail by local buckling and at high core densities >170 kgm^{-3} the core member is predicted to fail by face fracture.

Figure 8 shows two different corrugation configurations subjected to out-of-plane compressive loading. One is manufactured with a low density foam (figure 8a), Hierarchical 1, and another with an intermediate density foam (figure 8b), Hierarchical 2. Photographs clearly show that the core configuration with low density foam fails in a general buckling mode while the one with intermediate density foam fails through local buckling of the faces.
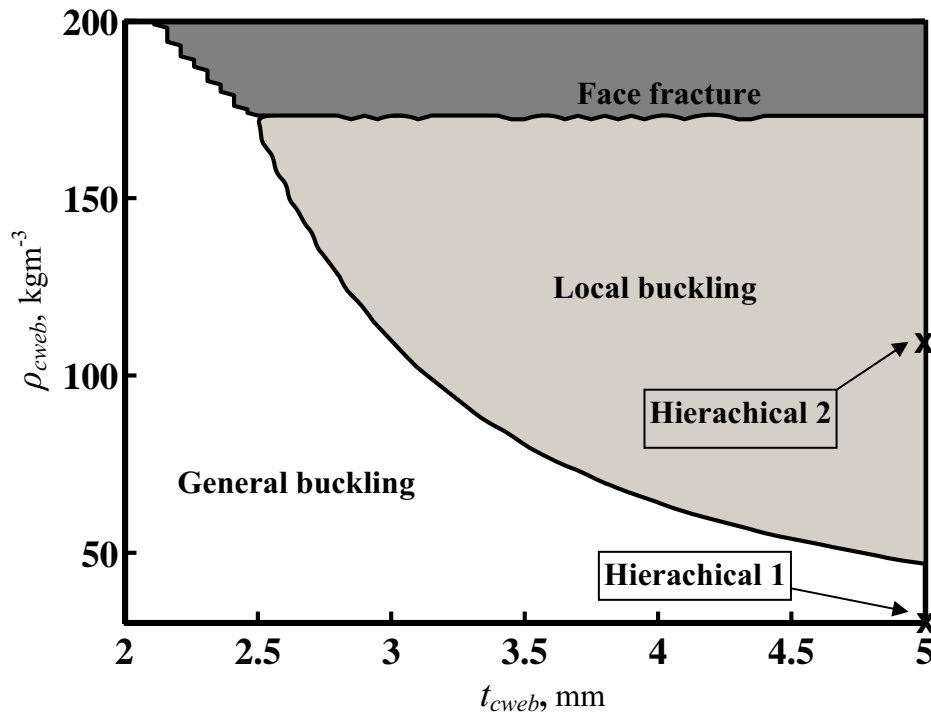
Figure 7: Failure mechanism map for a 45-degree corrugation with sandwich core members. The same failure mechanism map is found for both compression and shear loading in the case of a 45-degree corrugation. t_f = 0.2 mm and l_1=35.16 mm.

(a)   **(b)**
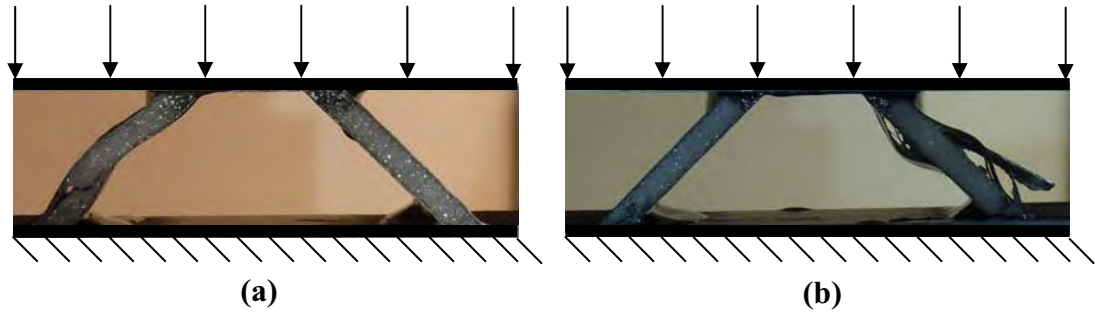
Figure 8: Photographs taken during out-of-plane compression experiment. (a) Hierarchical 1 configuration and (b) Hierarchical 2 configuration.

4 COMPARISON OF CORE DESIGNS

4.1 The out-of-plane compression response

Figure 9 shows a summary of the out-of-plane compressive strength of the three core designs. The core strength, which is normalised with the compressive strength of the material, is plotted as function of the total core density.
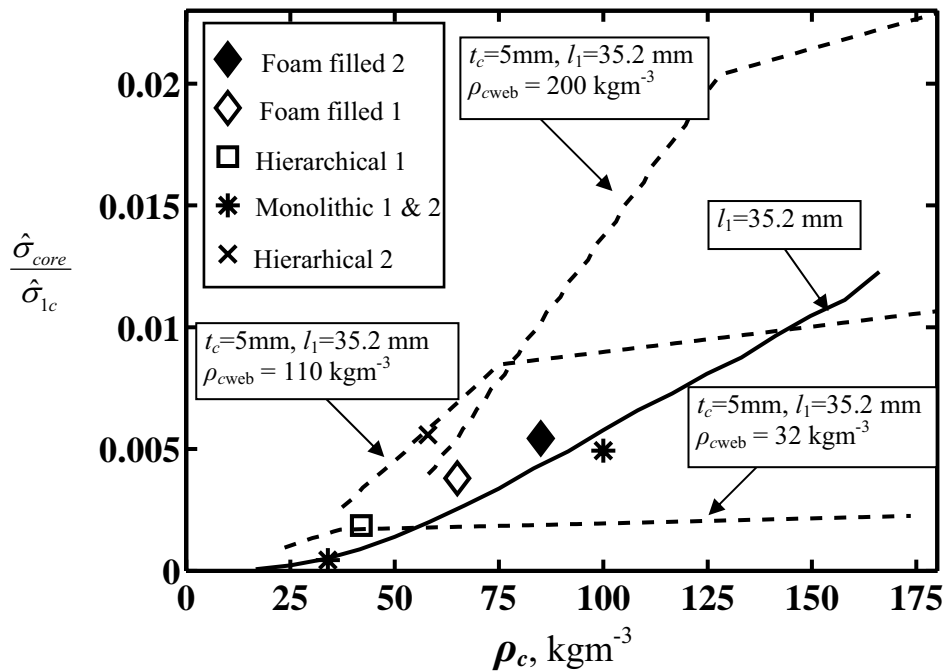
Figure 9: Out-of-plane compressive strength for the three different core designs. Solid line is the analytical model for a monolithic core with an initial imperfection of $0.7t$, dashed lines are the analytical models for the hierarchical structures with various core densities and the free points are mean values of the experimental results.

The strength of the hierarchical structures (dashed lines) is plotted for three different core member core densities as specified in the figure. The core member length is kept constant while the thicknesses of the faces/laminates have been altered. The sandwich core members have face thicknesses ranging from 0.1 mm to 1 mm and the monolithic core thicknesses range from 0.2 mm to 2 mm. Experimental results are included as free points.

4.1.1 Comparison of cores at low densities; $25 kgm^{-3} – 50 kgm^{-3}$

At low core densities the hierarchical structure with a core member core density $\rho_{cweb} = 32$ kgm^{-3} is 5 times stronger than the monolithic version. At a core density of 32 kgm^{-3} the failure mode shifts from local buckling to general buckling which results in a decrease of the slope angle. As the core density increases the monolithic core gains better performance than the $\rho_{cweb} = 32$ kgm^{-3} hierarchical structure. Recall that the hierarchical structures presented here are not optimised and by alternation of design variables such as core thickness, core density, face thickness etc. potentially better performance can be achieved.
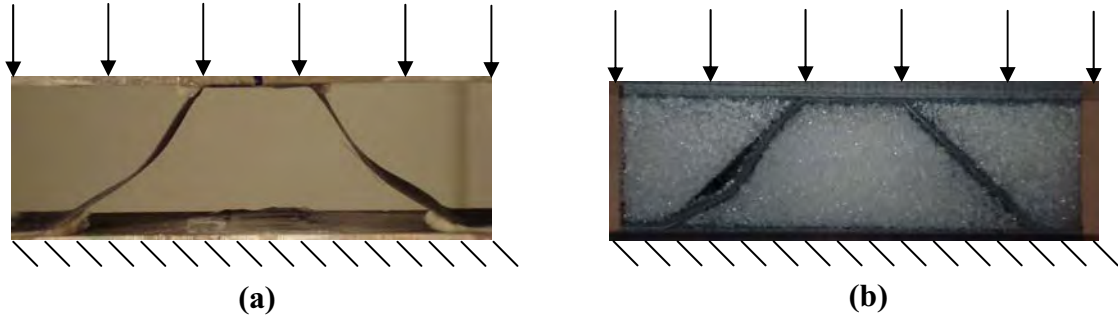

(a) **(b)**

Figure 10: Out-of-plane compression experiment for (a) monolithic core and (b) foam filled core.

4.1.2 Comparison of cores at intermediate and high densities; $50 kgm^{-3} – 175 kgm^{-3}$

As the total core density increases the $\rho_{cweb} = 110$ kgm^{-3} hierarchical structure outperforms both the monolithic core and the $\rho_{cweb} = 32$ kgm^{-3} hierarchical core. At a total density of 75 kgm^{-3} this core has approximately three times higher strength than the monolithic version.

At a total core density of approximately 75 kgm^{-3} the $\rho_{cweb} = 110$ kgm^{-3} and $\rho_{cweb} = 200$ kgm^{-3} hierarchical structure are equally strong. The decrease of the slope angle, seen at this point, is due to a failure mode shift from local buckling to general buckling. At the highest core densities studied here the $\rho_{cweb} = 200$ kgm^{-3} hierarchical structure outperforms the other core designs. This core fails through face fracture at low densities and at a density of 126 kgm^{-3} the failure mode shifts to shear buckling which results in a decrease of the slope angle. At a density of 169 kgm^{-3}, the failure mode shifts to general buckling. This failure mode shift does, however, not result in a change of slope angle.

Since the predominant failure mode of the monolithic cores at low densities are elastic buckling (see figure 10a), the inclusion of an elastic support increases the strength of the core, this is seen for the experimental results of the foam filled core. The improvement of the performance is, however, not as significant as for the hierarchical structure. This, since the foam filled cores add significantly more weight to the structure compared to the hierarchical

version. Figure 10b shows a foam filled core with a foam density of 32 kgm^{-3} loaded in out of plane compression. The failure mode is a combination of buckling on elastic foundation and compressive failure of the foam.

4.2 The shear response

Same observations are made for the shear response of the structure as for the compressive response, see figure 11. The experimental results for the Hierarchical 2 structure is however considerably lower than the analytical prediction. This is due to an unexpected peel of failure mode of the tensile loaded core member, see figure 12. The foam filled 2 structure failed at the interface between the shear blocks and the core. The true strength of this structure is thus expected to be higher.
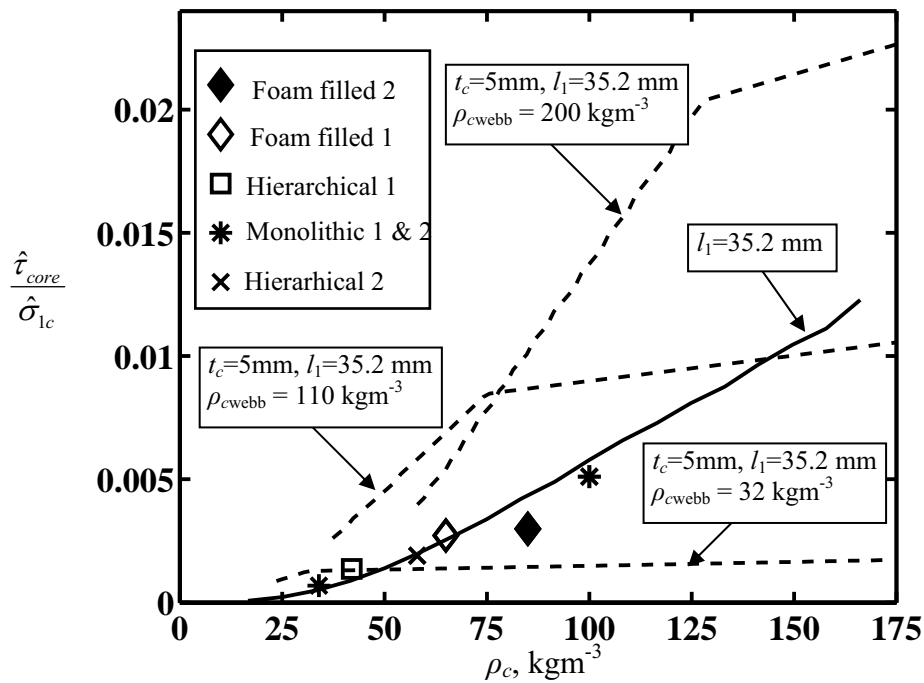
Figure 11: Shear strength for the three different core designs. Solid line is the analytical model for a monolithic core with an initial imperfection of 0.7t, dashed lines are the analytical models for the hierarchical structures with various core densities and the free points are mean values of the experimental results.

Figure 12: Shear testing of hierarchical 2 structure. The tensile loaded core member fails due to high peel-off stresses at the boundaries.

5   CONCLUDING REMARKS

The compressive and shear performance of three different all-composite core designs has been investigated: (i) A corrugation where each core element is a monolithic composite shell, (ii) a foam filled version of (i) and (iii) each core element is a sandwich plate (hierarchical sandwich structure). Previously developed analytical model for composite corrugations has been extended in order to predict the shear and compressive strength of a corrugated hierarchical sandwich structure. The model shows good agreement with the experimental strength results as well as the obtained failure modes.

The hierarchical structures tested in this study have at least three times higher weight specific strength compared to the monolithic version. Due to the large number of design variables, a fully optimised hierarchical structure potentially has even higher specific strength.

At low core densities, foam filled corrugation cores have higher specific strength compared to the monolithic version but lower strength compared to the hierarchical structure.

REFERENCES

[1]   Wadley HNG., "Multifunctional periodic cellular metals", *Philos T R Soc A*, 2006, 364, 31-68.

[2]   Kooistra GW, Deshpande VS, Wadley HNG., "Compressive behavior of age hardenable tetrahedral lattice truss structures made from aluminium", *Acta Mater.,* 2004, 52, 4229-4237.

[3]   McShane GJ, Radford DD, Deshpande VS, Fleck NA., "The response of clamped sandwich plates with lattice cores subjected to shock loading", *European Journal of Mechanics - A/Solids ,* 2006; 25, 2, 215-229.

[4]   Coté F, Deshpande VS, Fleck NA, AG Evans, "The out-of-plane compressive behaviour of metallic honeycombs", *Material Science and Engieneering A ,* 2004, 380, 272-280.

[5]   Coté F, Deshpande VS, Fleck NA, AG Evans, "The compressive and shear responses of corrugated and diamond lattice materials", *Int J Solid Struct.,* 2006, 43, 6220-6242.

[6]   Kooistra GW, Deshpande VS, Wadley HNG, "Hierarchical corrugated core sandwich panel concepts", *Journal of Applied Mechanics*, 2007, 74, 259-268.

[7]   Kazemahvazi S, Zenkert D., "Compressive and shear response of corrugated all-composite sandwich cores", Submitted for publication 2008.

[8]   Zenkert D. *An introduction to sandwich construction*, Engineering Materials Advisory Service, 1995, Sheffield, UK.

[9]   Hoff N.J. and Mautner S.E., "Buckling of sandwich type panels", *Journal of the Aeronautical Sciences*, 1945, 12, 285-297.

BUCKLING AND FRACTURE INVESTIGATION OF DEBONDED SANDWICH COLUMNS: AN EXPERIMENTAL AND NUMERICAL STUDY

R. Moslemian[*], **C. Berggreen**[*], **L. A. Carlsson**[†], **F. Aviles**[⁕] **and A. May**[⁕]

[*] Department of Mechanical Engineering
Technical University of Denmark
Nils Koppels Allé, Building 403, DK-2800 Kgs. Lyngby, Denmark
e-mail: rmo@mek.dtu.dk and cbe@mek.dtu.dk, web page: http://www.mek.dtu.dk

[†] Department of Mechanical Engineering
Florida Atlantic University
777 Glades Road, Boca Raton, FL 33431, USA
e-mail: carlsson@fau.edu, web page: http://www.me.fau.edu

[⁕] Centro de Investigación Científica de Yucatán, A.C., Unidad de Materiales
Calle 43 # 103, Col. Chuburná de Hidalgo, C.P. 97200 Mérida, Yucatán, México
e-mail: faviles@cicy.mx, web page: http://www.cicy.mx

Summary. *An experimental and numerical study of in-plane compression of foam core sandwich columns with implanted trough width face/core debond is presented. Experiments were conducted for columns with two different face thicknesses over different cores and debond lengths. The debonded region was monitored using digital image correlation (DIC) measurements. Finite element analysis and linear elastic fracture mechanics are employed to predict the residual compressive strength of columns. Finally, the numerical results are validated with column testing. Results show a good agreement between finite element and experimental results.*

Key words: Sandwich structures, Columns, Debond damages, Buckling, Fracture mechanics, Compressive strength.

1 INTRODUCTION

A sandwich structure consists of two strong and stiff face sheets adequately bonded to a mechanically weak low density core. The face sheets in the sandwich resist the in-plane and bending loads. The core separates the face sheets to increase the bending rigidity and strength of the composite structure, transfers load between the face sheets through shear stresses [1]. It is recognized that one of the weakest links in a sandwich structure is the bond between the

Ramin Moslemian, Christian Berggreen, Leif A. Carlsson, F. Aviles and A. May

face sheets and core [2-4]. A crucial problem arises when bonding between the face sheets and core is not adequate (debonding) either because of manufacturing flaws or due to damage originated during service, such as impact or blast situations. The behavior of sandwich structures containing imperfections or interfacial cracks subjected to axial loading has been investigated to a certain extent. Hohe and Becker [5] conducted an analytical investigation to study the effect of intrinsic microscopic face-core debonds due to the mismatch between the properties of the face sheets and core. Sankar and Narayan [6] studied the behavior of sandwich columns subject to axial compression by testing and numerical analysis. Their analysis includes computations of the global energy release rate, without considering mode-mixity and debond propagation. Those authors observed a peak in the energy release rate at the moment of buckling. Vadakke and Carlsson experimentally studied the compression failure of sandwich columns with a face/core debond [7]. They investigated the effect of core density and debond length on compressive strength of sandwich columns. El-Sayed and Sridharan [8] have proposed cohesive models implemented into FE codes to predict growth and kinking of interface cracks in double cantilever-type (DCB) sandwich specimens (considering only fracture mode I). Østergaard [9] applied cohesive models for debonded columns and investigated the relation between global buckling behavior and cohesive layer properties. The approach should be especially suitable for cases that present fiber bridging, but has the drawback of the ambiguity in the definition of the material properties of the cohesive layer. Only a few works have assessed detailed determination of fracture parameters, mode-mixity and debond propagation in debonded sandwich structures subject to axial loading, see [10, 11]. The research conducted by Berggreen [10] and Avilés and Carlsson [11], focused on sandwich panels containing embedded debonds. Although sandwich panels are more representative of a real sandwich structure, important insight can be gained from detailed fracture analysis of the simpler column case, and such a case has not been thoroughfully examined. Such an analysis is the objective for the present paper.

2 MANUFACTURING AND TEST SETUP

Twenty-seven sandwich columns with 2 mm satin weave 8.9 oz E-glass/epoxy face sheets over Divinycell H45, H100 and H200 PVC foam cores [12] and three debond lengths were tested, see Table 1. The core thickness was 50 mm. The columns were cut from panels manufactured at Florida Atlantic University. Mechanical properties of the foam cores employed are listed in Table 2. Face sheets were also considered isotropic with the properties listed in Table 3. A through-width debond was defined at the column center using one layer of Teflon film between the face and core layer at the middle of panels. However, due to unintended partial adhesion between face and core in the debonded area in the columns with thicker face sheets, the debond was further released using two very thin blades (0.35 and 0.43 mm thickness). The width and height of the columns are 38 and 153 mm respectively. A new test rig was designed and manufactured for axial compression testing, see Fig. 1. The test rig consists of four 25 mm diameter solid steel rods which support the upper and lower base plates of the test rig during compressive loading. Linear bearings were used to minimize friction between the base plates and rods. Steel clamps of 80 mm width were attached to the

upper and lower base plates to clamp the columns. The test rig was inserted into an MTS 100 kN servo-hydraulic universal testing machine. A 2 MPixel Digital Image Correlation (DIC) measurement system (ARAMIS 2M) was used to monitor 3D surface displacements and surface strains during the experiments. Ramp displacement control with a cross-head rate of 0.5 mm/min was applied in all experiments. A sample rate of one image per second was used in the DIC measurements.

Core type	Face thickness (mm)	Debond length (mm)	specimen
H45	2	25.4	3
		38.1	3
		50.8	3
H100	2	25.4	3
		38.1	3
		50.8	3
H200	2	25.4	3
		38.1	3
		50.8	3

Table 1: Sandwich columns specifications

Core type	Property	Value (MPa)	Fracture Toughness G_{Ic} (J/m^2)
H45	Young's Modulus	50	150
	Shear Modulus	15	
H100	Young's Modulus	130	310
	Shear Modulus	35	
H200	Young's Modulus	250	625
	Shear Modulus	85	

Table 2: Core Material properties [12, 14]

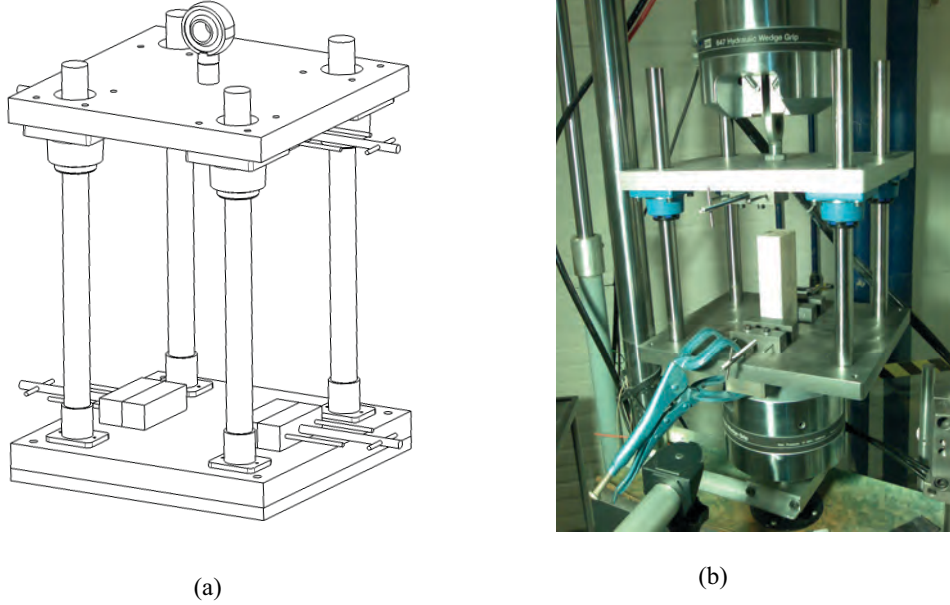| Property	Value
Modulus of Elasticity (GPa)	10
Shear Modulus (GPa)	2.5
Poisson's Ratio	0.3

Table 3: Face Material properties

(a)

(b)

Figure 1: Schematic representation of the test rig (a) and actual test set up (b).

3 FINITE ELEMENT ANALYSIS

A 3D finite element model was developed in the commercial finite element code, ANSYS version 11, using isoparametric linear elements (SOLID45). Load controlled geometrical nonlinear analyses were performed and initial imperfections introduced by small debond opening displacements in the first load step achieved from scaled eigen-buckling shapes. Because of geometrical and loading symmetry, only half model was created. Furthermore, overlapping of crack flanks was avoided by use of contact elements (CONTACT173 and TARGET170). To simulate the boundary conditions similar to those in the experimental setup, nodes at the top and bottom of the columns were fully constrained except in the vertical direction. Due to the need of a high mesh density at the crack front when performing the fracture mechanics analysis, a submodeling technique was employed. Interpolated degrees of freedom results at the cut boundaries in the global model were used as boundary conditions in the submodel at the different load steps, allowing a higher mesh density to be employed and thus improving the accuracy of the fracture mechanics analysis. The finite element model and submodel are shown in Figure 2. The calculation of fracture parameters is based on relative nodal pair displacements along the crack flanks obtained from finite element analysis. The Crack Surface Displacement Extrapolation (CSDE) method presented by Berggreen [10] is employed for the calculation of energy release rate and mode-mixity. Explicit formulations for the mode-mixity (in terms of a phase angle) and the energy release rate as functions of the relative crack flank displacements can be derived as [13]:

$$\psi_K = \arctan\left(\sqrt{\frac{H_{22}}{H_{11}}\frac{\delta_x}{\delta_y}}\right) - \varepsilon \ln\left(\frac{|x|}{h}\right) + \arctan(2\varepsilon) \qquad (1)$$

$$G = \frac{\pi(1+4\varepsilon^2)}{8H_{11}|x|}\left(\frac{H_{11}}{H_{22}}\delta_y^{\,2} + \delta_x^{\,2}\right) \qquad (2)$$

where δ_y is the opening and δ_x is the shearing relative displacement of the crack flanks, H_{11}, H_{22} and the oscillatory index ε are bimaterial constants related to the stiffness properties of the face and core. h is the characteristic length of the crack problem. In sandwich debonding problems the characteristic length is often chosen as the face thickness, which will approximately place the minimum at the fracture toughness distribution vs. mode-mixity at the phase angle $\psi_K = 0$. However, in order to compare calculated energy release rates with measured fracture toughness, the same characteristic length should be used in both mode-mixity definitions. Thus, using a finite element solution to calculate the relative nodal displacements of the crack flanks these two fracture parameters can be determined. For more details see [10].

(a)   (b)
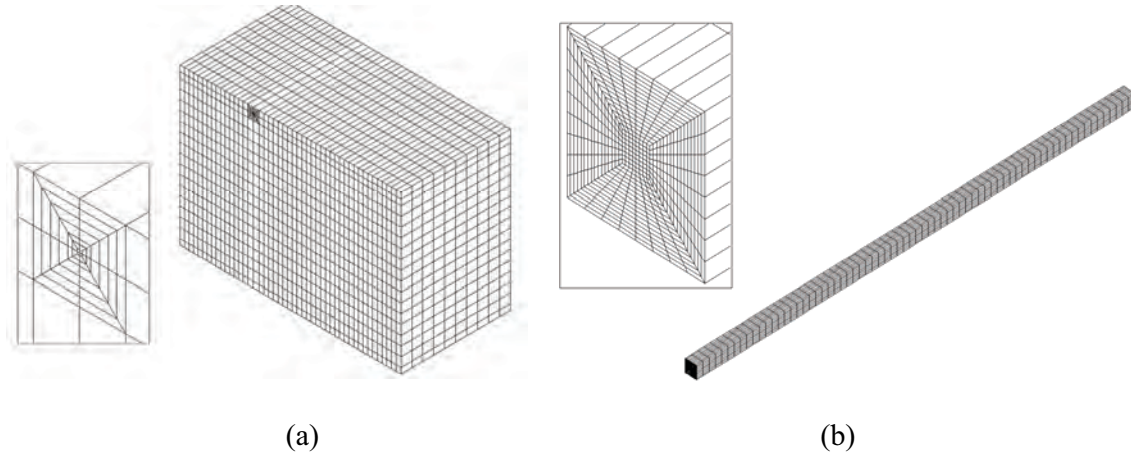
Figure 2: Finite element models. (a) half-model showing the mesh densities applied in the global model. Minimum element size is 0.2 mm. (b) sub-model showing the mesh density applied. Minimum element size is 0.01 mm

4 EXPERIMENTAL RESULTS

During the experiments it was observed from the DIC measurements that opening of the debond starts from one of the specimen edges, thus the opening is not symmetric, see Figure 3. This can be addressed to a slight misalignment of the fibers in the face sheets. It was also observed that for the columns where the debond was released using the thicker blade, the debond propagation load was considerably lower than for the other columns. Figure 4 shows

Ramin Moslemian, Christian Berggreen, Leif A. Carlsson, F. Aviles and A. May

two DIC images showing the initial amount of out-of-plane imperfection for two columns with the debond released using the two different blade thicknesses (0.35 and 0.43 mm). The maximum imperfection is seen to be approximately 0.25 mm and 0.51 mm for respectively the thin and thick blade. The majority of the tested columns failed by debond propagation at the face/core interface, see Figure 5. Crack kinking into the core was observed in some of the columns with H45 core. The fracture toughness of the low density H45 core material is low (150 J/m^2, see Table 2), and likely less than that of core/face resin interface, which would explain the observed crack propagation path. Both crack fronts of the debond rapidly propagated towards the column ends. Crack propagation occurred rapidly in low density cored columns (H45 and H100) and with lower propagation rate in columns with H200 core. All columns with H200 core and 25.4 mm debond length failed by compression failure of the face sheet above the debond location. This is explained by the proximity of the buckling load and the compression failure load (around 14.5 kN) for this sandwich column configuration, as determined from IITRI testing. The same failure mechanism was observed for one column with H45 and H100 core and 25.4 mm debond length.
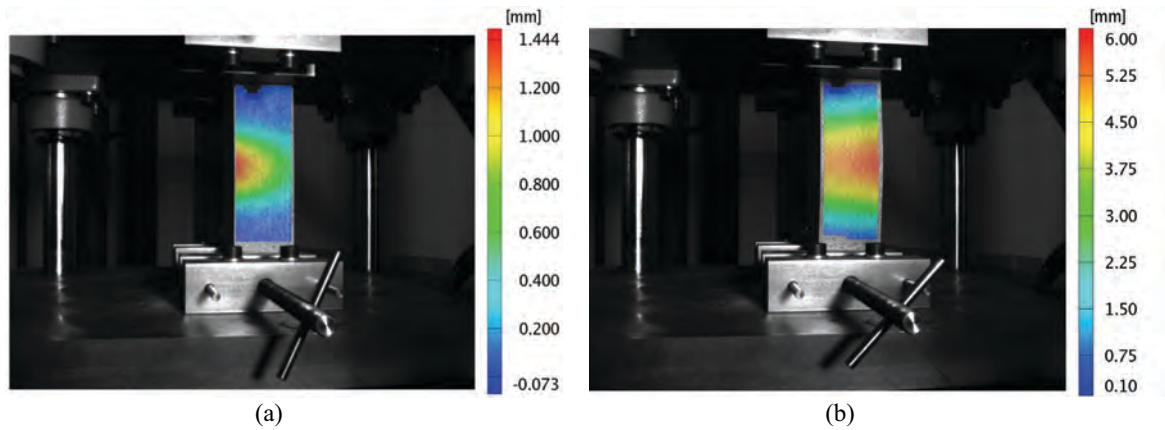

Figure 3: Debond opening (a) prior to propagation and (b) after propagation from DIC measurements.
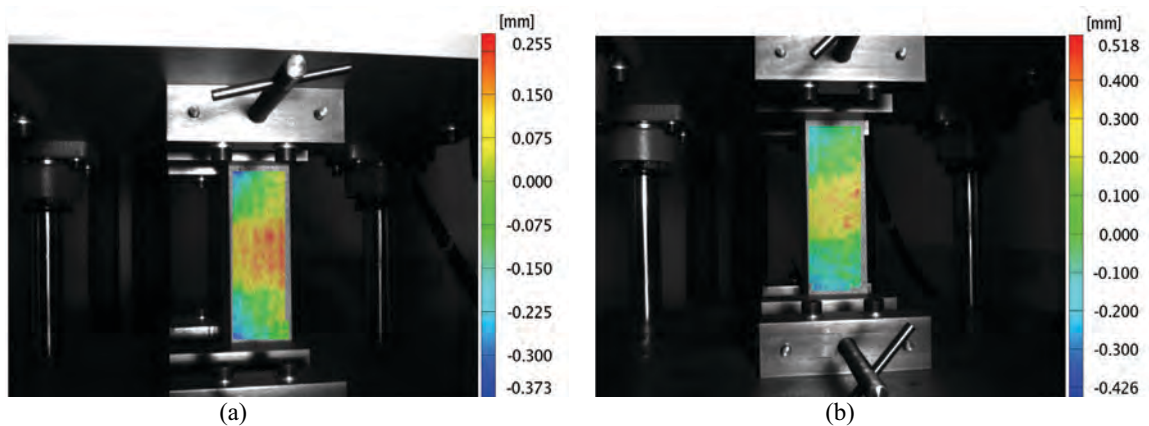

Figure 4: Initial imperfections from DIC measurements for columns where the debond was released using a (a) thin (0.35 mm) and (b) a thicker (0.43 mm) blade.
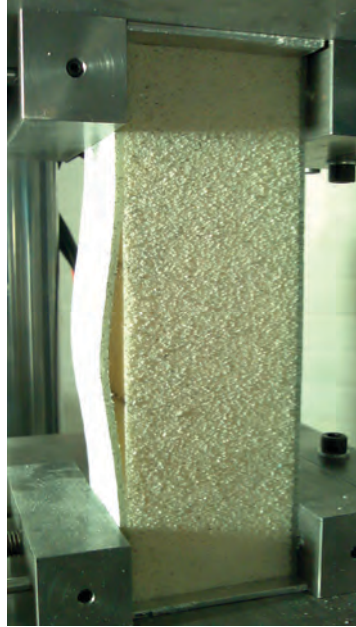
Figure 5: Debond propagation in a column with H100 core and 38.1 mm debond length

5   FINITE ELEMENT ANALYSIS RESULTS

Figure 6 shows the deformed shape of a debonded sandwich column with H100 core containing a 50.8 mm face/core debond. The local buckling mode resembles a half-sine with the maximum transverse deformation at the center, consistent with experimental testing

In order to examine the effect of initial imperfection, columns with three different initial imperfections of 0.1, 0.2 and 0.4 mm amplitudes were analyzed. Figure 7 shows out-of-plane deflection vs. load graphs for the debonded columns with H100 core determined from testing (two or three replicates are shown) and numerical analysis. It can be seen from both, experimental and numerical results, that the debond opening initially increases linearly with increasing load, but the trend becomes nonlinear as the load approaches the critical instability load. The non-linearity is more marked for the larger (38.1 and 50.8 mm) debonds. At the propagation point the load decreases while the out-of-plane displacement of the debonded face increases significantly. Increased out-of-plane deflection at any load level for the specimens with larger initial imperfections is also evidenced from the numerical analysis. Thus, columns with different initial imperfections show different nonlinear behaviors.
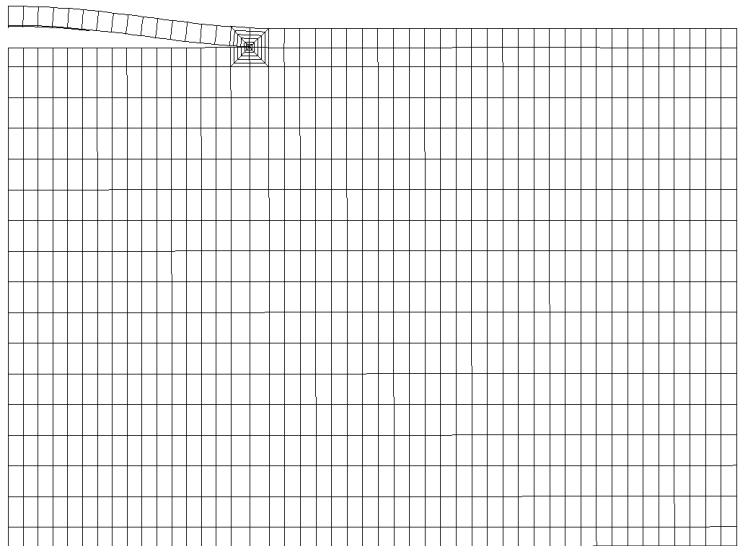
Figure 6: Deformed shape of the column model.

Table 4 summarizes the critical buckling/instability loads for the columns extracted from finite element analyses and experiments. For the finite element analysis 0.1 mm initial imperfection size was selected which is the value of imperfection measured in most of the columns. The instability loads were extracted applying the Southwell method [15]. Results show a good agreement between numerical analysis and experiments.

(a)

(b)
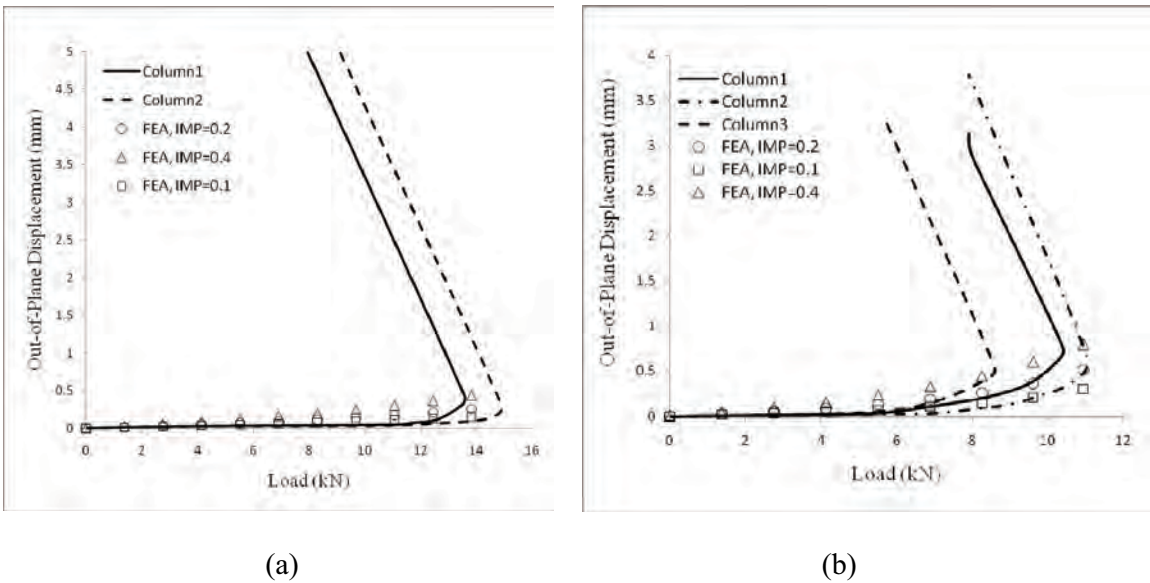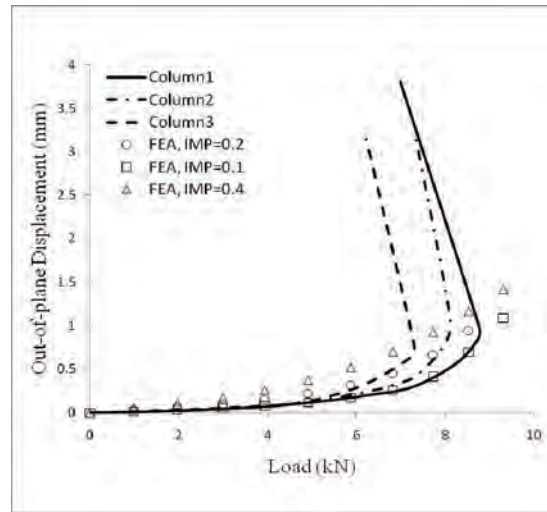
(c)

Figure 7: Out-of-plane vs. load diagram for columns with H100 core and (a) 25.4 mm debond, (b) 38.1 mm debond, (c) 50.8 mm debond length

Specimen	Experiment			Finite Element Analysis		
	Debond Length (mm)			Debond Length (mm)		
	25.4	38.1	50.8	25.4	38.1	50.8
Core	Instability Load (kN)			Instability Load (kN)		
H45	12.9±1.5	10.1±1.1	6.1±0.9	14.1	8.5	6.5
H100	14.8±0.8	10.5±1.7	8.7±0.6	15.2	11.6	8.3
H200	--	13±1.2	8.5±0.3	--	13.8	9

Table 4: Critical instability loads determined experimentally and from finite element analysis using 0.1 mm initial imperfections size.

In order to predict the debond propagation load, mode I fracture toughnesses (G_{Ic}) of the cores listed in Table 2 was applied. Numerically predicted and experimentally determined failure loads (at propagation) for the debonded columns are listed in Table 5. It can be seen that the numerical analysis is able to predict the failure load of the columns with good accuracy. Calculated mode-mixities from finite element analysis for the columns were low. These low mode-mixity values confirms that the fracture process is mode I dominated. From the results in Table 4 and 5 it can be concluded that the debond propagation load is close to the instability load which illustrates the important role of instability for debond propagation in sandwich columns.

Ramin Moslemian, Christian Berggreen, Leif A. Carlsson, F. Aviles and A. May

Specimen	Experiment			Finite Element Analysis		
	Debond Length (mm)			Debond Length (mm)		
	25.4	38.1	50.8	25.4	38.1	50.8
Core	Failure Load (kN)			Failure Load (kN)		
H45	13.5±1	9.8±1.4	5.9±0.8	11.4	7.6	6.1
H100	13.8±0.9	10±1.2	8±0.9	14.8	10.3	8
H200	--	12.3±1.7	7.8±0.2	--	13.8	8.9

Table 5: Predicted and experimental failure loads

8 CONCLUSION

The behavior of foam cored sandwich columns containing a face-to-core debond under uniform in-plane compression has been experimentally and numerically investigated. A new test rig was designed and manufactured for axial testing of the sandwich columns. Experiments were carried out on the sandwich columns with three foam core densities and three debond lengths. Final failure was governed by local buckling instability and debond propagation towards the column ends. The majority of the debonded columns failed by debond propagation, with only a few of them failing by compression failure of the face sheets. It was experimentally observed that for the columns with large initial imperfection size, the debond propagation load is considerably lower than for the columns with small imperfection. Using geometrically nonlinear finite element analysis and linear elastic fracture mechanics, instability and failure loads of the columns were predicted. In order to examine the effect of initial imperfection, columns with three initial imperfections were analyzed. Results showed the dependency of the out-of-plane deflection of the debonded face sheet combined with debond size and initial imperfection. Comparison of the measured out-of-plane deflection, instability, and debond propagation loads from experiments with finite element results furthermore showed good agreement.

ACKNOWLEDGEMENTS

REFERENCES

[1] D. Zenkert. An introduction to sandwich construction, London: EMAS, (1997)

[2] K. Shivakumar and H. Chen, "An evaluation of data reduction methods for opening mode fracture toughness of sandwich panels", *Journal of sandwich structures and materials*, Vol. 7, 77-90 (2005).

[3] Z. Xie and A. J. Vizzini, "Damage propagation in a composite sandwich panel subjected to increasing uniaxial compression after low-velocity impact"*, Journal of sandwich structures and materials*, Vol. 7, 269-90 (2005).

[4] H. Chen and R. Bai, "Postbuckling behavior of face/core debonded composite sandwich plate considering matrix crack and contact effect, Composite structures", Vol. 57, 305-313 (2002).

[5] J. Hohe and W. Becker, "Assessment of the delamination hazard of the core face sheet bond in structural sandwich panels", *International Journal of Fracture*, Vol. 109, 413-432 (2001).

[6] B. V. Sankar and M. Narayan, "Finite element analysis of debonded sandwiches beams under axial compression", *Journal of sandwich structures and materials,* Vol. 3, 197-219 (2001).

[7] V. Vadakke and L. A. Carlsson, "Experimental Investigation of Compression Failure of Sandwich Specimens with Face/Core Debond", *Composites Part B: Engineering*, 35, 583-590 (2004)

[8] S. El-Sayed and S. Sridharan. "Cohesive layer models for predicting delamination growth and crack kinking in sandwich structures", *International Journal of Fracture*, Vol. 117, 63-84 (2002).

[9] R. C. Østergaard, "Failure of compression loaded isotropic sandwich column containing a debond. In: Polymer composite materials for wind power turbines", *Proceedings. 27. Risø international symposium on materials science*, Risø (DK), p. 357-364 (2006).

[10] C. Berggreen and B.C. Simonsen, "Non-Uniform Compressive Strength of Debonded Sandwich Panels - II. Fracture Mechanics Investigation", *Journal of Sandwich Structures and Materials*, 7(6), 483-517 (2005).

[11] F. Avilés and L.A. Carlsson, "Post-Buckling and Debond Propagation in Panels Subjected to In-Plane Loading", *Engineering Fracture Mechanics*, 74, 794-806 (2007).

[12] DIAB, Divinycell H Technical Data, Laholm. From: http://www.diabgroup.com.

[13] J. Hutchinson and Z. Suo, "Mixed Mode Cracking in Layered Materials", Advances *in Applied Mechanics*, 29, 63-191 (1992).

[14] G.M. Viana and L.A. Carlsson, "Mechanical properties and fracture characterization of Cross-linked PVC foams", *Journal of Sandwich Structures and Materials*, 4, 99-113 (2002).

[15] R. Southwell, "On the Analysis of Experimental Observations in Problems of Elastic Stability", *Proceedings of the Royal Society of London,* 601–616 (1932).

AN OPTIMIZED SHAPE PARAMETER RADIAL BASIS FUNCTION FORMULATION FOR COMPOSITE AND SANDWICH PLATES USING A HIGHER ORDER FORMULATION

Carla M.C. Roque, António J.M. Ferreira, and Renato M.N. Jorge

*Faculdade de Engenharia da Universidade do Porto (FEUP)
Universidade do Porto
Rua Dr. Roberto Frias, 4200-465 Porto, Portugal
e-mail: croque,ferreira,rnatal@fe.up.pt, web page: http://www.fe.up.pt

Key words: Sandwich structures, Radial basis functions, Meshless methods.

Summary. *The purpose of this work is to use a meshless collocation method with multiquadric radial basis functions (RBFs), the third order shear deformation theory presented by Reddy [3] (TSDT), and optimal values of the shape parameter in the RBFs to analyze static deformations of sandwich plates. The multiquadric RBF method was introduced by Kansa [1, 2] for solving boundary-value problems governed by partial differential equations. Here we show that this method with optimal values of the shape parameter gives deflections of sandwich plates that agree very well with analytical solutions, for regular and irregular grids. An advantage of the meshless method is that it requires very little input data, thus the time required for preparing the data can be significantly reduced.*

1 INTRODUCTION

We use the third order shear deformation theory presented by Reddy [3] to compute the static deformations of simply supported sandwich plates under uniformly distributed load. This higher-order theory is briefly presented in section 2 and readers should refer to reference [6] for more details. In this paper we compare the analytical solution for several sandwich plates with the solution obtained with the meshless multiquadric radial basis functions method. The analytical solutions are obtained by the Navier procedure, presented in section 3.

The meshless multiquadric method, first presented by Kansa [1, 2], is well known for solving systems of partial differential equations with excellent accuracy. However, it has the problem of the choice of an adequate shape parameter for the multiquadric interpolation function. We use a statistical technique based on cross validation that overcomes the choice of the shape parameter to the simple indication of a user-defined interval. The examples in this paper show an improvement of the results when using this optimization technique, when compared to RBFs without optimal shape parameter.

2 THIRD ORDER THEORY

The third-order theory of Reddy [3, 6] is based on the same assumptions than the classical and first-order plate theories, except that the assumption of straightness and normality of a

transverse normal after deformation is relaxed by expanding the displacements (u, v, w) as cubic functions of the thickness coordinate.

The displacement field is then obtained as

$$
\begin{aligned}
u(x, y, z) &= u_0(x, y) + z\phi_x(x, y) - \frac{4}{3h^2}z^3\left(\phi_x(x, y) + \frac{\partial w(x, y)}{\partial x}\right) \\
v(x, y, z) &= v_0(x, y) + z\phi_y(x, y) - \frac{4}{3h^2}z^3\left(\phi_y(x, y) + \frac{\partial w(x, y)}{\partial y}\right) \\
w(x, y, z) &= w_0(x, y)
\end{aligned}
\tag{1}
$$

where u and v are the inplane displacements at any point (x, y, z), u_0 and v_0 denote the inplane displacement of the point $(x, y, 0)$ on the midplane, w is the deflection, ϕ_x and ϕ_y are the rotations of the normals to the midplane about the y and x axes, respectively. The thickness of the plate is denoted as h.

The strain-displacement relationships are given as:

$$
\left\{
\begin{array}{c}
\epsilon_{xx} \\
\epsilon_{yy} \\
\gamma_{xy} \\
\gamma_{xz} \\
\gamma_{yz}
\end{array}
\right\}
=
\left\{
\begin{array}{c}
\frac{\partial u}{\partial x} \\
\frac{\partial v}{\partial y} \\
\frac{\partial u}{\partial y} + \frac{\partial v}{\partial x} \\
\frac{\partial u}{\partial z} + \frac{\partial w}{\partial x} \\
\frac{\partial v}{\partial z} + \frac{\partial w}{\partial y}
\end{array}
\right\}
\tag{2}
$$

Therefore strains can be expressed as

$$
\left\{
\begin{array}{c}
\epsilon_{xx} \\
\epsilon_{yy} \\
\gamma_{xy}
\end{array}
\right\}
=
\left\{
\begin{array}{c}
\epsilon_{xx}^{(0)} \\
\epsilon_{yy}^{(0)} \\
\gamma_{xy}^{(0)}
\end{array}
\right\}
+ z
\left\{
\begin{array}{c}
\epsilon_{xx}^{(1)} \\
\epsilon_{yy}^{(1)} \\
\gamma_{xy}^{(1)}
\end{array}
\right\}
+ z^3
\left\{
\begin{array}{c}
\epsilon_{xx}^{(3)} \\
\epsilon_{yy}^{(3)} \\
\gamma_{xy}^{(3)}
\end{array}
\right\}
;
\quad
\left\{
\begin{array}{c}
\gamma_{xz} \\
\gamma_{yz}
\end{array}
\right\}
=
\left\{
\begin{array}{c}
\gamma_{xz}^{(0)} \\
\gamma_{yz}^{(0)}
\end{array}
\right\}
+ z^2
\left\{
\begin{array}{c}
\gamma_{xz}^{(2)} \\
\gamma_{yz}^{(2)}
\end{array}
\right\}
\tag{3}
$$

where

$$\left\{\begin{array}{c} \epsilon_{xx}^{(0)} \\ \epsilon_{yy}^{(0)} \\ \gamma_{xy}^{(0)} \end{array}\right\} = \left\{\begin{array}{c} \frac{\partial u_0}{\partial x} \\ \frac{\partial v_0}{\partial y} \\ \frac{\partial u_0}{\partial y} + \frac{\partial v_0}{\partial x} \end{array}\right\}; \quad \left\{\begin{array}{c} \epsilon_{xx}^{(1)} \\ \epsilon_{yy}^{(1)} \\ \gamma_{xy}^{(1)} \end{array}\right\} = \left\{\begin{array}{c} \frac{\partial \phi_x}{\partial x} \\ \frac{\partial \phi_y}{\partial y} \\ \frac{\partial \phi_x}{\partial y} + \frac{\partial \phi_y}{\partial x} \end{array}\right\}; \quad \left\{\begin{array}{c} \epsilon_{xx}^{(3)} \\ \epsilon_{yy}^{(3)} \\ \gamma_{xy}^{(3)} \end{array}\right\} = -c_1 \left\{\begin{array}{c} \frac{\partial \phi_x}{\partial x} + \frac{\partial^2 w_0}{\partial x^2} \\ \frac{\partial \phi_y}{\partial y} + \frac{\partial^2 w_0}{\partial y^2} \\ \frac{\partial \phi_x}{\partial y} + \frac{\partial \phi_y}{\partial x} + 2\frac{\partial^2 w_0}{\partial x \partial y} \end{array}\right\}$$

(4)

$$\left\{\begin{array}{c} \gamma_{xz}^{(0)} \\ \gamma_{yz}^{(0)} \end{array}\right\} = \left\{\begin{array}{c} \frac{\partial w_0}{\partial x} + \phi_x \\ \frac{\partial w_0}{\partial y} + \phi_y \end{array}\right\}; \quad \left\{\begin{array}{c} \gamma_{xz}^{(2)} \\ \gamma_{yz}^{(2)} \end{array}\right\} = -c_2 \left\{\begin{array}{c} \frac{\partial w_0}{\partial x} + \phi_x \\ \frac{\partial w_0}{\partial y} + \phi_y \end{array}\right\}$$

(5)

and $c_1 = \frac{4}{3h^2}, c_2 = 3c_1$.

A laminate can be manufactured from orthotropic layers (or plies) of pre-impregnated unidirectional fibrous composite materials. Neglecting σ_z for each layer, the stress-strain relations in the fiber local coordinate system can be expressed as

$$\left\{\begin{array}{c} \sigma_1 \\ \sigma_2 \\ \tau_{12} \\ \tau_{23} \\ \tau_{31} \end{array}\right\} = \left[\begin{array}{ccccc} Q_{11} & Q_{12} & 0 & 0 & 0 \\ Q_{12} & Q_{22} & 0 & 0 & 0 \\ 0 & 0 & Q_{33} & 0 & 0 \\ 0 & 0 & 0 & Q_{44} & 0 \\ 0 & 0 & 0 & 0 & Q_{55} \end{array}\right] \left\{\begin{array}{c} \varepsilon_1 \\ \varepsilon_2 \\ \gamma_{12} \\ \gamma_{23} \\ \gamma_{31} \end{array}\right\}$$

(6)

where subscripts 1 and 2 are respectively the fiber and the normal to fiber inplane directions, 3 is the direction normal to the plate, and the reduced stiffness components, Q_{ij} are given by

$$Q_{11} = \frac{E_1}{1-\nu_{12}\nu_{21}}; \quad Q_{22} = \frac{E_2}{1-\nu_{12}\nu_{21}}; \quad Q_{12} = \nu_{12}Q_{11};$$
$$Q_{33} = G_{12}; \quad Q_{44} = G_{23}; \quad Q_{55} = G_{31}; \quad \nu_{21} = \nu_{12}\frac{E_2}{E_1}$$

in which E_1, E_2, ν_{12}, G_{12}, G_{23} and G_{31} are materials properties of the lamina.

By performing adequate coordinate transformation, the stress-strain relations in the global x-y-z coordinate system can be obtained as

$$\left\{\begin{array}{c} \sigma_{xx} \\ \sigma_{yy} \\ \tau_{xy} \\ \tau_{yz} \\ \tau_{zx} \end{array}\right\} = \left[\begin{array}{ccccc} \overline{Q}_{11} & \overline{Q}_{12} & \overline{Q}_{16} & 0 & 0 \\ \overline{Q}_{12} & \overline{Q}_{22} & \overline{Q}_{26} & 0 & 0 \\ \overline{Q}_{16} & \overline{Q}_{26} & \overline{Q}_{66} & 0 & 0 \\ 0 & 0 & 0 & \overline{Q}_{44} & \overline{Q}_{45} \\ 0 & 0 & 0 & \overline{Q}_{45} & \overline{Q}_{55} \end{array}\right] \left\{\begin{array}{c} \varepsilon_{xx} \\ \varepsilon_{yy} \\ \gamma_{xy} \\ \gamma_{yz} \\ \gamma_{zx} \end{array}\right\}$$

(7)

The third-order theory of Reddy [3, 6] satisfies zero transverse shear stresses on the bounding planes.

The equations of motion of the third-order theory are derived from the principle of virtual displacements.

The virtual strain energy (δU), the virtual work done by applied forces (δV) are given by

$$
\begin{aligned}
\delta U = \int_{\Omega_0} & \left\{ \int_{-h/2}^{h/2} \left[\sigma_{xx} \left(\delta\epsilon_{xx}^{(0)} + z\delta\epsilon_{xx}^{(1)} - c_1 z^3 \delta\epsilon_{xx}^{(3)} \right) + \sigma_{yy} \left(\delta\epsilon_{yy}^{(0)} + z\delta\epsilon_{yy}^{(1)} - c_1 z^3 \delta\epsilon_{yy}^{(3)} \right) \right. \right. \\
& \left. \left. + \tau_{xy} \left(\delta\gamma_{xy}^{(0)} + z\delta\gamma_{xy}^{(1)} - c_1 z^3 \delta\gamma_{xy}^{(3)} \right) + \tau_{xz} \left(\delta\gamma_{xz}^{(0)} + z^2 \delta\gamma_{xz}^{(2)} \right) + \tau_{yz} \left(\delta\gamma_{yz}^{(0)} + z^2 \delta\gamma_{yz}^{(2)} \right) \right] dz \right\} dx\, dy \\
= \int_{\Omega_0} & \left(N_{xx}\delta\epsilon_{xx}^{(0)} + M_{xx}\delta\epsilon_{xx}^{(1)} - c_1 P_{xx}\delta\epsilon_{xx}^{(3)} + N_{yy}\delta\epsilon_{yy}^{(0)} + M_{yy}\delta\epsilon_{yy}^{(1)} - c_1 P_{yy}\delta\epsilon_{yy}^{(3)} + N_{xy}\delta\gamma_{xy}^{(0)} \right. \\
& \left. + M_{xy}\delta\gamma_{xy}^{(1)} - c_1 P_{xy}\delta\gamma_{xy}^{(3)} + Q_x\delta\gamma_{xz}^{(0)} + R_x\delta\gamma_{xz}^{(2)} + Q_y\delta\gamma_{yz}^{(0)} + R_y\delta\gamma_{yz}^{(2)} \right) dx\, dy
\end{aligned}
$$

and

$$
\delta V = - \int_{\Omega_0} q\delta w_0 \, dxdy \tag{8}
$$

where Ω_0 denotes the midplane of the laminate, q is the external distributed load and

$$
\begin{Bmatrix} N_{\alpha\beta} \\ M_{\alpha\beta} \\ P_{\alpha\beta} \end{Bmatrix} = \int_{-h/2}^{h/2} \sigma_{\alpha\beta} \begin{Bmatrix} 1 \\ z \\ z^3 \end{Bmatrix} dz; \qquad \begin{Bmatrix} Q_\alpha \\ R_\alpha \end{Bmatrix} = \int_{-h/2}^{h/2} \sigma_{\alpha z} \begin{Bmatrix} 1 \\ z^2 \end{Bmatrix} dz \tag{9}
$$

where α, β take the symbols x, y.

Substituting for $\delta U, \delta V$, into the virtual work statement, noting that the virtual strains can be expressed in terms of the generalized displacements, integrating by parts to relieve from any derivatives of the generalized displacements and using the fundamental lemma of the calculus of variations, we obtain the following Euler-Lagrange equations [6]:

$$
\frac{\partial N_{xx}}{\partial x} + \frac{\partial N_{xy}}{\partial y} = 0 \tag{10}
$$

$$
\frac{\partial N_{xy}}{\partial x} + \frac{\partial N_{yy}}{\partial y} = 0 \tag{11}
$$

$$
\frac{\partial \overline{Q}_x}{\partial x} + \frac{\partial \overline{Q}_y}{\partial y} + \frac{4}{3h^2} \left(\frac{\partial^2 P_{xx}}{\partial x^2} + 2\frac{\partial^2 P_{xy}}{\partial x \partial y} + \frac{\partial^2 P_{yy}}{\partial y^2} \right) + q = 0 \tag{12}
$$

$$
\frac{\partial \overline{M}_{xx}}{\partial x} + \frac{\partial \overline{M}_{xy}}{\partial y} - \overline{Q}_x = 0 \tag{13}
$$

$$\frac{\partial \overline{M}_{xy}}{\partial x} + \frac{\partial \overline{M}_{yy}}{\partial y} - \overline{Q}_y = 0 \tag{14}$$

with

$$\overline{M}_{\alpha\beta} = M_{\alpha\beta} - \frac{4}{3h^2} P_{\alpha\beta}; \qquad\qquad \overline{Q}_\alpha = Q_\alpha - \frac{4}{h^2} R_\alpha \tag{15}$$

The Euler-Lagrange equations can be written in terms of the displacements by substituting strains and stress resultants in (10)-(14).

3   NAVIER SOLUTIONS FOR TSDT

The Navier solutions for the third order shear deformation theory of Reddy (TSDT) can be found in [6]. For a simply supported square plate in edges $0, a$ the imposed boundary conditions are:

$$\text{in } x = 0, a : v = w = \phi_y = N_x = \overline{M}_x = 0 \tag{16}$$

$$\text{in } y = 0, a : u = w = \phi_x = N_y = \overline{M}_y = 0 \tag{17}$$

The boundary conditions in (16) and (17) are satisfied by:

$$u_0(x, y) = \sum_{n=1}^{\infty} \sum_{m=1}^{\infty} U_{nm} \cos(\alpha x) \sin(\beta y) \tag{18}$$

$$v_0(x, y) = \sum_{n=1}^{\infty} \sum_{m=1}^{\infty} V_{nm} \sin(\alpha x) \cos(\beta y) \tag{19}$$

$$w_0(x, y) = \sum_{n=1}^{\infty} \sum_{m=1}^{\infty} W_{nm} \sin(\alpha x) \sin(\beta y) \tag{20}$$

$$\phi_x(x, y) = \sum_{n=1}^{\infty} \sum_{m=1}^{\infty} \Phi x_{nm} \cos(\alpha x) \sin(\beta y) \tag{21}$$

$$\phi_y(x, y) = \sum_{n=1}^{\infty} \sum_{m=1}^{\infty} \Phi y_{nm} \sin(\alpha x) \cos(\beta y) \tag{22}$$

$$q(x, y) = \sum_{n=1}^{\infty} \sum_{m=1}^{\infty} Q_{nm} \sin(\alpha x) \sin(\beta y) \tag{23}$$

with

$$\alpha = \frac{m\pi x}{a}; \beta = \frac{m\pi x}{a} \tag{24}$$

$$Q_{nm} = \frac{4}{a^2} \int_0^a \int_0^a q(x, y) \sin \frac{m\pi x}{a} \sin \frac{n\pi y}{a} \, dx \, dy \tag{25}$$

Substituting equations (18)-(23) in equations (10)-(14) and solving for $U_{nm}, V_{nm}, W_{nm}, \Phi x_{nm}$ and Φy_{nm} allows us to compute $u_0(x, y), v_0(x, y), w_0(x, y), \phi_x(x, y)$ and $\phi_y(x, y)$ in (18)-(23).

4 THE MULTIQUADRIC METHOD

Consider the generic boundary value problem with a domain Ω with boundary $\partial\Omega$, and some linear differential operators L and B:

$$Lu(x) = f(x), \ x \in \Omega \subset \mathbb{R}^n; \qquad\qquad Bu|_{\partial\Omega} = q \qquad (26)$$

The function **u(x)** is approximated by:

$$\mathbf{u} \simeq \bar{\mathbf{u}} = \sum_{j=1}^{N} \alpha_j g_j \qquad (27)$$

were α_j are parameters to be determined after the collocation method is applied and N the total number of points in the boundary and domain. We consider a global collocation method where the linear operators L and B acting in domain $\Omega \backslash \partial\Omega$ and boundary $\partial\Omega$ define a set of global equations in the form

$$\begin{pmatrix} \mathbf{L}_{ii} & \mathbf{L}_{ib} \\ \mathbf{B}_{bi} & \mathbf{B}_{bb} \end{pmatrix} \begin{pmatrix} \alpha_i \\ \alpha_b \end{pmatrix} = \begin{pmatrix} f_i \\ q_b \end{pmatrix}; \qquad \text{or} \qquad [\mathcal{L}]\,[\alpha] = [\lambda] \qquad (28)$$

where i and b denote domain and boundary nodes, respectively; f_i and q_b are some external conditions in domain and boundary.

The function g represents a radial basis function. In the present case, we choose the multiquadric function, defined as:

$$g(r,c) = (\|x - x_j\|^2 + c^2)^{\frac{1}{2}} \qquad (29)$$

were r is the euclidian distance between two nodes and c is a shape parameter that improves the function surface so that convergence gets faster [1, 2]. Other radial basis functions could be used (gaussians, splines, etc). However, multiquadrics proved to be excellent for global, smooth, boundary-value problems [7].

5 AN OPTIMIZATION TECHNIQUE

An optimal shape parameter c (equation (29)) can be obtained for an interpolation problem $A\alpha = f, A = g(\|\mathbf{x}_j - \mathbf{x}_i, c\|)$, by the leave-one-out cross validation technique in regression analysis. The problem can be formulated as finding c in order to minimize a cost function given by the norm of an error vector $E(c)$ with components

$$E_i(c) = f_i - \sum_{j=1,j\neq i}^{N} \alpha_j^{(i)} g(\|\mathbf{x}_j - \mathbf{x}_i, c\|) \qquad (30)$$

Here $\sum_{j=1,j\neq i}^{N} \alpha_j^{(i)} g(\|\mathbf{x}_j - \mathbf{x}_i, c\|)$ is the function value predicted at the i-th data point using RBF interpolation based on a set of data that excludes the i-th point.

A more efficient algorithm, from a computational point of view, is given by the following formula [4, 5]:

$$E_i(c) = \frac{\alpha_i}{A_{i,i}^{-1}} \tag{31}$$

where α_i is the i-th coefficient for the full interpolation problem and $A_{i,i}^{-1}$ is the i-th diagonal element of the inverse of the corresponding interpolation matrix A. In the case of our boundary value problem, the error to be minimized is a residual error, of the form [8]:

$$E_i(c) = \lambda_i - \sum_{j=1, j \neq i}^{N} \alpha_j^{(i)} \mathcal{L}g(||\mathbf{x}_j - \mathbf{x}_i, c||) \tag{32}$$

Now the generalization of the cross-validation algorithm is straightforward. Our BVP is given by equation (28). We can then use the following formula which is analogous to (31):

$$E_i(c) = \frac{\alpha_i}{\mathcal{L}_{i,i}^{-1}}, \ i \in \Omega \tag{33}$$

where α_i is the i-th coefficient for the full collocation problem (28) and $\mathcal{L}_{i,i}^{-1}$ is the i-th diagonal element of the inverse of the corresponding collocation matrix $\mathcal{L}$.

6 NUMERICAL EXAMPLES

6.1 Three layer square sandwich plate, under uniform load

A simply-supported sandwich square plate, under uniform transverse load is considered. The material properties of the sandwich core are expressed in the stiffness matrix, $\overline{Q}_{core}$ as:

$$\overline{Q}_{core} = \begin{bmatrix} 0.999781 & 0.231192 & 0 & 0 & 0 \\ 0.231192 & 0.524886 & 0 & 0 & 0 \\ 0 & 0 & 0.262931 & 0 & 0 \\ 0 & 0 & 0 & 0.266810 & 0 \\ 0 & 0 & 0 & 0 & 0.159914 \end{bmatrix}$$

The skins material properties are related with the core properties by a factor R as

$$\overline{Q}_{skin} = R\overline{Q}_{core} \tag{34}$$

The transverse displacement is normalized through factor $\overline{w} = w\frac{0.999781}{hq}$. The Navier solution presented in tables 1 and 2 is computed with 71 terms. The optimization technique was applied to the interval [0.1-3].

In table 1 the central normalized deflection $\overline{w}$ is presented, for various values of R and n, where n is the number of points/ side in a regular grid. Results in table 1 are computed using the optimization technique described previously. The optimized shape parameter parameter found by the cross validation technique is indicated in each case by c_{opt}.

In table 2, previous results obtained by the authors with $c = 2/\sqrt{n}$ and regular grids are presented [7]. This shape parameter results from trial-error experiences.

In figure 1, the relative error computed by (35) using results from tables 1 and 2 is depicted. Using the optimization technique, a faster convergence is achieved. This is an important factor when dealing with large engineering problems.

$$\text{relative error}(\%) = \frac{||\text{computed rbf value} - \text{Navier solution}||}{||\text{Navier solution}||} \times 100 \qquad (35)$$

In figure 2, the Navier and RBF solutions for $u_0(x,y), v_0(x,y), w_0(x,y), \phi_x(x,y), \phi_y(x,y)$ are plotted using an irregular grid $n = 7 \times 7$ and the optimization technique.

R		Number of nodes/side, n						Navier	Exact
		7	9	11	13	15	17	Solution	solution[9]
5	$\overline{w}$	244.16	252.72	255.85	256.63	256.53	256.96	256.97	258.97
	c_{opt}	2.0	1.3	1.1	0.9	0.6	0.6		
10	$\overline{w}$	149.82	152.39	153.90	154.32	154.41	154.63	154.50	159.38
	c_{opt}	2.8	1.7	1.0	0.8	0.6	0.6		
15	$\overline{w}$	110.54	113.60	114.09	114.47	114.50	114.54	114.50	121.72
	c_{opt}	2.6	1.5	0.9	0.8	0.6	0.5		

Table 1: Central normalized deformation, for $a/h = 10$ with optimization technique

R	Number of nodes/side, n		
	11	15	21
5	253.671	256.2387	257.11
10	153.0084	154.249	154.6581
15	113.5941	114.3874	114.6442

Table 2: Central deformation, for $a/h = 10$, $c = 2/\sqrt{n}$. [7]

7 CONCLUSIONS

The third order shear deformation theory of Reddy was used with a meshless collocation method and an optimization technique for predicting the static deformation of simply supported sandwich plates.

The third order shear deformation theory is not adequate to model sandwich plates with a large difference of properties between the skin and the core.

The optimization technique reduced the number of points necessary to converge to the analytical solution, and in most cases is capable of choosing a good shape parameter even for irregular grids.

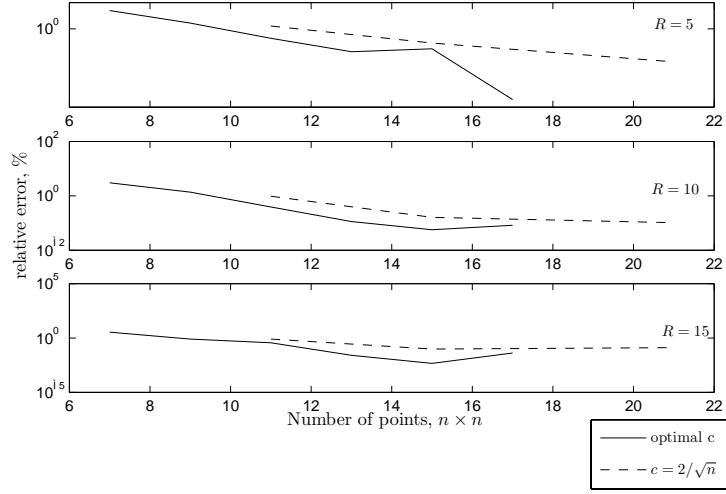Carla M.C. Roque, António J.M. Ferreira and Renato M.N. Jorge

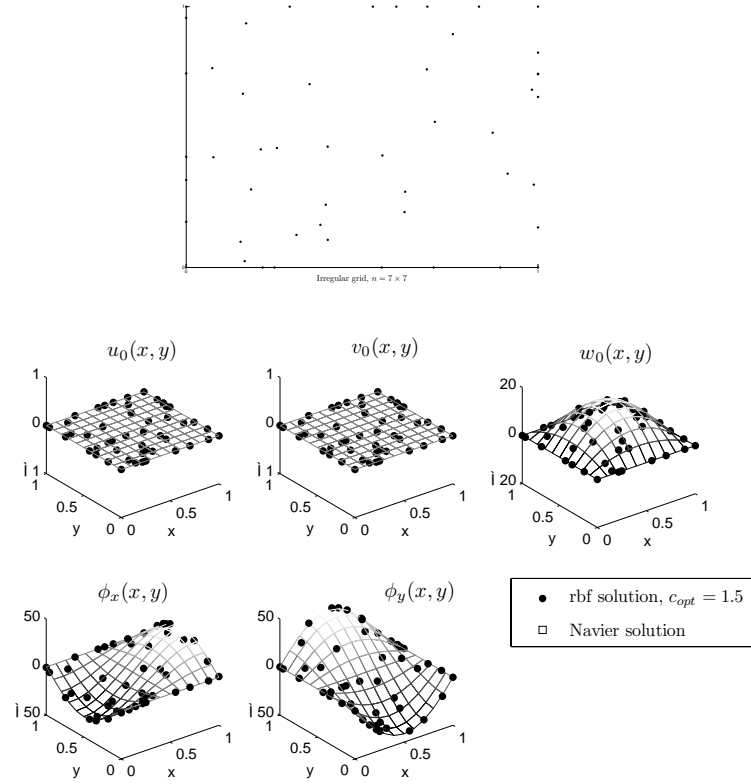Figure 1: Relative error in percentage with an optimal c and with $c = 2/\sqrt{n}$

Figure 2: Navier solution and rbf solution for an irregular grid with $n = 7 \times 7$, $R = 10$

REFERENCES

[1] E.J. Kansa. Multiquadrics. A scattered data approximation scheme with applications to computational fluid-dynamics. I. Surface approximations and partial derivative estimates. *Computers & mathematics with applications*, **19**, 127–145, 1990.

[2] E.J. Kansa. Multiquadrics. A scattered data approximation scheme with applications to computational fluid-dynamics. II. Solutions to parabolic, hyperbolic and elliptic partial differential equations. *Computers & mathematics with applications*, **19**, 147–161, 1990.

[3] J.N. Reddy. Simple higher-order theory for laminated composite plates. *Journal of Applied Mechanics, Transactions ASME*, **51**, 745–752, 1984.

[4] S. Rippa. An algorithm for selecting a good value for the parameter c in radial basis function interpolation. *Advances in Computational Mathematics*, **11**, 193–210, 1999.

[5] B.P. Wang. Parameter optimization in multiquadric response surface approximations. *Structural and Multidisciplinary Optimization*, **26**, 219–223, 2004.

[6] J.N. Reddy. *Mechanics of Laminated Composite Plates and Shells*, CRC Press, 2004.

[7] A.J.M. Ferreira, C.M.C. Roque, and P.A.L.S. Martins. Analysis of composite plates using higher-order shear deformation theory and a finite point formulation based on the multiquadric radial basis function method. *Composites Part B: Engineering*, **34**, 627–636, 2003.

[8] A.H.D. Cheng, M.A. Golberg, E.J. Kansa, and Q. Zammito. Exponential convergence and H-c multiquadric collocation method for partial differential equations. *Numerical Methods for Partial Differential Equations*, **19**, 571–594, 2003.

[9] S. Srinivas. Refined analysis of composite laminates. *Journal of Sound and Vibration*, **30**, 495–507, 1973.

MICROMECHANICAL MODELLING OF THE COMPOSITE REINFORCED FOAM CORE OF A 3D SANDWICH STRUCTURE MANUFACTURED BY THE NAPCO® TECHNOLOGY

J. Guilleminot★, S. Comas-Cardona★, D. Kondo†, C. Binetruy★ and P. Krawczak★

★Ecole des Mines de Douai
Polymers and Composites Technology & Mechanical Engineering Department
941 rue C. Bourseul, B.P. 10838, 59508 Douai, France
e-mail: binetruy@ensm-douai.fr, web page: http://www.ensm-douai.fr

†Université des Sciences et Technologies de Lille
Laboratoire de Mécanique de Lille-UMR CNRS 8107
Cité Scientifique, Bd. Paul Langevin, 59655 Villeneuve d'Ascq Cedex, France
e-mail: djimedo.kondo@univ-lille1.fr, web page: http://lmlm6-62.univ-lille1.fr/lml

Key words: 3D Sandwich Structures, Micromechanical Modelling, Manufacturing, Probabilistic Model.

Summary. *A key objective dealing with 3D sandwich structures is to maximize the through-thickness stiffness, the strength of the core and the core to faces adhesion. The Napco® technology was especially designed for improving such material properties and is under investigation in this paper. In particular, the potential of the process is characterized using a micromechanical modelling combined to a parametric probabilistic model. An experimental analysis is further detailed and validates the theoretical estimates of the core-related elastic properties. In particular, it is shown that the technology is able to produce parts with significantly improved mechanical properties.*

1 INTRODUCTION

In order to increase the load capacity of a sandwich construction without penalizing its lightness, one may try to maximize the through-thickness stiffness and strength of the core. One strategy of achieving this is to add through-thickness reinforcement to the core, with the ends of the reinforcement material embedded in composite facings. The best option is to have a continuous 3D reinforcement to increase the delamination strength and toughness between facings and core. In recent years several investigators have considered a number of innovative designs to improve the strength of foam cores such as 3D weaving [1], 3D Z-pins embedded in foam [16], stitch bonding [7] [12] and hollow integrated core sandwich [6]. Usually these solutions lead to a decrease of production rate and an increase of part cost. An alternative is the patented Napco® technology which produces, in a continuous way, 3D tailored sandwich structures while maintaining a production efficiency [11]. The main objective of this study is to show the potential of such a manufacturing process by evaluating the resulting enhancement of some mechanical properties. For this purpose, a micromechanical approach is first proposed

and integrates the anisotropy (due to the through-thickness reinforcements) of the reinforced foam core. Predictions of this multiscale modelling are then compared and discussed with respect to an experimental database which is also briefly described. Finally, in order to take into account the randomness of both the elementary constituents and the manufacturing process, a parametric probabilistic model is introduced.

2   THE NAPCO® TECHNOLOGY

The Napco® technology is a manufacturing process of 3D fibrous structures and 3D dry sandwich composites in which the facing fabrics and core are integrated together in one construction [8]. The sandwich construction is based on needle punching (Fig. 1). The through-thickness reinforcement is obtained from regular fabrics such as chopped strand mats or continuous fiber mats. A multi-needle arrangement, set at a desired pattern and density, penetrates the assembly of glass fabric layers and foam core on both sides (Fig. 2). During this process, needles catch and pull glass strands from the facings and carry them through the rigid foam, creating straight reinforcements perpendicular to the skins (see Figs. (1) and (2)). A part of the yarn is kept inside the facings, the rest being embedded within the foam core. Thus, note that the Napco® technology basically differs from the stitching technology, where the fibers do not come from the skin material. As the needles are withdrawn, fibers remain inside the core. Then the sandwich panel assembly is advanced by a desired spacing to produce the next set of vertical pile yarns. Once the 3D sandwich preform is produced, it can be impregnated by a liquid resin
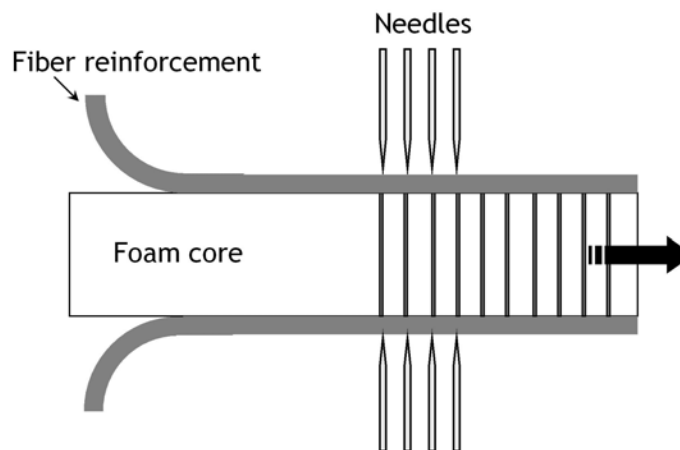

Figure 1: Schematic illustration of the Napco®technology

using of any composite molding technique. Closed-mold methods (Liquid Composite Molding) and continuous compression molding are found to be appropriate. For those technologies, it has been noticed that the transverse pile yarns are properly impregnated. In addition, they help to balance resin flow on both sides of the sandwich.
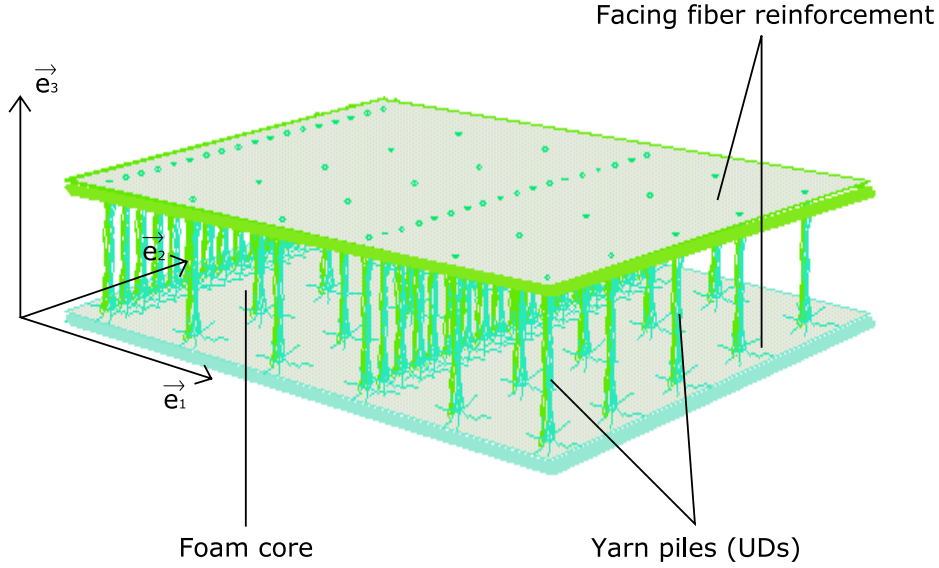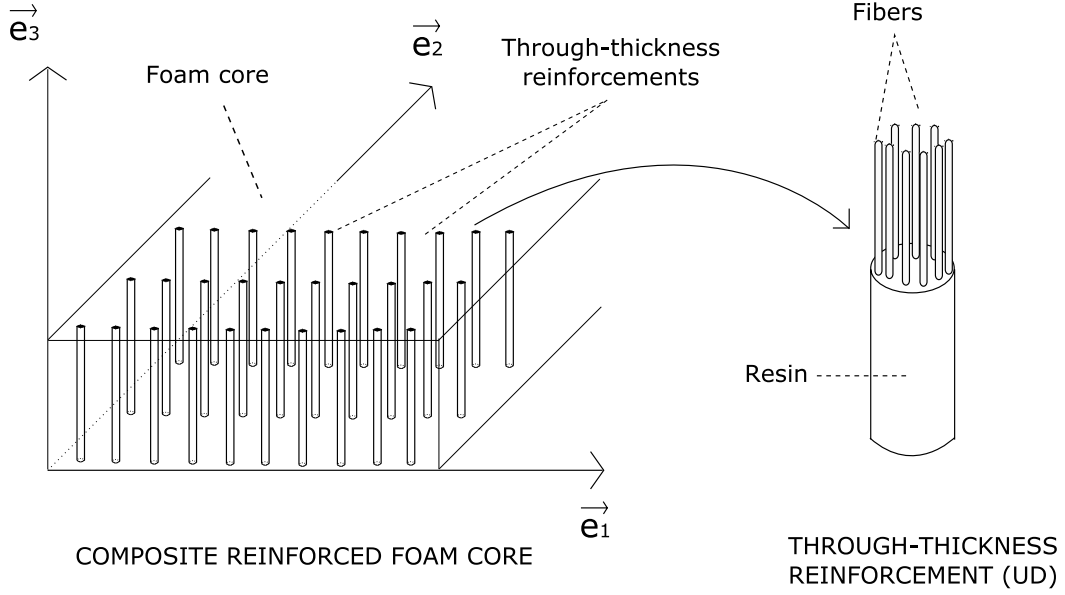
Figure 2: Schematic illustration of the 3D sandwich construction yielded by the Napco® technology (here, the technology was used to tailor specific mechanical requirements, yielding an anisotropic distribution of reinforcements in the plane $(\vec{e_1}, \vec{e_2})$)

3 MICROMECHANICAL MODELLING

The reinforced foam core is made up of a linearly elastic matrix (which is considered as isotropic) reinforced by unidirectional composites (UDs), as shown on figure 3. Hence, the overall mechanical response of the composite is transversely isotropic, allowing one to use a dedicated base tensors to easily derive the mechanical estimates (see [3] [17]). In order to assess the overall properties of the material, two successive homogenization procedures are carried out as follows (see Fig. (3)):

- the first one, denoted by (H1), is performed at the scale of the unidirectional composite and provides the estimate of the effective stiffness tensor of the UD, denoted by $\widetilde{\mathbb{C}}$;

- the second one, denoted by (H2), is carried out at the upper scale (the UDs being then considered as the inhomogeneities) and allows us to estimate the macroscopic stiffness tensor $\widetilde{\widetilde{\mathbb{C}}}$ of the composite reinforced foam core.

For this purpose, we consider the Mori-Tanaka estimate (see [2] [3] [9]), which allows to take into account the interactions between the inhomogeneities. The choice of this homogenization scheme is justified by the "matrix-inclusion" morphology of the studied material. In the case of
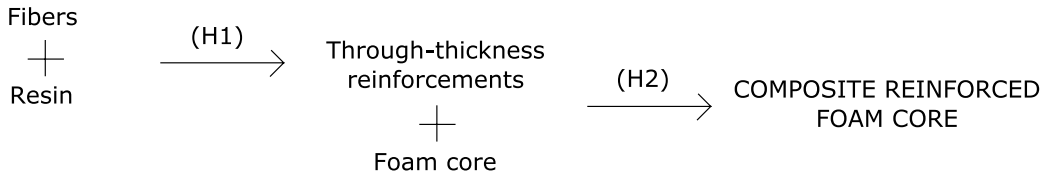
Figure 3: Modelling of the composite reinforced foam core.

the two-phase composite considered here, the overall stiffness tensor $\widetilde{\widetilde{\mathbb{C}}}$ is then given by:

$$\widetilde{\widetilde{\mathbb{C}}}^{\mathrm{MT}} = \mathbb{C}_1 + c_{H_2} \left(\widetilde{\mathbb{C}} - \mathbb{C}_1 \right) : \mathbb{A}_2^{\mathrm{MT}} \tag{1}$$

where $\widetilde{\widetilde{\mathbb{C}}}^{\mathrm{MT}}$ is the macroscopic stiffness tensor estimated by means of the Mori-Tanaka scheme, $\mathbb{C}_1$ and $\widetilde{\mathbb{C}}$ are the stiffness tensors of the matrix and the inhomogeneity respectively. c_{H_2} denotes the volume fraction of reinforcing material and $\mathbb{A}_2^{\mathrm{MT}}$ is the strain concentration tensor for the inhomogeneity, defined as:

$$\mathbb{A}_2^{\mathrm{MT}} = \left[\mathbb{I} + \mathbb{P}_1^2 : \Delta\mathbb{C} \right]^{-1} : \left[(1 - c_{H_2})\, \mathbb{I} + c_{H_2} \left[\mathbb{I} + \mathbb{P}_1^2 : \Delta\mathbb{C} \right]^{-1} \right]^{-1} \tag{2}$$

where $\Delta\mathbb{C} = \widetilde{\mathbb{C}} - \mathbb{C}_1$ and $\mathbb{P}_1^2$ is the Hill tensor corresponding to the inhomogeneity 2 (that is, the through-thickness reinforcement) embedded in the matrix 1. As an illustration, in the case

of the overall transverse shear modulus (which is critical for such materials) $\widetilde{\widetilde{\mu}}^t$, one has:

$$\widetilde{\widetilde{\mu}}^t = \mu_1 + \frac{c_{H_2}\left(\widetilde{\mu}^t - \mu_1\right)}{b_1\,b_2} \tag{3}$$

where

$$b_1 = 1 + (k_1 + 7\mu_1/3)\left(\widetilde{\mu}^t - \mu_1\right)/\left\{2\mu_1\left(k_1 + 4\mu_1/3\right)\right\}$$
$$b_2 = 1 - c_{H_2} + c_{H_2}/\left\{1 + (k_1 + 7\mu_1/3)\left(\widetilde{\mu}^t - \mu_1\right)/\left\{2\mu_1\left(k_1 + 4\mu_1/3\right)\right\}\right\} \tag{4}$$

Note that Eq. (3) is consistent with the result provided by Christensen (see [4], p. 89). Further details are provided in [5].

4   EXPERIMENTAL VALIDATION

The sandwich preforms are made using the Napco® technology with a polyurethane foam core (density of 40 kg.m^{-3}), two facings made of 1 ply of chopped strand glass mat (areal weight of 450 g.m^{-2}). The final panel is molded using continuous compression molding with unsaturated polyester resin. Three different types of needle pattern have been used to create different pile yarns (UDs) densities in the final sandwich structure. Compression between parallel plates and three-point bending tests were performed on a material-testing machine (Zwick) mounted with a 100kN-force cell. Here, we consider elementary constituents the properties of which are listed in Tab. (1).

Constituents	Elastic properties
Polyester resin	$E = 4\,000$ MPa, $\nu = 0.4$
E-Glass fibers	$E = 73\,000$ MPa, $\nu = 0.22$
Polyurethane foam	$E = 9.2$ MPa, $\nu = 0$

Table 1: Elastic properties of the elementary constituents.

The first homogenization procedure (H1) is performed (with a fiber volume fraction equal to the mean experimental value: $c_{H_1} = 4.1\%$) and provides the overall elastic properties of the UD, listed in Tab. (2).

In order to accurately compare the estimates with experimental data, we further introduce a correction index, denoted by r and defined as:

$$r_T = \frac{1}{N}\sum_{i=1}^{N}\frac{T_i^{Est.}}{T_i^{Exp.}} \tag{5}$$

Overall properties of the UD
$\widetilde{E^l} = 6\,834\,\text{MPa}$
$\widetilde{\mu^t} = 1\,524\,\text{MPa}$
$\widetilde{\mu^l} = 1\,538\,\text{MPa}$
$\widetilde{K} = 14\,900\,\text{Mpa}$
$\widetilde{\nu^l} = 0.39$

Table 2: Overall properties of the unidirectional composite.

where $T_i^{Est.}$ and $T_i^{Exp.}$ are the i-th estimated and experimental values of the elastic property T respectively, N is the total number of observations of T (one observation basically corresponds to one volume fraction in through-thickness reinforcements). The i-th corrected estimate is then defined as:

$$T_i^{Corr.} = \frac{T_i^{Est.}}{r_T} \tag{6}$$

Fig. (4) shows a comparison between the experimental data and the simulations in the case of the overall transverse shear modulus $\widetilde{\mu^t}$. It is seen that:

- the evolution of the elastic property is well predicted;

- the magnitude of the overall shear modulus is also well estimated, with a maximum relative error of 22% for the non corrected estimate and 4% for the corrected result.

The estimate of the overall shear modulus as a function of the volume fractions in both the UDs and the foam core was also investigated. It was shown that:

- the overall shear modulus is sensitive to the volume fraction of through-thickness reinforcement c_{H_2};

- the overall shear modulus is not sensitive to the volume fraction within the UDs c_{H_1}. Also, note that an increase of the volume fraction within the UD implies a rather small increase of the shear modulus of the UD: in the case of a 20% increase (from 10% to 30%), the shear modulus of the UD increases by 40% while the Young's modulus increases by 130% approximately;

- a significant increase of the property can be obtained.

Predictions of the overall longitudinal Young's modulus are discussed in [5]. In particular, the predictions of the overall shear modulus seemed to be more accurate compared to the estimate of the effective Young's modulus. This may be explained noticing that:

- basically, the micromechanical modelling does not integrate the effect of the skins, which may not be neglected in the case of a compression test;
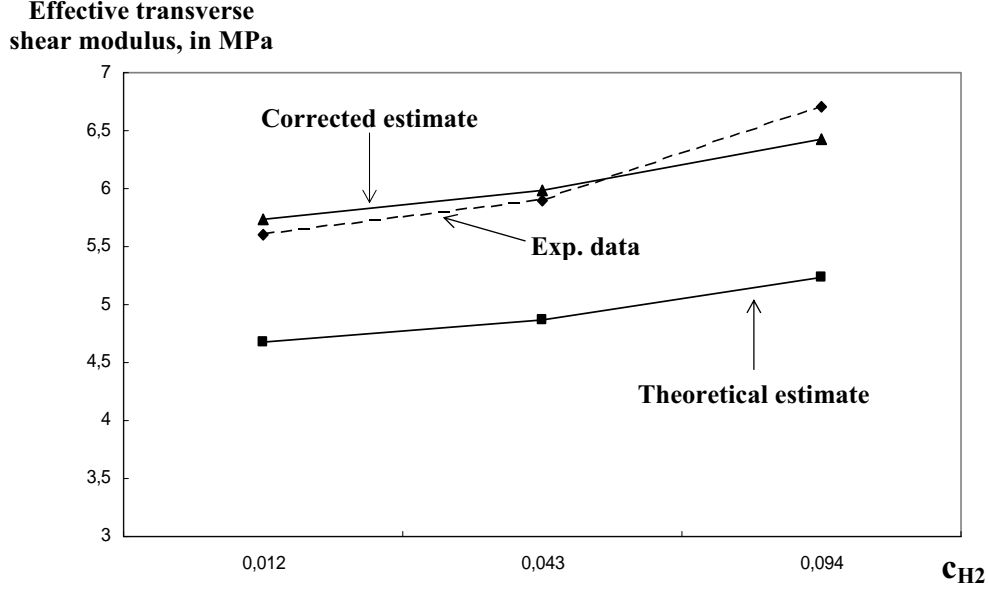
Figure 4: Comparison between exp. data and micromechanical predictions. Case of the overall transverse shear modulus $\widetilde{\widetilde{\mu}}^t$.

- also, the estimate of the overall Young's modulus is highly sensitive to the volume fraction within the UDs and thus, the difference between experimental and simulated curves may be due to volume fraction fluctuations (we recall that a mean value was considered in the model). This point will be discussed hereafter.

Also, we note that for a given elastic property, and especially in the case of the overall transverse shear modulus, the analysis carried out in this study shows that the parameter r_T is almost independent from the number of observations N and close to the unit. This means that:

- the variation of the elastic properties is correctly predicted ;

- only a few experimental measurements may be used for correcting the simulated results.

5 ON THE RANDOMNESS INDUCED BY THE MANUFACTURING PROCESS

Several micrographic pictures have been realized on the UDs reinforcing the foam core. Figure 5 shows that the needles carrying the fibers within the foam, that will create the UDs during the resin injection, induces high discrepancies from one UD to another. In particular,

it can be seen that the fiber volume fraction varies and that the UDs are basically resin-rich regions. Further experimental analysis of the fiber volume fraction within the through-thickness
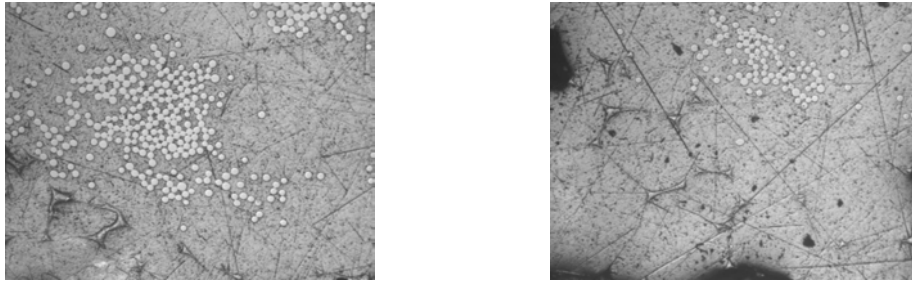

Figure 5: Example of UD cross-section micrographies (glass fibers appear white and resin appears grey)

reinforcement clearly shows the randomness of this quantity, mainly due to the randomness of the mat as well as to the manufacturing process itself. Then, a parametric probabilistic model associated to such a random volume fraction was constructed making use of the Maximum Entropy Principle (M.E.P.; see for instance [10] [14] [15] for a general overview). Numerical Monte-Carlo simulations were used as the stochastic solver in order to study the influence of this uncertainty on the overall mechanical behavior. Figure (6) shows the plot of the probability density function of the overall longitudinal Young's modulus.

6   CONCLUSION

The Napco® technology is a patented process that strengthens transversally foam core with fiber yarns taken from facings in sandwich assembly. In this study, we investigate the potential of this technology by means of a micromechanical analysis based on the Mori-Tanaka scheme. Comparisons between predictions and experiments are discussed and basically show the efficiency of the micromechanical modelling which can also be generalized to other configurations of reinforcements. The approach allows one to define easily both material and process parameters to tailor sandwich panel to specific core-related mechanical requirements. Furthermore, the randomness of the volume fraction within the through-thickness reinforcements is shown and integrated using a parametric probabilistic model. This information is of great help when designing and qualifying structures and can also be used in order to optimize the process itself. Finally, it is shown that such a technology can produce composite reinforced foam core with a significant improvement of the mechanical properties, and in particular the longitudinal Young's modulus as well as the transverse shear modulus.

7   ACKNOWLEDGMENT

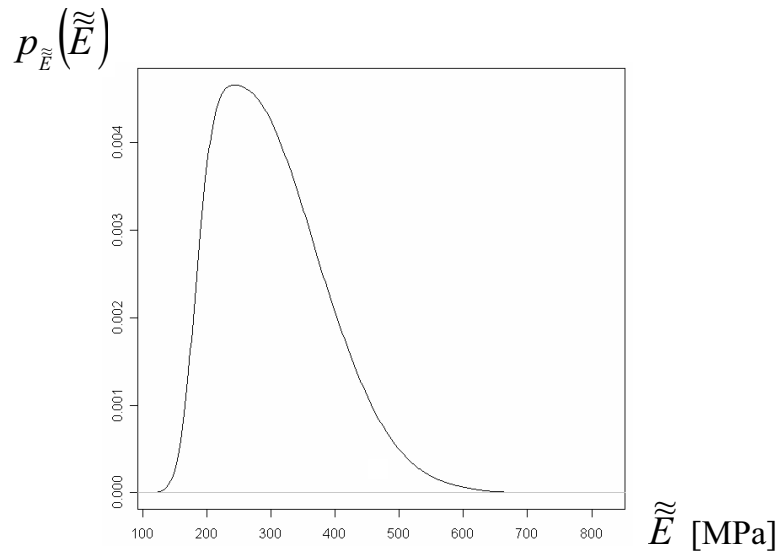$$p_{\widetilde{\widetilde{E}}}\left(\widetilde{\widetilde{E}}\right)$$

Figure 6: Probability density function of the overall longitudinal Young's modulus.

REFERENCES

[1] Bannister, M.K., Braemar, R., Crothers, P.J. "The mechanical performance of 3D woven sandwich composites", Composite Structures, Vol.47, No. 1-4, pp. 687-690, 1999.

[2] Benveniste, Y. "A new approach to the application of Mori-Tanaka's theory in composite materials", Mechanics of Materials, Vol. 6, pp. 147-157, 1987.

[3] Bornert, M., Bretheau, T., Gilormini, P. (Eds.) "Homogenization in Mechanics of Materials", Iste Publishing Company, 2006.

[4] Christensen, R. M. "Mechanics of Composite Materials, Rev. Ed.", Dover Publications, 2005.

[5] Guilleminot, J., Comas-Cardona, S., Kondo, D., Binetruy, C., Krawczak, P. "Multiscale modelling of the composite reinforced foam core of a 3D sandwich structure", Composites Science and Technology, Accepted for publication, 2008.

[6] Hosur, M. V., Abdullah, M., Jeelani, S. "Manufacturing and low-velocity impact characterization of hollow integrated core sandwich composites with hybrid face sheets", Composite Structures, Vol. 65, No.1, pp 103-115, 2004.

[7] Lascoup, B., Aboura, Z., Khellil, K., Benzeggagh, M. "On the mechanical effect of stitch addition in sandwich panel", Composites Sciences and Technology, Vol.66, No. 10, pp. 1385-1398, 2006.

[8] G. Le Roy, C. Binetruy and P. Krawczak. *Continuous manufacturing and performance of 3D reinforced sandwich structures*, 7th International Conference on Sandwich Structures (ICSS-7), in Sandwich Structures 7: Advancing with Sandwich Structures and Materials, O.T. Thomsen, E. Bozhevolnaya and A. Lyckegaard (Eds), Springer Publ., Aalborg, Denmark, pp. 693–702, 2005.

[9] Mori, T. and Tanaka, K. "Average stress in matrix and average elastic energy of materials with misfitting inclusions", Acta Metall. 21, pp. 571-574, 1973.

[10] Papoulis, A. "Probability, Random Variables, and Stochastic Processes, Third Edition", McGraw-Hill, 1991.

[11] European patent n EP 0 594 700 B1

[12] Potluri, P., Kusak, E., Reddy, T.Y. "Novel stitch-bonded sandwich composite structures", Composite Structures, Vol. 59, No.2, pp 251-259, 2003.

[13] Rubinstein, R.Y. "Simulation and the Monte-Carlo Method", John Wiley and Sons, New-York, 1981.

[14] Schuëller, G. I., et al. "A State-of-the-Art Report on Computational Stochastic Mechanics", Probabilistic Engineering Mechanics, Vol. 12 (4), pp. 197-321, 1997.

[15] Soize, C. "A nonparametric model of random uncertainties for reduced matrix models in structural dynamics", Probabilistic Engineering Mechanics, Vol. 15, pp. 277-294, 2000.

[16] Vaidya, U.K., Nelson, S., Sinn, B., Mathew, B. "Processing and high strain rate impact response of multi-functional sandwich composites", Composite Structures, Vol. 52, No. 3-4, pp. 429-440, 2001.

[17] Walpole, L.J. "On the overall elastic moduli of composite materials", Journal of Mechanics and Physics of Solids, Vol. 17, pp. 235-251, 1969.

LINEAR AND NONLINEAR FRACTURE MECHANICS MODELING OF INTERFACIAL DEBONDING IN MODERN SANDWICH PANELS

Oded Rabinovitch[*]

[*] Faculty of Civil and environmental Engineering
Technion, Israel Institute of Technology
Haifa, 32000, Israel
e-mail: cvoded@tx.technion.ac.il

Key words: Debonding, Cohesive zone, Energy release rate, High Order analysis, Soft-core sandwich panels.

Summary. *A nonlinear cohesive interface model for the debonding analysis of sandwich panel is developed. The nonlinear model automatically reacts to stress concentrations and responses with initiation and growth of an interfacial crack. The model also accounts for the coupling between the tangential and normal tractions-separation effects across the cohesive interface. The nonlinear model is compared with a linear fracture one that uses a sequential linear solution of sandwich panels comprised of fully bonded and completely delaminated regions. An algorithm that converts the sequence of linear solutions to the nonlinear equilibrium path of the debonding process is presented. A numerical study that compares the results of the nonlinear cohesive interface model and the linear fracture model in terms of deflections, stress resultants, inter-laminar stresses, and equilibrium paths is then presented.*

1 INTRODUCTION

Modern sandwich panels are usually made of a thick, compliant ("soft"), and lightweight core sandwiched between stiff, strong, and thin face sheets. This unique assemblage yields stiff, light, and versatile structural elements. On the other hand, the notable differences in the thickness and the elastic properties between the face-sheets and the core, the layered configuration, the loading and supporting conditions (which may vary from one face-sheet to another and to the core), and the manufacturing process make the sandwich panel vulnerable to interfacial debonding. The formation of such interfacial debonding downgrades or even neutralizes the ability of the interface to transfer shear. In case of separation, the out-of-plane interfacial stresses also vanish. These effects diminish the ability to develop a composite action of the face sheets and critically affect the functionality of the element. Furthermore, the stress concentrations that develop near the edges of the debonded region may trigger its growth, which may eventually lead to the total failure of the sandwich structure. These aspects make the analytical consideration of the debonding process a challenging task.

The delamination or debonding mode of failure is governed by an interfacial crack propagation mechanism. Therefore, its consideration through fracture mechanics based

concepts is called for. The nonlinear cohesive interface approach is a modern analytical tool that has gained recognition in the past decade (see for example [1-8]). The cohesive interface approach introduces an interfacial surface in which the tractions across the interface are nonlinearly connected to the crack opening and sliding (displacement jumps). When the cohesive interface separates, the magnitude of the tractions at first increases, reaches a maximum, and then approaches zero with increasing separation (Xu and Needleman [6]). A cohesive interface type of model was used by Ferracin et al [1] for a "wedge-peel test" simulation of sandwich panels under a steady state debonding mechanism. El Sayed and Sridharan [2] implemented a cohesive model with a normal traction – separation law in a finite element model to study the growth and kinking of interfacial cracks in soft-core sandwich panels. Sridharan and Li [3] compared two types of mode-I cohesive interface model with an energy based fracture criterion through nonlinear finite element codes. The models were used for the comparative study of the quasi-static and dynamic delamination process in sandwich beams. A mixed mode cohesive interface model and a fracture criterion based on the area under the nonlinear traction-separation curves were used by Li et al [4]. A cohesive interface model that couples the normal and the tangential traction-separation laws was developed by Volokh and Needleman [5] for the buckling analysis of sandwich beams. The Volokh-Needleman interface was used by Rabinovitch [7,8] for the debonding analysis of beams strengthened with externally bonded layers of composite materials.

Another approach that also stems from Fracture Mechanics uses the concept of the energy balance of the elastic energy release rate (ERR) versus the specific fracture energy (see, for example [9-15]). Opposed to the cohesive interface mode, which is nonlinear by nature, the ERR approach is applicable to linear systems modeled through linear structural models. In some cases, and mainly for simple geometries, loading, and supporting conditions, the energy release rate is directly evaluated through the compliance method. In more complicated cases, the energy balance approach includes a stress analysis phase and a fracture analysis phase. Huang et al [10] compared the results of the compliance method with ones obtained using the finite element and the crack closure integral approach for the stress analysis and fracture analysis phases, respectively. Alternatively, Ostergaard and Sorensen [13,14] applied the J-integral to closed form solutions for sandwich beams in order to evaluate the energy release rate and the mode mixity. The J-integral was also used by Rabinovitch and Frostig [15] for the debonding analysis of beams with externally bonded composite reinforcement.

In this paper, a cohesive interface nonlinear model for the analysis of modern "soft core" sandwich beams is developed. The model adopts the high order sandwich beam theory [16] as the basic analytical platform with emphasis the modeling approach and the integration of the nonlinear cohesive interface concept into the sandwich beam theory. The results are then compared with the linear fracture model. In the following sections, the nonlinear cohesive interface model and the linear fracture model are presented, the algorithms for the simulation of the debonding process are discussed, and numerical examples are presented.
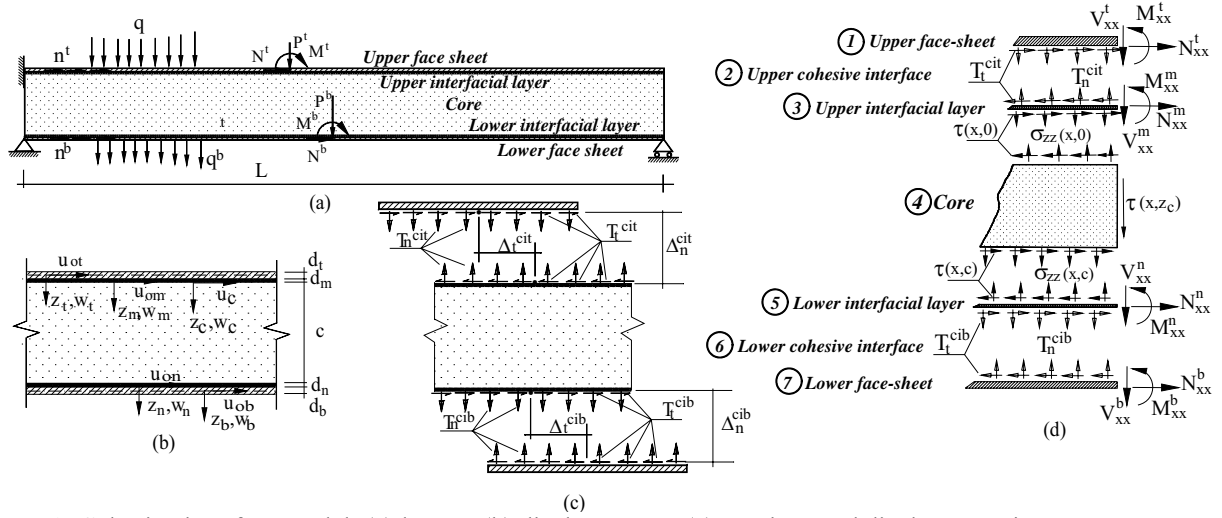
Figure 1: Cohesive interface model: (a) layout; (b) displacements; (c) tractions and displacement jumps across the interface (d) stress, tractions, and stress resultants

2 NONLINEAR COHESIVE INTERFACE AND LINEAR FRACTURE MODELING

The cohesive interface model follows the modeling approach developed in [7,8] and uses the notation and the sign convention of Fig. 1. The model considers seven layers through the depth of the sandwich section (see Fig. 1d). The upper and the lower layers are the face sheets (designated with "t" and "b") that are modeled as Bernoulli-Euler beams. The middle layer (designated with "c") is the core that is modeled as a 2D elastic medium with shear and vertical normal rigidities but with a negligible longitudinal stiffness [16]. Each core to face-sheet interface is modeled using two components. The first one represents a thin layer of core material in which the cells are saturated with the adhesive or resin used for bonding the core to the face sheets. These upper and lower interfacial layers (designated with "m" and "n") are also modeled as Bernoulli-Euler beams. The second component is the cohesive interface (designated with "cit" and "cib"). In the cohesive interface, the tangential and normal tractions are nonlinear functions of the longitudinal slip and the vertical separation across the interface (the displacement jumps). Excluding the cohesive interface, it is assumed that all components are linear elastic and all interfaces are perfectly bonded. It is also assumed that the displacements are small, the loads are exerted at the face sheets, and the stress and deformation fields are uniform through the width. Finally, it is assumed that the crack propagates at the interfaces and does not kink into the core or from one interface to another. The equilibrium equations for the various components are:

$$N_{xx,x}^{t} + bT_{t}^{cit} = -\lambda n^{t} \tag{1}$$

$$N_{xx,x}^{m} + b(\tau_{xz}(z_c = 0) - T_{t}^{cit}) = 0 \tag{2}$$

$$N_{xx,x}^{n} + b(T_{t}^{cib} - \tau_{xz}^{a}(z_c = c)) = 0 \tag{3}$$

$$N_{xx,x}^b - bT_t^{cib} = -\lambda n^b \tag{4}$$

$$M_{xx,xx}^t + bd^t T_{t,x}^{cit}/2 + bT_n^{ci} = -\lambda q^t \tag{5}$$

$$M_{xx,xx}^m + bd^m\left(T_{t,x}^{cit} + \tau_{xz,x}(z_c = 0)\right)/2 + b\left(\sigma_{zz}(z_c = 0) - T_n^{cit}\right) = 0 \tag{6}$$

$$M_{xx,xx}^n + bd^n\left(T_{t,x}^{cib} + \tau_{xz,x}(z_c = c)\right)/2 - b\left(\sigma_{zz}(z_c = c) - T_n^{cib}\right) = 0 \tag{7}$$

$$M_{xx,xx}^b + bd^b T_{t,x}^{cib}/2 - bT_n^{cib} = -\lambda q^b \tag{8}$$

$$\tau_{xz,x} + \sigma_{zz,z} = 0 \tag{9}$$

$$\tau_{xz,z} = 0 \tag{10}$$

where N_{xx}^i, and M_{xx}^i are the in-plane and the bending moment stress resultants, respectively, in the face sheets *(i=t,b)* and in the interfacial core layer *(i=m,n)*; τ_{xz} and σ_{zz} are the shear and vertical normal stresses in the core; z_c is the vertical coordinate of the core, n^i, q^i are distributed axial and vertical loads, respectively; λ is a loading factor; c and b are the thickness and width of the core, respectively; T_n^{cit}, T_n^{cib} and T_t^{cit}, T_t^{cib} are the normal and tangential tractions across the cohesive interfaces, respectively; and $\Delta_n^{cit}, \Delta_n^{cib}$ and $\Delta_t^{cit}, \Delta_t^{cib}$ are the normal (separation) and tangential (slip) displacement jumps across the cohesive interfaces, respectively. Adopting the Bernoulli-Euler beam theory for each face sheet and each interfacial core layer, the displacement jumps across the cohesive interface are:

$$\Delta_n^{cit} = w^m(x) - w^t(x); \quad \Delta_t^{cit} = u_o^m(x) + d^m \cdot w_{,x}^m(x)/2 - u_o^t(x) + d^t \cdot w_{,x}^t(x)/2 \tag{11}$$

$$\Delta_n^{cib} = w^b(x) - w^n(x); \quad \Delta_t^{cib} = u_o^b(x) + d^b \cdot w_{,x}^b(x)/2 - u_o^n(x) + d^n \cdot w_{,x}^n(x)/2 \tag{12}$$

where $w^i(x)$ and $u_o^i(x)$ are the out-of-plane (vertical) and in-plane (longitudinal) displacements, respectively, of the reference line of the face sheets and the interfacial core layers; d^j *(j=t,b,m,n)* is the depth of the each layer, and $(\,)_{,x} = \partial(\,)/\partial x$.

The tractions across the cohesive interface follow Volokh and Needleman [5] and read:

$$T_n^{cij} = T_n^{cij}\left(\Delta_n^{cij}, \Delta_t^{cij}\right) = \frac{\phi_n \Delta_n^{cij}}{\delta_n^2} \cdot \exp\left(-\frac{\Delta_n^{cij}}{\delta_n} - \frac{\left(\Delta_t^{cij}\right)^2}{\delta_n^2}\right) \tag{13}$$

$$T_t^{cij} = T_t^{cij}\left(\Delta_n^{cij}, \Delta_t^{cij}\right) = 2\frac{\phi_n \Delta_t^{cij}}{\delta_n^2} \cdot \left(1 + \frac{\Delta_n^{cij}}{\delta_n}\right) \cdot \exp\left(-\frac{\Delta_n^{cij}}{\delta_n} - \frac{\left(\Delta_t^{cij}\right)^2}{\delta_n^2}\right) \tag{14}$$

where ϕ_n is the work of separation per unit area, and δ_n is the characteristic length parameter.

Assuming a symmetric layup for the face sheets and an isotropic behavior of the interfacial core layers, the constitutive laws for these components are generally given by:

$$N_{xx}^j = A_{11}^j u_{o,x}^j \qquad M_{xx}^j = -D_{11}^j w_{,xx}^j \qquad j = fct, fcb, m, n \tag{15,16}$$

where A_{11}^j and D_{11}^j are the extensional and flexural rigidities of each components multiplied by its width. The constitutive relations of the core are:

$$\sigma_{zz} = E_c \varepsilon_{zz} \quad ; \quad \tau_{xz} = G_c \gamma_{xz} \tag{17,18}$$

where G_c, E_c are the shear modulus of the core and its vertical elastic modulus, respectively.

The stress and displacement fields of the core follow [16] and read:

$$\tau_{xz,z}(x, z_c) = \tau_{xz}(x) = \tau \tag{19}$$

$$\sigma_{zz}(x, z_c) = (w^m - w^n) E^c / c + \tau_{,x}(c/2 - z_c) \tag{20}$$

$$w_c(x, z_c) = -\tau_{,x} z_c (z_c - c)/(2E_c) + (w^m - w^n) z_c / c + w^m \tag{21}$$

$$u_c(x, z_c) = \frac{\tau}{G_c} z_c - \left(\frac{\tau_{,xx}}{E_c}\right)\left(\frac{c (z_c)^2}{4} - \frac{(z_c)^3}{6}\right) - \frac{(z_c)^2}{2c}\left(w_{,x}^m - w_{,x}^n\right) - w_{,x}^m z_c + \left(u_o^m - \frac{d^m}{2} w_{,x}^m\right) \tag{22}$$

The governing equations are derived by introducing the constitutive relations for the face sheets and the interfacial layers, the stress field of the core and the traction – displacement jump laws into the field equations and the longitudinal compatibility condition at the lower interface of the core. The governing equations take the following form:

$$A_{11}^t u_{o,xx}^t + bT_t^{cit} = -\lambda n^t \tag{23}$$

$$A_{11}^m u_{o,xx}^m - bT_t^{cit} + b\tau = 0 \tag{24}$$

$$A_{11}^n u_{o,xx}^n - b\tau + bT_t^{cib} = 0 \tag{25}$$

$$A_{11}^b u_{o,xx}^b - bT_t^{cib} = -\lambda n^b \tag{26}$$

$$D_{11}^t w_{,xxxx}^t - d_t bT_{t,x}^{cit} / 2 - bT_n^{cit} = \lambda q^t \tag{27}$$

$$D_{11}^m w_{,xxxx}^m - d^m bT_{t,x}^{cit} / 2 - (c + d^m)b/2 \cdot \tau_{,x} + bT_n^{cit} - bE_c(w^n - w^m)/2 = 0 \tag{28}$$

$$D_{11}^n w_{,xxxx}^n - (c + d^n)b/2 \cdot \tau_{,x} - d^n bT_{t,x}^{cib} / 2 + bE_c(w^n - w^m)/c - bT_n^{cib} = 0 \tag{29}$$

$$M_{xx,xx}^b + bd^b T_{t,x}^{cib} / 2 - bT_n^{cib} = 0 \tag{30}$$

$$D_{11}^b w_{,xxxx}^b - d^b bT_{t,x}^{cib} / 2 + bT_n^{cib} = \lambda q^b \tag{31}$$

$$u_o^m - u_o^n - (c^a + d^n) w_{,x}^n / 2 - (c^a + d^m) w_{,x}^m / 2 + \tau c / G_c - \tau_{,xx} c^3 / 12E_c = 0 \tag{32}$$

Due to the nonlinearity of the T−Δ relations, the governing equations are nonlinear and do not have a closed form general solution. Alternatively, the model is solved numerically using a multiple shooting algorithm and an arc-length continuation scheme.

The cohesive interface model responses to stress concentrations and automatically simulates the initiation and the growth of the interfacial debonding. Yet, the nonlinear solution requires considerable computational efforts and time. The softening branches of the $T-\Delta$ relations further require a special treatment in the form of arc-length algorithms. Another disadvantage results from the large number of empirical parameters in the $T-\Delta$ laws and the sensitivity of the model to these factors [17] (also see [8]). These drawbacks motivate the comparison of the nonlinear cohesive interface model to the classical linear fracture approach.

The linear fracture model uses the delaminated sandwich panel model [18], the J integral for the assessment of the energy release rate [19,15,8], and the unique procedure for the simulation of the crack growth mechanism [8]. The notation and the sign conventions used in the linear model appear in Fig. 2. The model uses three layers that include the face sheets and the core only and adopts the same assumptions used for these layers in the cohesive interface model. Opposed to the cohesive interface approach that unifies the stress analysis and the crack growth simulation, the linear approach uses separate stress analysis and fracture assessment phases. Based on the two phases, the crack growth process is simulated.
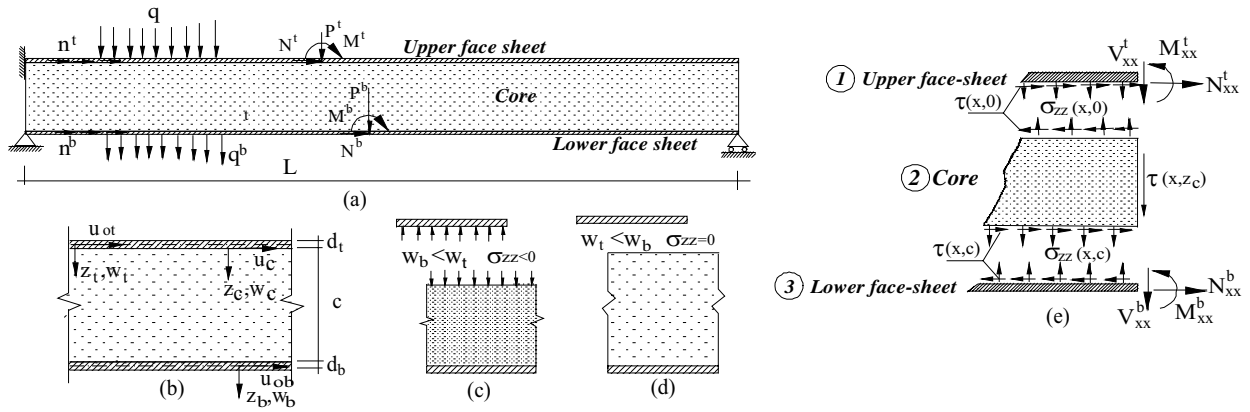

Figure 2: Linear model: (a) layout; (b) displacements; (c,d) debonded regions; (e) stresses and stress resultants

The stress analysis phase follows [18]. Contrary to the cohesive interface model, this model only considers the two limit cases of perfect bonding or complete separation. Thus, the delaminated sandwich panel is comprised of fully bonded regions and debonded regions. In the debonded regions, the surfaces can slip one with respect to another and cannot transfer shear stresses. They can, however, transfer vertical normal compressive stresses if contact exists. Thus, a distinction is made between delaminated regions with contact and delaminated regions without contact. In the fully bonded regions, the governing equations read [18]:

$$A_{11}^t u_{o,xx}^t + b\tau = -\lambda n^t \tag{35}$$

$$A_{11}^b u_{o,xx}^b - b\tau = -\lambda n_b \tag{36}$$

$$D_{11}^t w_{,xxxx}^t - (c + d_t)b/2 \cdot \tau_{,x} - bE_c(w^b - w^t)/c = \lambda q^t \tag{37}$$

$$D_{11}^b w_{,xxxx}^b - (c+d^b)b/2 \cdot \tau_{,x} + bE_c(w^b - w^t)/c = \lambda q^b \qquad (38)$$

$$u_o^t - u_o^b - (c+d^b)w_{,x}^b/2 - (c+d^t)w_{,x}^t/2 + \tau c/G_c - \tau_{,xx}c^3/12E_c = 0 \qquad (39)$$

In the debonded regions, the fifth equation (Eq. 40) as well as the terms that include τ or its derivatives vanish. In case contact does not exist, the term $bE_c/c(w^b\text{-}w^t)$ also vanishes. Note that the governing equations of the stress analysis phase are linear. As a result, the solution of these equations, along with the boundary and continuity conditions (which, for brevity, are not presented here) does not require significant computational efforts or special algorithms.

In the fracture analysis phase, the tendency of the interfacial debonding to grow is assessed. The criterion for the propagation of the interfacial debonding crack adopts the concept of the ERR. Propagation of the debonding crack occurs if the energy release rate G is larger than the critical fracture energy G_c. G is evaluated using the J-integral [19,15]:

$$G = J = \int_\Gamma \left(Wdy - \mathbf{T} \cdot \frac{\partial \mathbf{u}}{\partial x} ds \right) \qquad (40)$$

where Γ is the path surrounding the crack tip, $\mathbf{T}$ is the traction vector along the path Γ, $\mathbf{u}$ is the displacement vector, and W is the strain energy density function. Eq. (40) defines the energy release rate for a given debonded length and a given load. Yet, the analysis aims at describing the response of the sandwich structure through the debonding growth process. This type of response is given as a set of generalized points (equilibrium path) that satisfy the governing equations and the boundary conditions along with the following constraint:

$$G(\mathbf{u}, \lambda) = G_c \qquad (41)$$

where the load factor λ defines the level of load. The equilibrium path, which in the case of the cohesive interface approach is a direct outcome of the nonlinear solution, does not directly stem from the analysis but requires a special algorithm [8]. The first stage in this algorithm requires a series of solutions of the beam through the following steps:

1. Define a series of debonding lengths, $\mathbf{a}=[a_i]$ ($i=1..N_a$) ranging from 0 to L.
2. For the i`th debonding length, a_i, and an <u>arbitrary magnitude</u> of external load λ_0:
    2.1 Solve the stress analysis model and evaluate the displacement field: $\mathbf{u}_{0i}= \mathbf{u}(a_i, \lambda_0)$.
    2.2 Evaluate the ERR: $G_{0i}= G(a_i, \lambda_0)$ using Eq. (40).
3. Repeat steps 2.1-2.3 for all a_i's and generate the vector $\mathbf{G}_0=[G_{0i}]$ and vector-function $\mathbf{u}_0=[\mathbf{u}_{0i}]$ that correspond to the vector $\mathbf{a}=[a_i]$ and the arbitrary load magnitude λ_0.
4. Use $\mathbf{u}_0$ and $\mathbf{a}$ to construct the function $\mathbf{u}_0(a)$ and use the vectors $\mathbf{G}_0$ and $\mathbf{a}$ to construct the function $G_0(a)$ by means of any curve fitting technique.
5. Due to the linearity of the stress analysis model, the displacement and ERR under <u>any magnitude of load λ</u> are:

$$\mathbf{u}(a,\lambda) = \mathbf{u}(a,\lambda_0) \cdot (\lambda/\lambda_0); \quad G(a,\lambda) = G(a,\lambda_0) \cdot (\lambda/\lambda_0)^2 \qquad (42,43)$$

where $\mathbf{u}_0(a)$ and $G_0(a)$ are the functions constructed in step 4.

The second stage determines the path of the debonding process as follows:

I. Chose a crack length a

II. Solve Eq. (41) with $G(a,\lambda)$ given by Eq. (43) for $\lambda(a)$.

III. Substitute a (from step I) and λ (from step II) into Eq. (42) and evaluate $\mathbf{u}(a)$.

IV. The series of pairs $[\lambda(\mathbf{a}),\mathbf{u}(\mathbf{a})]$ defines the equilibrium path.

Note that the above procedure assumes that the contact conditions at the debonded interface (with or without contact) do not change through the debonding process. In practice, this is usually the case and the above assumption does not yield a major restriction or limitation. Also note that this procedure requires significantly less computational efforts that the cohesive interface model does. Yet, it critically depends on the availability of a qualitative description of the process in the form of the vector $\mathbf{a}$.

3 NUMERICAL STUDY
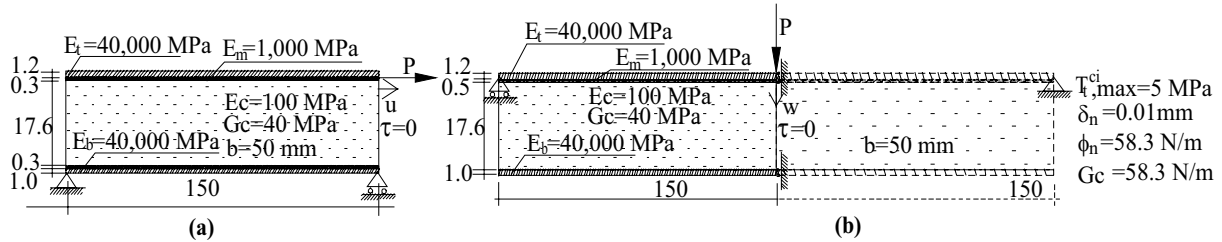
Figure 3: Numerical study - geometry and properties: (a) shear test; (b) three point bending

The numerical study examines two cases. The first one simulates a shearing test of a sandwich specimen and the second one examines a sandwich beam specimen under three point bending. The geometry and mechanical properties of the specimens appear in Fig 3. The distributions of the stresses in the core and the interfacial tractions in the cohesive interfaces under a relatively low level of shear load (P=108N) in the first case appear in Fig. 4. The results reveal that the peak peeling stresses develop near the lower support at x=0. Correspondingly, the peak normal tractions develop across the lower cohesive interface near the fixed support. It is also observed that due to the low stiffness of the interfacial layer, the magnitudes of the normal tractions across the cohesive interfaces are almost identical to the normal stresses at the core-face sheet interface. The peak interfacial tangential tractions across the cohesive interfaces also develop in the lower interface. The value at x=150 mm is slightly higher than the one near x=0 mm. However, the coupled effect of the shear and tensile tractions through the cohesive interface (Eqs. 11-12) imply that the critical point is located at the lower interface at x=0mm. The nonlinear cohesive interface model reacts to this combination and the interfacial crack initiates at x=0 and propagates at the lower interface towards the loaded edge.
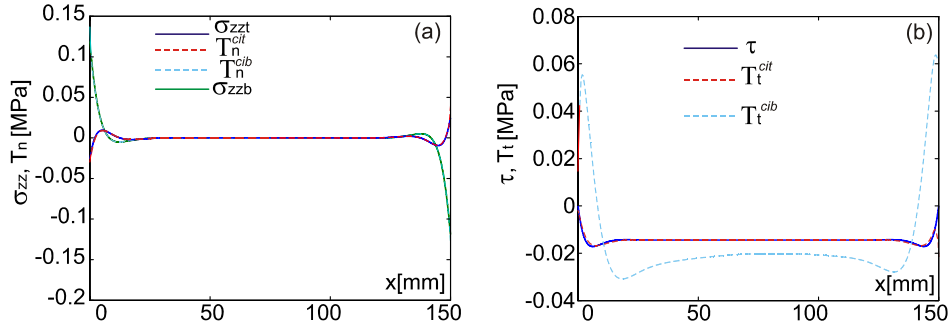
Figure 4: stresses and interfacial tractions under P=108.22 kN: (a) normal; (b) shear

The vertical deflections, the interfacial stresses, and the tractions across the cohesive interface after a crack growth of about 11.5 mm are compared in Fig. 5. The comparison reveals that both models well predict the separation of the upper face sheet in the debonded zone. The cohesive interface model further indicates that cracking occurs where the lower cohesive interface allows the separation of the lower face sheet from the interfacial core layer. The comparison of the interfacial stresses and the tractions across the cohesive interface reveals that the stresses in the bonded regions (x>11.5mm) are in fair agreement. In the debonded region, the linear fracture model predicts null stresses whereas the cohesive interface model predicts stresses that result from the interaction between the core and the interfacial layers. The nonlinear model also reveals a concentration of the normal and tangential tractions across the lower interface. These effects trigger the propagation of the debonding, which is studied next.
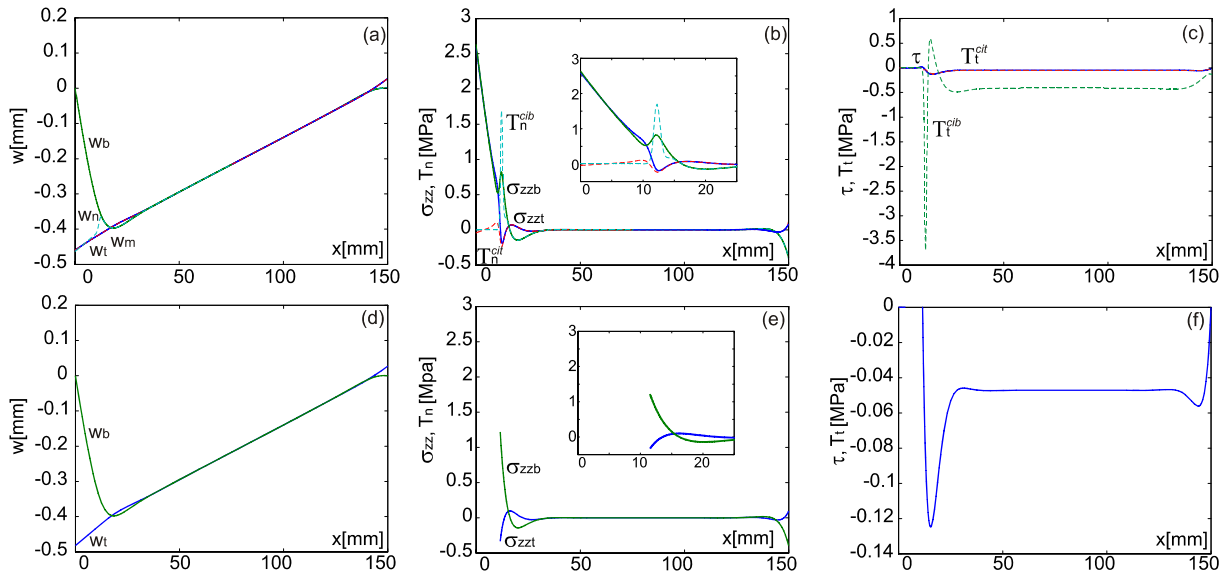

Fig. 5: Deformations, interfacial stresses and tractions: (a-c) cohesive interface model (d-f) linear fracture model
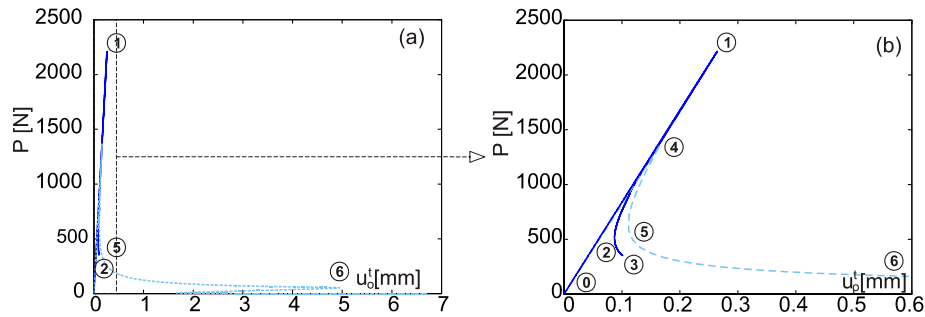
Figure 6: Equilibrium Paths: Shearing test

The equilibrium paths predicted by the cohesive interface model and simulated by the linear fracture models are compared in Fig. 6. Due to the long run time, the cohesive interface analysis was stopped at point 3 after more than 4200 steps. The linear fracture analysis was conducted until complete separation of the interface. The comparison shows that both models describe a similar pattern that involves a close to linear growth of the load up to a peak and then a snap back. Another fold is observed at a load level of about 500 N and afterwards, a growth in displacement along with a drop in load is observed. Quantitatively, the peak predicted by the linear fracture model at Point 4 is lower than the one predicted by the cohesive interface model at Point 1. This effect is attributed to the inability of the linear fracture model to account for the range of debonding conditions between perfect bonding and complete separation.

In physical terms, the two paths reflect an initially unstable debonding process. Under displacement control, it is expected that the crack will initiate and burst under a load of about 500 N and snap directly to points 2 or 5. From these points on, a stable growth of the crack with the increase of the displacement is expected. Adopting this interpretation, the critical load for practical purpose is not the one at Points 1 or 4 but the one that corresponds to Points 2 or 5. In these terms, the predictions of the two models are in fair agreement and the simplified linear fracture model allows a reasonable estimation of the nonlinear response predicted by the cohesive interface model.

The last case in the numerical study investigates a sandwich beam specimen under a three point bending loading scheme (Fig 3b). The analysis reveals that the peak interfacial tensile (peeling) stresses develop at the upper core-face sheet interface near the edges. Based on that, the cohesive interface model is slightly simplified and the unique interface is implemented at the upper core-face sheet interface only. Under these conditions, the model predicts crack propagation from the outer support towards midspan. This result is used for the construction of the vector **a** defining the crack growth process for the linear fracture model.

The equilibrium paths obtained by the cohesive interface model and simulated by the linear fracture model appear in Fig. 7 (the nonlinear analysis was stopped after 5150 steps and a debonding growth of about 12 mm). In this case, the unstable branch predicted by the cohesive interface model includes two folds before the final snap back. These branches are evidently unstable and this type of behavior is not expected in practice. The linear fracture model also predicts an unstable branch and a snap back behavior but with a lower peak load.

Excluding this discrepancy and the extra folds of the unstable branch, the predictions of the two models are in fair agreement.
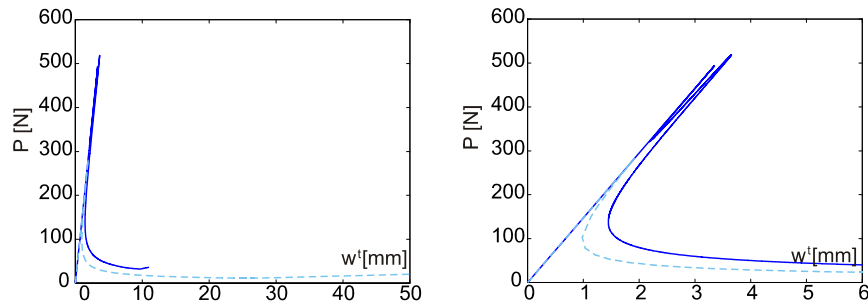

Figure 7: Equilibrium Paths: Three point bending

3   SUMMARY AND CONCLUSIONS

A nonlinear cohesive interface model for the debonding analysis of "soft-core" sandwich panels has been developed. The cohesive interface model has combined the advantages of the high order sandwich theory with the unique features of the cohesive interface concept. In particular, the ability to response to stress concentrations, to account for the coupling of the tangential and normal effects, and to independently quantify the interfacial debonding process has been designated. The cohesive interface model has been compared with a linear fracture model that is also based on the high order sandwich theory. This model does not account for the range of bonding conditions but limits the consideration to fully bonded interfaces and completely detached ones. The simulation of the interfacial debonding mechanism has been conducted using a special algorithm that uses a series of linear solutions. Thus, the simplicity and reduced computational efforts demands have been designated as the main advantages of the linear fracture model. On the other hand, this model critically depends on the availability of information on the crack growth pattern.

The nonlinear cohesive interface model and the linear fracture model have been adopted for the numerical study of sandwich specimens subjected to shearing and bending loads. The results have shown that the two models describe a similar stress and displacement patterns for a given length of debonding. Additional results in terms of the equilibrium paths that describe the response through the deboning process have shown that the two models describe unstable branches and a snap back type of response. On the other hand, it has been shown that while the simplified linear fracture model can simulate the nonlinear equilibrium path, it predicts lower values of the peak load. In practical terms, this critical load is located on an unstable branch that is not likely to be observed in practice. In terms of the critical transition between the unstable and the stable branch, a better correlation has been observed.

REFERENCES

[1] Ferracin, T., Landis, C.M., Delannay, F., and Pardoen, T. "On the determination of the cohesive zone properties of an adhesive layer from the analysis of the wedge-peel test" *International Journal of Solids and Structures* **40**(11):2889–2904 (2003)

[2] El-Sayed, S. and Sridharan, S. "Cohesive layer models for predicting delamination growth and crack kinking in sandwich structures" *Int. Journal of Fracture* **117**(1):63-84 (2002)

[3] Sridharan, S. and Li, Y. Static and Dynamic Delamination of Foam Core Sandwich Members *AIAA Journal,* **44**(12), 2937-2948 (2006)

[4] Li, S., Thouless, M.D., Waas, A.M., Schroeder, J.A., and Zavattieri, P.D. Mixed-mode cohesive-zone models for fracture of an adhesively bonded polymer–matrix composite *Engineering Fracture Mechanics* **73**(1) 64–78 (2006)

[5] Volokh, K.Yu. and Needleman, A. "Buckling of sandwich beams with compliant interfaces" *Computers and structures* **80**(14-15):1329-1335 (2002)

[6] Xu, X.-P, and Needleman, A. "Numerical simulations of fast crack growth in brittle solids" *Journal of Mechanics and Physics of solids*, **42**(9):1397-1434. (1994)

[7] Rabinovitch, O. "Cohesive Interface Modeling of Debonding Failure in FRP Strengthened Beams", *Submitted.*

[8] Rabinovitch, O. "Debonding Analysis of Fiber Reinforced Polymer strengthened Beams: Cohesive Zone Modeling Versus a Linear Elastic Fracture Mechanics Approach", *Engineering Fracture Mechanics,* In press.

[9] Ural, A., Zehnder, A.T., and Ingraffea, A.R. "Fracture mechanics approach to facesheet delamination in honeycomb: measurement of energy release rate of the adhesive bond" *Engineering Fracture Mechanics* **70**(1):93–103 (2002)

[10] Huang, S.J. and Lin, Y.C. (2004) "Fracture analysis of an adhesively bonded sandwich beam under Mode-I loading" *Journal of Adhesion Science and Technology* 18(7):833–847

[11] Berkowitz C.K. and Johnson W.S. "Fracture and Fatigue Tests and Analysis of Composite Sandwich Structure" *J. of Composite Materials*, **39**(6):1417-1431 (2005)

[12] Minghui, F. and Zuoqiu, L. "Delamination Analysis of Sandwich Beam: High-Order Theory" *AIAA Journal,* **40**(5):pp. 981-986. (2002)

[13] Østergaard, R.S. and Sørensen, B.F. "Interface crack in sandwich specimen" *International Journal of Fracture* **143**(4):301–316 (2007)

[14] Østergaard, R.S. and Sørensen, B.F. and Brøndsted, P. "Measurement of Interface Fracture Toughness of Sandwich Structures under Mixed Mode Loadings" *Journal of Sandwich Structures and Materials* **9**(5) 445-466 (2007)

[15] Rabinovitch, O. and Frostig, Y. "Delamination Failure of RC Beams Strengthened with FRP Strips – a Closed-Form High-Order and Fracture Mechanics Approach", *Journal of Engineering Mechanics* **127**(8):852-861. (2001)

[16] Frostig, Y., Baruch, M., Vilnai, O. and Sheinman, I. "High-Order Theory for Sandwich-Beam Bending with Transversely Flexible Core" *J. Engr. Mech.* **118**(5):1026-1043 (1992)

[17] Volokh, K.Yu. "Comparison between cohesive zone models" *Communications in numerical methods in engineering* **20**(11):845-856. (2004)

[18] Frostig, Y. "Behavior of delaminated sandwich beams with transversely flexible core - high order theory", *Composite Structures,* **20**(1):1-16. (1992)

[19] Rice, J.R. "A path independent integral and the approximated analysis of strain concentration by notches and cracks", *Journal of Applied Mechanics,* **35**(6), pp. 379-386 (1968)

CHARACTERISATION OF DUCTILE CORE MATERIALS

Mark Battley[*] and Magnus Burman[†]

[*] Centre for Advanced Composite Materials (CACM)
University of Auckland, Private Bag 92019, Auckland, New Zealand
e-mail: m.battley@auckland.ac.nz, web page: www.mech.auckland.ac.nz/Composites/CACM.html

[†] Department of Aeronautical and Vehicle Engineering
Division of Lightweight Structures, KTH SE-100 44, Stockholm, Sweden
e-mail: mburman@kth.se, web page: http://www.ave.kth.se

Key words: Sandwich structures, Experimental mechanics, Core materials.

Summary. *This paper describes an experimental investigation of characterization methods for ductile core materials. Full field optical strain measurement methods are used to determine the strain distributions in standard testing methods such as block shear and four point beam testing, particularly for highly ductile cores subjected to large deformations. The results show that the stress and strain fields in both block shear and sandwich beam tests are very different to those assumed by the testing standards. The test methods result in complex post yield states of stress in the core materials, meaning the core shear strength and ultimate shear strain should not be calculated by classical methods in the post yield region.*

1 INTRODUCTION

Polymeric foam materials are widely used as cores for sandwich structures. Many of these materials such as linear PVC foams have high levels of ductility, providing excellent performance for dynamically loaded structures such as the hull panels of marine vessels [1]. However the high ductility of these materials results in very large specimen deformations during traditional shear test methods such as block shear [2-3] and four point loaded beams [4]. Other studies, e.g. [5] has addressed the problem of standard shear test methods for core materials that show high elongation to failure. Figures 1 and 2 show typical deformed shapes of linear PVC cored specimens (Airex R63.80) during block shear and beam tests.

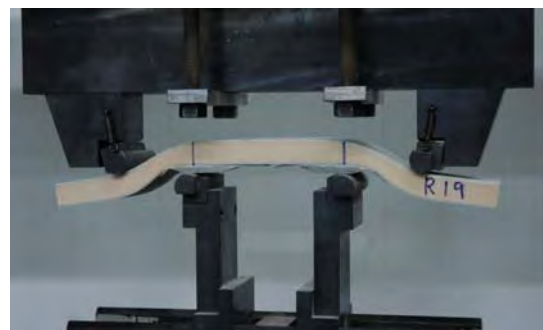Figure 1: Block shear deformation of ductile core

Figure 2: Large deformation of ductile core beam

Changes in the geometry of the test specimens at large deflections means that the shear loaded regions of the specimens are no longer subject to a uniform state of stress as assumed by the testing standards. Beam specimens also often fail by skin fracture under the loading points, meaning that the maximum measured load and strain to failure may not actually represent the true core properties. Testing of such materials in dynamically loaded panels has shown much higher strengths than are achieved by block shear or beam testing methods, with highly ductile cores performing two to three times better as a panel than in block shear and beam tests [1], suggesting that the traditional characterization methods do not accurately measure the relevant material properties. Strength data reported in manufacturers' material data sheets does not always explicitly define whether the strength is taken at material yield, or at the maximum load, which can be very sensitive to the details of the test method

The aim of this paper is to use a full-field optical strain measurement system to determine the strain distributions in the common standardised testing methods of block shear and four point beam testing. Two types of core materials were chosen for this investigation; Rohacell S51 (52 kg/m^3), a low elongation core for high temperature applications and processing, mainly used in aircraft applications, and Airex R63.80 (90 kg/m^3) which is a high elongation, very ductile material often used for dynamically loaded structures such as marine vessel hulls.. This study investigates the strain fields in the cores in the linear region before significant yielding occurs, at yield, and in the post-yield region.

2 OVERVIEW OF TESTING METHODS

2.1 Block Shear Testing

This method is based on bonding rectangular blocks of core material to two steel fixtures which are displaced relative to each other to apply a shear deformation to the core material. Commonly used standards include ASTM C273 and ISO 1922, the primary difference being that ASTM C273 aligns the loading axis with the diagonal of the test sample whereas in ISO 1922 the loading axis is aligned along the vertical centerline of the specimen. Both standards can be used to determine shear strength and shear modulus. In the case of ASTM C273, (Clause 3.1) it is noted that "From a complete load-deflection curve, it is possible to compute core shear stress at any load (such as the shear stress at proportional limit, at yield, or at maximum load) and to compute an effective core shear modulus. ASTM C273 also notes that (Clause 3.2) "The test does not produce pure shear, but the specimen length is prescribed so that secondary stresses have a minimum effect". The calculation of shear strength and shear strain are based on assumptions that the entire volume of core material is in a state of uniform shear stress and shear strain. The shear strain is normally calculated from the relative displacement of the two loading plates measured by an extensometer. ASTM C273 (Clause 8.2) also notes that core materials with high elongation, i.e. that yield more than 2%, should use the 2 % offset method for the yield strength calculation. In the ISO standard the maximum applied load is used for the strength calculation.

Figure 3 shows typical shear load/deflection curves from ASTM C273 tests of low elongation (Rohacell S51) and high elongation (Airex R63.80) core materials. The low

elongation material fails at approximately 1 mm deformation which corresponds to 4.5% shear strain, while the high elongation core material achieves a deflection close to 20 mm which corresponds to a maximum engineering shear strain of more than 60%. The extensometer attached to the loading blocks reached its maximum limit at a deformation of 13 mm, while the "simulated extensometer" strain is based on the recorded longitudinal deformation measured by the DSP system and correlates very well with the extensometer. The high elongation core has an initial linear region, it yields (at similar load and deflections as the low elongation materials), then shows extended post yield deformation with increasing load.
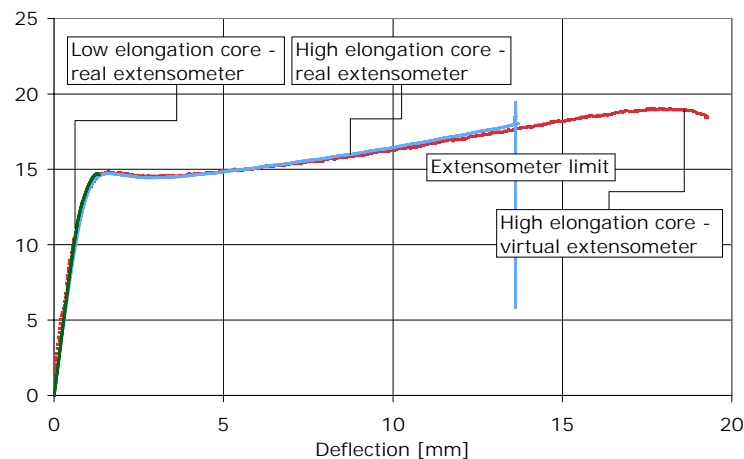
Figure 3 Load/deflection results from block shear tests of low and high elongation core materials. Deflection is measured with an extensometer and also calculated using the optical measuring system.

2.2 Sandwich Beam Testing

Flexural testing of sandwich beams such as to ASTM C393 can be used to determine both skin and core properties. Typically the beams are loaded in four point bending (Figure 2), with the centre region of the beam in pure bending and the outer spans subjected to a bending moment that increases from the outer ends of the beams to the inner loading points. Between the inner and outer support the transverse force is constant. With a core much softer than the faces this is assumed to produce a constant shear force in the core. The loading spans are normally chosen based on the material properties of the beam in order to achieve either bending or shear failure as required. Determination of core shear strength properties requires relatively short beams to minimize the maximum bending moment and avoid premature skin failures. It is also possible to determine shear modulus from this testing method, however this requires additional measurements to be undertaken to separate the deformations due to bending from those of shear. Techniques include testing beams of different spans, or measuring skin strains or beam curvatures. This method enables the sandwich structure to be tested as it may be used in an application, so tests other properties such as the core-skin bond. In order to avoid premature failure the supports and load introduction points need to be carefully designed and should either be able to rotate around a neutral axis, or pads with soft edges used to achieve a smooth load transfer. A sharp corner will induce high local

compressive loading on the core in addition to the shear load and hence the specimen will fail, either in local buckling or face compression, before the material's ultimate shear performance has been reached. Figure 4 shows typical load/deflection results from four point.bend testing of the low and high elongation core materials. Both materials have almost identical properties before yield, but the low elongation core fails at a deflection of approximately 7mm, while the high elongation specimen deforms for more than 30mm. The final failure for the high elongation specimen is skin fracture under a loading point, not core fracture. The shear stress is taken as the load divided by the beam width and the distance between the mid-plane of the skins according to the standard.
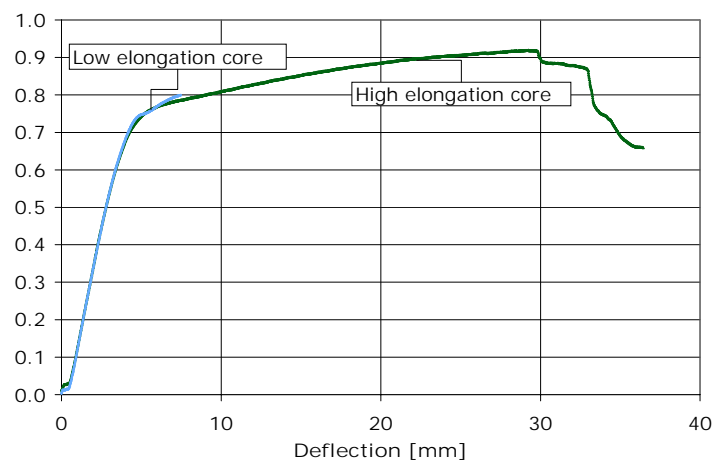
Figure 4 Stress/deflection results from four point bend tests of low and high elongation core materials. Stress is used herein because the two materials tested had different thickness

2.3 Optical strain measurement

During the loading the strain is measured on the front side surface of the specimen. For the strain measurements, the optical system ARAMIS 1.3M (GOM mbH)[6] is used. The measurements are based on a contact-free, whole-field optical technique also known as the digital speckle photography (DSP). In this study, one CCD cameras (1280x1024 pixels) was employed allowing for in-plane (2D) measurements. A reference image corresponding to the un-deformed state is taken before loading of the specimen. Thereafter, the images are sampled at a frequency of 1 Hz throughout the testing. By means of the digital image correlation algorithm, the displacement field is computed. Strains are then calculated by differentiating the displacement field. The accuracy of strain measurements is approximately 0.05% strain. The computer controlling the actual test and the load and extensometer recording is synchronized with the image capturing. This enables all results to be correlated to a time step (TS) which is crucial when both strain and stress magnitudes and distributions change throughout the test. The principal function of the DSP equipment is shown in Figure 5.

The system may express the measured strain either as true strain (logarithmic) or as engineering strain. For small shear angles (small deformation) the difference between the two

is negligible but not for large deformations. As will be shown the deformations post yield are highly localized and hence it is questionable to discuss homogenous strain fields. However, for visualization purposes the computed engineering strain as given by the DSP-system has been used when illustrating the deformation variation through the thickness. The shear strain is otherwise calculated as the relative in-plane deformation of the two faces in relation to the original material thickness as more thoroughly described in the following.
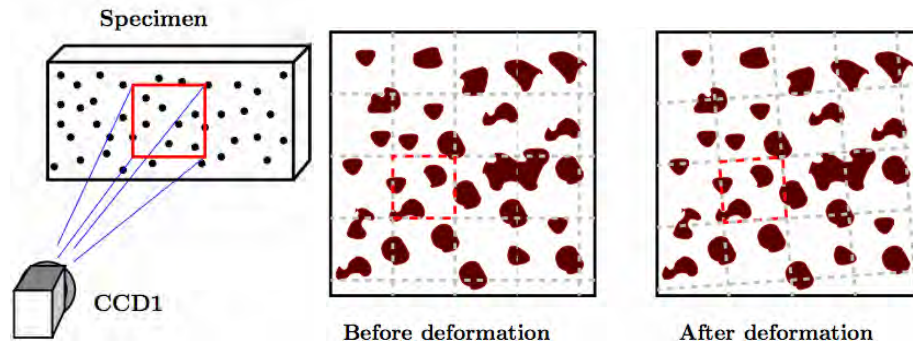
Figure 5 Principal sketch of DSP equipment function

3. RESULTS

3.1 Block Shear Testing

Figure 6 shows the test specimen and DSP system used for the block shear testing, with the DSP camera at the far left of the image. The foam specimens were 300mm long, 75mm wide and 30mm thick. The front side of the specimen and loading plates are sprayed with a speckle pattern for optimal recording with the DSP equipment and the extensometer is fitted on the back of the sample as shown on Figure 7. The data from the extensometer and the calculated shear strain from the optical system correlate very well as shown in Figure 3.
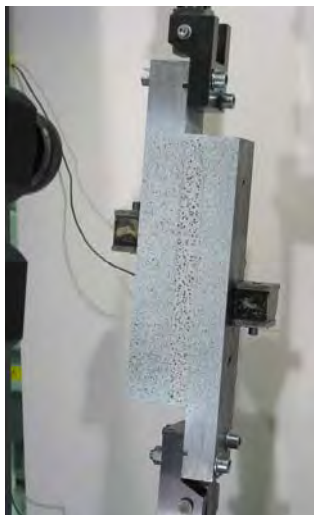

Figure 6. DSP system used for the block shear testing according to ASTM C273.

Figure 7. Deformed shape of Airex R63.80 foam during block shear testing.

Figure 8 shows a typical shear stress/strain curve for the high elongation core material which achieved a maximum nominal shear strain of more than 60%. The data shows an initial linear region, with yield occurring at approximately 5% strain and a stress of 0.65 MPa (similar to the strain and stress at failure of the S51), then extended post yield deformation. The nominal shear stress drops slightly, but then increases at higher strains, resulting in a maximum apparent shear stress of approximately 0.85 MPa. However at this stage of the test the core material has deformed so far that the loading is no longer pure shear, meaning that the simplistic shear stress calculation method used within the standard (load divided by specimen length and width) is no longer valid.
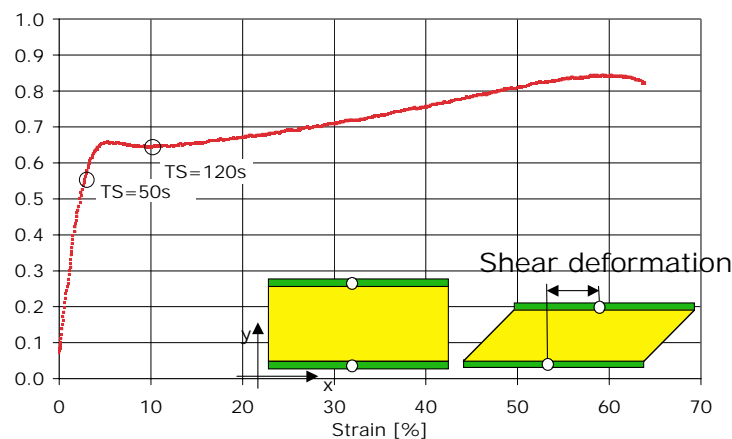
Figure 8 Shear stress-strain curve for Airex R63.80. Strain is based on the beam deformation measured using the DSP. The shear strain is calculated from the relative horizontal displacement of the two faces as illustrated.

The DSP system provides significant insight into the strain fields before, at and after yield. Figure 9 shows a strain contour of the specimen at two different time steps, TS=50s and TS=120s, i.e. before and after yield as shown in Figure 8. The results show that before yield the shear strain is relatively uniform over the specimen surface and the through thickness strains are small. After the yield point the through thickness strain is no longer insignificant and there is a region of localized high shear deformation on the diagonal between the loading points. Equivalent contour plots for the low elongation core in Figure 10 show similar behavior. In the linear elastic region (i.e. prior to yield) there is an even shear strain distribution and very limited through thickness deformation. Just prior to failure localized areas with high strain can be noticed indicating local failure that initiates the complete failure.

Further insight can be gained by study of the change in strain profiles across the material thickness prior to and after "yield". Figure 11 (a) shows that for the low elongation material the strain field has a similar shape before and after yield, although it is not uniform across the core thickness as is assumed by the testing standards. In the case of the R63.80 material shown in Figure 11 (b), in the linear region the shear stress is relatively evenly distributed through thickness whilst post yield the strain is much higher in the centre of the core than towards the edges.
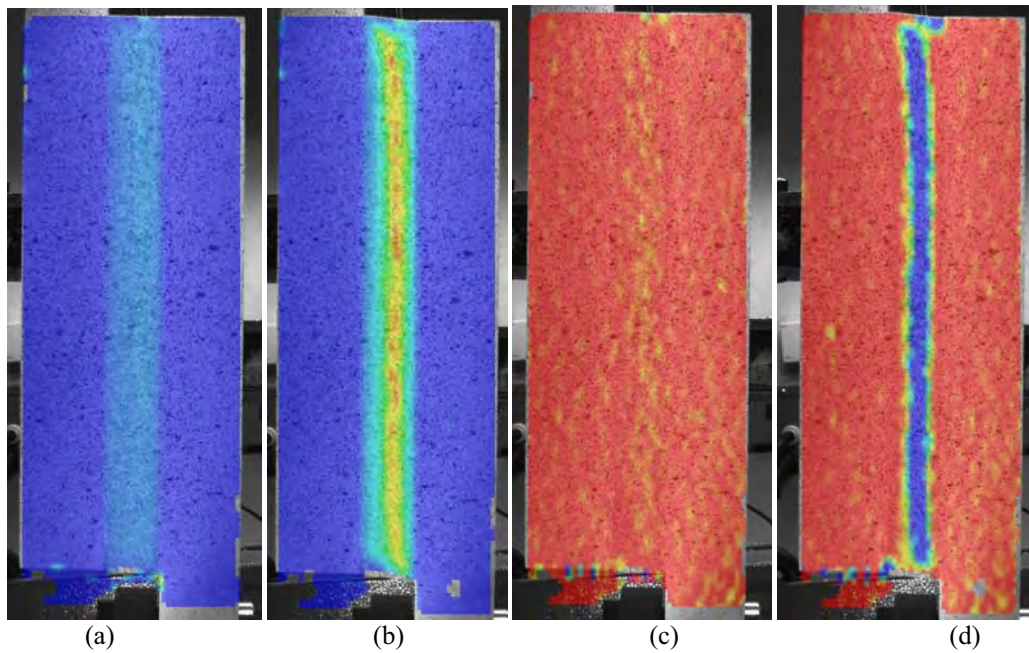
Figure 9 Strain plots from block shear test of the high elongation core material. (a) and (b) display the shear strain distribution before and after the yield point (c) and (d) show through thickness strain distribution before and after the yield point
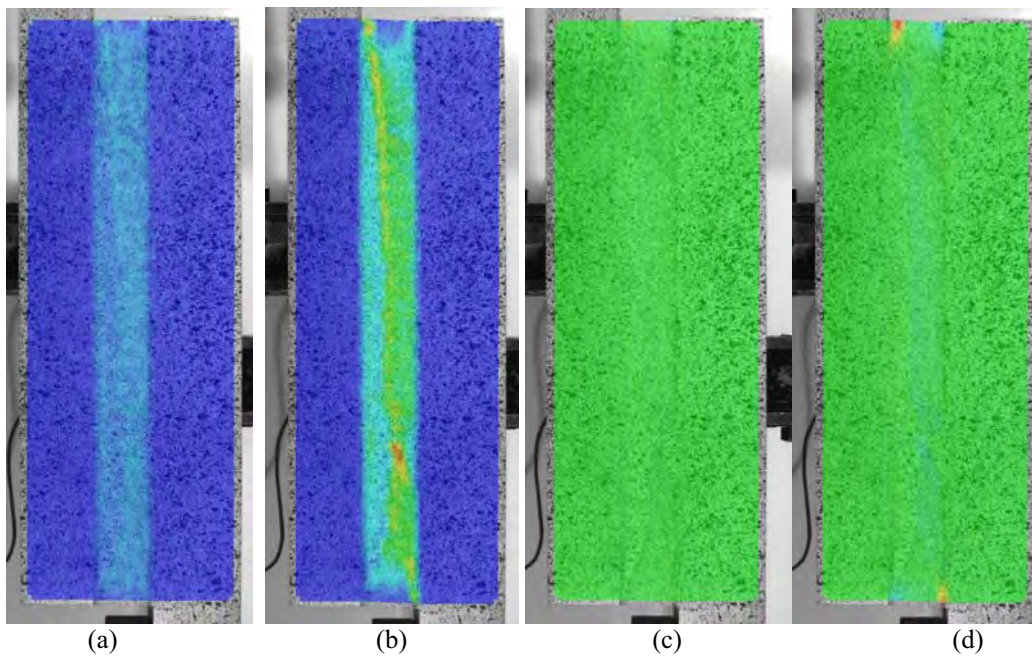

Figure 10 Strain plots from the block shear test of the low elongation core material. (a) and (b) displays the shear strain distribution well before and just prior to final failure (c) and (d) shows through thickness strain distribution well before and just prior to final failure

(a)

(b)
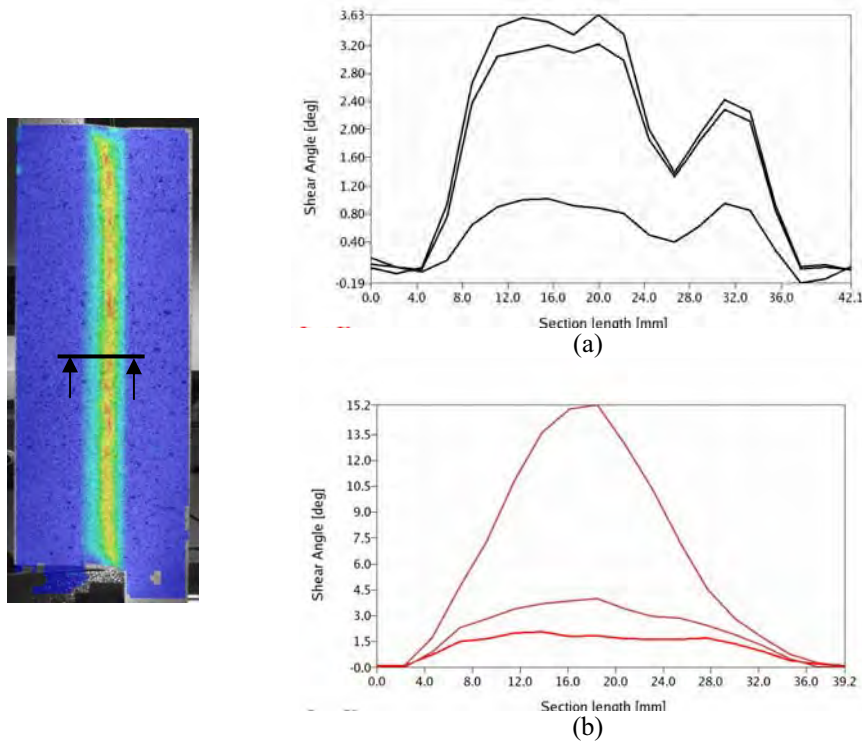
Figure 11 Shear strain distribution through the thickness of the specimens at three different time stages; (a) is the low elongation material, with the lower curve at TS=50s, the middle at TS=120s and the top most is at failure, TS=128s, (b) is for the high elongation material, with the three lines being at TS=50, 72 and 150.. The coarseness of these curves is caused by the limited of output points chosen. Note that the section lengths are larger than the total specimen thickness

Characterising the volumetric change also demonstrates that a state of pure shear does not exist post yield for the ductile core. A pure shear produces no volume change, so in a shear case there is no contribution of gas pressure to the shear modulus [7]. The volume change is calculated from the DSP results as the (original thickness-present thickness)/original thickness. The volumetric change in a block shear test is shown in Figure 12 together with the nominal shear stress. This shows that there is virtually no volumetric change prior to yield, then a steadily increasing reduction in volume, suggesting that crushing of cells is occurring. While any changes in specimen width were not measured, by visual inspection these appeared to be negligible in comparison to the thickness changes.
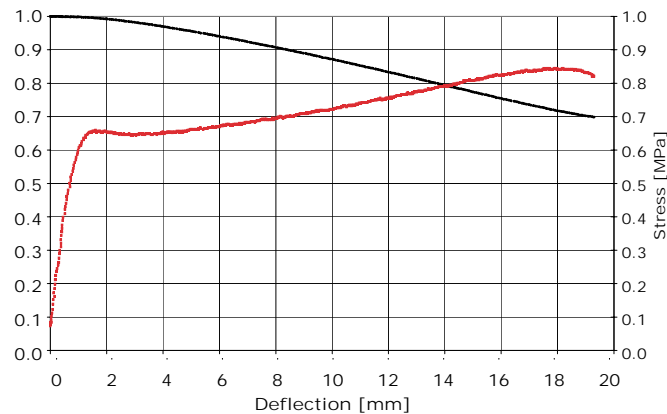
Figure 12 Volumetric change during block shear test of high elongation foam

3.1 Sandwich Beam testing

Flexural testing was undertaken as per ASTM C393 for R63.80 and S51 cored specimens with dimensions of 500mm length and 50mm width. The S51 cored beams had a core thickness of 39mm, the R63.80 30mm. Skins were four layers of non-crimp quasi-isotropic glass fibre mats infused with polyester resin with a thickness of 3.2 mm. The testing fixture had outer supports 360 mm and inner supports 180 mm apart, and the loading rate was constant at 0.1 mm/s. Figure 13 shows the overall shear and transverse compression strains measured by the DSP system on the right axis and the nominal average shear stress calculated as per the standard on the left axis. The shear stress is calculated according to ASTM C393 which assumes that the applied load is taken as shear stress in the core and not as stresses in the faces. The shear angle is calculated by the DSP system from the relative displacement of two points on the faces positioned vertically above each other midway between the inner and outer supports, divided by the core thickness. The compressive strain is based on the relative through thickness deformation of the same two points on the faces.
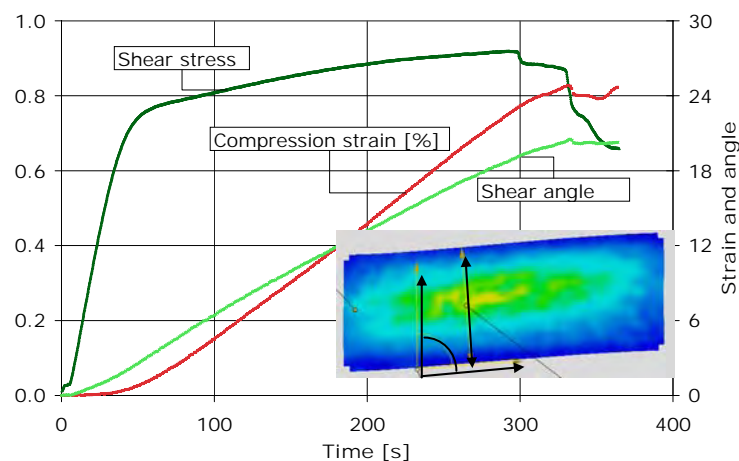

Figure 13 Shear stress and shear angle vs time plot.

It is clear from Figure 13 that during the initial loading in the linear elastic region (up to approximately 30s) the principal deformation of the core is shear, with virtually no deformation through the core thickness being observed. After the yield point the material deforms plastically with a slow increase in the load. It can be observed that the shear strain remains constant whilst the through thickness deformation increases linearly. At time step 300s and at 325 s local collapses can be observed in the specimen just prior to the final failure which was face failure / local buckling at the inner supports.

Figure 14 shows the shear and transverse compression strain contours at different stages throughout the specimen loading. The shear contour of Figure 15 (a), TS=50s, is at yield, (b) TS=80s, is just post yield, and (c), TS=150s, is part way through the post-yield deformation. Figures (d), (e) and (f) are the compressive strains at the same time steps. The figures clearly show that the region of yield and compressive deformation is highly localized to the centre of the specimen.
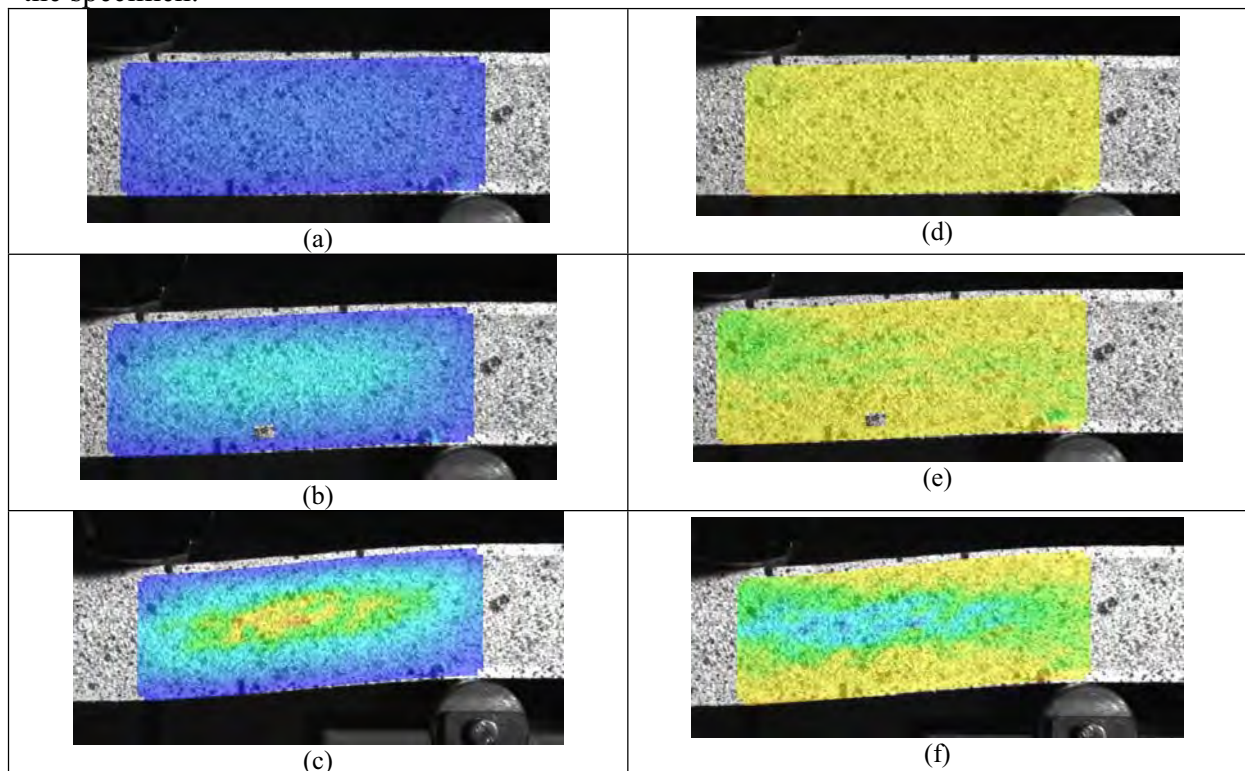

(a)

(d)

(b)

(e)

(c)

(f)

Figure 14 Shear and transverse compression strain contour plots from four point bending test of high elongation core material. (a) - (c) shows the shear strain and (d)-(f) shows the through thickness strains. (a) and (d) are from the linear part of the stress strain curve (TS=25s), (b) and (e) is at yield (T=50s) and (c) and (f) shows the strains at post yield (TS=80s).

Figures 15 and 16 show shear and transverse compression strain distributions through the central region of the specimen (location shown in Figure 13) at each stage of the test. The figures show that prior to yield (TS=50s) the shear strain is almost uniform across the thickness of the specimen, apart from lower regions at the top and bottom of the core and a very slight peak in the middle. At this stage the through thickness compressive strain is

virtually zero.

Immediately post yield (TS=80s), the shear strain at the centre of the core is higher than that in the rest of the specimen, and the compressive strain has begun to increase. With increased yield (TS=150s) the shear strain is much higher in the centre of the specimen than at the edges, and there is substantial compressive deformation, with a maximum compressive strain of 7%
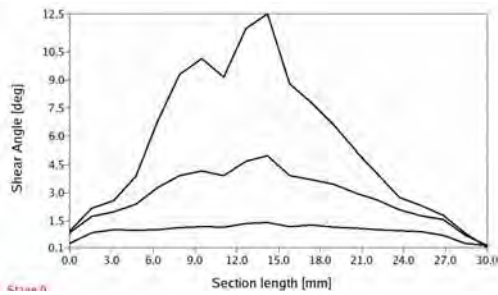

Figure 15 Through thickness shear strain variation for beam test of high elongation core at TS=25, 50, and 80s
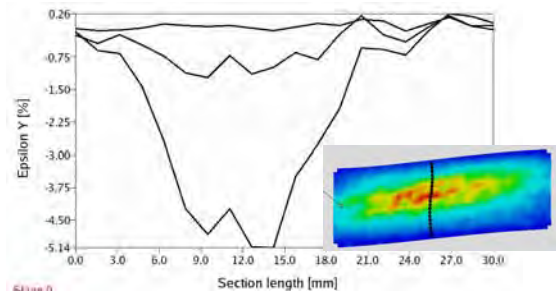

Figure 16 Through thickness compressive strain variation for beam test of high elongation core at TS=25, 50, 80s

Figure 17 shows equivalent strain contours for shear and through thickness deformations of the low elongation core. The results are presented at two stages; during the linear part of the stress strain curve (a and c) and at failure (b and d) are at failure. The strain contours show that the region of shear loaded core is relatively small, and there are very high local strains at the supports.
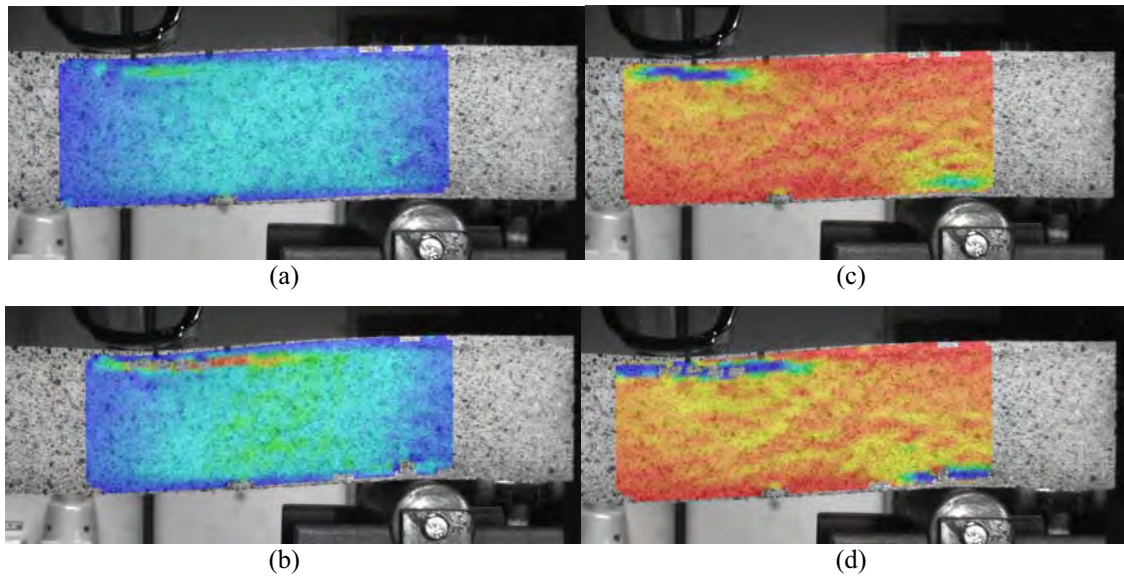

(a)

(c)

(b)

(d)

Figure 17 Strain contour plots from four point bending test of low elongation core material. (a) and (c) are from the linear part of the stress strain curve, (b) and (d) are at failure. (a) and (b) shows the shear strain and (c) and (d) the through thickness strains.

5   CONCLUSIONS

The block shear test does not result in a uniform state of strain in the specimen, even for low elongation materials which show significant strain variations across the thickness of the specimens, particularly near to failure. When yield occurs for high elongation materials it is concentrated in the centerline of the specimen. The test generates significant compressive strain and volumetric strain change in the material, confirming that post-yield it can not be considered to be a pure shear test. While the load at yield can be considered to be a reasonable estimate of the shear yield strength of the material, the maximum load from the block shear test should not be used as a representation of shear strength.

Flexural testing of sandwich beams also does not result in a state of uniform shear as assumed by common testing standards and classical sandwich theory. The maximum shear strain is in a central region of the specimen, and when yield occurs is associated with significant compressive deformation. Post yield high local shear and compressive strains are present in the centre of the specimen, meaning that the classical sandwich theory assumptions used within the testing standard to calculate shear strength are no longer valid.

The results show that the stress and strain fields in both block shear and sandwich beam tests are very different to those assumed by the testing standards. The test methods result in complex post yield states of stress in the core materials, meaning the core shear strength and ultimate shear strain should not be calculated by classical methods in the post yield region.

REFERENCES

[1]   Downs-Honey, R., Edinger, S., Battley, M., "Slam testing of Sandwich panels", SAMPE Journal, Volume 42, No. 4, July/August 2006

[2]   ASTM C273 – 00, "Standard Test Method for Shear Properties of Sandwich Core Materials", Annual Book of the ASTM Standards, American Society for Testing and Materials, www.astm.org, PA, USA

[3]   ISO 1922 "Rigid cellular plastics -- Determination of shear strength", International Standard Organisation (ISO), www.iso.org, Switzerland

[4]   ASTM C393 – 00, "Standard Test Method for Flexural Properties of Sandwich Constructions", Annual Book of the ASTM Standards, American Society for Testing and Materials, www.astm.org, PA, USA

[5]   Juntikka, R., and Hallström, S., "Shear Characterization of Sandwich Core Materials Using Four-point Bending" J of Sandwich Structures and Materials Vol. 9—January 2007, http//:jsm.sagepub.com

[6]   Aramis-Deformation measuring system, GOM mbH, www.gom.com, Switzerland

[7]   Gibson L.J. and Ashby M.F., Cellular Solids – Structure and Properties, 2:nd edition, Cambridge University Press, Cambridge, UK, 1997.

DAMAGE TOLERANCE OF A SANDWICH PANEL WITH A CRACKED SQUARE HONEYCOMB CORE LOADED IN SHEAR

I. Quintana Alonso and N.A. Fleck

Cambridge University, Department of Engineering, Trumpington Street, Cambridge, CB2 1PZ, UK
e-mail: iq201@cam.ac.uk; naf1@cam.ac.uk

Keywords: finite element analysis, fracture toughness, elastic behaviour, honeycomb

Summary. *We explore the shear fracture strength of a sandwich panel made from an elastic brittle diamond-celled honeycomb, containing a centre-crack. The honeycomb fails when the local stress attains the tensile or compressive strength of the solid, or by local buckling. Finite element predictions are given for the unnotched strength, and for the fracture toughness. These predictions, together with conventional linear elastic fracture mechanics, are used to construct a failure map with axes given by the geometry of the cracked sandwich panel. The strength of the sandwich structure is calculated according to the dominant failure mechanisms, which depend upon the tensile failure strain of the solid and upon the relative density of the honeycomb. The relevance of the failure map is illustrated through material-property charts. An extension of the method to cyclic loading is discussed.*

1 INTRODUCTION

Honeycomb materials are often used in applications where severe mechanical loads and operating conditions lead to damage. Examples include catalytic converters for automobiles, filters for liquid metal, absorbers for solar receivers, supports for space mirrors, and orthopaedic implants for bone repair. Cracks can exist in the honeycomb and cause a significant decrease of its fracture strength. Commonly, the honeycomb core is loaded in a sandwich panel configuration with stiff and strong face-sheets. The damage tolerance of these sandwich structures is of concern and motivates the present study.

In this paper we explore the *shear* fracture strength of a sandwich panel made from an elastic brittle diamond-celled honeycomb. The core contains a central crack, and loading is parallel to the faces of the sandwich panel, see Fig. 1a. Finite element simulations and simple analytical models are used to determine the strength of the sandwich structure.

A recent numerical study of the *tensile* fracture strength of a cracked sandwich panel [1], revealed that linear elastic fracture mechanics applies when a K-field exists on a scale larger than the cell size. But there is also a regime of geometries for which no K-field exists. In this regime the stress concentration at the crack tip is negligible and the net strength of the cracked specimen is comparable to the unnotched strength. We anticipate similar behaviour for a sandwich panel subjected to remote shear.
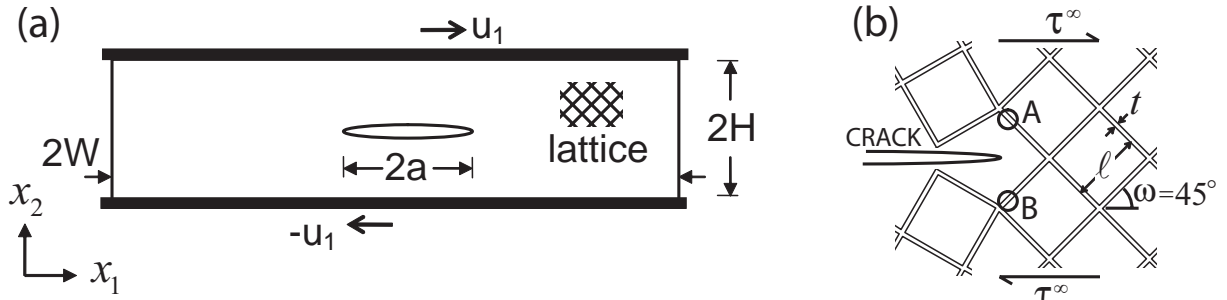
Ignacio Quintana-Alonso and Norman A. Fleck.

Fig. 1 (a) Sandwich panel containing a cracked diamond-celled honeycomb core subjected to shear loading. (b) Sketch of the diamond-celled topology.

Quintana-Alonso and Fleck [1] assumed that local failure occurs when the maximum tensile stress at any point in the lattice attains the tensile fracture strength of the solid. In contrast, a sandwich panel subjected to remote shear may fail by (i) local buckling of the cell walls, (ii) local compressive failure or (iii) local tensile failure of the cell walls. We examine all three possibilities in the current study.

1.1 Description of the problem

Consider the sandwich geometry shown in Fig. 1a. The panel is of width $2W$, height $2H$, and contains a centre-crack of length $2a$. Shear displacements are applied to the top and bottom nodes of the core in order to simulate the relative motion of the face-sheets.

The geometry of the diamond-celled lattice, sketched in Fig. 1b, is described by its cell size ℓ and wall thickness t. A fixed core angle of $\omega = 45°$ is assumed. The relative density of the core $\bar{\rho}$, defined as the density of the honeycomb divided by that of the solid from which it is made, scales with stockiness $\bar{t} = t/l$ as

$$\bar{\rho} = \bar{t}\left(2 - \bar{t}\right) \qquad (1)$$

The solid material is linear elastic to fracture. It has a Young's modulus E_s, a tensile fracture strength σ_t, and a compressive fracture strength σ_c.

The normalised gross fracture stress τ^{∞}/σ_t is a function of the geometric non-dimensional groups t/ℓ, a/ℓ, H/ℓ, and H/W; and of the material groups σ_t/E_s and σ_t/σ_c. We shall explore the effect of these parameters upon the shear fracture strength, τ^{∞}/σ_t, but limit attention to the practical case where H/W is small.

1.2 Scope of the study

First, the unnotched strength of the sandwich panel with a honeycomb core is determined. Second, the mode II fracture toughness of the lattice is calculated. These predictions are used

to construct a fracture map for the centre-cracked panel, with non-dimensional axes given in terms of the sandwich geometry. The relevance of the fracture map to engineering materials is illustrated through material-property charts. Finally, the study is extended to the fatigue strength of lattices.

2   UNNOTCHED STRENGTH OF THE SANDWICH PANEL

2.1   Local Tensile or Compressive Failure of the Cell Walls

Consider a sandwich panel subjected to a shearing displacement of $\pm u_1$ on its faces, as shown in Fig. 1a. In the absence of a crack, the stress state within the honeycomb can be determined by classical beam theory. The cell walls in the $+45°$ direction are loaded in tension, while those in the $-45°$ direction are in compression.

Straightforward analysis reveals that the unnotched shear strength τ_u^T for *tensile local failure* scales with the tensile fracture strength of the solid σ_t and with $\bar{t}$ according to

$$\tau_u^T = \frac{\bar{t}}{1 + 3\bar{t}/2}\sigma_t \tag{2}$$

This expression takes into account both stretching and bending of the cell walls. It is acceptable to neglect the bending contribution at low relative densities ($\bar{t} < 0.1$), and Eq. (2) then reduces to

$$\tau_u^T = \bar{t}\,\sigma_t \tag{3}$$

The unnotched shear strength for *compressive local failure* τ_u^C takes the same functional form as Eq. (3), but now scales with σ_c, as given in Table 1. It is evident that the local dominant failure mechanism depends upon the ratio of tensile to compressive fracture strength of the solid material σ_t/σ_c.

LOCAL FAILURE	UNNOTCHED STRENGTH	FRACTURE TOUGHNESS
Tensile	$\tau_u^T = \bar{t}\,\sigma_t$	$K_{IIC}^T = 0.44\bar{t}\,\sigma_t\sqrt{l}$
Compressive	$\tau_u^C = \bar{t}\,\sigma_c$	$K_{IIC}^C = 0.44\bar{t}\,\sigma_c\sqrt{l}$
Buckling	$\tau_u^B = 1.88\bar{t}^3 E_s$	$K_{IIC}^B = 2.75\bar{t}^3 E_s\sqrt{l}$

Table. 1. Unnotched strength of the sandwich panel and fracture toughness of the lattice.

2.2   Cell Wall Buckling

The honeycomb may also fail by elastic buckling of its cell walls. Finite element simulations indicate that buckling occurs in a periodic cruciform manner, see Fig. 2. Each cell wall behaves as an Euler strut of length ℓ, but with end rotational restraint provided by the adjoining tensile bars. The buckling load is [2]

$$P_{\text{crit}} = \frac{n^2 \pi^2 E_s I}{\ell^2} \tag{4}$$

with $I = t^3/12$ per unit depth. The factor n describes the rotational stiffness of the joints where the cell walls meet. If rotation is freely allowed, $n = 0.5$; if no rotation is possible, $n = 2$. The unnotched shear strength for local buckling follows from equilibrium, giving

$$\tau_u^B = n^2 \frac{\pi^2}{12} \bar{t}^3 E_s \tag{5}$$

Finite element calculations suggest $n = 1.51$. A simple direct estimate for n can be obtained. In the buckled state, the tensile bars inclined at $+45°$ are subjected to alternating point torques of $\pm T$, from one joint to the next (Fig. 2). The joints also rotate by $\pm\phi$, and simple beam theory for the tensile bars provides the desired torsional stiffness $T/\phi = 4E_s I/\ell$. Newmark [3] gives a useful approximate formula for the dependence of n in Eq. (5) upon the value of T/ϕ; his formula implies $n = 1.44$, which is in satisfactory agreement with the FE result of $n = 1.51$.

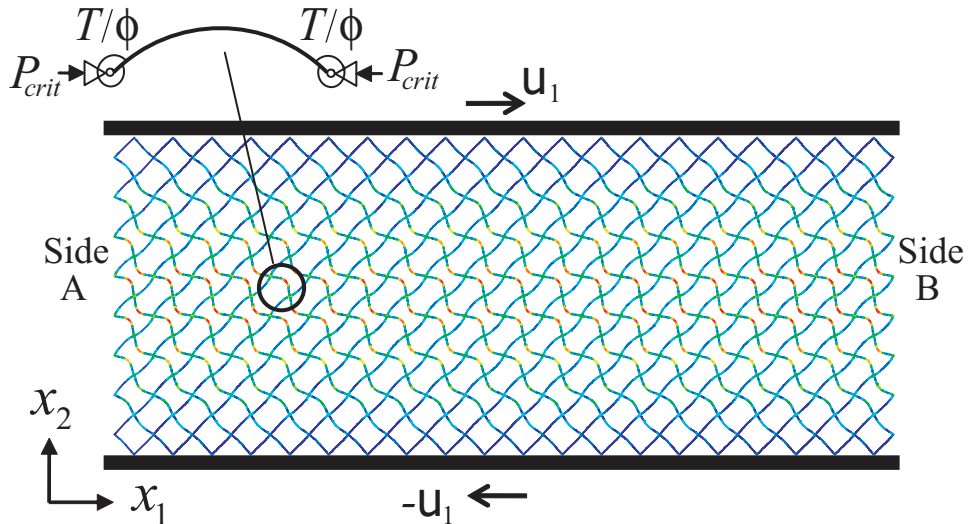

Fig. 2. Buckling of an unnotched panel subjected to remote shear. The face-sheets are allowed to displace in the x_2-direction, but rotation is not permitted. The boundary conditions on the sides of the specimen are: $u_1^A = u_1^B$; $u_2^A = u_2^B$; $\theta^A = \theta^B$.

3   PREDICTION OF FRACTURE TOUGHNESS

The fracture toughness of the diamond-celled honeycomb is obtained by considering a cracked lattice, with an outer K-field, following Romijn and Fleck [4]. The displacement field **u** associated to a K-field is applied to the outer boundary of this lattice, as given by Sih et al. [5], see Fig. 3.

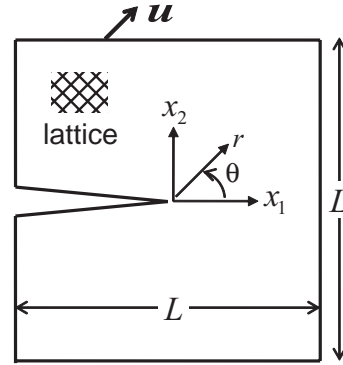Fig. 3. Finite element model used in the fracture toughness predictions.

Linear elastic calculations were performed using the commercial finite element code Abaqus (version 6.7-1). The lattice was meshed with Timoshenko beam elements (type *B21* in Abaqus notation). A mesh convergence study suggested that a mesh of side $L = 600\ell$ is adequate.

The mode II fracture toughness for *tensile local failure* K_{IIC}^{T} is calculated by equating the maximum tensile stress at any point in the mesh to the tensile strength σ_t of the solid. A series of FE simulations have been performed with $\bar{t}$ in the range 10^{-3} to 10^{-1}. The results show that K_{IIC}^{T} scales linearly with $\bar{t}$ and is represented by the regression

$$K_{IIC}^{T} = 0.44\sigma_t\bar{t}\sqrt{\ell} \tag{6}$$

to within a few percent.

Alternatively, the fracture toughness for *compressive local failure* K_{IIC}^{C} is calculated by equating the minimum compressive stress at any point in the mesh to the compressive strength σ_c of the solid. Eq. (6) again applies, but with $\left(K_{IIC}^{T}, \sigma_t\right)$ replaced by $\left(K_{IIC}^{C}, \sigma_c\right)$, as listed in Table 1. The failure site within the honeycomb is shown in Fig. 1b: it is labelled A for tensile failure, and B for compressive.

Local buckling can also occur at the crack tip. An eigenvalue extraction is used in the FE calculations to determine the bifurcation load for buckling, giving a mode II fracture toughness of

$$K_{IIC}^{B} = 2.75E_s\bar{t}^{3}\sqrt{\ell} \tag{7}$$

Selected nonlinear elastic simulations with small initial imperfections confirm the validity of Eq. (7). In the post-buckling regime, the levels of tensile and compressive strain are significantly elevated near the crack tip, and it is concluded that K_{IIC}^B serves as a useful fracture parameter.

Figure 4 shows the deformed mesh near the crack tip for (a) the fundamental equilibrium path, and for (b) the first eigenmode. The fundamental solution is characterised by bending of the cell walls. Narrow zones of high bending stress emanate from the crack tip along the $\pm45°$ radial directions. The length of these zones scales inversely with $\bar{t}$, as discussed by Fleck and Qiu [6]. The first eigenmode involves buckling of the crack tip struts.
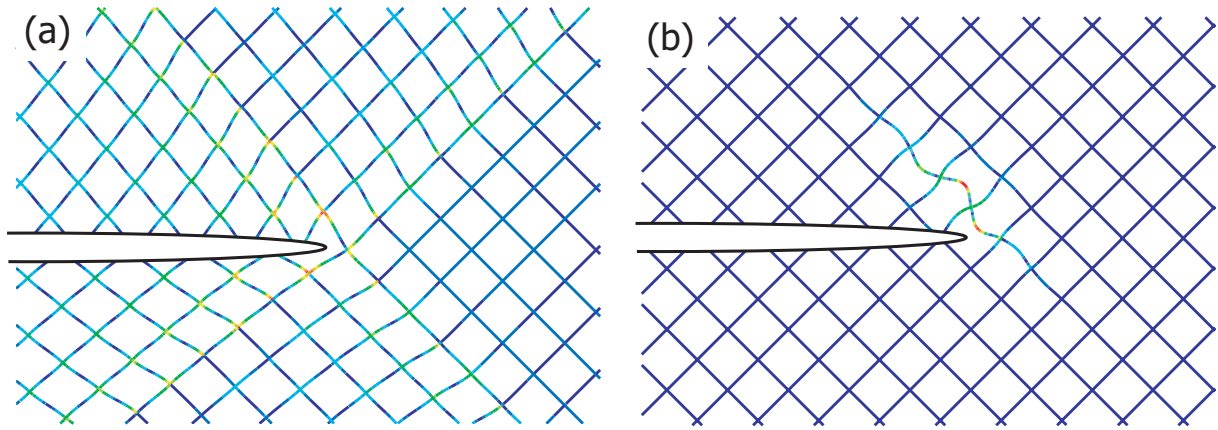

Fig. 4. Deformed mesh near the crack tip of a lattice subjected to a remote K-field on its outer boundary. (a) Fundamental equilibrium solution. (b) First eigenmode.

4   FAILURE MAPS FOR THE CRACKED SANDWICH PANEL

The above results are summarised in Table 1. They can be used to construct a fracture map, with suitably chosen non-dimensional axes. The mode II fracture toughness K_{IIC} of the diamond-celled lattice is taken as $\min\left(K_{IIC}^C, K_{IIC}^T, K_{IIC}^B\right)$. It depends upon the lattice geometry and the material properties of the solid from which it is made. Likewise, the unnotched shear strength τ_u of the sandwich panel is $\min\left(\tau_u^C, \tau_u^T, \tau_u^B\right)$.

We limit attention to materials which satisfy $\sigma_c/\sigma_t > 1$, so that compressive local failure of the unnotched lattice and of the cracked lattice never occur. This is not a severe restriction on material choice: almost all engineering solids have the characteristic $\sigma_c/\sigma_t > 1$.

Note from Table 1 that the unnotched strength is buckling-governed when $\tau_u^B/\tau_u^T \equiv 1.88\bar{t}^2 E_s/\sigma_t < 1$. Similarly, the fracture toughness is buckling-governed when $K_{IIC}^B/K_{IIC}^T \equiv 6.25\bar{t}^2 E_s/\sigma_t < 1$. Thus, the value of the non-dimensional group $\Sigma \equiv \sigma_t/\bar{t}^2 E_s$ dictates whether the unnotched strength and the fracture toughness are due to buckling or tensile local failure. This competition of local failure criteria is summarised in Table 2.

$\Sigma \equiv \dfrac{\sigma_t}{E_s \bar{t}^2}$	UNNOTCHED STRENGTH		FRACTURE TOUGHNESS	
	Buckling?	Tensile Failure?	Buckling?	Tensile Failure?
<1.88	—	✓	—	✓
$1.88-6.25$	✓	—	—	✓
>6.25	✓	—	✓	—

Table 2. The unnotched strength and fracture toughness are controlled by local cell wall buckling or by local tensile failure. The weakest mode of local failure is dictated by the value of Σ.

Now consider the fracture strength of the sandwich panel containing a finite centre-crack of length $2a$, for any given value of Σ. It is instructive to construct a failure map for the cracked sandwich panel using axes $\left(\ell/a, \ell/H\bar{t}\right)$, as shown in Fig. 5.
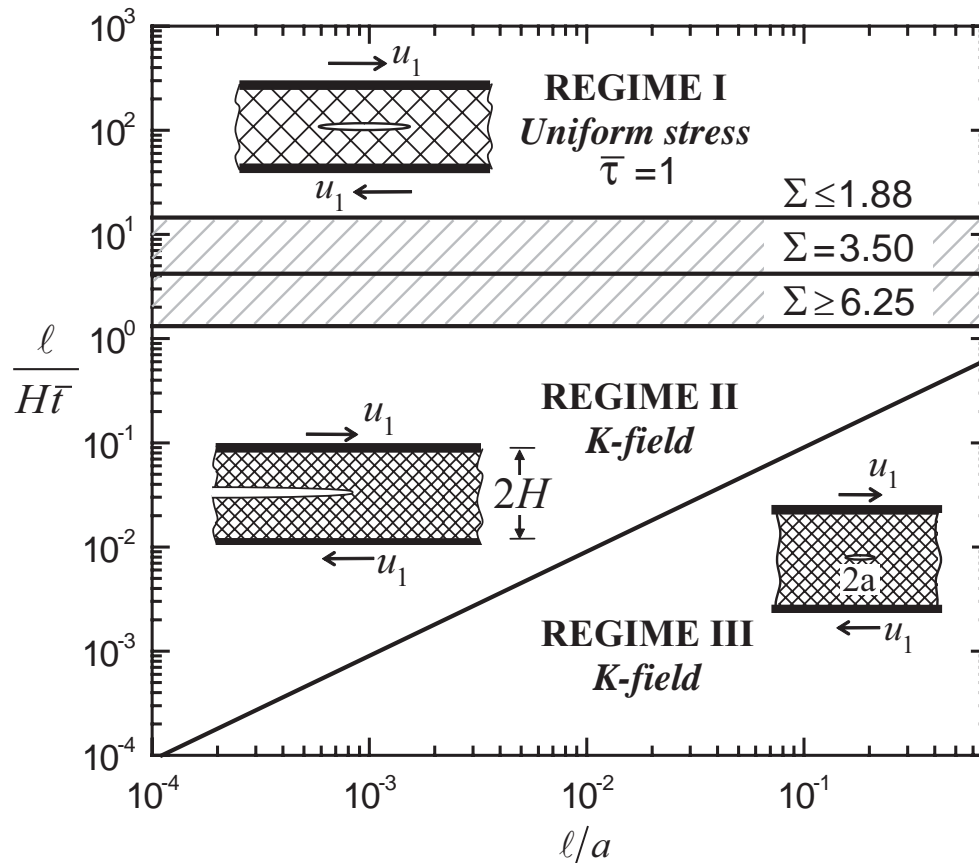

Fig. 5. Fracture map for a panel containing a centre crack and subjected to prescribed shear displacements. The map is valid for small H/W.

Three distinct regimes of the map can be identified. In Regime I, no stress concentration exists and the net-section strength equals the unnotched strength. In Regimes II and III, LEFM applies and the net-section strength is dictated by the fracture toughness. Regime II relates to cracks which are much longer than the height of the panel $2H$, while Regime III exists for short cracks. The details are as follows.

Define the non-dimensional net-section strength as

$$\overline{\tau} \equiv \frac{\tau^{\infty}}{(1-a/W)\tau_u^{T}} \quad , \quad \Sigma \leq 1.88 \tag{8}$$

and

$$\overline{\tau} \equiv \frac{\tau^{\infty}}{(1-a/W)\tau_u^{B}} \quad , \quad \Sigma > 1.88 \tag{9}$$

consistent with Table 2. In order to construct the map we consider the value of $\overline{\tau}$ for each regime in turn.

Regime I: No stress concentration exists at the crack tip. The stress state within the lattice is such that the bending component is negligible with respect to the stretching contribution. It is a damage tolerant regime: the net strength of the panel equals the unnotched strength, and $\overline{\tau} = 1$.

Regime II: The crack is sufficiently long compared to the height of the sandwich panel that the core behaves as an orthotropic elastic strip with a semi-infinite crack. The stress intensity factor for this geometry is given by

$$K_{II} = F_{II} \tau^{\infty} \sqrt{H} \tag{10}$$

where the calibration function is $F_{II} = 2^{3/4}\sqrt{\overline{t}}\,(1-a/W)^{-1}$, see reference [1]. Failure occurs when the stress intensity factor, K_{II}, reaches the critical value, K_{IIC}. Consequently, we have

$$\overline{\tau} = 0.141\left(\ell/H\overline{t}\right)^{1/2} \quad , \quad \Sigma \leq 1.88$$

$$\overline{\tau} = 0.140\Sigma\left(\ell/H\overline{t}\right)^{1/2} \quad , \quad 1.88 < \Sigma < 6.25 \tag{11}$$

$$\overline{\tau} = 0.872\left(\ell/H\overline{t}\right)^{1/2} \quad , \quad \Sigma \geq 6.25$$

Regime III: The crack is much smaller than the height and width of the sandwich panel. The K-calibration for an orthotropic panel containing a short central crack of length $2a$ is approximately

$$K_{II} = \frac{\tau^{\infty}\sqrt{\pi a}}{(1-a/W)} \tag{12}$$

as reported in [1]. Upon equating K_{II} to K_{IIC} we obtain

$$\bar{\tau} = 0.248 \left(\ell/a \right)^{1/2} \quad , \quad \Sigma \leq 1.88$$

$$\bar{\tau} = 0.132 \Sigma \left(\ell/a \right)^{1/2} \quad , \quad 1.88 < \Sigma < 6.25 \qquad (13)$$

$$\bar{\tau} = 0.872 \left(\ell/a \right)^{1/2} \quad , \quad \Sigma \geq 6.25$$

The boundaries of the map follow immediately from equating $\bar{\tau}$ in neighbouring regimes. Boundary between Regimes I / II:

$$\ell/H\bar{t} = 14.61 \qquad , \quad \Sigma \leq 1.88$$

$$\ell/H\bar{t} = 51.38/\Sigma^2 \qquad , \quad 1.88 < \Sigma < 6.25 \qquad (14)$$

$$\ell/H\bar{t} = 1.32 \qquad , \quad \Sigma \geq 6.25$$

Boundary between Regimes II / III:

$$\ell/\bar{t}H = 0.90 \left(\ell/a \right) \qquad , \quad \text{for all } \Sigma \qquad (15)$$

A physical constraint on the minimum crack length is also imposed on the map: the minimum crack length in the lattice is $a/\ell = \sqrt{2}$. The resulting universal fracture map is shown in Fig. 5. Contours of $\bar{\tau}$ could be added, but their precise value is dependent on the choice of Σ.

We emphasise that $\bar{\tau} = 1$ in Regime I, while in Regime II the values of $\bar{\tau}$ are given by Eq. (11), and in Regime III by Eq. (13). A similar map has been constructed for tensile loading of the cracked sandwich panel [1]. Again, three regimes exist, and the failure map has been validated by extensive FE simulations of specific cracked geometries. Studies were undertaken over a wide range of $(\bar{t}, \ell/a)$. Good agreement between analytical formulae and numerical predictions has been noted for all regimes of behaviour, with a marked transition between regimes. These results give confidence in the fracture map presented here for remote shear loading.

4.1   Application to Engineering Materials

Recall that the competition between cell wall buckling and local tensile failure is dictated by the value of Σ, as summarised in Table 2. Σ scales with the material index σ_t/E_s and with $1/\bar{t}^2$. Thus, the value of Σ is dependent upon material choice, for any given $\bar{t}$.

A chart of the tensile strength σ_t plotted against the Young's modulus E_s has been generated for engineering materials using the commercial package CES [7], see Fig. 6. We limit materials to those which are elastic-brittle, with zero tensile ductility $\varepsilon_f = 0$. Data for a given class of materials (e.g. technical ceramics) are enclosed in property-envelopes.

Lines of constant Σ have been added to Fig. 6 for $\bar{t} = 0.01$ and 0.1. For stocky lattices with $\bar{t} = 0.1$, almost all materials possess a value of Σ which is much less than 1.88; consequently, the unnotched strength and the fracture toughness are governed by local tensile

failure. In contrast, for the more slender lattice, $\bar{t} = 0.01$, the lines $\Sigma = 1.88$ and 6.25 cut through much of the data. Therefore, there is a close competition between buckling and local tensile failure of the cell walls, and the active failure mechanism is material dependent.
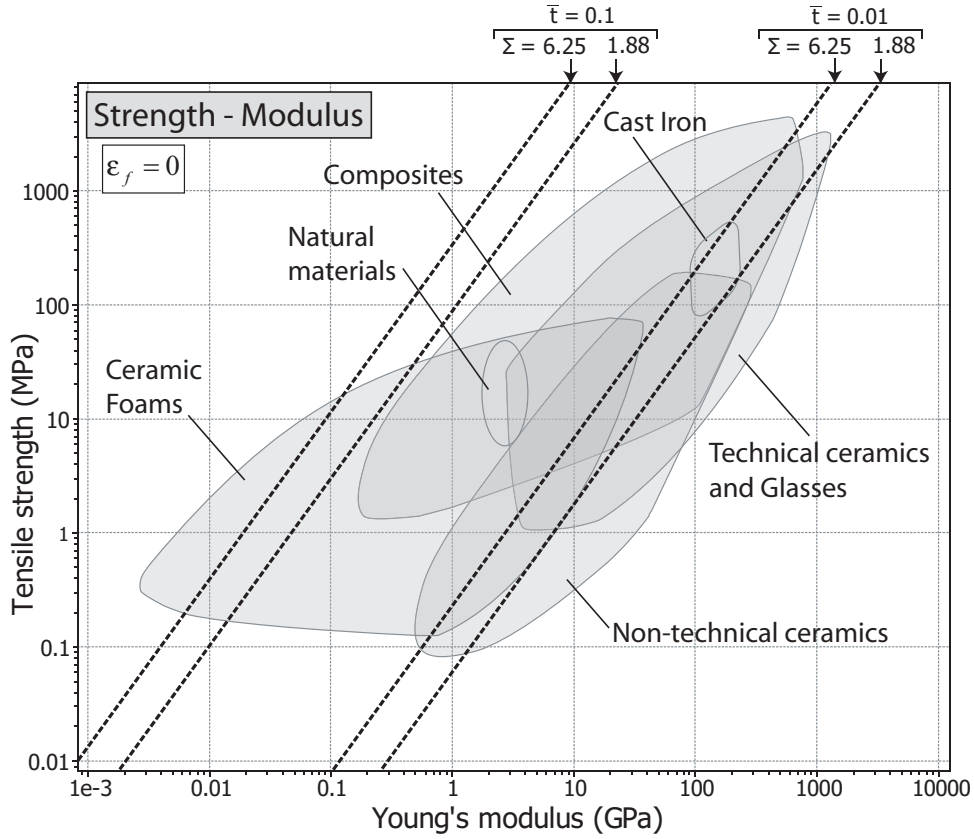

Fig. 6. Tensile strength versus Young's modulus. Materials with no tensile ductility, $\varepsilon_f = 0$.

The fracture map presented in this study (Fig. 5) also describes the *fatigue strength* of lattice materials, with the following slight modification. Replace the tensile strength σ_t by the amplitude of fatigue loading σ_e of the solid at the endurance limit (10^7 cycles). Also, replace τ^∞ by the amplitude of fatigue loading τ_a at the endurance limit for the cracked sandwich panel. Then, the unnotched fatigue strength of the lattice is given by Eq. (2), and the mode II fatigue threshold is given by

$$\left(\Delta K_{II} \right)_{th} = 0.88 \sigma_e \bar{t} \sqrt{\ell} \tag{16}$$

via Eq. (6). Buckling remains a possibility under cyclic loading and Eqs. (5) and (7) still hold. The expressions (8)-(15) apply, but with the substitution $\left(\sigma_t, \tau^\infty \right) \rightarrow \left(\sigma_e, \tau_a \right)$ for cyclic loading.

It is straightforward to also generate a fatigue chart of engineering materials using CES, with the endurance limit σ_e as the y-axis and the Young's modulus E_s as the x-axis (Fig. 7). Lines of $\Sigma = 1.88$ and 6.25 are again included in Fig. 7 for $\bar{t} = 0.01$ and 0.1.
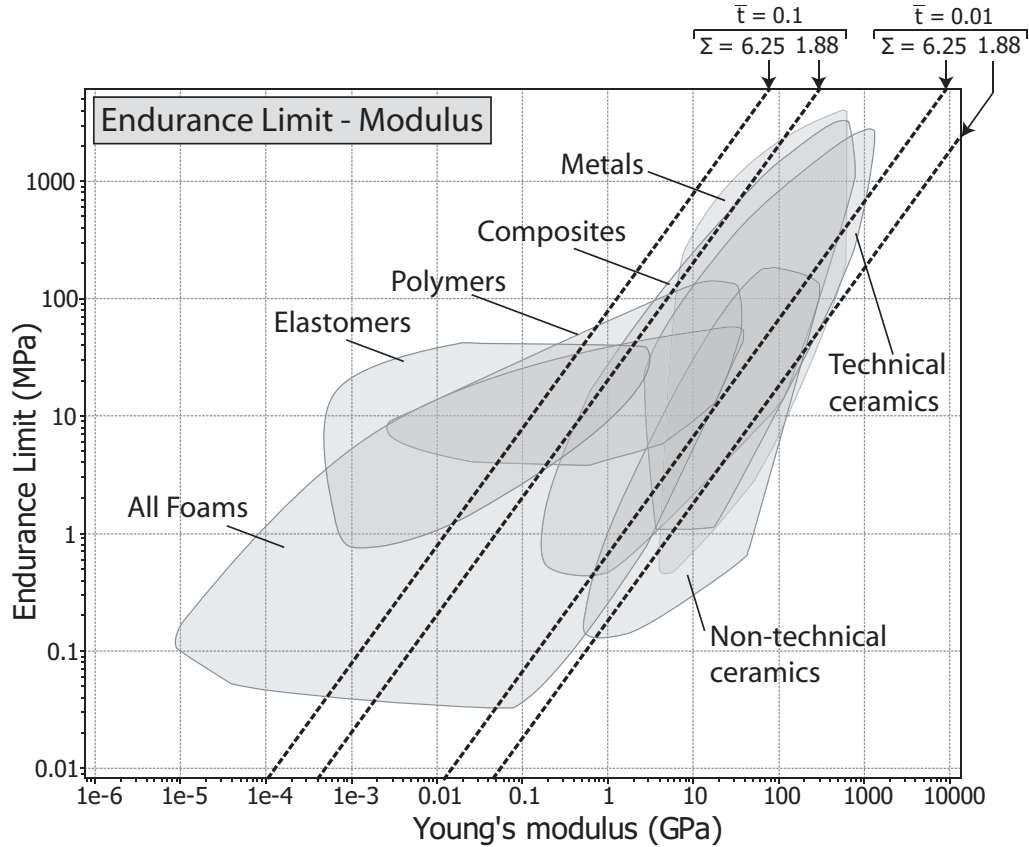

Fig. 7. Endurance limit versus Young's modulus. Note that $\Sigma \equiv \sigma_t / E_s \bar{t}^2$.

The ratio of endurance strength to tensile strength, σ_e / σ_t, is termed the fatigue ratio. It is of the order of $0.35 - 0.5$ for metallic alloys, and of the order of unity for ceramics. We note that the value of Σ is reduced by the fatigue ratio under cyclic loading.

We have included all engineering materials in the fatigue property chart of Fig. 7 in view of the fact that the cyclic stress state is given by the elastic solution at the endurance limit. Thus, in the fatigue case, our elastic-brittle analysis is not restricted to solids of low ductility. It is clear from Fig. 7 that materials exist which undergo cell wall buckling at the endurance limit for both small $\bar{t} = 0.01$ and large $\bar{t} = 0.1$. These materials include elastomers, polymers and foams. Most metallic alloys undergo fatigue failure at the cell-wall level for $\bar{t} = 0.1$, but buckle at $\bar{t} = 0.01$.

5   CONCLUDING REMARKS

We have investigated the damage tolerance of a sandwich panel containing a centrally cracked diamond-celled honeycomb core. Expressions for unnotched shear strength and mode II fracture toughness are obtained by finite element calculations. A fracture map has been constructed with axes given by the sandwich geometry. It is a useful guide for calculating the strength of the damaged sandwich structure. The dominant local failure mechanism depends upon the tensile failure strain σ_t / E_s of the solid and upon the strut stockiness $\bar{t}$.

It is recognised that brittle solids exhibit a scatter of failure strength: variable flaw sizes and a random orientation within the brittle cell walls lead to variations in the tensile strength of the solid material σ_t. Statistical variations in the cell wall strength are usually quantified by assuming a Weibull distribution. The effect of specimen geometry and Weibull modulus m upon the fracture map can then be explored. It is expected that the larger the sandwich panel the more likely it is to be strength-controlled, for a given cell size of the honeycomb. Also, the domains of toughness-controlled fracture will shrink as the Weibull modulus is decreased. This is not explored further here, but is discussed for the tensile loading of a cracked sandwich panel in [1].

Microstructural imperfections such as wavy struts and displaced joints are expected to have a knock-down effect upon the fracture properties of elastic-brittle honeycombs. The sensitivity of fracture toughness to imperfections in the form of displaced joints has been explored by Romijn and Fleck [4]. Their analysis indicates that the fracture toughness of the diamond-celled topology is imperfection-sensitive. Their results can be used to modify the strength predictions of the cracked sandwich panel with imperfections present at the cell wall level.

REFERENCES

[1] I. Quintana Alonso and N.A. Fleck, "The Damage Tolerance of a Sandwich Panel Containing a Cracked Honeycomb Core," *J. Appl. Mech.* In print.

[2] S.P. Timoshenko and J.M. Gere, *Theory of Elastic Stability*, 2nd ed. McGraw-Hill, New York (1961).

[3] N.M. Newmark, "A Simple Approximate Formula for Effective End-Fixity of Columns," *J. Aero. Sci.*, 16, 116 (1949).

[4] N.E.R. Romijn and N.A. Fleck, "The Fracture Toughness of Planar Lattices: Imperfection Sensitivity," *J. Mech. Phys. Solids*, 55(12), 2538-2564 (2007).

[5] G.C. Sih, P.C. Paris and G.R. Irwin, "On Cracks in Rectilinearly Anisotropic Bodies," *Int. J. Fract. Mech.* 1(3), 189-203 (1965).

[6] N.A. Fleck and X. Qiu, "The Damage Tolerance of Elastic-Brittle, Two-Dimensional Isotropic Lattices," *J. Mech. Phys. Solids*, 55(3), 562-588 (2007).

[7] CES EduPack 2007, The Cambridge Engineering Selector, Granta Design, Rustat House, 62 Clifton Road, Cambridge CB1 7EG, UK.

IMPACT

BARELY VISIBLE IMPACT DAMAGE DETECTION BY DISTRIBUTED STRAIN MEASUREMENT ALONG EMBEDDED OPTICAL FIBER WITH 10 CM SPATIAL RESOLUTION

Shu Minakuchi[*], Tadahito Mizutani[*], Yoji Okabe[†] and Nobuo Takeda[*]

[*] Dept. of Advanced Energy, Graduated School of Frontier Sciences
The University of Tokyo
5-1-5 Kashiwanoha, Kashiwa-shi, Chiba 277-8561, Japan
e-mail: shu@smart.k.u-tokyo.ac.jp, mizu@smart.k.u-tokyo.ac.jp, takeda@smart.k.u-tokyo.ac.jp
web page: http://www.smart.k.u-tokyo.ac.jp/index.html

[†] Institute of Industrial Science
The University of Tokyo
4-6-1 Komaba, Meguro-ku, Tokyo 153-8505, Japan
e-mail: okabey@iis.u-tokyo.ac.jp, web page: http://www.okabeylab.iis.u-tokyo.ac.jp/

Key words: Impact damage, Residual dent, Modeling, Health monitoring, Optical fiber.

Summary. *Impact damage detection system for sandwich structures was developed by using a specific response of pre-pump pulse Brillouin optical time domain analysis (PPP-BOTDA) sensing system to non-uniform strain distribution along an optical fiber. The innovative PPP-BOTDA sensing system employs stimulated Brillouin scattering in the optical fiber and realizes distributed strain measurement with spatial resolution of 10 cm, sampling interval of 5 cm and sensing range of more than 1 km. In our previous study, it was revealed that strain gradient broadens a width of a Brillouin gain spectrum, which is a respondency of the PPP-BOTDA. The specific response of the PPP-BOTDA was employed to detect non-uniform strain distribution along a residual facesheet dent in a damaged area. First, the response simulation of the optical fiber sensor network formed in the adhesive layer was conducted to clarify the effectiveness and limitation of the proposed damage detection technique. Then the system was validated by an experiment. As the damage became larger, the width of the Brillouin gain spectra became broader. Consequently, location and size of barely visible damage could be estimated. The developed system is quite useful in a first inspection of large-scaled sandwich structures in aerospace applications.*

1 INTRODUCTION

Composite sandwich structures are attracting considerable attention as a way to maximize the potentials of advanced composite materials [1,2]. The composite sandwich structures are integral constructions consisting of two composite facesheets and a lightweight core. The facesheets primarily resist in-plane and lateral (bending) loads, and the core maintains the distance between two facesheets and carries transverse forces. Since the composite sandwich

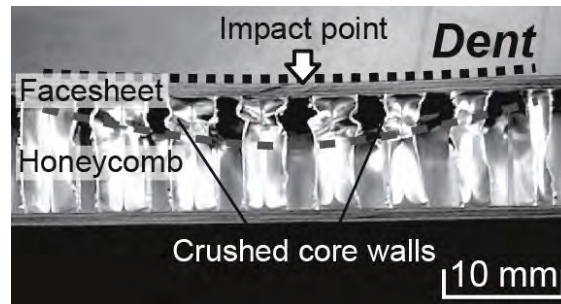Shu Minakuchi, Tadahito Mizutani, Yoji Okabe and Nobuo Takeda.

Figure 1: Cross-sectional view of impact damage

structures have extremely high specific stiffness and inherent multifunctionality, they are expected to be applied to primary structures in aerospace applications [3-5]. However, since the composite facesheet is very thin and the lightweight core is weak, they can be easily damaged when an impact or indentation load is applied [6]. The core under the loading point crushes and a dent in the facesheet remains, as presented in Figure 1. The dent significantly degrades the stiffness and strength of the sandwich structures, even when it is small and barely visible (BVID). The perturbed geometry of the facesheet and the deteriorated mechanical property of the damaged core alters the stress field in the structures, and, as a result, damages in the facesheet and the core initiate under rather low loading condition [7,8]. In order to quantitatively determine the damage growth mechanism under the transverse localized loading, the present authors developed a "segment-wise model" and conducted theoretical simulation of the indentation response of honeycomb sandwich beams [9,10]. The beam was divided into many segments based on the periodic shape of the honeycomb and the complete crushing-stretching characteristics of the core were integrated in each segment, resulting in the superiority of the new model over the conventional elastic-perfectly plastic model. It was revealed that the facesheet dent is introduced by the severely damaged core near the loading point and the dent generates significantly high residual stress field in an undamaged part of the core, which might be a source of further damage growth. It was also confirmed that relatively high non-uniform strain is induced along the convex and concave parts of the facesheet corresponding to the damage size. Residual strain of more than 1000 $\mu\varepsilon$ remains on the dented facesheet even in the case of barely visible damage [10].

In this study, impact damage is detected by measuring the residual strain along the dent using a specific response of the PPP-BOTDA sensing system. The developed system effectively realizes barely visible impact damage monitoring of large-scaled structures with a very limited number of the optical fiber sensors. First, the measurement principle and the specific response of the PPP-BOTDA to the non-uniform strain are briefly introduced. Then the damage detection system using a sensor network formed in the adhesive layer is proposed and, further, the effectiveness and limitation of the system is clarified through response simulation of the sensor network using non-uniform strain distribution calculated from an extended segment-wise model. Finally the validity of the proposed system is confirmed through a quasi-static indentation damage detection test using a honeycomb sandwich panel, where a single optical fiber is embedded in the adhesive layer at even intervals of 5 cm.

Shu Minakuchi, Tadahito Mizutani, Yoji Okabe and Nobuo Takeda.

2 IMPACT DAMAGE DETECTION SYSTEM USING OPTICAL FIBER SENSOR

2.1 PPP-BOTDA sensing system and its specific response to non-uniform strain

A schematic of the PPP-BOTDA sensing system (Neubrescope, Neubrex Co., Ltd) is illustrated in Figure 2. The PPP-BOTDA sensing system employs a stimulated Brillouin scattering (SBS) technique [11]. Two laser beams, a pump pulse having unique wave profile and a continuous wave (CW) probe light, are injected into an optical fiber from its both ends. The interaction of these two laser beams excites acoustic waves, due to their different frequencies. The pump pulse is backscattered by the phonons, and part of its energy is transferred to the CW. The power gain of the CW, which is called the Brillouin gain spectrum (BGS), as a function of frequency difference between the two laser beams, is measured at the output end of the probe light while the frequency of the probe light is scanned. The value of the strain can be estimated by measuring the peak frequency of BGS (Brillouin frequency), while its position along the fiber is calculated from the light round-trip time. This measuring system realizes spatial resolution of 10 cm, sampling interval of 5 cm, and sensing range of more than 1 km with ±0.0025% strain measurement accuracy. The PPP-BOTDA sensing system has been successfully utilized for distributed strain measurement of large-scaled structures [12].

The authors recently investigated effects of the strain profile within the spatial resolution on the response of the PPP-BOTDA sensing system [13]. It was revealed that BGS becomes broader due to non-uniform strain along the optical fiber. The phenomenon was theoretically supported by simulating the change of the spectra using developed software. The effect of the strain profile on the shape of the BGS can be interpreted as below (Figure 3). When the uniform strain is applied to the optical fiber, the Brillouin frequency is also uniform, and thus the BGS has only one sharp narrow peak (Figure 3 (a)). When the non-uniform strain is introduced, on the other hand, the Brillouin frequency also becomes non-uniform, since the Brillouin frequency at each point on the optical fiber is determined by the strain at the point. As a result, the BGS consisting of the entire Brillouin scattering within the spatial resolution
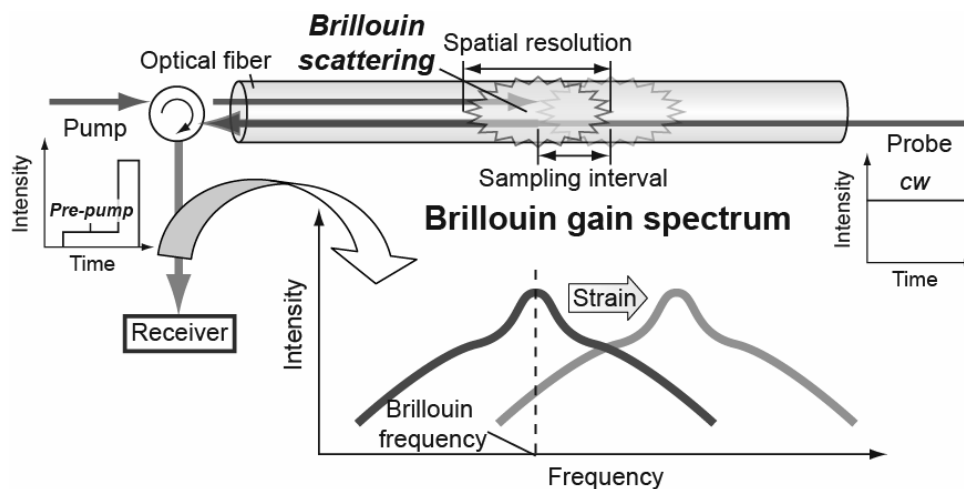

Figure 2: Schematic of PPP-BOTDA sensing system

Shu Minakuchi, Tadahito Mizutani, Yoji Okabe and Nobuo Takeda.

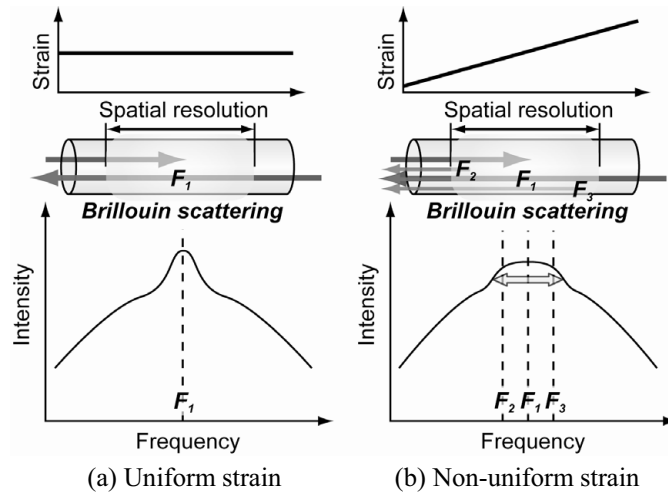(a) Uniform strain   (b) Non-uniform strain

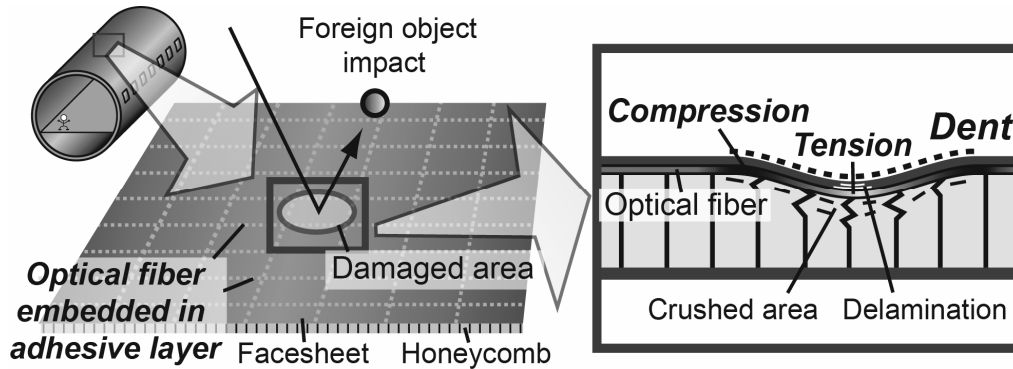Figure 3: Response of PPP-BOTDA depending on strain profiles

Figure 4: Schematic of impact damage detection system for large-scaled sandwich structure

becomes broad (Figure 3 (b)). Moreover, the width of the BGS changes corresponding to the non-uniformity of the strain distribution.

2.2 Damage detection technique using optical fiber sensor network

The PPP-BOTDA sensing system not only realizes distributed strain measurement along the optical fiber of 1 km in length, but also responds to the non-uniform strain within the spatial resolution of 10 cm. In this study, the specific response of the PPP-BOTDA is employed to detect non-uniform strain distribution along the residual facesheet dent in the impact damaged area. A schematic of the proposed system is illustrated in Figure 4. The optical fibers are embedded in the adhesive layer between the facesheet and the core in a reticular pattern [14]. The interval of the sensing network is determined by unacceptable impact damage size. Since the PPP-BOTDA has very long sensing range (> 1 km), a limited number of the optical fibers are sufficient to cover the whole structure. There are two key points to understand the effectiveness of the proposed system. First, the facesheet dent induces tensile and compressive strain along the optical fiber at its concave and convex parts.

This non-uniform strain changes the response of the PPP-BOTDA sensing system, as explained above, and thus the impact damage can be detected. Second, the residual dent in the facesheet after impact loading is relatively large, even when the dent depth is small and the damage is barely visible. So we can considerably reduce sensor density. The optical fibers are embedded in the adhesive layer to detect internal cracks [14,15], and the impact damage detection is also realized with the sensing network bonded on the surface of the structures.

3 RESPONSE SIMULATION OF OPTICAL FIBER SENSOR NETWORK

In this section, the effectiveness and limitation of the impact damage detection system is illustrated by simulating the response of the sensor network to the impact damage. First, the segment-wise model, which addressed only the sandwich beams, is extended to the more practical plate problem and the non-uniform strain distribution along the residual facesheet dent is calculated. Then the strain is used to simulate the change in the shape of the BGS depending on the damage size and location. Finally, the practical damage detection procedure is proposed.

3.1 Extension of segment-wise model for indentation simulation of sandwich plate

The segment-wise model assumed that through-thickness stress field of the core with a small cell size is governed by the transformation of adjacent intersection lines, defined as line joints between honeycomb cell walls. And the sandwich beam was divided into many segments centering around the intersection lines and each segment had uniform material property determined from the through-thickness deformation of the intersection lines [9]. In the sandwich plate problem, an axisymmetric formulation was applied, since the hexagonal honeycomb is rotationally-symmetric. The sandwich plate was divided into circular strip-shaped segments of a constant length a_{segp} as depicted in Figure 5 (a). Although the location of the intersection lines in the segments may significantly change depending on the positional relation between the loading point and the honeycomb geometry, the extended model assumed that the intersection lines are uniformly distributed in each segment and the representative intersection line, whose deformation determines the material property, is located at the center of each segment. A schematic of the model is presented in Figure 5 (b). The upper facesheet,

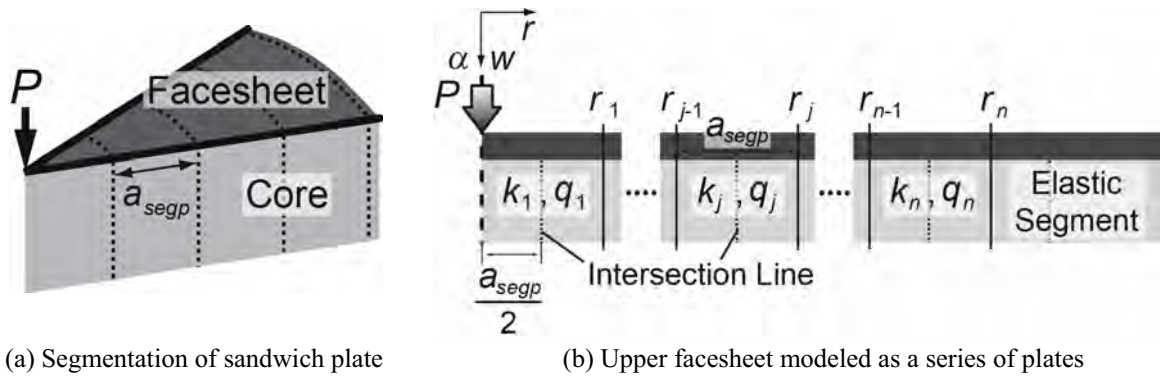(a) Segmentation of sandwich plate   (b) Upper facesheet modeled as a series of plates

Figure 5: Schematic of segment-wise model extended to plate problem

to which the indentation load P is applied, is modeled as a series of plates of bending rigidity D_{fp}. The equilibrium of the plate in segment j ($r_{j-1} < r < r_j$) is governed by the following equation

$$\left(\frac{d^2}{dr^2} + \frac{1}{r}\frac{d}{dr} \right)\left(\frac{d^2 w(r)}{dr^2} + \frac{1}{r}\frac{dw(r)}{dr} \right) + \frac{k_j w(r) + q_j}{D_{fp}} = 0 \tag{1}$$

where $w(r)$ is a transverse deflection of the facesheet, k_j is the stiffness of the core and q_j is the constant stress supplied from the core. The values of the foundation parameters k_j and q_j are determined from modified flatwise compression tests of the core and change corresponding to the deformation of the intersection line. The indentation response for a given indentation displacement α can be calculated by determining P and all the integral constants included in general solutions obtained from Eq. (1), using boundary conditions. And we can conduct damage growth simulation by renewing the foundation parameters as α increases. The detailed procedure of the theoretical simulation is presented in Ref. [9].

The extended model was validated through an experiment. The specimen consisted of carbon fiber reinforced plastic (CFRP) facesheets (UT500/#135, Toho Tenax Co.,Ltd., [(0,90)$_3$], D_{fp} = 9580 N-mm, 100 × 100 × 1.38mm^3), the aluminum honeycomb core (AL 3/16-5052-.001, Showa Aircraft Industry Co., thickness : 20 mm), and thermoplastic adhesive films (AF-163-2K, 3M Co.). The specimen was bonded on a flat steel plate with an adhesive to eliminate the overall bending. A steel flat-bottom cylinder of 5 mm in diameter was attached to a material testing system (AG-50kNI, Shimazu Co.), and an indentation load was applied to the center of the specimen with a constant displacement rate of 0.5 mm/min. The specimen was unloaded after a maximum indentation displacement of 0.5 or 1.0 mm was reached. Four electric-resistance strain gages (KFG-1N-120-C1-11L1M2R, Kyowa Electronic Instruments Co., Ltd.) were bonded on the surface of the upper facesheet in both of 0° and 45° fiber directions in order to monitor the non-uniform strain distribution along the dent. The load-displacement curves and the strain distributions are compared between the experiment

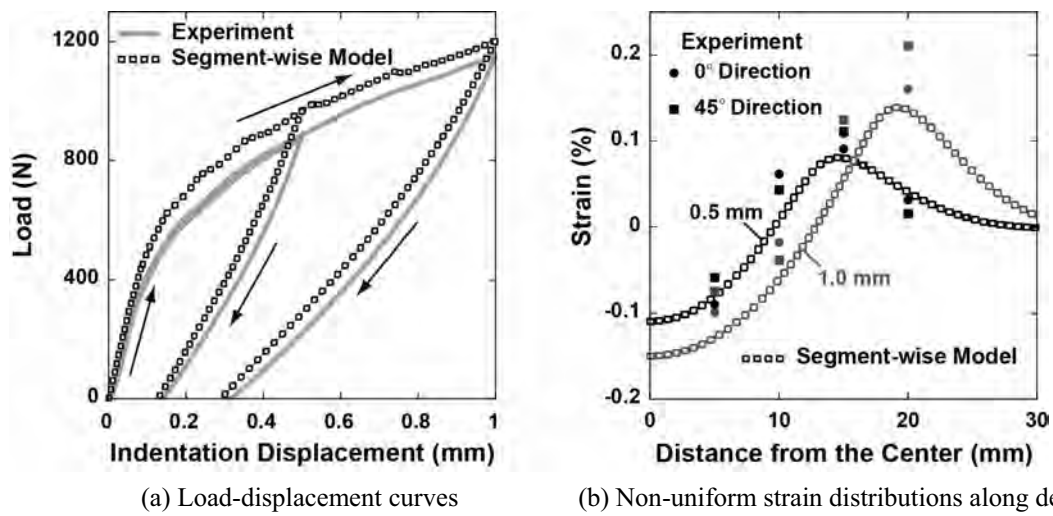(a) Load-displacement curves   (b) Non-uniform strain distributions along dent

Figure 6: Comparisons of indentation responses

and the analysis in the Figure 6. Although the segment-wise model tends to slightly overestimate the indentation load, the softening phenomenon in the loading process and the residual dent formation in the unloading one were well reproduced. The calculated strain distributions also fit well with the measured one, confirming the validity of the extended model. In the next session, the responses of the sensor network to the small (0.5 mm) and large (1.0 mm) damage are simulated using the calculated strain distributions.

3.2 Response of sensor networks depending on impact damage size and location

First, the impact damage was introduced right above the embedded optical fiber. The strain distribution along the optical fiber was estimated by reversing the sign of the strain distribution along the upper surface of the facesheets, and the BGS obtained from each measure point in the damaged area was calculated. Figure 7 presents the calculated spectra. The intensity of each spectrum is normalized by the intensity of the highest component. The spectrum at strain-free state is also shown as a reference. As the measure point gets closer to the damaged area, the spectra starts to become broader because of the non-uniform strain along the dent in the facesheet (Figure 7 (b)). Then the width of the spectrum broadens

(a) -200 ~ -100 mm

(b) -100 ~ 0 mm

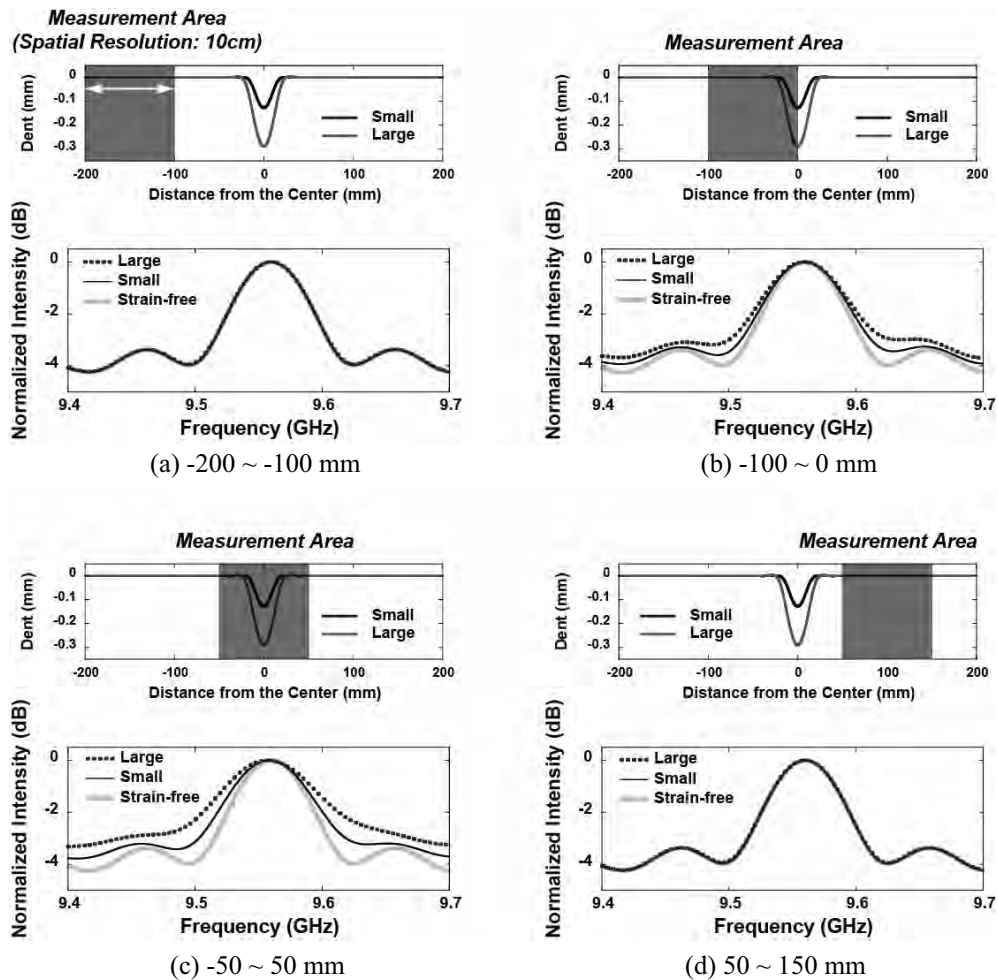(c) -50 ~ 50 mm

(d) 50 ~ 150 mm

Figure 7: BGS obtained from each measurement point

corresponding to the damage size (Figure 7 (c)), since the larger damage generates higher and wider non-uniform strain distribution along the residual dent. Finally, the spectrum recovers its original shape in the undamaged area (Figure 7 (d)), confirming that the proposed system is quite sensitive to both of the damage location and size.

In practical applications, however, the impact damage is randomly induced to the sensor network position, not right above the optical fiber. Hence, when we built the sensor network in the sandwich structures, we need to decide the sensor density to robustly detect the damage occurrence with no effect of its location. Now, we take Figure 8 (a) as an analogy. One grid of the sensor network formed at even interval of 30 mm is presented and the small or large impact damage is introduced at the center of the grid. Since the optical fibers are the farthest from the damage in this case, the strain along the optical fiber induced by the damage is the smallest, reducing the response of the sensor network. Figure 8 (b) presents the BGS obtained from the measurement area depicted in Figure 8 (a). Even though the BGS changed in the case of the large damage, the sensor network did not respond to the small damage. This means that the sensor network cannot robustly detect the small damage, and thus the structure needs to be designed to tolerate the small damage. From a viewpoint of building the sensor network, on the other hand, we need to determine the minimum sensor density by considering the unacceptable damage size depending on the structural site.

Damage detection procedure is specifically presented in Figure 9. First, the Brillouin gain spectra are measured throughout the optical fiber embedded in the whole structure or the area where the impact damage is suspected to be induced. This is conducted before or after the operation of the structure. Second, the width of each spectrum is automatically calculated. A full width at -1 dB from maximum F_{-1dB} (illustrated in Figure 9) is selected as a representative value for the width of the BGS. When the impact damage is introduced, only the damaged area has unusually large value of F_{-1dB}, depending on the extent of the damage. Hence, the damage location and size can be roughly estimated from the distribution of F_{-1dB} along a single optical fiber. This intuitive system is quite useful in first inspection of impact damage in large-scaled sandwich structures. In the next section, the validity of the proposed system is confirmed by detecting barely visible damage in a honeycomb sandwich panel.

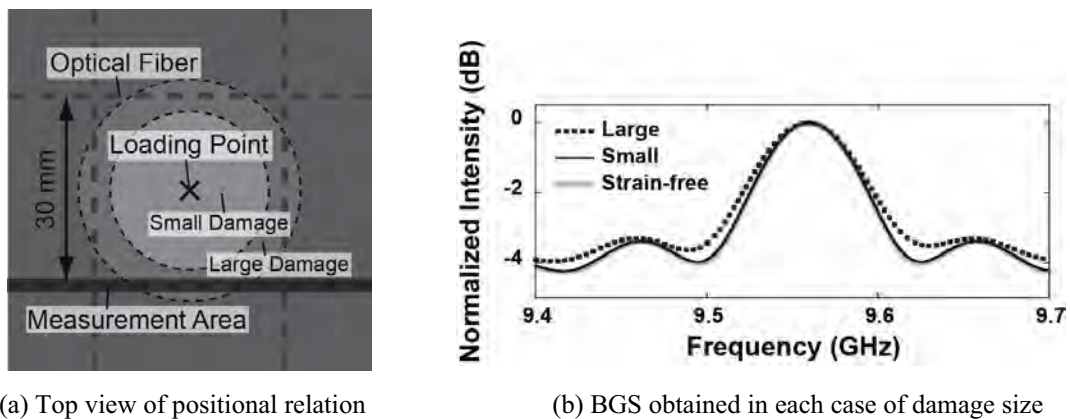(a) Top view of positional relation   (b) BGS obtained in each case of damage size

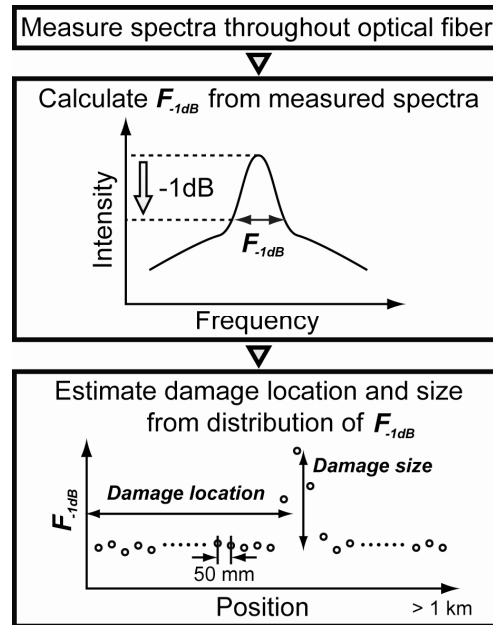Figure 8: Response simulation in the most difficult case for damage detection

Figure 9: Damage detection procedure using distribution of BGS width

4 VERIFICATION TEST

4.1 Experimental set-up

Figure 10 (a) depicts a schematic of the specimen. The sandwich panel consisted of CFRP facesheets (T700S/2500, Toray Industry, Inc., $[0/90]_{3S}$, thickness of 1.5 mm), an aluminum honeycomb core (AL 1/4-5052-.001, Showa Aircraft Industry Co.) and thermoplastic adhesive films (AF-163-2K, 3M Co.). A single optical fiber was embedded between the preliminary molded upper facesheet and the adhesive layer. The upper facesheet was manufactured a little larger than the core and the lower facesheet for handling the optical fiber. Figure 10 (b) presents the experimental setup. A hemispherical steel indenter (diameter: 12.7 mm) was attached to a material testing system (AG-50kNI, Shimazu Co.) and a quasi-static indentation loadings were applied in order to introduce simulated low velocity impact damage. The loading point was set a little bit away from the center of the specimen to investigate the sensitivity to the damage location. After a predetermined maximum indentation displacement was reached, the crosshead reversely moved up. The tests of five kinds of the maximum displacement 1, 2, 3, 4, and 6.5 mm were conducted. After each test, the Brillouin gain spectra were measured throughout the specimen using the PPP-BOTDA sensing system (Neubrescope) connected to both ends of the optical fiber. By comparing the width of the spectra obtained in each test, the response of the proposed damage detection system depending on the damage size was investigated in detail. Additionally, damaged area was checked and recorded after each test by visual inspection and by using electric-resistance strain gages bonded at some points on the surface of the upper facesheet.

Shu Minakuchi, Tadahito Mizutani, Yoji Okabe and Nobuo Takeda.

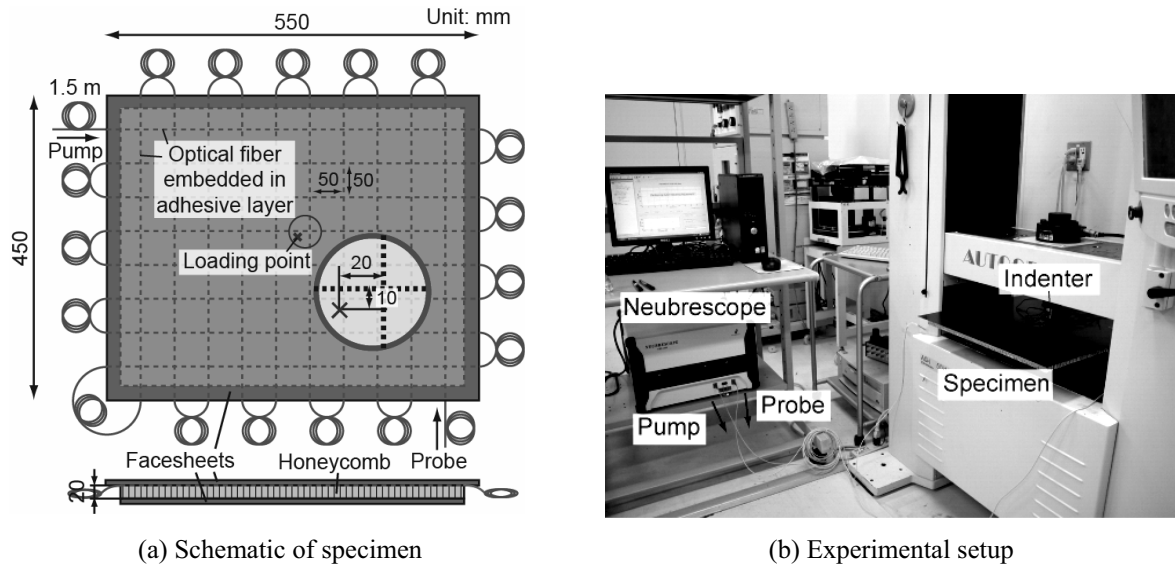(a) Schematic of specimen   (b) Experimental setup

Figure 10: Indentation damage detection test for system verification

4.2 Results

As the maximum indentation displacement increased, the residual dent became deeper and wider and, finally, a residual dent depth of 2.5 mm remained on the upper facesheet after the test of the maximum displacement 6.5 mm. Before the test, the BGS had almost uniform value of F_{-1dB} of 80 MHz in the whole specimen. However, after the damage was introduced, the non-uniform strain was generated along the facesheet dent and thus BGS began to broaden from the vicinity of the loading point. Figure 11 gives the spectra obtained at the nearest measurement point to the loading point. The intensity of each spectrum is normalized by the intensity of the highest component. As the damage became larger, the width of the BGS gradually increased and finally became more than half time of that before the test. The distributions of F_{-1dB} after each test are presented in Figure 12. Each line presents the F_{-1dB} distribution along each line of the embedded optical fiber. Only the vicinity of the loading point is shown, since the other area did not mark significant changes in the width of the BGS. After the test of maximum indentation displacement of 1 mm (residual dent depth: 0.3 mm, Figure 12 (a)), only a line III of the optical fiber, which was the nearest to the loading point, responded and F_{-1dB} increased near the damaged area due to the non-uniform strain along the dent in the facesheet. As the damage became large, both of a number of the responding lines and value of F_{-1dB} near the damaged area increased. After the test of maximum indentation displacement of 3 mm (residual dent depth: 1.1 mm, Figure 12 (b)), two lines, i.e. III and VI, reacted significantly and one line of VII responded slightly. It is interesting to note that VI and VII were 20 and 30 mm away from the loading point, respectively. Even though a difference between the values of the distance from each line to the loading point was only 10 mm, the responses of both lines differed vastly, confirming quite high sensitivity and resolution of the proposed damage detection system. After the test of maximum indentation displacement of 6.5 mm (residual dent depth: 2.5 mm, Figure 12 (c)), all the four lines
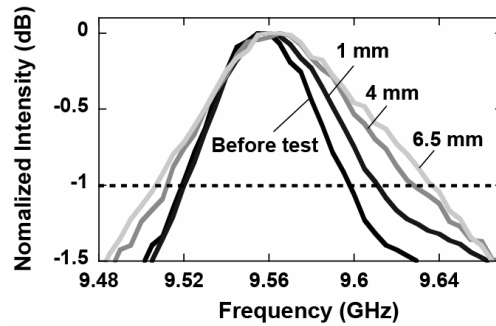
Figure 11: BGS measured at the nearest measure point to loading point after each test

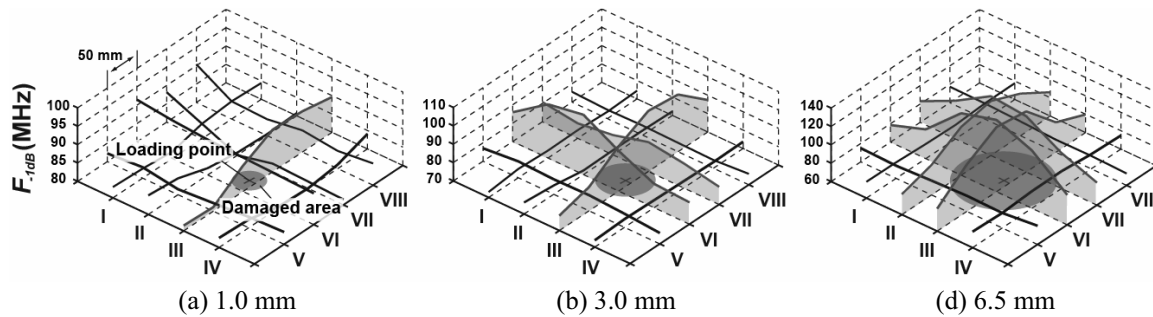(a) 1.0 mm (b) 3.0 mm (d) 6.5 mm

Figure 12: Distribution of F_{-1dB} in the vicinity of loading point after each test

surrounding the loading point, i.e. II, III, VI, and VII, pronouncedly responded.

It was clearly demonstrated that the proposed damage detection system using the width of the BGS can detect an occurrence of the BVID with a high sensitivity and, moreover, roughly estimate damage location and size. In the near future, by addressing an optimum sensor network form and a proper damage detection algorithm, more effective and robust quantitative impact damage detection system will be developed. Extension of the system to impact damage detection in foam cored sandwich structures is also planned.

5 CONCLUSIONS

Impact damage detection system using the PPP-BOTDA sensing system was proposed and validated. The specific response of the PPP-BOTDA to the non-uniform strain along the optical fiber was employed to detect non-uniform strain distribution along the residual facesheet dent induced in the damaged area. The proposed system could detect BVID with a high sensitivity and, moreover, roughly estimate the damage location and size.

REFERENCES

[1] D. Zenkert (ed.), *The Handbook of Sandwich Construction*, EMAS Publishing, (1997).
[2] J.R.Vinson, *The Behavior of Sandwich Structures of Isotropic and Composite Materials*,

Technomic Publishing Company, (1999).

[3] A.S. Herrmann, P.C. Zahlen and I. Zuardy, "Sandwich Structures Technology in Commercial Aviation Present Applications and Future Trends", *Proceedings of the 7th International Conference on Sandwich Structures (ICSS-7)*, Aalborg, 13-26 (2005).

[4] T.S. Gates, X. Su, F. Abdi, G.M. Odegard and H.M. Herring, "Facesheet delamination of composite sandwich materials at cryogenic temperatures", *Composites Science and Technology*, 66(14), 2423-2435 (2006).

[5] P. Feraboli, "Damage Resistance Characteristics of Thick-Core Honeycomb Composite Panels", *Proceedings of 47th AIAA/ASME/ASCE/AHS/ASC Structures, Structural Dynamics, and Materials Conference*, AIAA 2006-2169, (2006).

[6] S. Abrate, "Localized impact on sandwich structures with laminated facings", *Applied Mechanics Reviews*, 50(2), 69-82 (1997).

[7] F. Edgren, L.E. Asp and P.H. Bull, "Compressive failure of impacted NCF composite sandwich panels - characterisation of the failure process", *Journal of Composite Materials*, 38(6), 495-514 (2004).

[8] J.S. Tomblin, K.S. Raju, J. Liew, B.L. Smith. "Impact damage characterization and damage tolerance of composite sandwich airframe structures", *Final Report, DOT/FAA/AR-00/49*, (2001).

[9] S. Minakuchi, Y. Okabe, and N. Takeda, ""Segment-wise model" for theoretical simulation of barely visible indentation damage in composite sandwich beams: Part I - Formulation", *Composites Part A: Applied Science and Manufacturing*, 39(1), 133-144 (2008).

[10] S. Minakuchi, Y. Okabe, and N. Takeda, ""Segment-wise model" for theoretical simulation of barely visible indentation damage in composite sandwich beams: Part II - Experimental verification and discussion", *Composites Part A: Applied Science and Manufacturing*, 38(12), 2443-2450 (2007).

[11] K. Kishida, C.-H. Li and K. Nishiguchi, "Pulse pre-pump method for cm-order spatial resolution of BOTDA", *Proceeding of the SPIE*, 5855, 559-562 (2005).

[12] A. Guzik, Y. Yamauchi, K. Kishida and C.-H. Li, "The robust pipe thinning detection method using high precision distributed fiber sensing", *Proceeding of Asia-pacific Workshop on Structural Health Monitoring*, Yokohama, Japan, 24, 2006.

[13] S. Minakuchi, Y. Okabe, and N. Takeda, "Barely visible impact damage detection in sandwich structures using non-uniform strain along optical fiber sensors", *Proceedings of the 16th International Conference on Composite Materials*, Kyoto, MoIA2-03 in CD-ROM (2007).

[14] S. Minakuchi, Y. Okabe and N. Takeda, "Real-time detection of debonding between honeycomb core and facesheet using a small-diameter FBG sensor embedded in adhesive layer", *Journal of Sandwich Structures and Materials*, 9(1), 9-33 (2007).

[15] N. Takeda, S. Minakuchi and Y. Okabe, "Smart composite sandwich structures for future aerospace application -damage detection and suppression-: a review", *Journal of Solid Mechanics and Materials Engineering*, 1(1), 3-17 (2007).

AIRCRAFT SANDWICH STRUCTURES WITH FOLDED CORE UNDER IMPACT LOAD

S. Heimbs[*], P. Middendorf[*], C. Hampf[†], F. Hähnel[†], K. Wolf[†]

[*] EADS
Innovation Works Germany
81663 Munich, Germany
e-mail: sebastian.heimbs@eads.net, web page: http://www.eads.net

[†] Institut für Luft- und Raumfahrttechnik
Technische Universität Dresden
Marschnerstraße 32, 01307 Dresden, Germany
web page: http://www.tu-dresden.de/mwilr

Key words: Sandwich structures, Folded core, Low velocity impact, Dynamic simulations.

Summary. *Folded structures made of composite materials have gained interest in the aerospace industry as a promising sandwich core structure. In this paper the mechanical behaviour of such a sandwich structure with a folded core made of carbon fibre-reinforced plastic under low velocity impact loads is investigated experimentally and numerically. At first the core properties under compressive and transverse shear loads are characterised building a basis for the validation of the simulation models. Low velocity impact tests under various energy levels are described with respect to the evaluated damage of face and core and are finally simulated with LS-DYNA. These simulations were used to investigate the influence of different parameters on the impact behaviour numerically.*

1 INTRODUCTION

Sandwich structures with composite faces and a cellular core are known for their outstanding weight-specific stiffness and strength properties and have therefore been used in aircraft structures for many decades. Examples are aerodynamic fairings (belly fairing, leading and trailing edge fairings) or control surfaces (rudders, ailerons) [1]. Since weight reduction is a main driver in aircraft design, the application of sandwich structures is constantly increasing. Even concepts for the utilisation of sandwich structures in the primary structure, i.e. the aircraft fuselage, have been developed in the past for large airliners [2]-[4] and have already been realised in smaller business jets [5]-[8]. One main issue is to identify an adequate sandwich core material for these purposes. Nowadays, Nomex® honeycomb cores are prevalently used in aircraft sandwich structures because of their favourable mechanical and fire safety properties. But these closed honeycomb cells can lead to an inclusion and accumulation of condensation water, which increases weight and reduces the properties [8]-[10]. Therefore, folded sandwich core structures have gained interest of the aerospace industry in the past years as an alternative allowing for a ventilation through drainage

channels and also for efficient fabrication processes [11]-[14]. Such folded core structures can be manufactured from a variety of materials and in unlimited geometries and can therefore be tailored for a specific application.

One known shortcoming of sandwich structures is their low resistance against impact loads acting normal to the sandwich plane, which is a result of the typically very thin faces and the low resistance of the core against local compressive loads. Impact scenarios affecting aircraft structures range from low velocity impacts (e.g. tool drop, hail on ground) over intermediate velocity impacts (e.g. runway debris, tire fragments) to high velocity impacts (e.g. bird strike, hail in flight, engine parts).

This paper presents an experimental and numerical investigation of the low velocity impact behaviour of a composite sandwich structure with a folded core made of carbon fibre-reinforced plastic (CFRP). First the core and sandwich structure are characterised by their material, geometry and manufacturing process. Then the experimental test series for the determination of the mechanical properties of the core and the impact behaviour under various energy levels is presented. Based on these data numerical simulation models of the sandwich structure were generated and dynamic impact simulations with LS-DYNA were conducted to gain further insights into the stress states during impact and to perform various parameter studies.

2 MATERIALS AND MANUFACTURING

The focus of this paper is a composite sandwich structure made of the following constituents:

The faces were fabricated from the aerospace grade carbon fibre/epoxy (CF/EP) prepreg Cytec 977-2/HTS in a 16-ply quasi-isotropic lay-up of $[45°/90°/-45°/0°/45°/90°/-45°/0°]_S$ and were cured in an autoclave. The resulting face thickness was 2 mm.

The folded core structure is also made of CF/EP and was manufactured by the Kazan State Technical University/Russia (Figure 1).
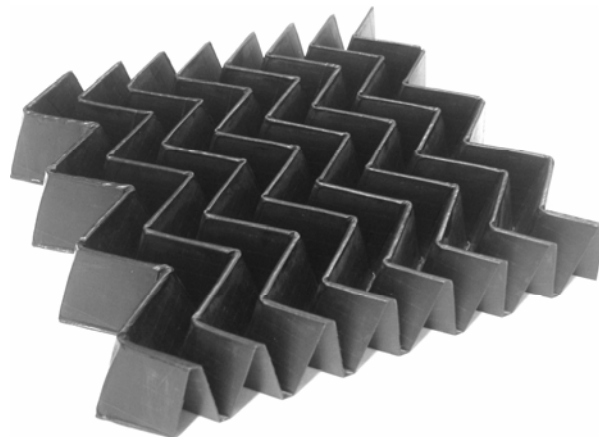

Figure 1: CFRP folded core structure

In this case a 3-ply [0°/90°/0°] lay-up of unidirectional prepreg layers was used as the cell wall material of the folded core (Figure 2). The manufacturing process is based on the forming of the flat laminate between two matrices [15]. But in contrast to deep drawing, the matrices are transformable so that the prepreg material is folded without being elongated. After folding it is cured in an autoclave. The folding pattern is a simple zigzag shape, based on the unit cell geometry in Figure 3. The top folding edge consists more of a plateau than a sharp edge resulting from the matrices, which reduces the curvature and the extent of potentially broken fibres. The total density of the CFRP folded core was 102 kg/m³.
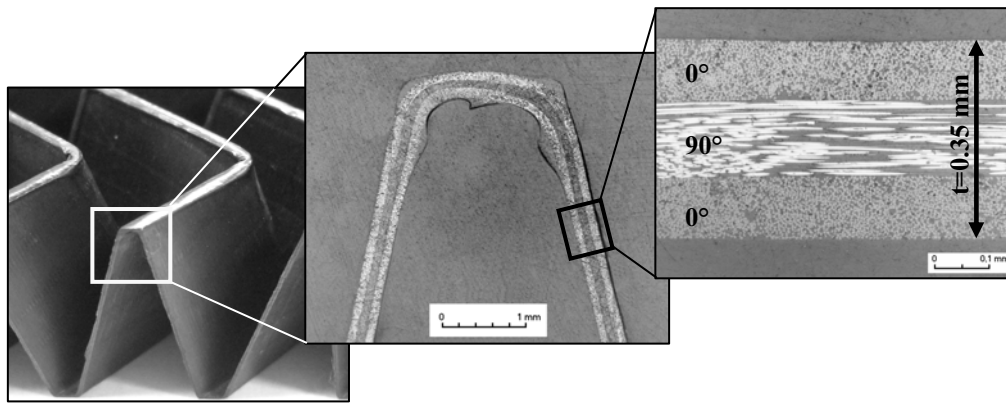
Figure 2: Micrographs of top folding edge and CFRP cell wall laminate
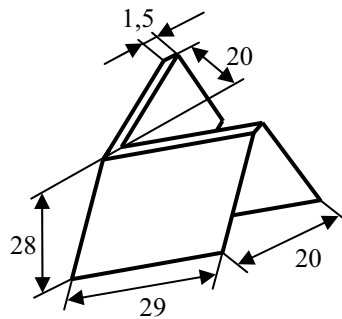
Figure 3: Unit cell of CFRP folded core with measures in mm

The faces were bonded onto the folded core using the epoxy-based structural adhesive Epibond 1590 A/B. In this manner the sandwich structure was fabricated on a hot press during 4 h at 75°C and 3 bar.

3   EXPERIMENTS

The experimental part is divided into the characterisation of the CFRP folded core's mechanical properties under compressive and transverse shear loads, which gives important data for the validation of the numerical model, and the low velocity impact testing.

3.1 Mechanical properties

Both for the compression tests according to DIN 53291 and the transverse shear tests according to DIN 53294 sandwich specimens of 150 mm x 150 mm and an Instron universal testing machine with a laser-controlled displacement measurement system were used (Figure 4).
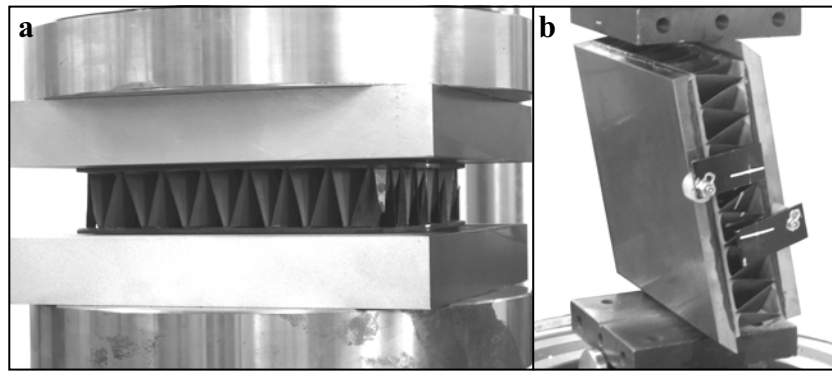

Figure 4: Compression (a) and transverse shear testing (b) of CFRP folded core

The compressive behaviour was dominated by a cell wall fracture in the middle of the specimens after initial buckling. The angular geometry leads to a loss of contact and load transfer between the upper and lower side resulting in a drop of the stress level to low values. As the compression continues more cell walls come into contact and are crushed at the opposite side leading to the progressive curve up to the densification region (Figure 5).

In addition to quasi-static testing, dynamic compression tests at 300 s^{-1} and 500 s^{-1} were conducted on a drop tower facility to investigate the rate-dependency of the compressive behaviour [16]. However, no strain rate effect occurred, i.e. the stress level was not influenced by the loading rate. This could be expected since the crushing stress of CFRP at these strain rates is regarded as not or at most marginally rate-dependent [17].
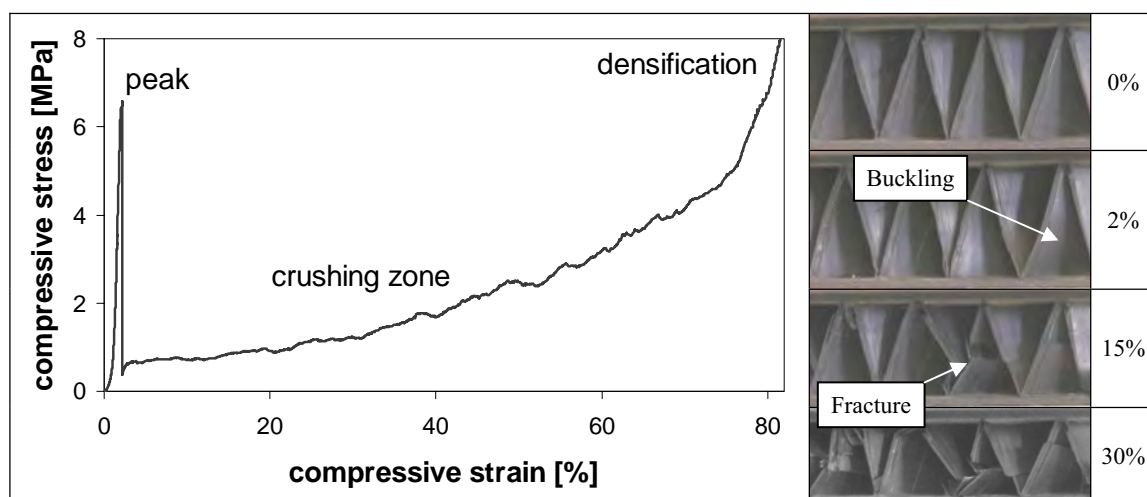

Figure 5: Compressive stress diagram and cell wall behaviour of CFRP folded core (with percentage strain)

The shear testing turned out to be limited by the high strength of the CFRP structure leading to a debonding between core and loading plates at some point of the experiment. However, besides the shear stiffness the results of these tests give additional information on the bonding quality. A closer look at the surface shows that the separation is driven by a delamination of the outer CFRP layer of the folded core (Figure 6). Local cohesive failure of the bonding material can be found as well, but no adhesive failure occurred.
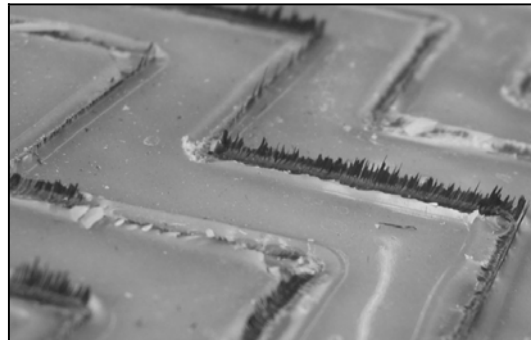
Figure 6: Surface of the debonded sandwich specimen

The CFRP laminate for the face layers is a well-known aerospace standard material and experimentally determined mechanical properties were available. Therefore, no additional testing on the face material was performed in the framework of this study.

3.2 Low velocity impact tests

The low velocity impact tests were performed on a Dynatup 8250 drop tower with a spherical impactor of 1 in. (25.4 mm) diameter and a mass of 1.15 kg. The sandwich plate of 300 mm x 300 mm used for the impact testing was fixed on a solid support (Figure 7). With the zigzag pattern marked on the top surface a specific impact location on the folded core cell walls or in-between could be targeted. In this study all impacts were uniformly located in the middle of a cell wall edge. Impact energies of 5 J, 10 J, 20 J, 30 J, 50 J and 75 J were tested by increasing the drop height, respectively.
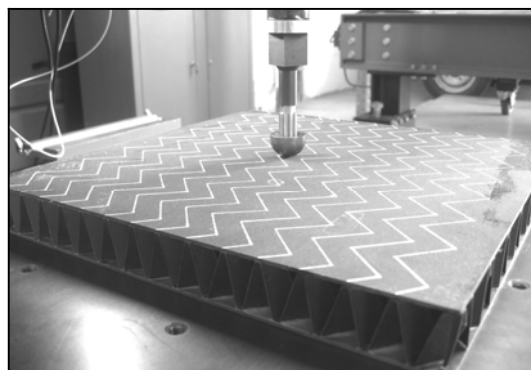

Figure 7: Impact testing on a drop tower facility

The impact damage caused in the upper CFRP face was evaluated using ultrasonic C-scan inspection as a non-destructive testing method. The core failure was analysed by cutting cross-sections through the impact point.

Figure 8 gives an overview of these results. The C-scan inspection proved delaminations between multiple layers of the upper face laminate to occur already for the lowest energy level tested. The failure mechanism known from impact studies on thin monolithic laminates, where matrix cracks are initiated at the back side of the laminate due to bending and progress through delaminations to the upper layers [18], seems to be valid for this case as well. Interestingly, the propagation of these delaminations is limited by the neighbouring cell edge attachments leading to rectangular delamination patterns for higher energies and a very localised damage.

Also a damage of the folded core can be figured out for the lowest energy level of 5 J. The cell directly under the impact point is crushed in the upper part, while the neighbouring cells seem to be undamaged. At 50 J about one third of the cell is crushed, at 75 J the cell is crushed almost completely.

The corresponding impact force plots are shown in Figure 9. The drops in the curve indicate intra- and interlaminar failure taking place inside the laminates. It can be seen that the maximum load level for energies higher than 10 J is almost the same and does not exceed 8 kN. The elastic energy of the system, leading to a rebound of the impactor, was almost constant with approx. 5 J for all energy levels (3 J for the 5 J impact). The rest of the initial kinetic energy was absorbed by the sandwich panel by creating fracture surfaces.
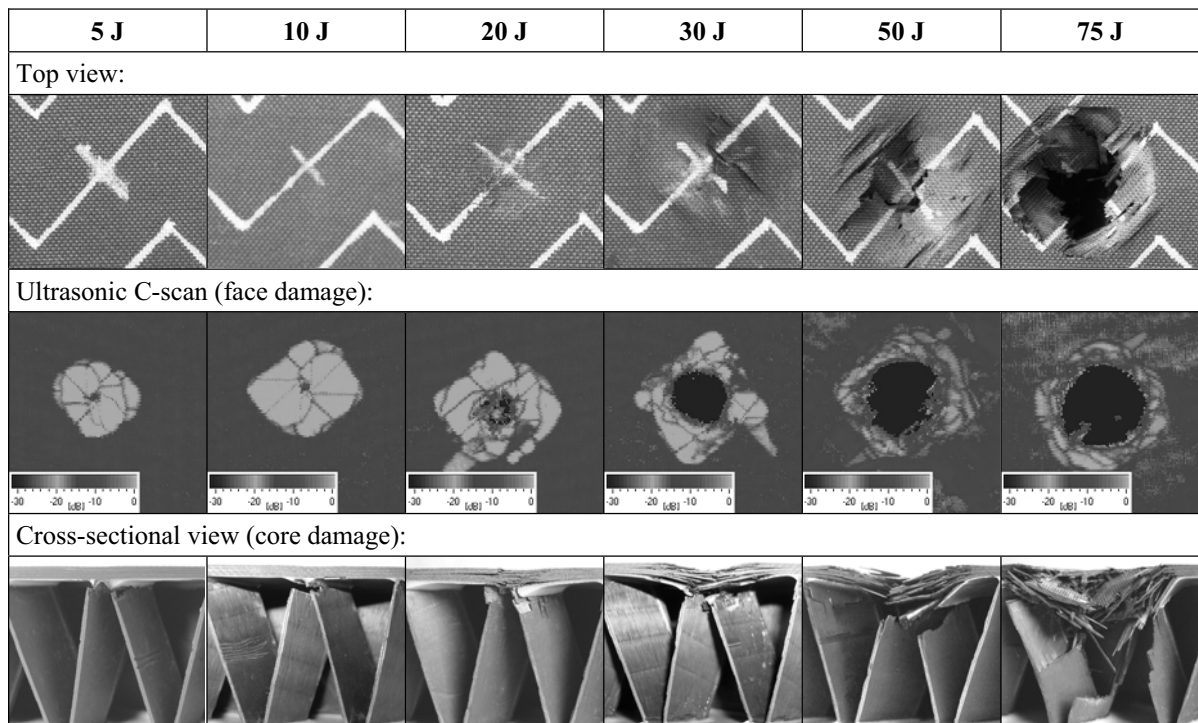

Figure 8: Damage evaluation results of low velocity impact tests
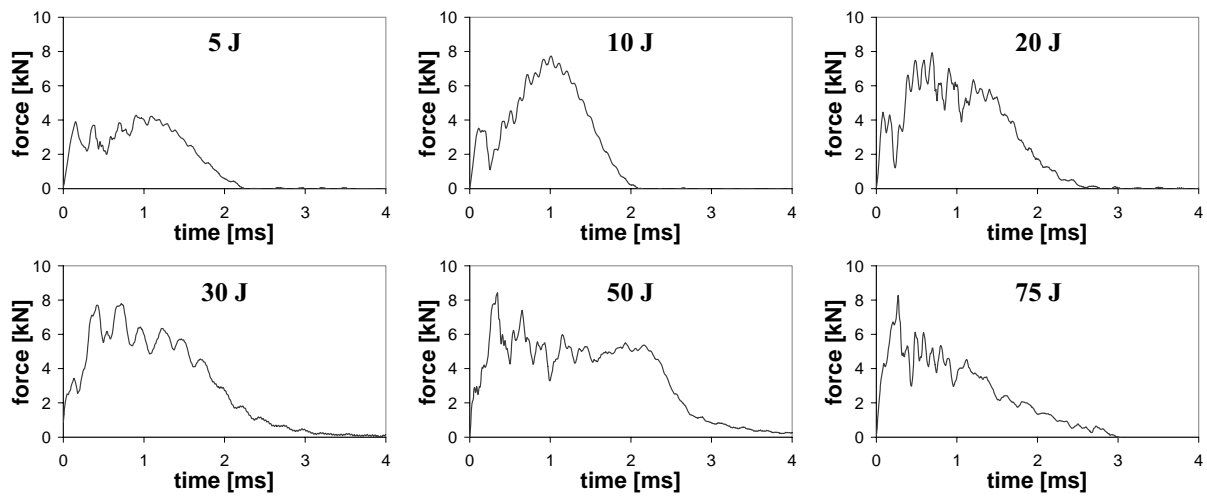
Figure 9: Impact force results of low velocity impact tests

4   NUMERICAL SIMULATION

Although various data can be recorded during an experiment and afterwards by destructive or non-destructive damage evaluation methods, finite element (FE) simulations offer the opportunity of more detailed analyses of failure initiation and propagation or stress levels during loading. Furthermore, parameter studies can be performed numerically allowing for an efficient investigation of different factors influencing the structural behaviour. Therefore, a numerical analysis of the low velocity impact tests using the commercial explicit FE- software LS-DYNA was conducted.

4.1 Model development

The model generation was done on a parametric basis reducing the pre-processing work and offering an efficient way of investigating different folded core geometries [19]. Both for the faces and the folded core's cell walls bilinear shell elements with uniformly reduced integration and the composite material model MAT54 in LS-DYNA were used. This constitutive law is based on orthotropic linear elastic behaviour and brittle failure with failure criteria by Chang/Chang. The connection of face and core elements was done by a tied contact formulation without failure. The impactor was modelled as a spherical rigid body.

In order to separately validate the folded core model, simulations of the compression and shear tests were performed (Figure 10). In this study the influence of mesh size was also investigated and found out to be significant. Furthermore, the compressive stiffness was over-predicted in the FE-model, which could be explained by a visible distortion of the laminate's fibre orientation resulting from the manufacturing process, i.e. the 0°-layers were not oriented in parallel to the cell wall edges but distorted about 7°. Such and other imperfections, which normally occur in all cellular structures, influence the mechanical behaviour and have to be accounted for in a meso-scale FE-model [19]. The model was calibrated accordingly.
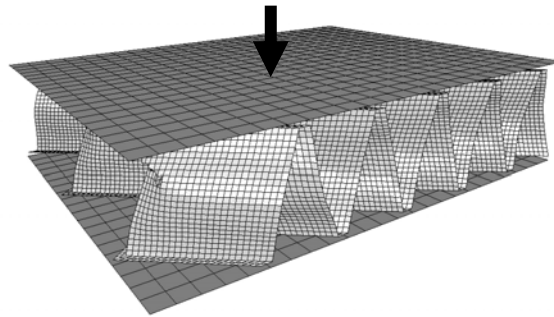
Figure 10: Model validation of folded core structure by compression test simulation

Shell elements were used for the 16-ply sandwich face laminates. However, these 2D-elements are not able to represent delaminations as an interlaminar failure mode, although the experiments showed that these delaminations play a predominant role for the energy absorption. One solution is the utilisation of a number of separate shell elements in thickness direction connected by delamination contact laws in-between [20]. But to limit the modelling and computational effort, in this study a simplification was investigated. The energy absorbed by delamination was to be represented by an alternative mechanism in the model, as it was done in previous studies before [21], [22]. In this case, instead of a brittle failure the stress level of the face material was kept at a constant level for compression and tension in matrix direction and compression in fibre direction. A complete failure could only occur under tensile fibre rupture.

4.2 Impact simulations

The impact simulations were conducted for all tested energy levels and the results were compared to the experimental data (Figure 11). In general, the force and energy curves showed good consistency (Figure 12) and the local core failure was comparable to the cross-sectional views in Figure 8. However, the faces in the models turned out to be slightly too stiff, which led to an under-prediction of the indentation depth, especially for higher energies. This is ascribed to the lack of delamination modelling, since the interlaminar failure reduces significantly the transverse shear strength of the laminate and allows for larger deformations under transverse loads in reality.

The evaluation of the simulation results approved the theory that the impact loading is limited to a very local area of the sandwich structure. The impacted folded core cell as well as the neighbouring cells on both sides are stressed, any further core cells and the respective face areas are unstressed, even for the highest energies (Figure 11). This is the result of the very stiff structure. The core inhibits bending deformations of the upper face and only crushes locally. Only at these areas of lost support the face is bended and damaged consequentially.

The predominant failure mode of the upper face laminate is matrix tensile failure initiated in and propagating from the bottom ply, which is the tensile side under bending load. When reducing the impact velocity in the model, i.e. the corresponding energy level, to evaluate the energy at damage initiation, it was found out that damage in the face laminate is initiated at a much lower energy level as it is in the core structure.
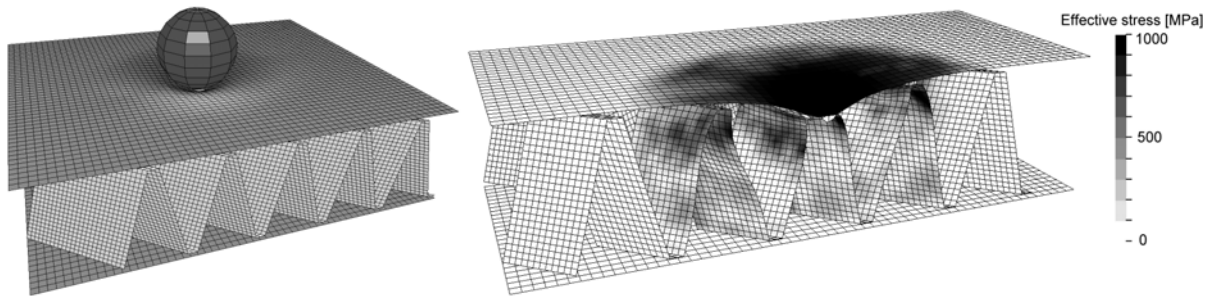
Figure 11: Impact simulation (left) and cross-sectional view of effective stresses (right)
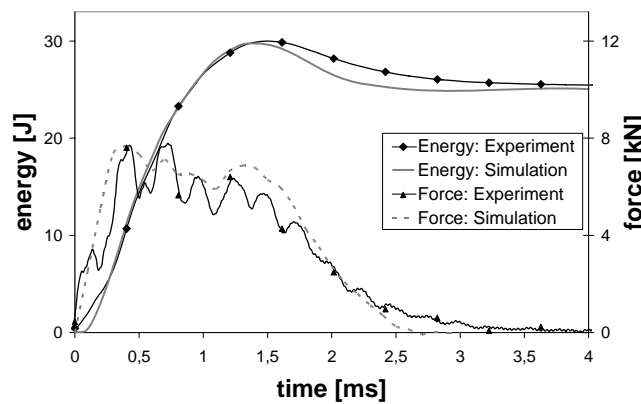(here: 30 J impact, moment of maximum indentation)

Figure 12: Force and energy plots of experiment and simulation (here: 30 J impact)

4.3 Parameter studies

The simulation model was used - in consideration of its known simplifications - for several parameter studies to investigate e.g. the influence of the clamping conditions, the influence of the impact location and the influence of the folded core geometry.

When the sandwich plate is supported only at the edges instead of the whole surface of the lower face, a larger bending deformation of the complete structure under impact load is permitted. On the one hand, the sum of elastic deformation of the structure is higher, and therefore the transformation of the kinetic energy into internal fracture is lower. On the other hand, in this case not only the upper but also the lower face laminate is damaged.

The impact location only has a minor influence on the simulation results. Besides impacting the middle of the folded core cell edges as before, the corner of two cell edges as well as the space between two cell walls were impacted (Figure 13a). In the latter case the indentation depth was marginally higher because less support of the core against local bending is present.

In the third study the folded core geometry was modified in the model by changing the zigzag measures while maintaining the same global density of the core structure. The cell space between two cells was lower for the modified geometry (Figure 13b). Therefore, the stressed area was even more localised than in the former case.
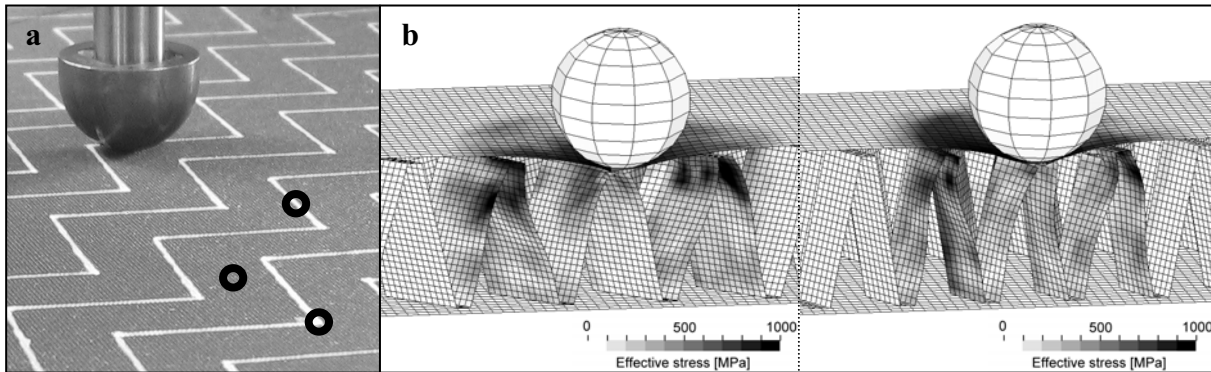
Figure 13: Parameter studies: Influence of impact location (a) and folded core geometry (b)
(here: 20 J impact, cross-sectional view of effective stresses, moment of maximum indentation)

5   CONCLUSIONS

The mechanical behaviour of CFRP sandwich structures with folded core under low velocity impact loads was analysed experimentally and numerically. Preliminary compression and shear tests showed high stiffness and strength values leading to a very localised failure under impact loads, since a global bending deformation of the impacted upper face layer is inhibited. Additionally, the delamination propagation in the face laminate is limited by the adjacent core cell connections. Simulation models of the sandwich structure with folded core based on the composite material model in LS-DYNA were generated and calibrated. Despite the simplification with respect to the treatment of delaminations, simulation results with an acceptable consistency could be obtained permitting the utilisation of these models for subsequent numerical parameter studies regarding impact location, boundary conditions or folded core geometry. While such composite sandwich structures are characterised by a very complex failure behaviour, numerical simulations showed the ability to be a useful tool to get a deeper insight into the stress distribution in the structure and the damage initiation. Such simulations can also be used for an enhancement of the sandwich structure's impact behaviour with respect to core geometry or material.

Potential of improvement for further studies is seen in the incorporation of delamination contacts or cohesive interface elements to better cover the energy absorption of interlaminar failure. Furthermore, the extension of experimental test series will allow for a comparison with other folded core materials or other established sandwich core structures also with respect to their residual strength.

ACKNOWLEDGEMENTS

REFERENCES

[1] A.S. Herrmann, P.C. Zahlen and I. Zuardy, "Sandwich structures technology in commercial aviation", In: O.T. Thomsen et al. (eds.), *Sandwich Structures 7: Advancing with Sandwich Structures and Materials*, Proceedings of the 7th International Conference on Sandwich Structures, Aalborg, Danmark, 29-31 August 2005, pp. 13-26, (2005).

[2] R. Kehrle and M. Kolax, "Sandwich structures for advanced next generation fuselage concepts", *SAMPE Europe Technical Conference*, Toulouse, France, 13-14 September 2006, pp. 11-16 (2006).

[3] M. Kolax, "Concept and technology: advanced composite fuselage structures", *JEC Composites*, 10(6/7), 31-33 (2004).

[4] B.Y. Kolesnikov and L. Herbeck, "Carbon fiber composite airplane fuselage: concept and analysis", *ILA International Conference*, Berlin, Germany, 11–12 May 2004.

[5] M.J.L. van Tooren, *Sandwich Fuselage Design*, Delft University Press (1998).

[6] J. Tomblin, T. Lacy, B. Smith, S. Hooper, A. Vizzini and S. Lee, "Review of damage tolerance for composite sandwich airframe structures", Report DOT/FAA/AR-99/49, U.S. Department of Transportation, Washington D.C., USA (1999).

[7] R. Abbott, "Damage tolerance evaluation of composite honeycomb structures", *43rd Int. SAMPE Symposium*, Anaheim, CA, USA, 31 May-4 June 1998, pp. 376-386 (1998).

[8] R. Wong, "Sandwich construction in the starship", *37th International SAMPE Symposium and Exhibition*, Anaheim, CA, USA, 9-12 March 1992, pp. 186-197 (1992).

[9] E.F. Schiantarelli, "Core composites in Swissair aircraft", *1st Core Conference*, Zurich, Switzerland, 20-21 October 1988.

[10] V. Vavilov, A. Klimov, D. Nesteruk, V. Shiryaev, "Detecting water in aviation honeycomb structures by using transient IR thermographic NDT", *Proceedings of the SPIE - The International Society for Optical Engineering*, Vol. 5073, ThermoSense XXV Silver Anniversary Meeting, Orlando, FL, USA, 22-24 April 2003, pp. 345-355 (2003).

[11] D. Hachenberg, C. Mudra and M. Nguyen, "Folded structures - an alternative core material for future sandwich concepts", *DGLR Conference*, Munich, Germany 17-21 November 2003, pp. 165-174 (2003).

[12] K. Drechsler and R. Kehrle, "Manufacturing of folded core-structures for technical applications", *25th International SAMPE Europe Conference*, Paris, France, 30 March-1 April 2004, pp. 508-513 (2004).

[13] I.M. Zakirov and K.A. Alexeev, "New folded structures for sandwich panels", *51st International SAMPE Symposium*, Long Beach, CA, USA, 30 April-4 May 2006.

[14] E.A. Elsayed and B.B. Basily, "A continuous folding process for sheet materials", *Int. J. Mater. Prod. Technol.*, 21(1/2/3), 217-238 (2004).

[15] V.I. Khaliulin and I.V. Dvoyeglazov, "On technological problems of fabrication of relief designs by isometric transformations of thin sheet", *Trans. Nanjing Univ. Aeronaut. Astronaut.*, 18(1), 11-16 (2001).

[16] S. Heimbs, *Sandwichstrukturen mit Wabenkern: Experimentelle und numerische Untersuchung des Schädigungsverhaltens unter statischer und kurzzeitdynamischer Belastung*, Ph.D. thesis, Kaiserslautern University of Technology, Germany (2008).

[17] J.F. Newill and J.R. Vinson, "Some high strain rate effects on composite materials", *9th International Conference on Composite Materials*, ICCM-9, Madrid, Spain, 12-16 July 1993, Part 5, pp. 269-277 (1993).

[18] S. Abrate, *Impact on Composite Structures*, Cambridge University Press (1998).

[19] S. Heimbs, P. Middendorf, S. Kilchert, A.F. Johnson and M. Maier, "Numerical simulation of advanced folded core materials for structural sandwich applications", *CEAS European Air and Space Conference*, Berlin, Germany, 10-13 Sept. 2007, pp. 2889-2896 (2007).

[20] R. Borg, *Simulation of Delamination Initiation and Growth in Fiber Composite Laminates*, Ph.D. thesis, Linköping University, Sweden (2002).

[21] K.M. Mikkor, R.S. Thomson, I. Herszberg, T. Weller and A.P. Mouritz, "Finite element modelling of impact on preloaded composite panels", *Compos. Struct.*, 75, 501-513 (2006).

[22] M.Q. Nguyen, S.S Jacombs, R.S. Thomson, D. Hachenberg and M.L. Scott, "Simulation of impact on sandwich structures", *Compos. Struct.*, 67, 217-227 (2005).

LOW VELOCITY IMPACT RESPONSE OF SANDWICH STRUCTURES WITH TRANSVERSELY FLEXIBLE CORE AND FML FACE SHEETS

S.Mohammad R. Khalili [*] **, Keramat Malekzadeh** [†]

[*] Professor, Centre of Excellence for Research in Advanced Materials and Structures,
Faculty of Mechanical Engineering, K.N. Toosi University of Technology,
Pardis St., MolaSadra Ave., Vanak Sq., Tehran, Iran
e-mail: smrkhalili2005@gmail.com

[†] Assistant Professor, Department of Mechanical Engineering, Malek Ashtar University,
Karaj Makhsous Rd., Tehran, Iran
e-mail: kmalekzadeh@mut.ac.ir

Key words: Sandwich panels, Low-velocity impact, Fiber metal laminate.

Summary. *Fiber–Metal Laminates (FMLs) are high-performance hybrid structures based on alternating stacked arrangements of fiber-reinforced polymer-matrix composite plies and metal alloy layers. In this paper, the effect of material and thickness of FMLs face-sheets and the core density on low-velocity impact response of composite sandwich panels are investigated. Impacts are assumed to occur normally over the top face sheet in arbitrary location. The FMLs face sheets are considered as ordinary thin or thick plates. The staking sequences of laminate in the top and the bottom face sheets are assumed symmetric or antisymmetric. The core is assumed to behave in a linear elastic manner with small deformations, although its height may change and its transverse plane takes a nonlinear shape after deformation. The interaction between the impactor and the panel is modeled with the help of a new system having three degree of freedom consisting of spring-mass-damper-dashpot (SMDD).The dynamic response of the panel is based on improved higher order sandwich plate theory (IHSAPT). Numerical impact results on sandwich panels with Fiber–Metal Laminated face sheets that hitherto not reported in the literature have been presented in this paper. Effect of the aluminum 2024-T3 alloy layers on dynamic response of composite sandwich panel is studied.*

1 INTRODUCTION

About 18 years ago a new class of materials, made of alternating metallic and fiber-reinforced plastic (FRP) layers, generally known as 'Fiber-Metal Laminates' (FMLs) was proposed [1]. The basic scope in developing FMLs was to combine the good fatigue behavior of FRPs with the excellent impact resistance of matals. The variant with aramid fibres is usually called ARALL, while GLARE incorporates glass fibres. Although extensive research has been dedicated to the impact behavior of composite laminates in general [2, 3], the work on sandwich structures is somewhat limited. Anderson [4] describes an investigation of single-degrees-of-freedom models for large mass impact on composite sandwich laminates. Malekzadeh et al. [5] proposed a new equivalent three-degree-of-freedom (TDOF) spring-mass-damper-dashpot (SMDD) model to predict the low-velocity impact response of composite sandwich panels with transversely flexible core. In this paper, an improved higher-order sandwich plate theory (IHSAPT) [6] has been used only for modeling the sandwich panel (without the impactor), whereas the analytical force function [5] can be implemented to handle the contact force between the impactor and the panel.

2 FORMULATION OF PROBLEM

The rectangular sandwich flat panel studied in this paper is composed of two FMLs composite laminated and symmetric face sheets and a core of thickness h_c. The panel is assumed to have a length a, width b and a total thickness $h,$ as shown in Figure 1 (Ref. [6]), where coordinates and sign conventions are also shown. The assumptions used in the present analysis are those encountered in linear elastic small deformation theories [5]. The contact loads $q_i (i = t, b)$ are assumed to be represented by a double Fourier series expansion and are separable into functions of time and position.

The improved high order sandwich plate theory was presented by Malekzadeh et al. [6] using the principle of virtual work. Then the governing equations and the boundary conditions are derived using Hamilton's principle which requires that:

$$\delta \int_{t_1}^{t_2} \left[U_e + V_e + W^{nc} - T_e \right] dt = 0 \tag{1}$$

where T_e, U_e , V_e and W^{nc} are respectively, the kinetic, internal potential, external energies and the structural damped energy and δ is the variational operator. The variable t represents time and the limit of variation is taken over the time interval $t_2 - t_1$.

The impact solution for a rectangular plate with simply-supported boundary conditions at the top and bottom face sheets is assumed to be in the following form:

$$
\begin{bmatrix}
u_{0j}(x,y,t) \\
v_{0j}(x,y,t) \\
w_{0j}(x,y,t) \\
\psi_{xj}(x,y,t) \\
\psi_{yj}(x,y,t) \\
\tau^c_{xz}(x,y,t) \\
\tau^c_{yz}(x,y,t)
\end{bmatrix}
= \sum_{m=1}^{\infty}\sum_{n=1}^{\infty}
\begin{bmatrix}
u_{0jmn}(t).\cos(\alpha_m x).\sin(\beta_n y) \\
v_{0jmn}(t).\sin(\alpha_m x).\cos(\beta_n y) \\
w_{0jmn}(t).\sin(\alpha_m x).\sin(\beta_n y) \\
A_{0jmn}(t).\cos(\alpha_m x).\sin(\beta_n y) \\
B_{0jmn}(t).\sin(\alpha_m x).\cos(\beta_n y) \\
T_{cxmn}(t).\cos(\alpha_m x).\sin(\beta_n y) \\
T_{cymn}(t).\sin(\alpha_m x).\cos(\beta_n y)
\end{bmatrix}
\tag{2}
$$

The above double Fourier series functions can satisfy some boundary conditions for a plate i.e., simply-supported on all edges. In equation (2) $u_{0jmn}, v_{0jmn}, w_{0jmn}, A_{0jmn}, B_{0jmn}, T_{cxmn}$ and T_{cymn} are time dependent unknown Fourier coefficients, m and n are respectively the half wave numbers in x and y directions. By applying the Galerkin's method, the governing equations are reduced to the following system of ordinary differential equations:

$$
[M]\{\ddot{\chi}\} + [C_e]\{\dot{\chi}\} + [K]\{\chi\} = \{Q\}
\tag{3}
$$

Therefore, the problem of impact on sandwich panel is reduces to the standard structural response equation. $[M]$ is the $(10mn)\times(10mn)$ square symmetric mass matrix, $[K]$ is the $(10mn)\times(10mn)$ square symmetric stiffness matrix and $\{Q\}$ is the $(10mn)\times 1$ vector of impact forces [6]. The interaction between the impactor and the panel is modeled with the help of a new system having three degree of freedom consisting of spring-mass-damper-dashpot (SMDD) (see Ref. [5]). Using an improved higher-order sandwich plate theory (IHSAPT) and a new equivalent three-degree-of-freedom (TDOF) spring-mass-damper-dashpot (SMDD) model, the problem of simultaneous double sides transverse low-velocity impacts on a composite sandwich panel have been studied in this paper.

The system damping is simulated by proportional viscous damping terms. Equation (3) can be readily solved with a suitable numerical integration procedure [6]. For the case of general dynamic analysis, the vector $\{\chi(t)\}_{[(10\times m\times n),1]}$ contains ten sets of time dependent unknowns: u_{0t} and v_{0t}, the in-plane deformations of the mid-plane of the top face sheet respectively in x and y directions; u_{0b} and v_{0b}, the in-plane deformations of the mid-plane of the bottom face sheet respectively in x and y directions; w_{0t} and w_{0b}, the vertical deflections of the top and the bottom face sheet respectively; ψ_x and ψ_y, the rotations of the normal section respectively about the y and x axes of each face sheet; and τ^c_{xz} and τ^c_{yz}, the shear stresses in the core in the vertical direction.

3 VERIFICATION AND DISCUSSIONS OF THE RESULTS

In order to validate the formulation of the problem, the results obtained from the present method are compared with those already reported by other authors in the literature.

3.1 Numerical accuracy of the solution procedure for sandwich panels subjected to low-velocity impact

Material data of the face sheets and the core, geometrical properties and types of the panels used for the large mass impact are shown in Table 1, 2 and 3. To validate the proposed TDOF model, the results are compared with experimental and numerical force histories of large mass impact obtained by Anderson [4] on sandwich panels with edge support to verify the accuracy of the procedure. The work described in Ref. [4] consists of an investigation of simplified dynamic models (SDOF) incorporating energy dissipation for the impact behavior of the foam and honeycomb sandwich laminates. The dynamic impact modeles examined consist of nonlinear spring elements in parallel or series with energy dissipating elements [4].

In the first four panels of Table 1, the face sheets were comprised of either $[0/90/0]$ or $[0_2/90_2/0_2]$ configurations, and are denoted throughout this study as 'thin' (three plies) and 'thick' (six plies) face sheets respectively. Also, for the rest four hybrid panels of Table 1, the top and bottom face sheets were comprised of $[A_2/90_2/A_2]$, $[A/90/A]$, $[A/0/90_2/0/A]$, $[A/-30/30_2/-30/A]$ and $[A/-45/45_2/-45/A]$. 'A' is denoted for 2024-T3 aluminum alloy lamina with thickness of 0.264 mm. All specimens incorporated a core of 12.7 mm thickness and overall dimensions of 76.2×76.2 mm. In this paper, the composite sandwich panels are simple supported (SSSS B.C.) around all four edges of the top and the bottom face sheets. The boundary conditions of the top and the bottom face sheets are independent. The mass of the impactor is 1.8 Kg and three different initial potential energy levels of impactor: 3.58J, 8.07J and 12.55J are considered. The tip of impacting mass had a diameter of 25.4 mm. Thickness of all layers in the face sheets of the panels are assumed identical and 0.264 mm.

Figure 2 shows the predicted and the experimental contact force histories of the panel at the center of top face sheet of the panel (panel type: 2 of Table 1) for the impact energy levels of 3.58J, 8.07J, and 12.55J. The contact force histories are compared with the numerical and experimental results of Ref. [4]. There are only small differences in the phase and the magnitude of contact force results obtained from the present analysis and the experimental results of Ref. [4]. Contact force history for simply supported panel obtained from the present method is in good agreement with that obtained from the experimental tests [4], while, the accuracy of numerical results of Ref. [4] based on single-degree-of-freedom spring mass model (SDOF) is smaller than the accuracy of the present analytical results. The theoretical predictions based on the proposed SM model, shown in Figure 2 indicate that the largest error in the maximum contact force obtained from the present analysis vis-a-vis the measured experimental values [4] correspond to the impactor energy (E=12.55J) is about 4.5%.

3.1.1 Effect of aluminum 2024-T3 alloy laminas in the face sheets on dynamic response of simply supported square symmetric/anti-symmetric sandwich panels with hybrid face sheets and high density foam core

Figure 3 shows that the aluminum 2024-T3 alloy laminas decrease the maximum contact force and increase the contact duration slightly. The thickness of panels 2, 5, 7, 8 are the

same and the face sheets of these panels are thick while, the face sheets of panel 6 are thin (see Table 1, 2 and 3). The panels 7 and 8 are anti-symmetric. The maximum contact force of the panel 6 is less than the maximum contact forces of the other panels. Because the face sheets of panel 2 do not have aluminum 2024-T3 alloy laminas and therefore, the face sheets are not hybrid laminate, the maximum contact force of panel 2 is more than the maximum contact force of other hybrid panels.

Figure 4 shows the effect of aluminum 2024-T3 alloy laminas in face sheets on central transverse deflection histories of top face sheets of the hybrid panels. Figure 4 shows that the aluminum 2024-T3 alloy laminas decrease the maximum central transverse deflection of the top face sheet and increase the contact duration. The maximum central transverse deflection of the panel 6 is more than the maximum central transverse deflection of the other panels. The face sheets of panel 6 are thin. Because the top face sheets of the anti-symmetric panels 7 and 8 are identical hybrid laminate, the maximum central transverse deflection of panels 7 and 8 are almost the same. Therefore, the effect of ply sequence and fiber orientation in the bottom face sheet of the panel on the maximum central transverse deflection of the top face sheet is small.

3.1.2 Effect of density of the core layer and thickness of face sheets on dynamic response of simply supported square sandwich panel

Figure 5 shows the effect of core density and thickness of the face sheets on contact force histories of the panels (Types 1 to 4) at the center of top face sheets of the panels. Figure shows that for panels of types 2 and 4 (see Table 1 and 2) in which the cores are high density but with different material and the face sheets are thick with identical material and thickness, the contact force histories are almost the same. Because the transverse stiffness of high density honeycomb core is more than the transverse stiffness of high density foam core, the maximum contact force for panel 4 is slightly more than for panel 2 while, the contact duration for panel 4 is slightly less than for the panel 2. Figure shows that with replacing of thick face-sheets with thin face-sheets of panel 2 (creating panel 1), the maximum contact force decreases, while the contact duration increases. Also, when both the thick face sheets and high density foam core of panel 2 are replaced with thin face sheets and low density honeycomb core respectively, (creating panel 3), the maximum contact force decreases very much, while the contact duration increases. Figure 5 shows increasing in contact force and decreasing in contact duration with increasing in density of the core layer of the panel. As can be seen in Figure 5, for the panels with identical geometrical properties (see Table 3), the effect of density of the core is more than the effect of thickness of the face sheets on the contact force and the contact duration.

Conclusions

A new equivalent three degrees-of-freedom (TDOF) spring-mass-damper (SMD) model and a new procedure in impact analysis had presented and used to predict the low-velocity impact response of composite sandwich panels with soft/stiff flexible core. The present results are in excellent agreement with the exact solutions and experimental test results. Since the impact occurs within a very short period of time, damping of the structure is usually neglected

in the low-velocity impact analysis and has small effects on impact response of sandwich panel. With increasing the impactor potential energy, vertical deflection of the panel are increased. The applicability of the present approach covers a wide range of impact problems, with varying material combinations, geometric features, side and site of the impact and boundary conditions. The effect of core density and face sheets thickness as well as the effect of aluminum 2024-T3 alloy layers on dynamic response of composite sandwich panel is studied.

REFERENCES

[1] L.B. Vogelesang, A. Vlot, "Development of fibre metal laminates for advanced aerospace structures", J Mater Process Tech., 103,1-5(2000).

[2] S. Abrate, *Impact on Composite structures*, Cambridge Univ. Press, (1998).

[3] M.R. Khalili, "Analysis of the dynamic response of large orthotropic elastic plates to transverse impact and its application to fiber reinforced plates", Ph.D. Thesis , Indian Institute of Technology, Delhi, (1992).

[4] A. Anderson Todd, "An investigation of SDOF models for large mass impact on sandwich composites", J. Composites: part B., 36 (2), 135-142 (2005).

[5] K. Malekzadeh, M.R. Khalili and R.K. Mittal, "Analytical prediction of low-velocity impact response of composite sandwich panels using new TDOF spring-mass-damper model", J. composite materials, 40 (18), 1671-1689 (2006).

[6] K. Malekzadeh, M.R. Khalili and R.K. Mittal, "Local and global damped vibrations of sandwich plates with a viscoelastic soft flexible core: An improved high-order approach", J. Sandwich Structures & Materials, 7 (5), 431-456 (2005).

Panel type	Face sheets types	Sandwich core types	Lay ups of the panels
1	Thin (top and bottom)	Foam (high density)	$[0/90/0/core/0/90/0]$
2	Thick (top and bottom)	Foam (high density)	$[0_2/90_2/0_2/core/0_2/90_2/0_2]$
3	Thin (top and bottom)	Honeycomb (low density)	$[0/90/0/core/0/90/0]$
4	Thick (top and bottom)	Honeycomb (high density)	$[0_2/90_2/0_2/core/0_2/90_2/0_2]$
5 (Hybrid)	Thick (top)- Thick (bottom)	Foam (high density)	$[A_2/90_2/A_2/core/A_2/90_2/A_2]$
6 (Hybrid)	Thin(top and bottom)	Foam (high density)	$[A/90/A/core/A/90/A]$
7 (Hybrid)	Thick (top)- Thick (bottom)	Foam (high density)	$[A/0/90_2/0/A/core/A/-30/30_2/-30/A]$
8(Hybrid)	Thick (top)- Thick (bottom)	Foam (high density)	$[A/0/90_2/0/A/core/A/-45/45_2/-45/A]$

Table 1: Types of sandwich panels

Properties	Face sheet	Foam core(high density)	Honeycomb core(high density)	Honeycomb core(low density)	Aluminum layer 2024-T3
$E_{11}(Gpa)$	54	0.18	0.000703	0.000352	71
$E_{22}(Gpa)$	54	0.18	0.000359	0.000179	71
$E_{33}(Gpa)$	4.84	0.18	0.4137	0.1379	71
$G_{12}(Gpa)$	3.16	0.07	0.000883	0.000441	26.2
$G_{13}(Gpa)$	1.87	0.07	0.08963	0.04482	26.2
$G_{23}(Gpa)$	1.87	0.07	0.04481	0.02413	26.2
v_{12}	0.06	0.286	0.333	0.333	0.29
v_{13}	0.313	0.286	0.0	0.0	0.29
v_{23}	0.313	0.286	0.0	0.0	0.29
$\rho(kg/m^3)$	1511	110	96	48	2710
$h_c(mm)$	-	12.7	12.7	12.7	-
$t_f(mm)$	0.264	-	-	-	0.264
$a(mm)$	76.2	76.2	76.2	76.2	76.2
$b(mm)$	76.2	76.2	76.2	76.2	76.2
Material	LTM45EL-CF0111 Carbon fiber	110WF Polymethacryimide foam	HRH-10-1/8-6.0	HRH-10-1/8-3.0	2024-T3 Aluminum Alloy

Table 2: Material constitutive properties of the sandwich panels [4]

Panel type	a/b	a/h	h_c/h	Assumed loss factor of the core layer
1	1	5.3346	0.8891	0.47
2	1	4.8021	0.8004	0.47 [4]
3	1	5.3346	0.8891	0.20
4	1	4.8021	0.8004	0.25
5 (Hybrid)	1	4.8021	0.8004	0.47
6 (Hybrid)	1	5.3346	0.8891	0.47
7 (Hybrid)	1	4.8021	0.8004	0.47
8(Hybrid)	1	4.8021	0.8004	0.47

Table 3: Geometrical and loss factor properties of sandwich panels
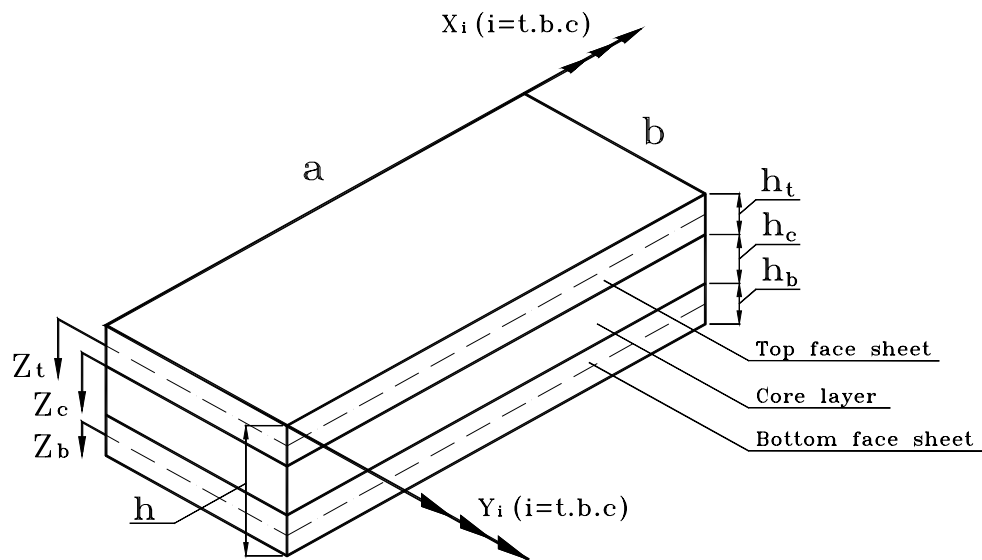
Figure 1: Sandwich composite plate with laminated face sheets.
Plate coordinates and plate dimensions are also shown.
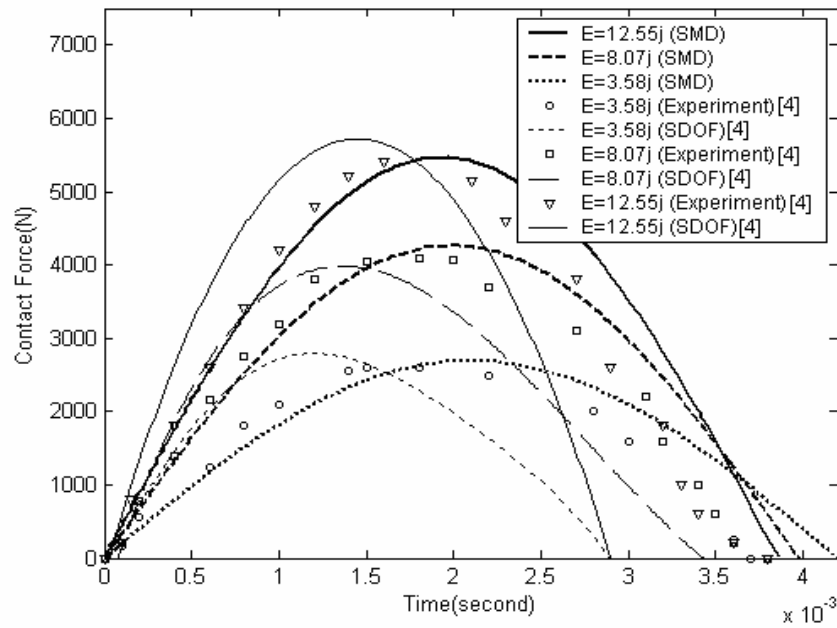
Figure 2: Predicted and experimental contact force histories of the panel at the center of top face sheet of the panel (panel type: 2) for the impact energy levels: 3.58j, 8.07j, and 12.55j
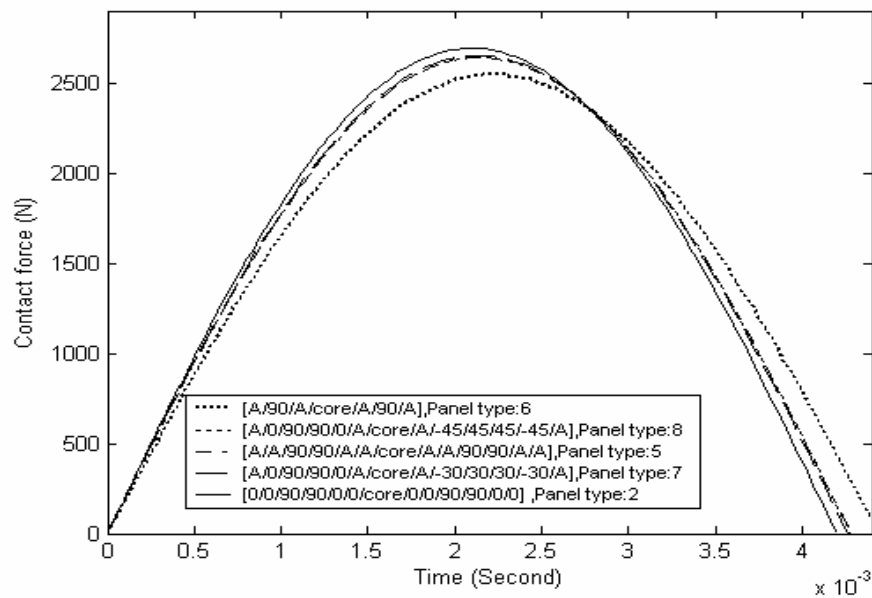
Figure 3: Effect of aluminum 2024-T3 alloy laminas in face sheets on contact force histories at the center of top face sheet of the hybrid panels (Types 2,5,6,7 and 8) .
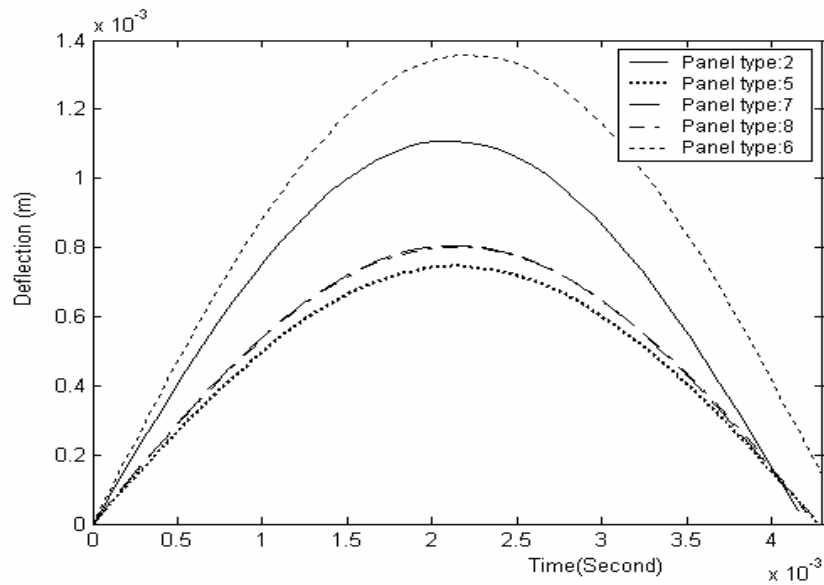
Figure 4: Effect of aluminum 2024-T3 alloy laminas in face sheets on central transverse deflection histories of top face sheets of the hybrid panels.
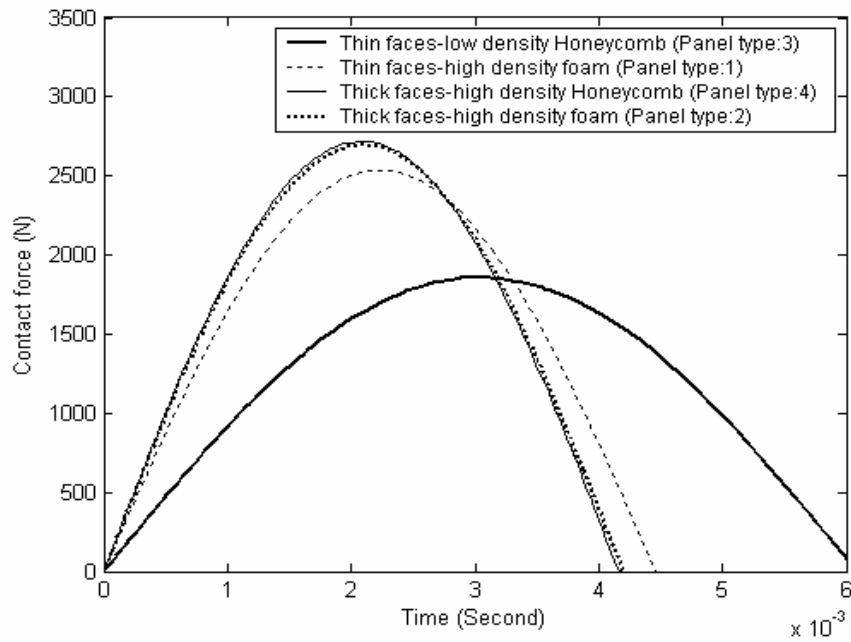
Figure 5: Effect of the core density and face-sheet thickness on contact force histories of the panels at the center of top face sheet of the panel (Types 1 to 4).

ENERGY ABSORPTION OF SANDWICH PANELS WITH GEOMETRICAL TRIGGERING FEATURES

Anders Lindström and Stefan Hallström

Division of Lightweight Structures
Department of Aeronautical and Vehicle Engineering
Royal Institute of Technology (KTH)
SE-100 44 Stockholm, Sweden
e-mail: alm99@kth.se and stefanha@kth.se, web page: http://www.ave.kth.se

Key words: Sandwich structures, Energy absorption, In-plane compression

Summary. *The influence of triggering topologies on the energy absorption of in-plane compressed sandwich panels is investigated. Sandwich panels with different geometrical triggering features are manufactured and tested experimentally. As expected the investigated triggering features reduce the extreme load peaks. Another, less expected result is that the subsequent plateau load tends to be higher for panels with triggering features. Both results are favourable for the crash performance of panels in vehicle applications.*

1 INTRODUCTION

Sandwich panels can with advantage be used in vehicle structures due to their relatively high bending stiffness and strength, compared to weight. If they are to be used in load bearing vehicle structures, their energy absorbing capability must however be comparable with corresponding metal structures and, above all, their absorption needs to be predictable. Even though the energy absorbing capability of composite materials can exceed that of metallic structures [1, 2] they are rarely used in mass produced vehicles. One reason for this is the complex damage propagation in composite structures, which makes it difficult to predict the energy absorption. This means that expensive experimental work is needed to determine the behaviour of such structures during crash events. In this study the behaviour of in-plane compression loaded sandwich panels are investigated and some means to controll their crushing behaviour are presented and compared.

During quasi-static in-plane loading of sandwich structures their structural behaviour is linear elastic until initiation of damage in the structure. This initial damage can be global buckling, local buckling (wrinkling) or face-sheet failure [3]. Another possible initial damage is core failure, but for most structural sandwich panels the ultimate strain of the core material exceeds that of the face-sheets. When the structure is compressed beyond failure initiation damage will propagate in the structure. Mamalis et. al [4] identified three types of post-initiation collapse modes; global buckling, unstable sandwich disintegration and progressive end-crushing. Face-sheet damage can initiate delaminations in the face-sheets and debonds in the face-core interface. If the fracture toughness of the interface is low the debonds may grow uncontrollable, resulting in momentaneous and complete disintegration of the face-sheets from the core. If the fracture

toughness of the face-core interface is sufficiently high in relation to the bending stiffness and strength of the face-sheets, the structure will not be as prone to fail catastrophically [5]. This leads to a more stable end-crushing collapse mode which promotes a higher energy absorption. Even if high compressive load bearing capacity is favourable for energy absorption of a panel, high peak loads are generally unwanted in automotive applications. This is due to associated high acceleration pulses for neighbouring structures as well as for passengers in the vehicle.

1.1 TRIGGERING

Different kinds of triggering means, in the following referred to as triggers, can be used to initiate damage at lower peak loads and to ensure more repeatable damage propagation in structures. The triggers can either be in the form of geometrical features or dyes that introduce stress concentrations into the structure, which in turn reduce peak loads and ensure more favourable collapse behaviour. The details of the mechanisms behind the improved collapse behaviour of sandwich structures are not yet entirely understood and one of the long-term goals of this work is to explore this behaviour further.

Structural components designed for efficient energy absorption have been used in automotive industry for several decades. These components are mostly different kinds of tubes, frusta and struts [6]. In primary structure such components have almost exclusively been made of steel. In recent years, and predominantly in more extreme cars, composite and even sandwich components have been introduced. The failure mechanisms of metal and composite structures during compression are different. Metal structures which are ductile mainly deform through plastic deformation, whereas composite materials in general deform in a more brittle manner [7]. Different triggers are used for different material concepts. In metallic tubes, imperfections can be used to ensure stable progressive plastic folding of the structure. Dyes are other commonly used triggers for metal tubes, where the tubes for example can be forced to invert or split [6]. In brittle composite tubes different geometrical features as chamfered or tulip shaped edges [8, 9] are used to trigger progressive crushing. Previous studies on sandwich structures include both metallic triggers and edges of different shape [10, 11]. Velecela et al. [11] investigated the influence of face-sheet thickness, length/width aspect ratio and different triggering features on the specific energy absorption of both monolithic laminates and sandwich panels. Three types of triggering features on the plate edges were investigated; chamfered, pyramidal and triangular. A triangular triggering shape gave the best results, promoting stable progressive end crushing.

In this study two conceptually different triggering features were investigated. The first was chamfering of the face-sheets of sandwich panels and the second was grooves at the loaded edges, as illustrated in figure 1. By chamfering the face-sheets the initial failure load is lowered. The effective stiffness and strength of the structure are also expected to be reduced. The grooves reduce the effective load carrying area and thereby reduce the effective stiffness and initial failure load in a similar way as chamfering. Failure is expected to initiate in or at the crests between the sawed grooves. The grooves also prohibit the damage to grow in-plane, perpendicular to the direction of the applied load as such damage propagation is interrupted at the grooves.

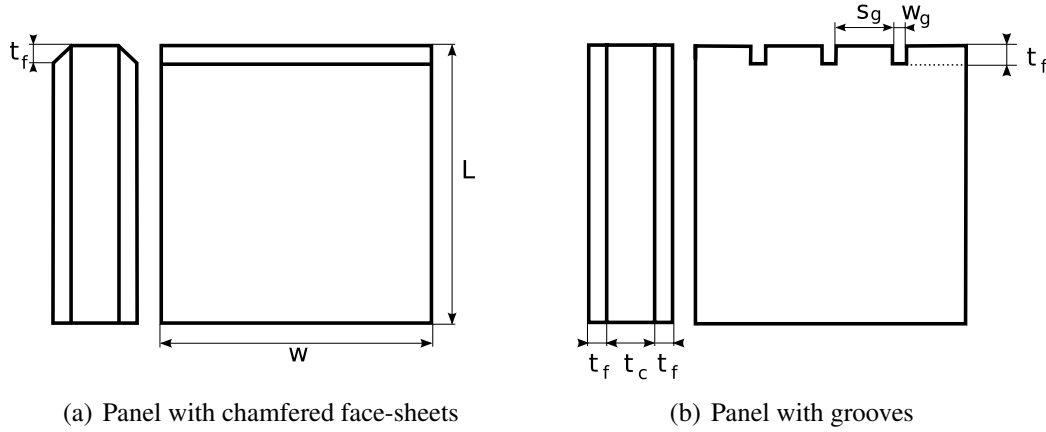(a) Panel with chamfered face-sheets　　　(b) Panel with grooves

Figure 1: Triggering topologies

2 EXPERIMENTS

The investigated sandwich panels consisted of sheet molding compound (SMC) glass fibre face-sheets and a balsa wood core. This is the same material concept as in the study by Lindström and Hallström [12], but from another manufacturing batch. Panels with dimensions of approximately 100x100x15.5 mm were manufactured. Special care was taken to ensure that the loaded edges were plane and mutually parallel. Sandwich panels without triggering features were used as reference. Samples with chamfered face-sheets or 4, 9 or 19 sawed grooves were manufactured. The width of the grooves w_g was 1.7 mm.

The sandwich panels were compressed in an Instron 4505 universal testing machine between two horizontal metal plates, without additional boundary support, using a 100 kN load cell. During the experiments the cross-head motion of the machine was 5 mm/min. A Redlake MotionPro X-3 Plus high speed camera was used to record the failure progression in sandwich panels with different triggering features. The pictures were recorded with a rate of 50 fps continuously during 120 s, which corresponds to 10 mm deformation of the panels. The relatively high recording rate ensured capture of the failure initiation.

3 NUMERICAL ANALYSIS

The influence of grooves on the failure initiation in sandwich panels was investigated through finite element (FE) analysis, using the software ABAQUS [13]. Face-sheets with either 4 or 19 grooves were modelled. The face-sheet was modelled using shell elements of the type S4R, which is a four noded element with reduced integration [13]. The material was considered to be isotropic and linear elastic. The model was loaded by applying a predefined compressive vertical displacement. Two cases were studied and compared. Apart from the applied vertical displacement the loaded edges were either simply supported or pinned. The simply supported constraints implied that only rigid body motions were prevented, representing absence of friction. The pinned constraints implied that all horizontal displacements were prevented,

representing infinite friction.

4 RESULTS

4.1 RESULTS FROM EXPERIMENTS

The results from the experiments are illustrated in figure 2 and in table 1, where the load values are presented together with standard deviations, per unit width. The different load and

Panel	Peak load $\hat{P}$ [kN/m]	Average Plateau load P_p [kN/m]	Total specific energy absorption W_s [kJ/kg]	Specific energy absorption during plateau region W_{ps} [kJ/kg]
Reference	397.5 ± 16.6	71.4 ± 3	2.11 ± 0.05	1.65 ± 0.06
Chamfered	184.3 ± 6.4	96.9 ± 4.9	2.36 ± 0.13	2.27 ± 0.14
4 grooves	395.3 ± 86.6	109.2 ± 9.8	2.86 ± 0.12	2.56 ± 0.26
9 grooves	382 ± 17.9	120.5 ± 14.7	2.91 ± 0.37	2.71 ± 0.4
19 grooves	288.5 ± 22.7	124.8 ± 2.5	2.93 ± 0.07	2.9 ± 0.04

Table 1: Results from experiments

energy variables are defined by studying the structural response of the reference panel illustrated in figure 2(a). The structural response was linear until the peak load $\hat{P}$ was reached and during the following compression the load was at a fairly constant plateau load. The average plateau load P_p is defined as the average load in the region illustrated in figure 2(a), where the maximum displacement is limited to 10 mm due to the gauge length of the deformation measurements. The total work W of the force P acting on the sandwich panel during a compression is here defined as

$$W = \int_0^\delta P d\delta. \tag{1}$$

When comparing the results from different panels it can be better to use the absorbed energy per unit weight deformed material, often referred to as specific energy absorption [8]. The total specific energy absorption W_s is defined as

$$W_s = \frac{W}{A\rho\delta}, \tag{2}$$

where A is the cross section area and ρ is the density of the panels. As the pre-failure energy absorption only is a small share of the total energy absorption during extensive crushing of structures, it is interesting to compare the resulting specific energy absorption W_{ps} during the plateau load. This specific energy absorption is defined as

$$W_{ps} = \frac{P_p}{A\rho}. \tag{3}$$

(a) Load and energy definitions

(b) Reference panels

(c) Chamfered panels

(d) Panels with 4 grooves

(e) Panels with 9 grooves
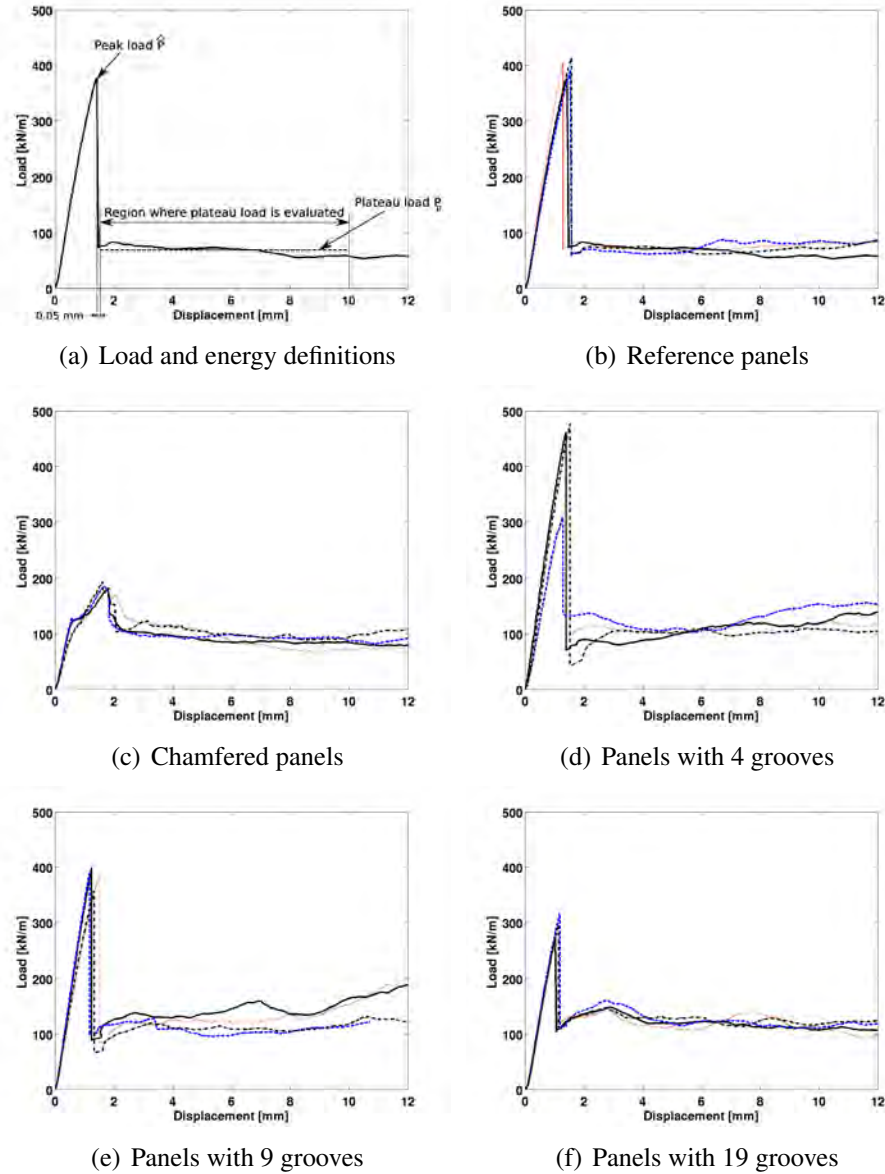
(f) Panels with 19 grooves

Figure 2: Load-displacement curves from experiments

The damage progression in panels with the different triggering features are presented in figures 3-6. Delamination cracks initiate at relatively low displacements during the compression of the sandwich panels with chamfered face-sheets. When the peak load is reached ($\delta = 1.745mm$) a delamination crack is clearly visible in both face-sheets, as shown in figure 3(c). During the following compression, the face-sheets delaminate and split further giving a broom-like structure. The panels with grooves showed no damage in the face-sheets prior to the peak

load. During the following compression delaminations and/or debonds are formed.

(a) δ=0.6 mm   (b) δ=1 mm   (c) δ=1.8 mm   (d) δ=3.5 mm
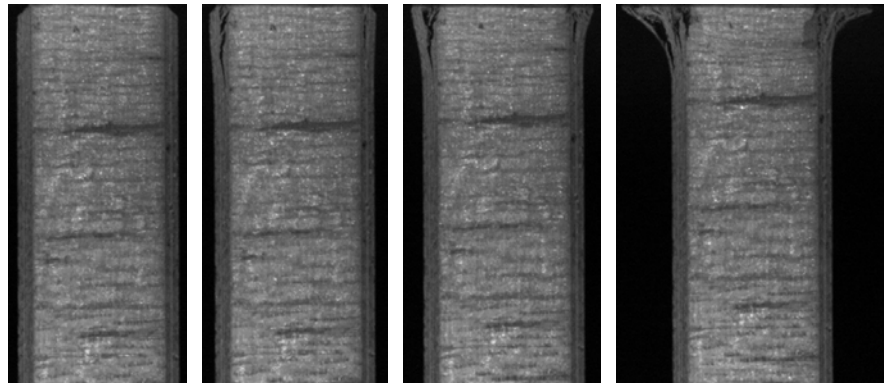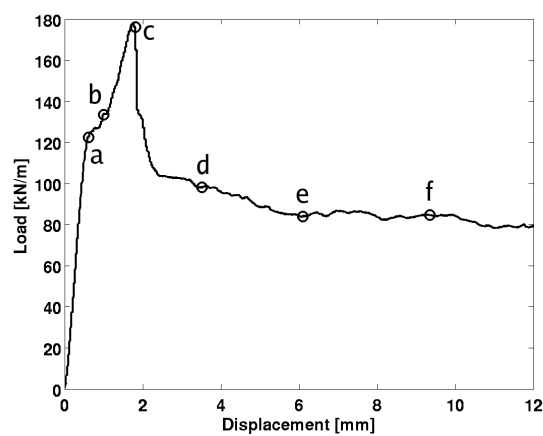
(e) δ=6.1 mm   (f) δ=9.4 mm

(g) Load displacement curve, with a-f marking the corresponding photo of damage progression

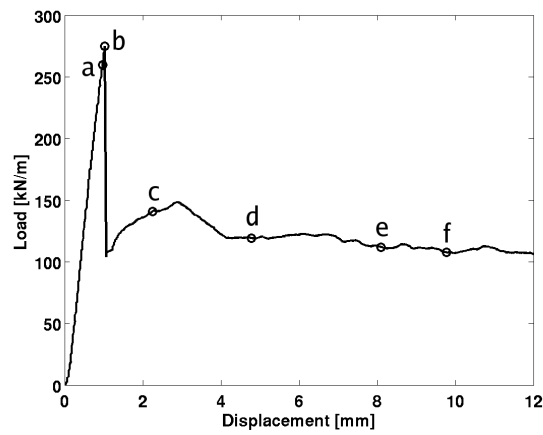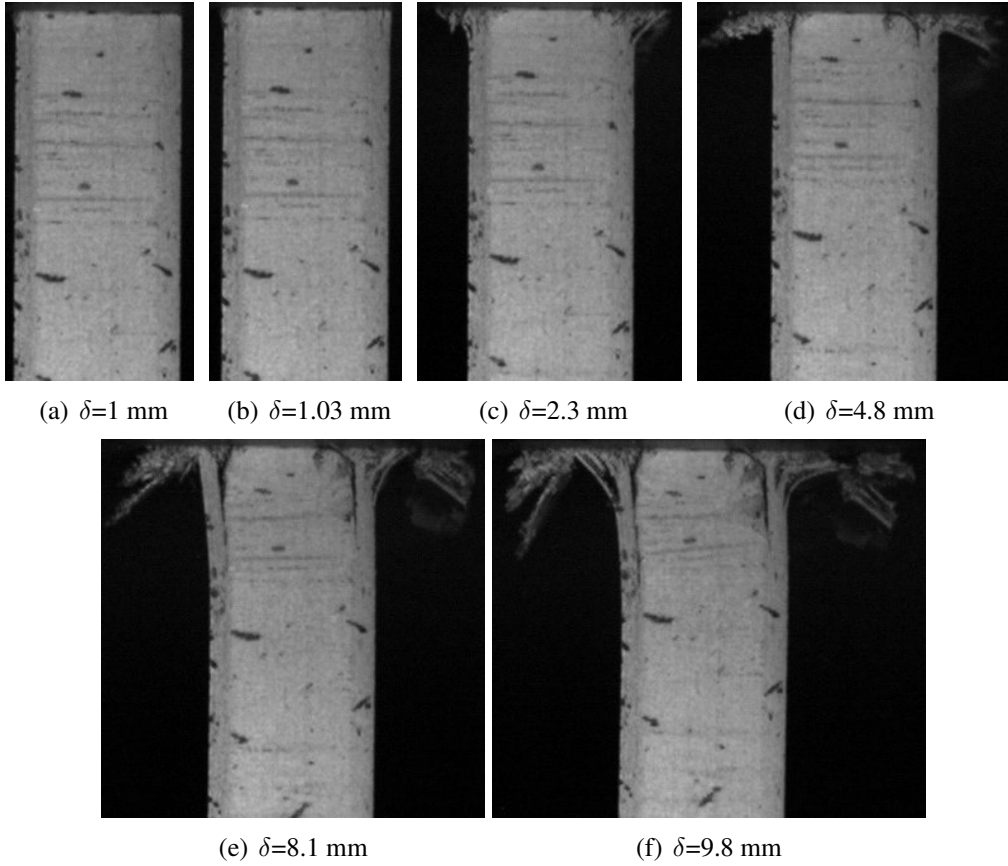Figure 3: Failure progression in panel with chamfered face-sheets
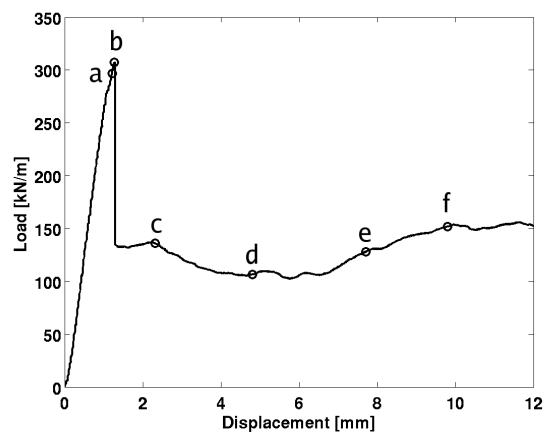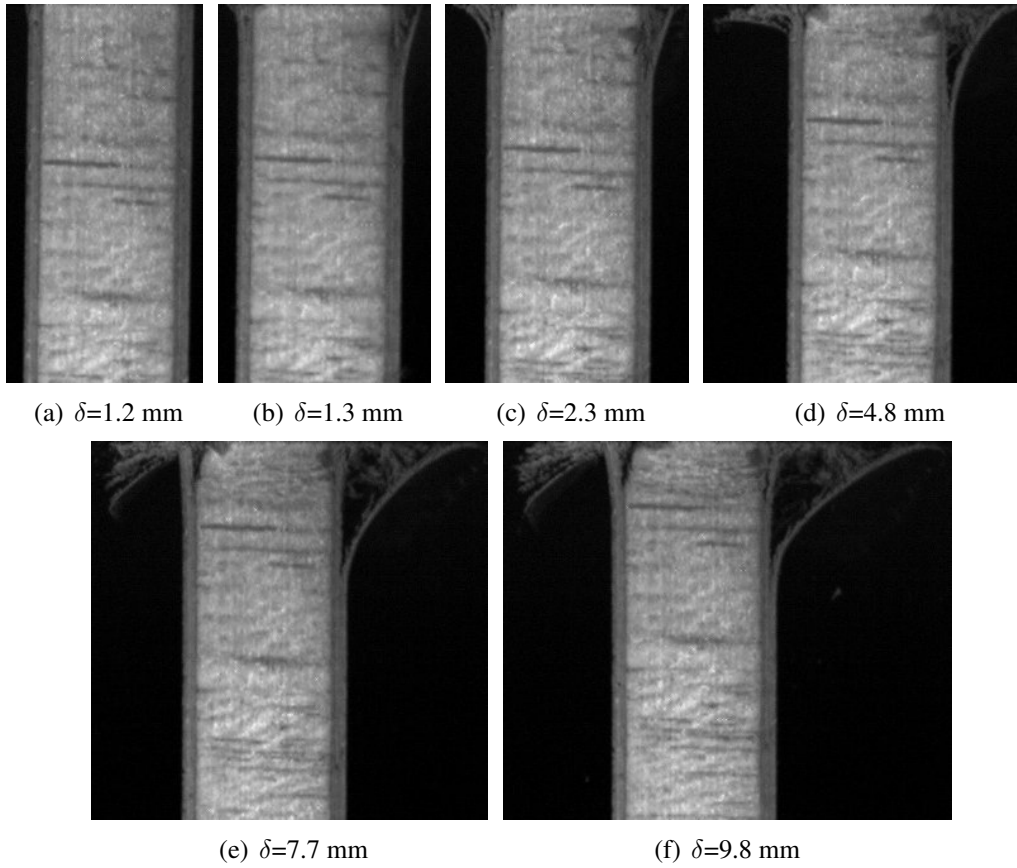
(a) δ=1.2 mm   (b) δ=1.3 mm   (c) δ=2.3 mm   (d) δ=4.8 mm

(e) δ=7.7 mm   (f) δ=9.8 mm

(g) Load displacement curve, with a-f marking the corresponding photo of damage progression

Figure 4: Failure progression in panel with 4 grooves
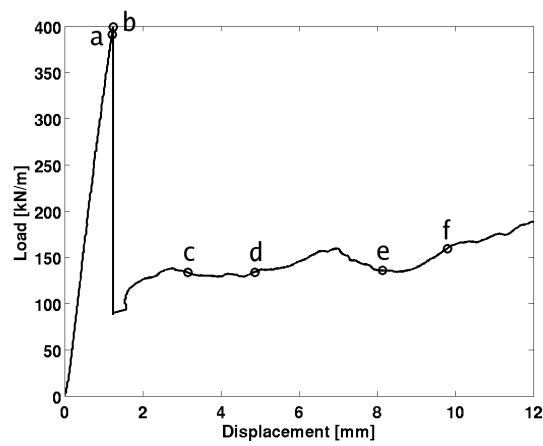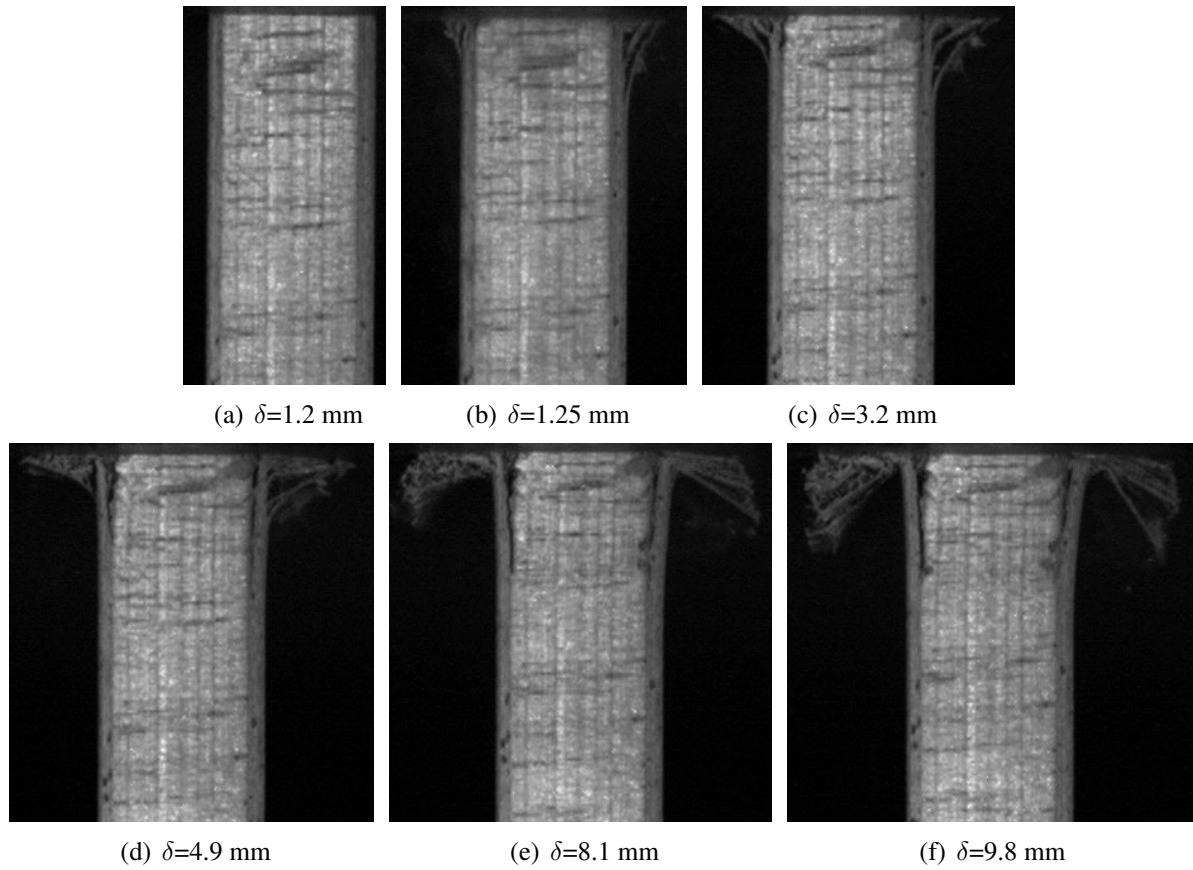
Anders Lindström and Stefan Hallström

(a) δ=1.2 mm   (b) δ=1.25 mm   (c) δ=3.2 mm

(d) δ=4.9 mm   (e) δ=8.1 mm   (f) δ=9.8 mm

(g) Load displacement curve, with a-f marking the corresponding photo of damage progression

Figure 5: Failure progression in panel with 9 grooves

(a) δ=1 mm   (b) δ=1.03 mm   (c) δ=2.3 mm   (d) δ=4.8 mm

(e) δ=8.1 mm   (f) δ=9.8 mm

(g) Load displacement curve, with a-f marking the corresponding photo of damage progression

Figure 6: Failure progression in panel with 19 grooves

4.2   RESULTS FROM NUMERICAL ANALYSIS

The stress distributions in the horizontal and vertical direction in a panel with 4 grooves are illustrated in figure 7. Figure 8 illustrates the stress in the vertical direction on the upper and lower edge for panels with 4 and 19 grooves with either simply supported edges or pinned edges.

(a) Stress in horizontal direction for panel with pinned edges

(b) Stress in horizontal direction for panel with simply supported edges

(c) Stress in vertical direction for panel with pinned edges

(d) Stress in vertical direction for panel with simply supported edges
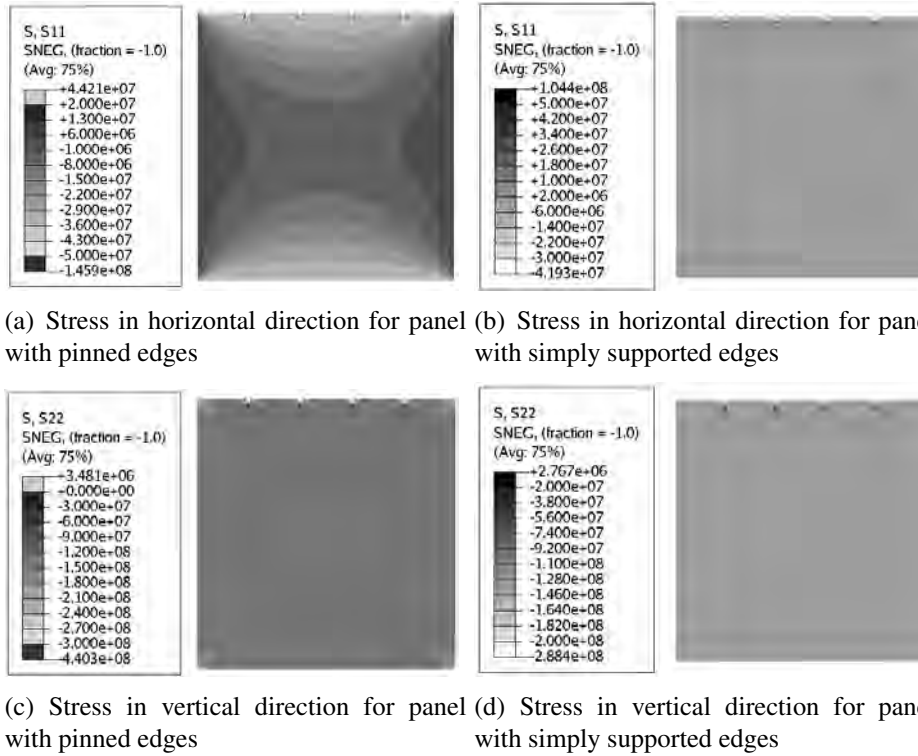
Figure 7: Stress distribution on panel with 4 grooves

5   DISCUSSION

It is clearly shown in figure 2 that the load reduction from peak to plateau load levels was lower and more gradual for the panels with chamfered face-sheets than for the reference and grooved panels. This can be beneficial for vehicle applications, where resulting acceleration pulses then are likely to be reduced correspondingly. The resulting plateau load of the panels with chamfered face-sheets was however lower than for panels with grooves. It can further be noted from figure 2 that the plateau load is rising for panels with 4 and 9 grooves, but dropping for panels with 19 grooves and chamfered face-sheets. The reason for this is however yet unknown.

The peak loads of the panels with grooves were not reduced in proportion to the area reduction. The area reduction of the panels with 4, 9 and 19 grooves were approximately 7%,
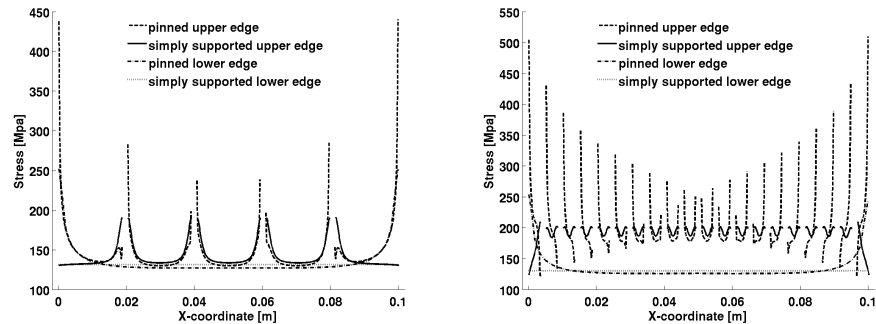
(a) Stress in vertical direction for panel with 4 grooves

(b) Stress in vertical direction for panel with 19 grooves

Figure 8: Stress distribution on upper and lower edges for panels with 4 and 19 grooves

15% and 32%, respectively. The peak load reduction, however, was only 0.5%, 4% and 27%, respectively. It should be noted that the scatter in peak load of the panels with four grooves was relatively high. Two panels had peak loads higher than the reference panels, whereas the peak loads of the other two panels were lower than expected. One of the panels failed at the edge without grooves, which indicates that four grooves was insufficient to ensure triggering. The other tested configurations showed surprisingly low scatter for the type of sandwich material.

By studying figures 3-6 it can be noted that the initial delaminations are more concentrated to the upper edge of the panel with 19 grooves compared to panels with other triggering features. This is believed to contribute to the more stable progressive end-crushing and higher plateau load observed for those panels.

The influence of the two different boundary conditions used in the FE analysis is clearly shown in figures 7-8. The boundary effects are more dominant for panels with more grooves. The stress levels at the lower edge is naturally independent of the number of grooves, whereas the stress levels increase at the upper edge with increasing number of grooves. It must however be noted that the stress levels at the edges are mesh dependent due to the singular stress fields at the corners.

6 CONCLUSIONS

There is a clear trend that the specific energy absorption of panels with triggering features is increased in comparison to that of the reference panels. Four grooves do not ensure that damage is initiated where intended and the panels with 19 grooves have the highest average specific energy absorption. The difference between the panels with 9 and 19 grooves is however relatively small and not statistically certain.

7   ACKNOWLEDGEMENTS

REFERENCES

[1] G.L. Farley. Energy absorption of composite materials. *Journal of Composite Materials*, 17:267–279, May 1983.

[2] A.G. Mamalis, M. Robinson, D.E. Manolakos, G.A. Demosthenous, M.B. Ioannidis, and J. Carruthers. Review crashworthy capability of composite material structures. *Composite structures*, 37(2):109–134, February 1997.

[3] N.A. Fleck and I. Sridhar. End compression of sandwich columns. *Composites:Part A*, 33:353–359, 2002.

[4] A.G. Mamalis, D.E. Manolakos, M.B. Ioannidis, and D.P. Papapostolou. On the crushing response of composite sandwich panels subjected to edgewise compression: experimental. *Composite Structures*, 71:246–257, 2005.

[5] A. Lindström. Strength of sandwich panels loaded in in-plane compression, Licentiate thesis, KTH Engineering Sciences, Stockholm, 2007.

[6] A.A.A. Alghamdi. Collapsible impact energy absorbers: an overview. *Thin-Walled Structures*, 39:189–213, 2001.

[7] J.J. Carruthers, A.P. Kettle, and A.M. Robinson. Energy absorption capability and crashworthiness of composite material structures: A review. *Applied Mechanics Reviews*, 51(10):635–649, October 1998.

[8] D. Hull. A unified aproach to progressive crushing of fibre reinforced composite tubes. *Composites Science and Technology*, 40:377–421, 1991.

[9] P.H. Thornton and R.A. Jeryan. Crash energy management in composite automotive structures. *International Journal of Impact Engineering*, 7(2):167–180, 1988.

[10] G. Pitarresi, J.J. Carruthers, A.M. Robinson, G. Torre, J.M. Kenny, S. Ingleton, O. Velecela, and M.S. Found. A comparative evaluation of crashworthy composite sandwich structures. *Composite Structures*, 78:34–44, 2007.

[11] O. Velecela, M.S. Found, and C. Soutis. Crushing energy absorption of GFRP sandwich panels and corresponding monolithic laminates. *Composites: Part A*, 38:1149–1158, 2007.

[12] A. Lindström and S. Hallström. Energy absorption of sandwich panels subjected to in-plane loads. In *8th Biennial ASME Conference on Engineering Systems Design and Analysis*. ASME, 2006.

[13] ABAQUS. Online users manual,version 6.7. www.simulia.com, 2007.

ON THE PERPENDICULAR AND IN-PLANE IMPACT BEHAVIOR OF CORE MATERIALS IN SANDWICH STRUCTURES

Lars Massüger[*], Roman Gätzi[*], Fabian Dürig[†], Ivo Lüthi[†] and Jochen Müller[†]

[*]Alcan Airex AG
Industrie Nord, CH-5643 Sins, Switzerland
e-mail: lars.massueger@alcan.com, web page: http://www.alcanairex.com

[†]Institute of Polymer Technology
University of Applied Sciences Northwestern Switzerland (FHNW)
Steinackerstrasse 5, CH-5210 Windisch, Switzerland
e-mail: jochen.mueller@fhnw.ch, web page: http://www.fhnw.ch

Keywords: Sandwich structures, Core materials, Perpendicular and In-plane Impact, Dynamic Testing.

Abstract Sandwich structures with various typical core materials as well as monolithic composite materials have been tested dynamically under perpendicular and in-plane impact conditions. Load-time and load-displacement diagrams were synchronized with high speed movies to analyze failure mechanisms and performance under dynamic conditions. The BALTEK® balsa core material showed the most constant and highest amount of impact energy absorption. The new type of monolithic composite material, AIREX® PX, performed superior in comparison with tests performed on common plywood panels.

1 INTRODUCTION

Nowadays, still most of the sandwich parts are designed according to design rules which apply for quasi-static loads. But in reality, e.g. in a crash, structural parts are subjected to load rates exceeding the static design loads. Therefore, impact testing of samples or parts produced using approved processes and materials, is a routine process in the aerospace industry for components made of advanced composites. In contrast, other industries such as the automotive lack such procedures, because of big quantities and expected costs. The fundamental parameters for optimizing the crash performance of a composite part are: constant absorption of the impact energy, non-catastrophic failure and appropriate methods of construction and manufacturing. Furthermore, understanding the dynamic behavior of composite materials is crucial, because in many cases the load rates cannot be considered as quasi-static anymore.

The impact tester *H+* (patent pending) developed for the present study allows impact testing of panels. The force of the impact is determined indirectly via oscillation measurements at the test anvil table. In that way, the loads as well as the displacement during

the entire load process, i.e. also beyond the linear load force/deformation limit, are measured more accurately, than in conventional instrumented drop weight impact tests [1], [2].

2 EXPERIMENTAL

To obtain comparable results of various core materials and identical skins, impact tests with the new type of impact tester *H+* were performed. In the initial tests presented in the following only three panels per core material, were tested. Load- and displacement-time diagrams were measured dynamically during each test and evaluated further.

2.1 Sample Preparation

The sandwich test panels only differed in the type of core material, all the skin laminates were of identical configuration. The layer composition was as follows: alternating layers of 600 g/m^2 woven rowing (WR) and 300 g/m^2 chopped strand mat (CSM). The core thickness in all the panels was 10 mm. A view of the sandwich assembly of a test panel before vacuum bagging is shown in figure 1. The final test specimens were cut from about 1x1 m^2 panels produced by vacuum infusion using the epoxy resin system: *Araldite*® *LY564* with *Aradur*® *22962 hardener*, both obtained from Huntsman Advanced Materials.
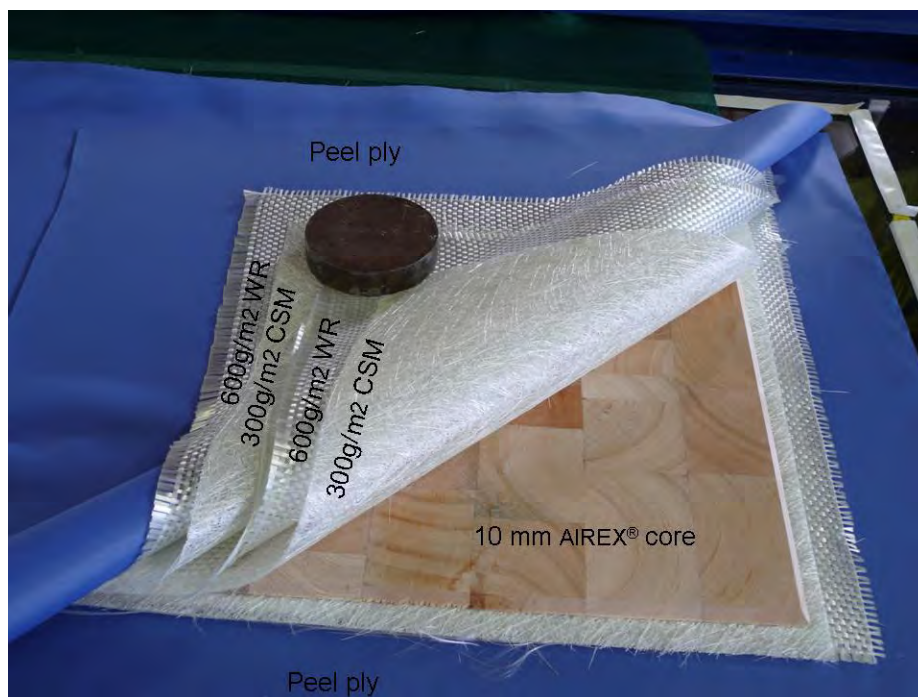
Fig. 1: View of the layer configuration of the sandwich test panels

Sandwich panels with a size of 300 mm x 300 mm were tested perpendicular to the surface of the panel. Test panels with a size of 300 mm x 100 mm were tested in in-plane condition. In table 1 the different types of core materials and their typical mechanical properties are summarized.

Core Material	BALTEK® SB.150	AIREX® T91.100	AIREX® C70.75
Density [kg/m³]	247	110	80
Compr. Modulus [N/mm²]	7982	65	97
Compr. Strength [N/mm²]	26.3	1.2	1.3
Shear Modulus [N/mm²]	309	18	30
Shear Strength [N/mm²]	4.9	0.75	1.2

Table 1: Core materials and their mechanical properties (AIREX® datasheet values)

Additional tests were performed on monolithic panels with identical dimensions cut from the following monolithic materials: Plywood (Okoume Marine Grade), AIREX® PXc.245 and AIREX® PXw.320 (mechanical properties see table 2). The AIREX® PX family is based on foamed polyurethane (PUR) reinforced with continuous fibers (AIREX® PXc.245) or with continuous fibers combined with woven roving reinforcements (AIREX® PXw.320).

Monolithic Materials	Plywood	AIREX® PXc.245*	AIREX® PXw.320*
Density [kg/m³]	470	240	320
Compr. Modulus [N/mm²]	-	56	72
Compr. Strength [N/mm²]	-	2.6	1.5
Shear Modulus [N/mm²]	-	63	44
Shear Strength [N/mm²]	-	2.1	0.9

Table 2: Monolithic panels and their mechanical properties (* preliminary AIREX® datasheet values)

2.2 The Impact Test Equipment

For dynamical investigation of the behavior of different sandwich panels loaded on impact, the impact tester *H+* was designed to the requirements of the Institute of Polymer Technology and produced at the University of Applied Sciences in Windisch, Switzerland. Monolithic or sandwich specimens can be tested in perpendicular and in-plane loading. The impact tester and its detailed configuration are shown in figure 2. A more detailed description of the impact tester H+ and detailed testing instructions can be found in [3].
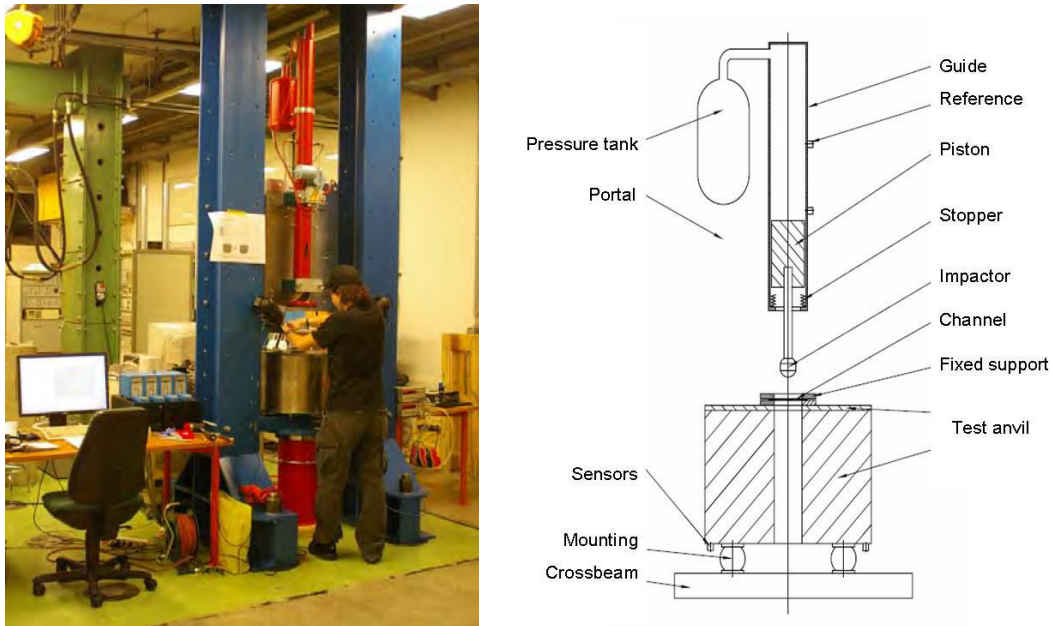
Fig. 2: The impact tester *H+* (left) and a detailed view of the testing equipment only (right)

The complete installation is about 4 m in height. The test equipment consisting of the impactor and its mechanics is carried by two vertical steel girders. A lower crossbeam carries a steel anvil with a specimen frame fixture for the two load cases to maintain the test panel in position during loading. The impactor is accelerated by pneumatic pressure, which allows various loading rates. Thus, the impactor hits the specimen panel with a well-defined kinetic energy. The acceleration during impact is measured as a function of time via the oscillations of the testing anvil by the attached sensors. The seismic mass of the whole setup is high, hence its elevated own frequency avoids interference with the oscillations of the specimen. After the measurement the harmonics from the anvil and the fixed sample support are removed from the signal by a Butterworth lowpass filter [4]. The data is converted into a load-time and further into a load-displacement diagram. Finally, the total energy of the impact is calculated by integration of the load-time plot. In addition, all the tests are recorded with a high-speed camera at a frame-rate of 10 kHz and a resolution of 512 x 512 pixels. In all the tests the impactor was accelerated to a constant speed of 18.45 m/s (66.6 km/h respectively), which equals a typical average speed in transportation.

2.3 Perpendicular Impact Tests

For the perpendicular impact tests a spherical impactor with a diameter of 57 mm and a weight of 7.99 kg was used. During the tests, the panels with a size of 300 x 300 mm are restrained using a fixed support (see figure 3). The impactor penetrates the panels in the direction perpendicular to the core material plane. The maximum energy absorption occurs, when maximum damage is caused. Thus, for representative results in terms of the energy absorption of a sandwich, a complete penetration of the test panels is essential.

Fig. 3: Fixed support and the corresponding impactor for the perpendicular impact tests

2.4 In-plane Impact Tests

For the in-plane tests, an impactor with a cylindrical shape (diameter 22 mm, axis perpendicular to the panel plane) and a weight of 7.7 kg had to be used, to avoid delamination between the core and skins related to the shape of the impactor. In addition, a special kind of fixed support had to be designed to keep the panels in position and prevent lateral slip during testing (see figure 4).
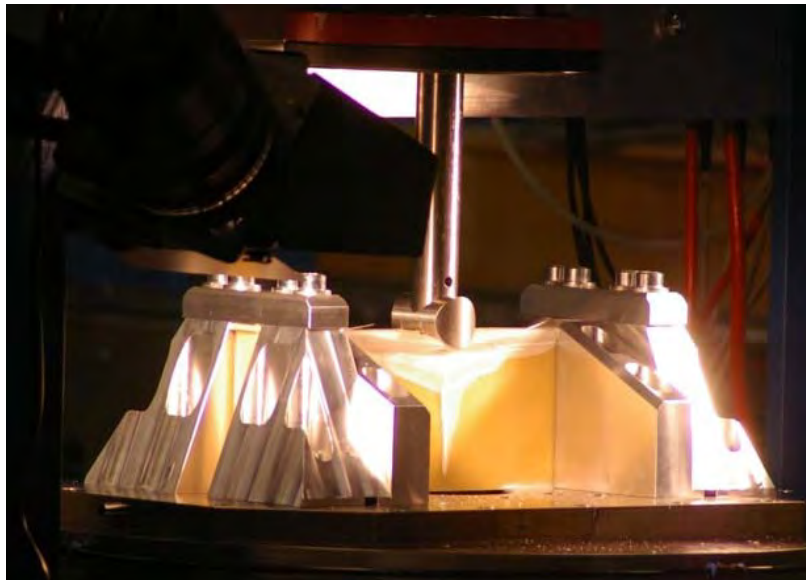
Fig. 4: Fixed support and impactor as used for the in-plane tests

3 RESULTS

The perpendicular and in-plane impact tests were evaluated as described below. In a first step the high-speed movies were synchronized with the load-time and the load-displacement diagrams, respectively. On the basis of the synchronization the diagrams were analyzed and interpreted. The following characteristic values were determined for each test: the maximum load F_{max} during impact, the total displacement q and the overall absorbed energy W. Mean values were determined of three impact tests for each type of core and monolithic material. The duration of a perpendicular test was in the range of 5 ms, an in-plane test toke about 8-9 ms.

3.1 Perpendicular Impact

Figure 5 shows the comparison between representative load-displacement diagrams, one for each of the core materials tested. In figure 6, the same comparison for the monolithic materials is shown. Compared to the polymer core materials, the balsawood core material (BALTEK® SB.150) performed best. Both of the synthetic foam cores (AIREX® T91.100 and C70.75) show a distinct drop in the load after the initial linear-elastic behavior.
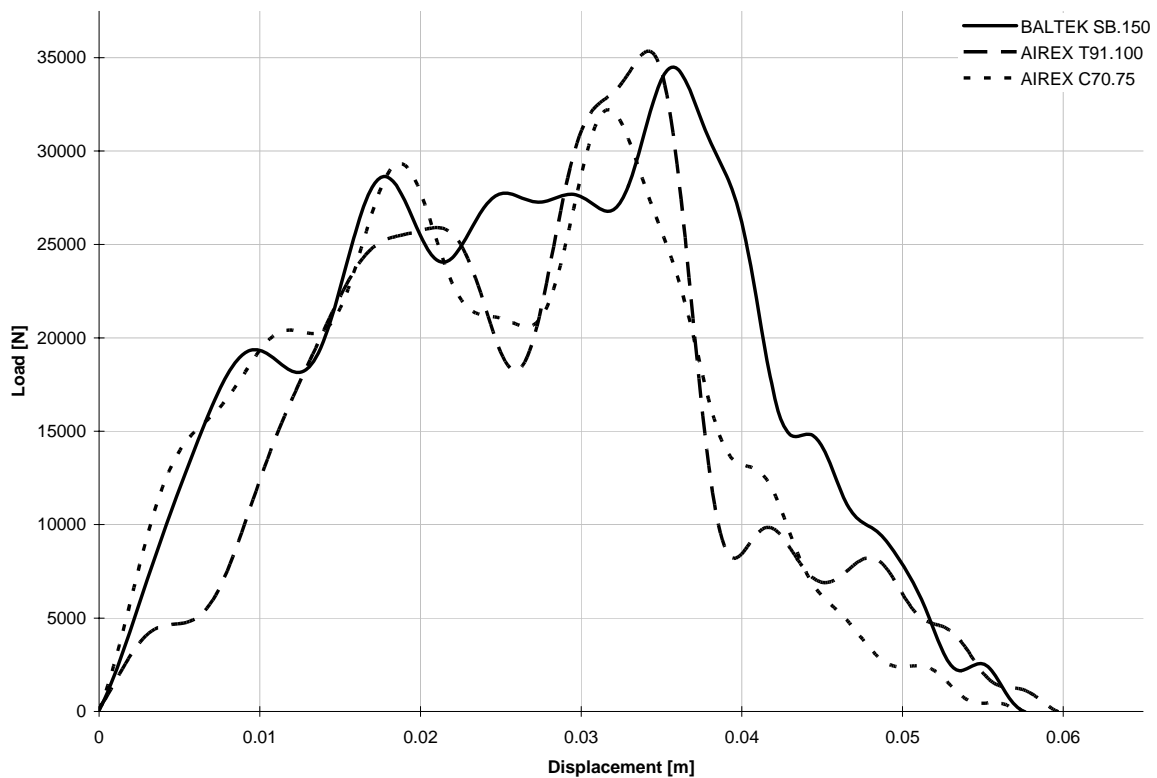
Fig. 5: Comparison of representative load-displacement curves, one for each type of the core material tested perpendicularly
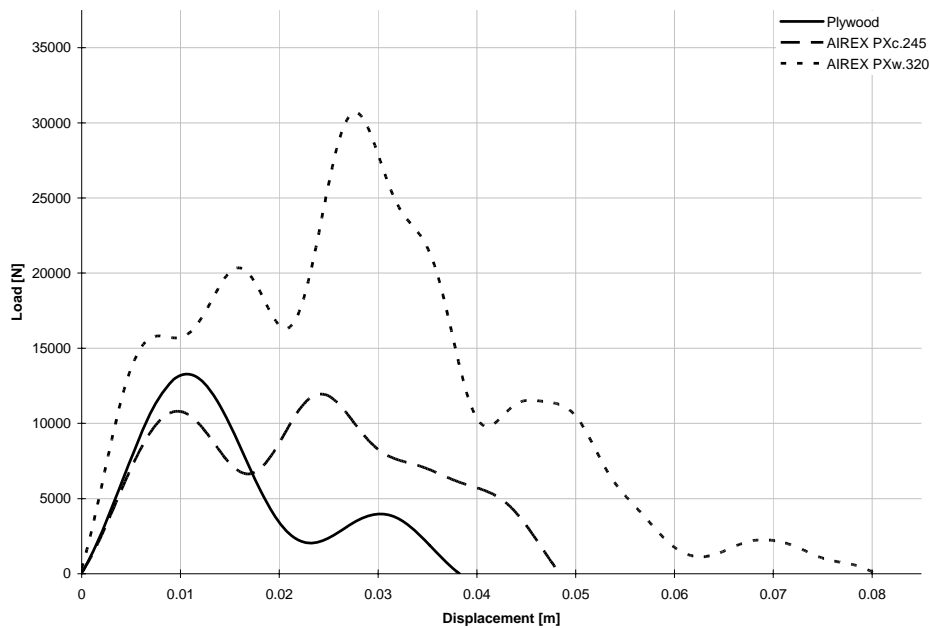
Fig. 6: Comparison of representative load-displacement curves for the monolithic panels

The monolithic material AIREX$^{®}$ PXw.320 clearly outperforms the plywood and the AIREX$^{®}$ PXc.245 core. In table 3, the average characteristic values for the perpendicular impact of the different sandwich types are summarized.

	F_{max} [N]	q [mm]	W [J]
Core Material			
BALTEK$^{®}$ SB.150	33242 ± 2277	63 ± 13	1049 ± 107
AIREX$^{®}$ T91.100	34983 ± 2330	62 ± 6	868 ± 14
AIREX$^{®}$ C70.75	34549 ± 2848	60 ± 7	906 ± 54
Monolithic Panels			
Plywood	-	37 ± 1	194 ± 19
AIREX$^{®}$ PXc.245	-	46 ± 3	321 ± 27
AIREX$^{®}$ PXw.320	-	79 ± 9	913 ± 47

Table 3: Average characteristic values for the perpendicular impact test

Comparing the total absorbed energies of the systems, the sandwich with the balsa BALTEK$^{®}$ SB.150 core is superior. The maximum force during its impact test is less than for the other systems. The woven fabric reinforced polyurethane PXw.320 shows properties, which are comparable to the PET (AIREX$^{®}$ T91.100) and PVC (AIREX$^{®}$ C70.75) cores. Figure 7, shows a BALTEK$^{®}$ SB.150 cored test panel after testing.
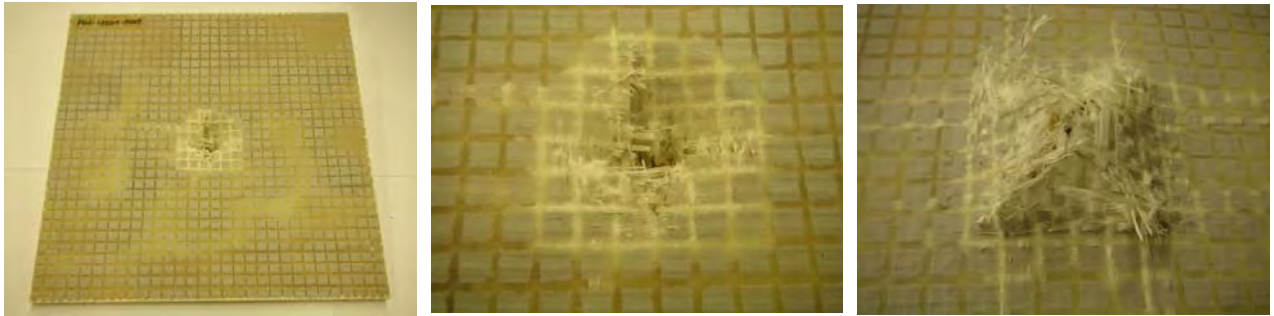
Fig. 7: A BALTEK® SB.150 test panel after the perpendicular impact test (left to right: overview front, close-up entry- and exit-side)

3.2 In-plane Impact

In figures 8 and 9, a representative load-displacement curve for each of the tested core materials and the monolithic panels are shown, respectively. In general, the PET core (AIREX® T91.100) performed worst, while the results for balsa (BALTEK® SB.150) and the cross-linked PVC (AIREX® C70.75) core are comparable. It has to be stated that in the case of the PVC core folding of the skins and slip-out from the frame fixation occurred during the tests. This effect results in additional energy consumption and therefore distorts the results. In fact, energy absorption only related to the deformation and damage to the structure, is expected to be less for the AIREX® C70.75 core.
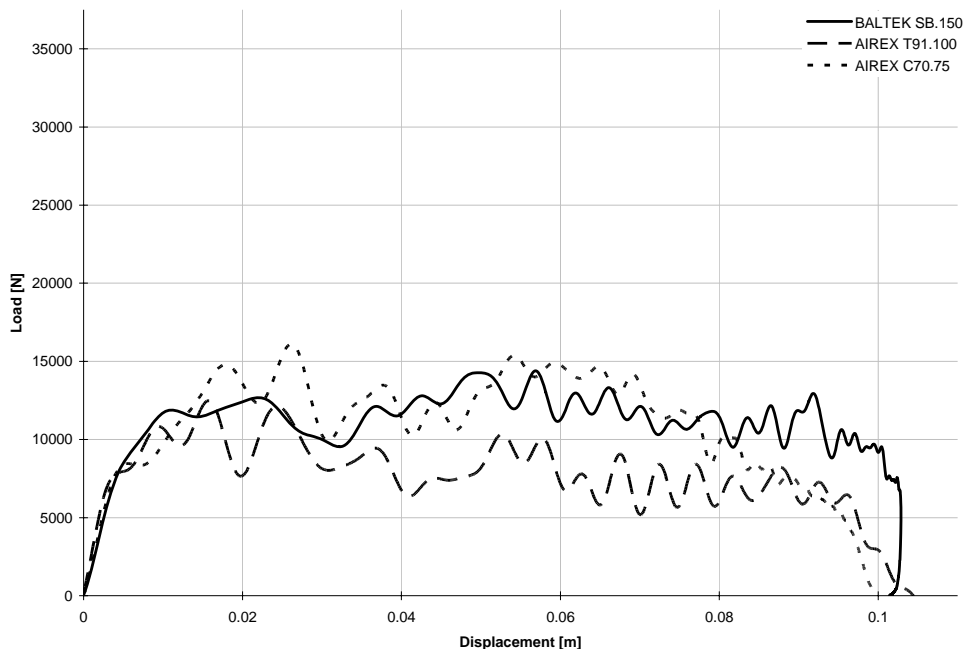
Fig. 8: Comparison of representative load-displacement curves for the core materials for in-plane impact

For the monolithic panels, the in-plane behavior of plywood and the continuous and woven roving reinforced polyurethane (AIREX® PXw.320.) in the elastic part is similar. But in all, the most energy is absorbed by the AIREX® PXw material.
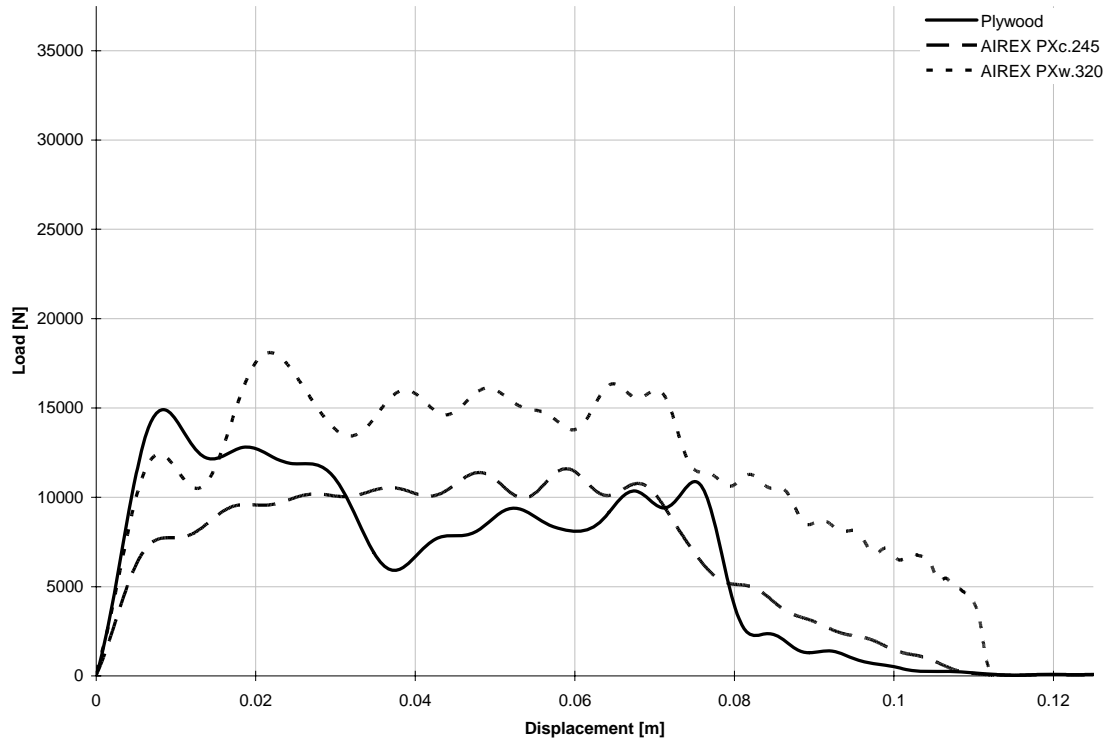

Fig. 9: Representative load-displacement curves for each of the monolithic panels, in-plane tested

Table 4 summarizes the average characteristic values for the in-plane impact tests of the different materials.

	F_{max} [N]	q [mm]	W [J]
Core Material			
BALTEK® SB.150	14666 ± 248	103 ± 5	1109 ± 50
AIREX® T91.100	12696 ± 337	105 ± 1	808 ± 6
AIREX® C70.75	14939 ± 1069	114 ± 22*	1070 ± 31
Monolithic Panels			
Plywood	-	136 ± 20	845 ± 61
AIREX® PXc.245	-	113 ± 12	782 ± 21
AIREX® PXw.320	-	111 ± 3	1342 ± 6

Table 4: Average characteristic values for the in-plane impact tests (* folding of the skins during all the tests)

4 DISCUSSION

Dependant on the load rate during the impact, its energy is dissipated through different mechanisms taking place in the composite. Below a certain energy level, only reversible elastic deformation occurs, which does not cause any permanent damage. With increasing magnitude of the impact, not all the energy can be absorbed elastically, hence as a result permanent plastic deformation occurs. Finally, the remaining energy is absorbed by structural damage and ultimately its complete failure.

4.1 CoreMaterials - Perpendicular

In the tests of the present work, the impact energy was chosen in order to achieve catastrophic failure, i.e. complete penetration of the specimen. The images (figure 10. a – d) below show the different stages of a perpendicular impact test of a sandwich with a PET (AIREX® T91.100) core. Their connection to the load-time and load-displacement diagrams is shown and discussed, as are the energy absorption mechanisms in the composite.
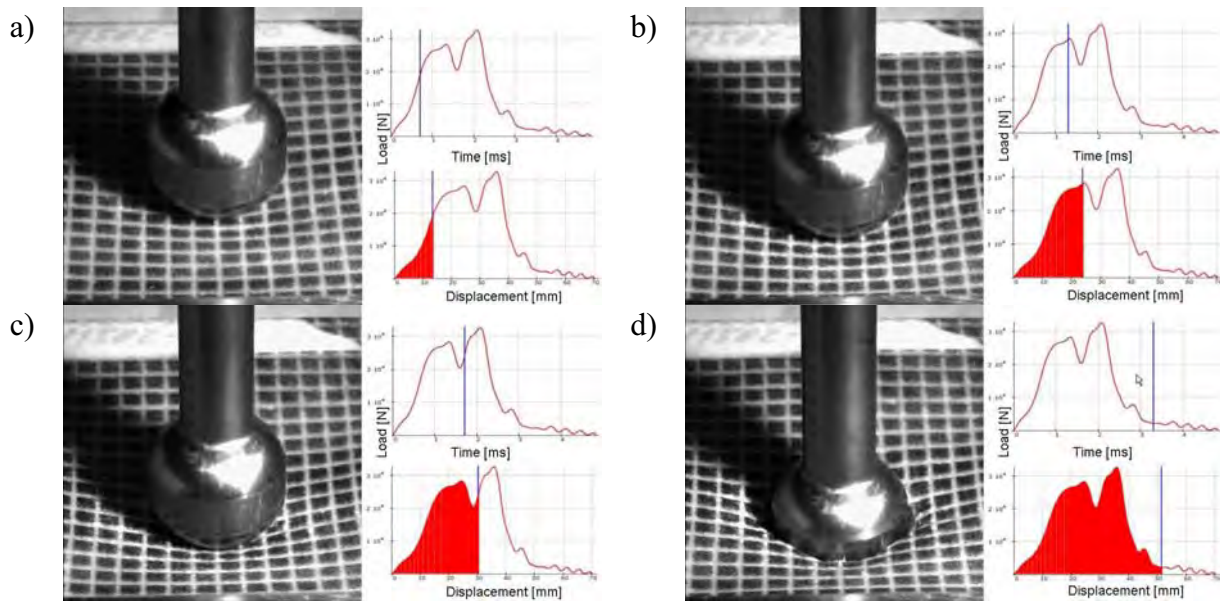
Fig. 10: Different stages of damage propagation during a perpendicular impact test and the corresponding load-time and load-displacement diagrams

In an initial phase, shown in figure 10.a) a nearly linear-elastic behavior is found, followed by plastic deformation of the core and finally a load drop, due to crack initiation (first peak maxima) in the top skin (figure 10.b)), occurs. In figure 10.c) the crack appears on the surface of the top skin followed by further energy consumption through linear-elastic deformation of the second skin, until at the second maxima, at which this skin fails too. Finally, the impactor penetrates the second skin (figure 10.d)) and the oscillations of the panel come to a halt. As can be seen from the load-displacement curves shown in figure 5, the balsa BALTEK® SB.150 core absorbs the most energy with a maximum load peak in the range of the two

synthetic foam cores. This effect is related to the by magnitudes higher compressive and shear strength/modulus of the balsa core, which allows a more efficient load transfer from the top to the lower skin laminate. The PET (AIREX® T91.100) and the cross-linked PVC (AIREX® C70.75) cores show a more distinct drop in the load after the initial linear-elastic slope, related to the cracking of the top skins and deformation of the core.

4.2 Core Materials – In-plane

In the in-plane tests a quite different behavior was found. Figure 11.a), the impactor enters the sample, the core is deformed and the skins fail, which results in a linear-like slope. Delamination of the core and the skins is initiated at the site of the impact (figure 11.b), the skins are torn apart further. Finally, the core is torn apart in the plane parallel to the surface (figure 11.c). The combination of cracking and shear of the core, propagates further (figure 11.d) until the impactor exits the sample.
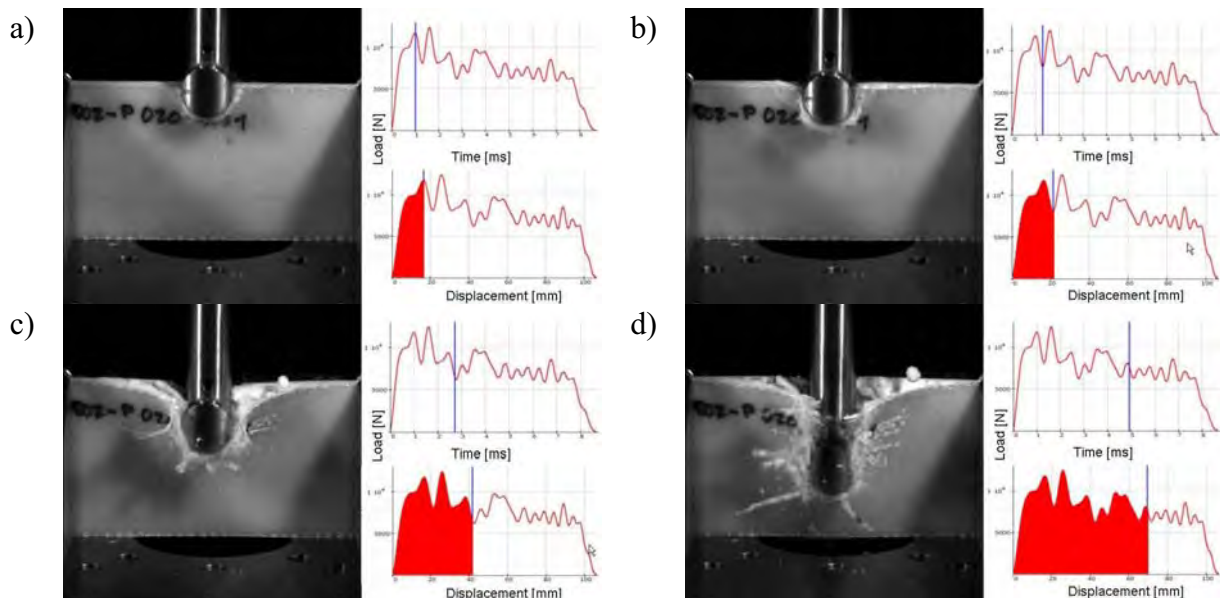

Fig. 11: Synchronized pictures from a high speed camera and the corresponding load-time and load-displacement diagrams

The balsa (BALTEK® SB.150) and PVC (AIREX® C70.75) cores consume about the same amount of energy. The PET (AIREX® T91.100) core consumes less, which could be related its more brittle behavior.

4.2 Monolithic Materials

In general, the energy absorption of the monolithic specimens is less constant than for the sandwich panels and the difference between perpendicular and in-plane impact is much more significant. The load is transmitted more or less directly from the beginning of the impact, after the maximum load, a constant drop occurs until penetration of the panel.

5 CONCLUSIONS

Sandwich and monolithic panels have been dynamically tested in perpendicular and in-plane loading with respect to impact behavior. By means of load-time and load-displacement diagrams synchronized with high speed movies, the mechanisms of damage propagation could be identified and analyzed.

With respect to energy absorption, the balsa (BALTEK® SB.150) core clearly outperformed the other materials, but not as clearly as could be expected on the basis of its shear strength/modulus. In applications requiring high weight to stiffness ratios, the AIREX® C70.75 and the AIREX® T91.100 gain in attractiveness. For the monolithic panel of polyurethane (AIREX® PXw.320) continuous fiber combined with woven roving reinforcements, impact energy absorption comparable to the foam cores was found. As a matter of fact, this material could be used as a substitute for plywood or even for some sandwich parts, where the weight to stiffness ratio is not crucial.

For a more thorough investigation and validation of the impact test equipment, the test procedure and the different types of core materials, a statistically more relevant number of panels made from different core materials, should be tested.

As a further consequence from the above results on energy absorption, tests should be performed to further investigate the influence of the strength, stiffness and stress-strain behavior of the skin laminate, which might dominate the results obtained in the present work.

6 REFERENCES

[1] L. Berger, R. Stadelmann, C. Dransfeld, K. Loiselet, S. Derler and R. Stämpfli, *in Proc. 22nd SAMPE Europe Conference, Paris,* SAMPE Europe, Aalsmer 2001, pp. 549-560

[2] M. Morgenthaler, L. Berger, P. Fritzsche, I. Wyss, J. Müller, S. Derler and R. Stämpfli, *in Proc. 24th SAMPE Europe Conference, Paris,* SAMPE Europe, Aalsmer 2003, pp. 213-220

[3] F. Dürig und I. Lüthi, *Impactverhalten von Faser-Kunstoff-Verbunden für die Transportindustrie*, Diplomarbeit, Fachhochschule Nordwestschweiz (2007)

[4] MATLAB User's Guide

[5] J. Müller, P. Fritzsche, W. Berchthold, Ch. Kissling, C. Dransfeld and R. Stadelmann, *in Proc. 5th Int. Conf. Sandwich Constr., Zurich,* EMAS, Solihull, UK, 2000, pp. 719-726

TESTING

ADVANCED MECHANICAL TESTING OF SANDWICH MATERIALS

Brian Hayman[*]**, Christian Berggreen**[†]**, Claus Jenstrup**[†] **and Kasper Karlsen**[†]

[*] Section for Structural Integrity and Laboratories, Det Norske Veritas AS, N-1322 Høvik, Norway
and
Department of Mathematics, University of Oslo, PO Box 1053, Blindern, N-0316 Oslo, Norway
e-mail: brian.hayman@dnv.com, web page: http://www.dnv.com and http://www.math.uio.no

[†] Department of Mechanical Engineering
Technical University of Denmark
Nils Koppels Allé, Building 403, DK-2800 Kgs. Lyngby, Denmark
e-mail: cbe@mek.dtu.dk, web page: http://www.mek.dtu.dk

Key words: Sandwich structures, Experimental mechanics, PVC cores, Face laminates, Digital Image Correlation, DIC.

Summary. *An advanced digital optical system has been used to measure surface strains on sandwich face and core specimens tested in a project concerned with improved criteria for designing sandwich X-joints. The face sheet specimens were of glass reinforced polyester and were tested in tension. The core specimens were of PVC foam and were tested in compression. The tests were performed in order to validate the use of the measurement system on these materials and to obtain material data for use in numerical simulations. While some limitations were identified, the optical system performed well and appears suitable for use in such a context.*

1 INTRODUCTION

The advent of advanced digital optical equipment for measuring and recording the deformation of materials and structures under mechanical loadings is providing a vast range of new capabilities in laboratory testing. Such a Digital Image Correlation (DIC) system (ARAMIS 4M), based on photo-grammetric and speckle interferometric principles with the use of two digital cameras, has been used to measure surface strain fields on sandwich face and core material specimens and on structural specimens representing an X-joint at a typical bulkhead-deck junction in a composite sandwich ship [1]. The structural sandwich specimens consisted of full X-joint specimens tested under compressive loading and beam specimens subjected to face pull-off loading. The results of these beam and X-joint tests have been presented, and compared with numerical simulations, in previous publications [2,3,4]. The current paper describes the face and core material tests, which were performed in order to validate the use of the measurement system on these materials and to obtain material data for use in the numerical simulations. A further objective was to compare measured elastic properties for foam cores with previously unpublished results from earlier studies.

2   FACE LAMINATE TESTS

2.1 Purpose

The sandwich face sheet material is a quasi-isotropic laminate consisting of a polyester matrix with four non-crimp E-glass reinforcement mats of type Devold DBLT 850-E10-1. Linear-elastic properties and the ultimate strength were required for use in finite element modelling studies on the X-joints using ABAQUS. The objectives of the tests were to obtain the required material properties in tension, to verify the accuracy of the DIC system, and to check for non-uniformity of the stress distribution in a way that is not possible using conventional instrumentation systems.

2.2 Laminate test specimens and test procedure

Face laminate tensile tests were performed in accordance with ISO 527-1 [5], using four parallel-sided specimens of type 3 according to ISO 527-4 [6]. These specimens, referred to here as type L, were 25 mm wide by approximately 3 mm thick and fitted with bonded aluminium tabs 150 mm apart. Three additional specimens of "dog-bone" shape, type 1 according to ISO 527-4, were also tested. These are designated here as type TL specimens.

The testing was performed in two stages. A speckle pattern was applied to one face of each specimen for use with the DIC system. In the first stage a conventional extensometer was also attached to the middle region of the specimen. The Young's modulus E and Poisson's ratio v were estimated from the measurements. In the second stage the extensometer was removed and the test continued to failure.

2.3 Elastic modulus

The tensile stress was calculated by dividing the load applied by the test machine by the mean cross-sectional area of the specimen in the central region. In the linear-elastic range the longitudinal strain was obtained by three methods:

- Directly from the extensometer
- Indirectly from the DIC system by taking the change in distance between two fixed points (stage points) P1 and P2 approximately 25 mm apart on the longitudinal axis of the specimen and dividing by the original distance between them.
- Directly from the DIC system for a point P0 close to the centre of the specimen

The stress-strain relations obtained for the four L-type specimens based on strains established by the first and second methods showed very close agreement. There was some variation between the four specimens, but this was extremely small in the initial, linear region. The results obtained by the third method showed some oscillation but otherwise agreed well with the first and second methods. Each digital image is divided into a number of small facets used for strain/displacement calculation and position identification in the two digital images for each load stage [7]. The oscillation in the direct DIC strain results is believed to have been caused by the selection of a smaller than optimal facet size. Figure 1 shows the results from each of the three methods, averaged for the four type L specimens. It also shows the averaged

results for the type L specimens tested in the elastic regime, for the type L specimens in the initial part of the ultimate strength test, and for the type TL specimens. From the right-hand plot a value 14.5 GPa is concluded for the elastic modulus in the longitudinal direction of the specimens.
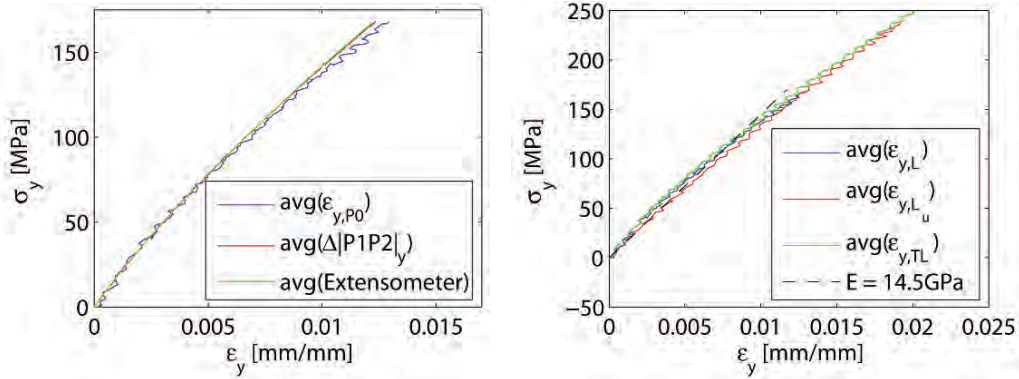

Figure 1: (Left) Plot of average results from all four L-type laminate specimens in tension. The results are from the point strain, point-point distance and extensometer measurements, respectively. (Right) Averaged stress-strain relations in the elastic regime for the different specimen types.

2.4 Poisson's ratio

From the DIC measurements it was possible to obtain the transverse strain ε_x as well as the longitudinal strain ε_y, thus enabling a direct estimation of Poisson's ratio for the laminate. Figure 2 shows the ε_x-ε_y plot obtained from three different sets of measurement data:

- The average strain readings from the tests on the four parallel-sided type L specimens in the linear-elastic range
- The average strain readings from the ultimate strength tests on the four type L specimens
- The average strain readings from the ultimate strength tests on the three dog-bone type TL specimens
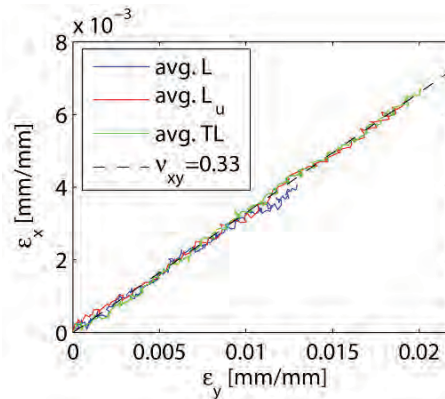

Figure 2: Plot of transverse strain against longitudinal strain for laminates, averaged for each test/specimen type, with trendline.

Also shown in Figure 2 is the straight line given by $\varepsilon_x/\varepsilon_y = 0.33$, which gives a very good fit to all the test data. Thus it is concluded that Poisson's ratio v_{xy} may be taken as 0.33 for this laminate material.

2.5 Ultimate strength

Figure 3 (left) shows the DIC images for the longitudinal strain ε_y in the four type L specimens at approximately the same load level, close to the ultimate strength. These demonstrate that there are strain concentrations in the regions adjacent to the aluminium tabs, but these concentrations decay over a distance less than 15 mm. Otherwise the strain levels are quite uniform over the specimen surfaces. In these specimens fracture was initiated in the regions close to the tabs, while in the dog-bone specimens fracture occurred close to the end of the region with reduced width (Figure 3, right).
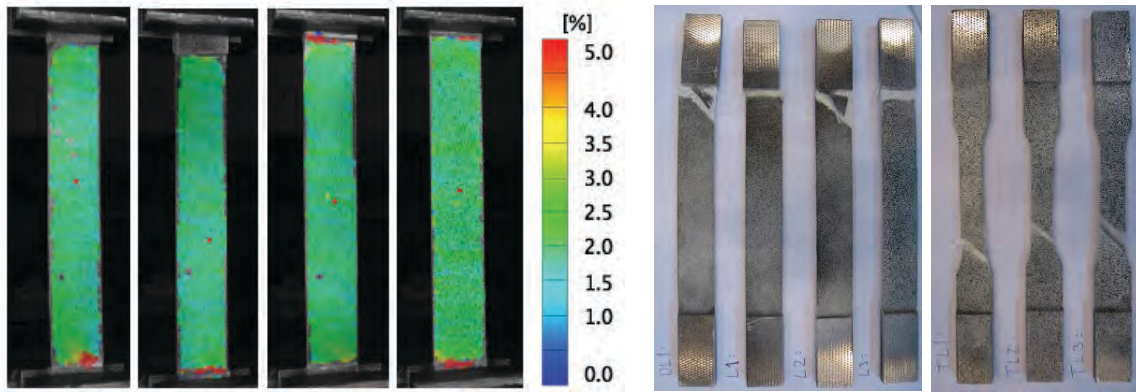
Figure 3: (Left) Longitudinal tensile strains in four face laminate specimens at approximately equal load levels approaching failure, from DIC measurements. (Right) Laminate specimens after testing to failure.

Specimen	Strain (%)	Stress (MPa)
L1	2.13	277
L2	2.44	253
L3	2.60	251
L4	2.85	259
TL1	2.02	275
TL2	3.21	270
TL3	2.48	276
Mean	2.53	266
Std. deviation	0.41	11
COV	0.16	0.04

Table 1: Ultimate strains and stresses for laminate specimens

Table 1 shows the stress and strain at failure for each of the specimens tested. The stresses are obtained by dividing the maximum load recorded by the test machine by the area of cross-section of the specimen. The strains are those indicated by the DIC system at distances greater than 15 mm from the end tabs. Note that the scatter in strain values is much greater than the scatter in stress values.

3   FOAM CORE COMPRESSION TESTS

3.1 Background and purpose of tests

The sandwich core material studied is Divinycell H200, a structural closed-cell PVC foam of nominal density 200 kg/m^2. Material properties for this material were required for use in modelling studies on the sandwich X-joints. The main focus was on obtaining properties for use with the non-linear crushable foam material model in ABAQUS, but the elastic properties were also studied.

The establishment of linear and non-linear properties for foam core materials presents special challenges because the material is in practice neither homogeneous nor isotropic. It is common practice in modelling of sandwich structures to neglect these effects, however, at least as far as the linear-elastic properties are concerned. Thus linear FE modelling requires the selection of a Young's modulus value E and a Poisson's ratio value v that give the best representation of the response. Given these properties, and assuming isotropic behaviour, the shear modulus G is given by the well-known relationship

$$G = \frac{E}{2(1+v)} \tag{1}$$

A further elastic modulus that is sometimes of interest for sandwich structures is the effective modulus E' for deformation in the thickness direction when the sandwich face sheets, which are much stiffer than the foam core, inhibit in-plane deformation. This modulus is needed, for example, when calculating the natural frequency for through-the-thickness vibrations. For the limiting case when in-plane strains are totally prevented, it can be shown from the three-dimensional Hooke's law relationships that

$$E' = \frac{E(1-v)}{(1+v)(1-2v)} \tag{2}$$

Note that, for $v = 0.3$, $E'/E = 1.35$ whilst for $v = 0.4$, $E'/E = 2.14$. During tensile or compressive testing of foam core specimens there is often some uncertainty about the extent to which strains perpendicular to the loading direction are restricted by the conditions at the interface between the test specimen and the test fittings. If the test specimen is bonded at its ends these strains are clearly inhibited at the ends but the effect of the restraint will decay as the distance from the ends increases. In a compression test without bonding there may be significant frictional stresses at the specimen ends that produce a similar effect. This throws some doubt on the accuracy of measurements of both E and v when carried out on specimens whose length in the load direction is not significantly greater than the transverse dimension.

In the late 1980's some limited tests (hitherto unpublished) were carried out at Det Norske Veritas to find the effective E and v values for a Divinycell H200 foam by a novel method. Firstly the shear modulus G for out-of-plane shear deformation was measured by a conventional block shear test in accordance with ISO 1922 [7]. Then a test was performed to measure E' directly. This was performed by bonding a disc of core material 30 mm thick and 280 mm in diameter between two thick, steel discs of slightly larger diameter. This was then tested in compression and the relative movement of the two steel discs was measured using LVDTs at opposite ends of a diameter. Two such specimens were tested and the mean of the two results taken. The test results indicated $G = 89$ MPa (which agrees well with the value 90 MPa stated in the manufacturer's data sheet at that time) and $E' = 466$ MPa. The elastic properties back-calculated from these results using equations (1) and (2) were $E = 246$ MPa and $v = 0.38$, which are quite different from those being quoted by the manufacturer and others at the time. The elastic modulus being quoted by the manufacturer for compression was 390 MPa, which lies between the E and E' values obtained from the DNV tests. The value of Poisson's ratio being quoted by the manufacturer was 0.32.

In 1996, tensile tests on the H200 material were carried out at the Norwegian Defence Research Institute as part of the project EUCLID RTP3.8 [9]. These tests, whose results have not been previously published, used a fairly long, cylindrical specimen with conical ends. Extensometers were fitted to measure both longitudinal and transverse strains. Similar tests were performed in compression but using cube-shaped specimens. The tests confirmed the value of Poisson's ratio found previously by DNV: a value of 0.37 was found from the tensile tests and a value of 0.39 from the compressive tests. The measured mean tensile modulus in the thickness direction was 256 MPa, just 4% higher than DNV's value, the values agreeing within the experimental scatter. The measured mean compressive modulus was 319 MPa, but, as mentioned above, this was from cube-shaped specimens in which there may well have been some restraint of transverse deformation. For limitingly small stress levels one would expect the tensile and compressive moduli to be equal. Modulus values were also obtained for specimens cut from material in such a way that they were loaded in the in-plane direction of the core sheet. These showed somewhat lower modulus values in both tension and compression, confirming that the material is not isotropic.

Branner [10] made a detailed study of predictions of elastic properties of structural foams and showed that values of Poisson's ratio between 0.35 and 0.4 could be expected from theoretical considerations for a typical PVC foam in this density range. However, like the manufacturers, he quoted 0.32 as a most typical value.

The availability of the DIC measurement system opened up for a more thorough study of elastic properties, including Poisson's ratio, as it makes possible the direct simultaneous measurement of longitudinal and transverse strains and captures the variation of these strains over the surface of a specimen.

3.2 Foam core test specimens and procedure

Four different specimen types were used for testing the foam core material (Figure 4):

- Square cross-section specimens with tapered ends, as specified in ISO 844 [11]; the prismatic part is a 50 x 50 x 50 mm cube. These specimens are designated type Q.
- Circular cross-section specimens with tapered ends, as specified in ISO 844 [11]; the prismatic part is 50 mm high with 50 mm diameter. Designated type C.
- Rectangular block specimens, 70 x 70 x 50 mm without tapered ends, designated *cube*.
- Circular cylindrical specimens 50 mm high with 50 mm diameter, without tapered ends, designated *cyl*.
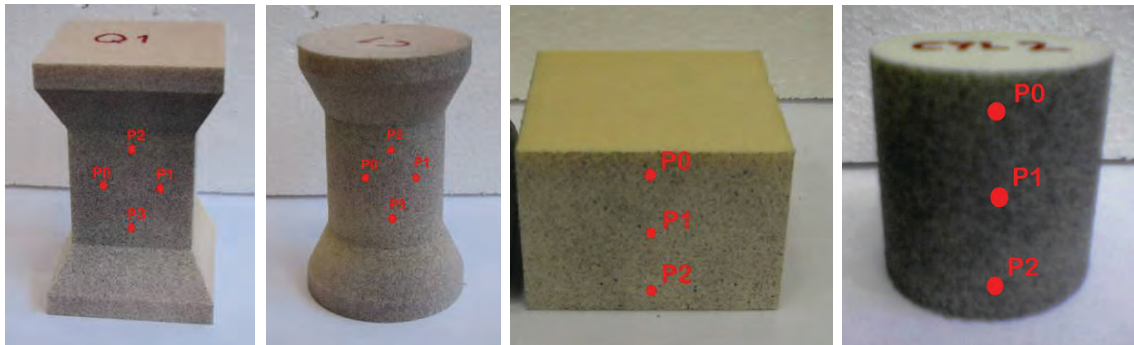
Figure 4: The four types of foam core specimens for compression testing (Q, C, cube and cyl), with approximate indications of stage point locations

For each Q type specimen the test was performed in two stages, the first being within the elastic range and the second proceeding well into the crushing and densification ranges. One face of each specimen was prepared with a speckle pattern for the DIC system. This enabled surface displacements and strains to be determined in both stages of the tests. A conventional extensometer with gauge length 25 mm was used in addition to measure axial strains in the first (elastic) stage. For all other specimen types the specimen was subjected to a single test covering the elastic, crushing and densification ranges, with the DIC system in operation but without the use of an extensometer. In the elastic range the results were used to obtain values of Young's modulus and Poisson's ratio, in addition to displaying information about variation of strain levels over the specimen surface. This is particularly interesting for the material in question in view of the comments made in Section 3.1. In the non-linear range the results were used to establish the full stress-strain curve for use with the foam crushing material model.

3.3 Elastic modulus

In the elastic range the responses were processed for the five Q-type specimens in the same three ways as described for the corresponding laminate tests (Section 2.3). The three strain measurement methods were found to be consistent. Figure 5 shows the point strain pictures for strains in the loading direction for three of these specimens when subject to approximately the same load level. In each specimen some strain concentration is observed at the transition to the tapered part. Otherwise the strains are fairly uniform over the face, though there is some

evidence of slightly increased strain in the central region of the right-hand specimen; this is probably be due to a slightly lower density in this region, which is quite common in sheets of foam material.

Figure 6 (left) shows the results from each of the three methods, averaged for the five type Q specimens. Figure 6 (right) shows the averaged results for the Q, C and "cyl" type specimens obtained directly from the DIC system for the centre stage points, and taken somewhat beyond the elastic range. For the Q type specimens the figure includes both the initial test confined to the elastic range and the second test (denoted Q_u) carried on into the non-linear range. In the elastic range the plots are compared with the line representing $E = 250$ MPa. This value agrees very closely with the results reported from previous studies in Section 3.1.
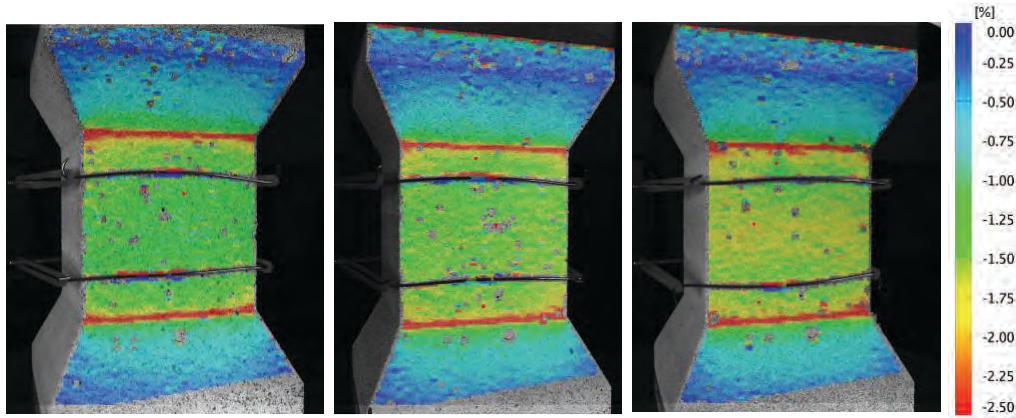
Figure 5: DIC images of longitudinal strain in foam core specimens Q3, Q4 and Q5 exposed to approximately the same magnitude of compressive loading.
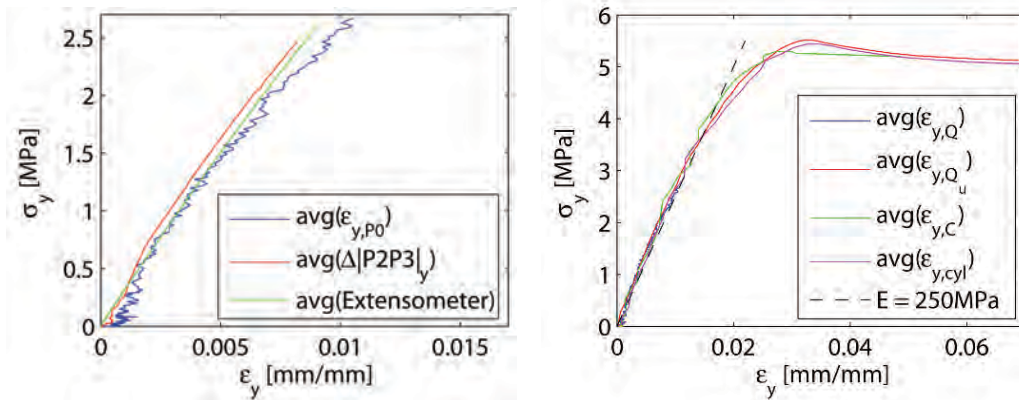
Figure 6: Stress-strain curves for foam core specimens (left) averaged values for Q-type specimens for each measurement method, and (right) averaged values for each specimen/test type obtained from point strain measurements at centre of specimen face..
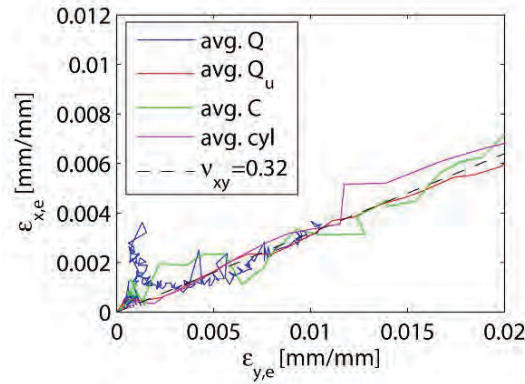
Figure 7: Transverse strain ε_x plotted against the longitudinal strain ε_y, for foam core, averaged results for each specimen type/test, showing also the line implied by Poisson's ratio = 0.32.

3.4 Poisson's ratio

Figure 7 shows the transverse strain ε_x plotted against the longitudinal strain ε_y, as was done with the laminate test results. These results are based on the average figures for each of the four specimen types, using the DIC point strain measurements. It is seen that, at low strain levels, the Q type specimens give highly irregular results, most likely due to a small misalignment of the loaded specimen surfaces, which introduce a slightly uneven initial strain distribution in the specimens. The results are otherwise reasonably compatible with a Poisson's ratio of 0.32, the data sheet value. However, an adequate fit is also obtained with v = 0.35. Although inconclusive, these results do not appear to support the values of about 0.38 reported from earlier tests in Section 3.1.

3.5 Non-linear response

In the inelastic range the DIC system was found to be able to cope with compressive strains up to about 20%; beyond this the surface became too distorted for the software to continue recognising the speckle pattern, so that the only way of estimating strains was to use the test machine cross-head displacement. While this can be expected to introduce some error, it is considered acceptable at such large strains as were achieved in the tests and in view of the low stiffness of the specimen to that of the loading arrangement in the test machine. Figure 8 shows vertical compressive strains from the DIC system at two load levels in the crushing regime. The deformation is seen to be somewhat concentrated in the central part of the specimen, where the density is lowest.

Figure 9 shows stress-strain relations derived for the "cyl" and "cube" type specimens. The left-hand graph shows nominal engineering strains while the right-hand graph shows "true" logarithmic strains. Following the initial, linear-elastic regime, a crushing regime is seen, during which the stress increases more slowly with increasing strain. The strain at crushing initiation was found to be in the region of 2% for all the specimens tested. Finally, for strains above about 44% densification of the foam occurs. Both graphs show in addition two straight

lines that can be used to approximate the material response by means of two stiffnesses representing the crushing and densification regimes.
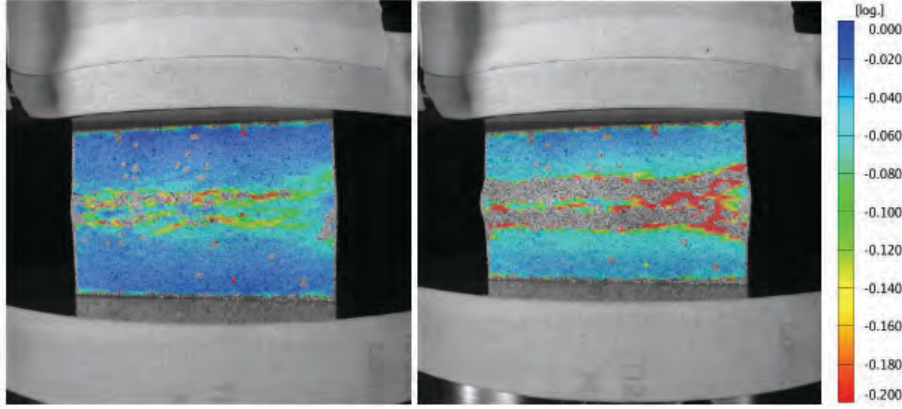

Figure 8: Compressive strains in a rectangular foam core specimen at two load levels in the crushing regime, showing concentration of deformation in the central region at which the density is lower.
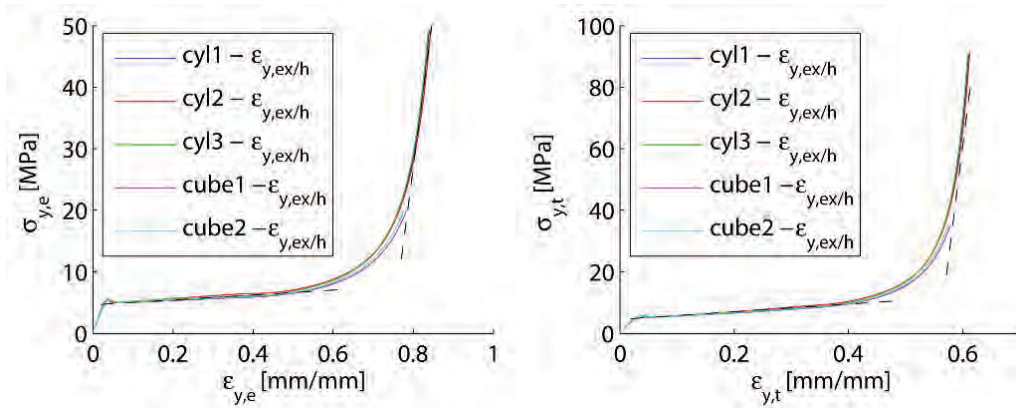

Figure 9: Stress-strain relationships for the foam material with nominal engineering strain (left) and "true" logarithmic strain (right)

CONCLUSIONS

Material properties for use in finite element analysis of sandwich structures have been obtained from tests on Divinycell H200 core with the assistance of an advanced optical strain measurement DIC system. In the linear-elastic regime measurements by the DIC system showed good consistency with traditional extensometer measurements and good agreement was achieved when comparing with earlier measurements of both E-modulus and Poisson's ratio. In the non-linear regime, where conventional extensometer measurements are difficult to perform without damage to the extensometer, the DIC system continued to perform well; in the case of the foam core it could measure strains up to about 20%. Stress-strain relations were measured successfully clearly indicating both crushing initiation and densification. The

test method demonstrated here makes it possible to acquire in a simple and uncomplicated way advanced stress-strain material data for foam materials.

ACKNOWLEDGEMENTS

REFERENCES

[1] K. Karlsen and C. Jenstrup, *Design of core inserts in sandwich X-joints – Experimental and numerical analysis*, MSc Thesis, Department of Mechanical Engineering, Technical University of Denmark, (2007).

[2] C. Berggreen, C. Lundsgaard-Larsen, K. Karlsen, C. Jenstrup and B. Hayman, "Improving performance of polymer fibre reinforced sandwich X-joints in naval vessels – Part I: Design aspects", *16th Int. Conf. on Composite Materials, Kyoto, Japan*, (2007).

[3] C. Lundsgaard-Larsen, C. Berggreen, K. Karlsen, C. Jenstrup and B. Hayman, "Improving performance of polymer fibre reinforced sandwich X-joints in naval vessels – Part II: Damage Tolerance", *16th Int. Conf. on Composite Materials, Kyoto, Japan*, (2007).

[4] B. Hayman, C. Berggreen, C. Lundsgaard-Larsen, K. Karlsen, and C. Jenstrup, "Design of X-joints in sandwich structures for naval vessels", *PRADS 2007, Houston, Texas, USA*, (2007).

[5] ISO 527-1:1993, edition 1, *Plastics – Determination of tensile properties – Part 1: General principles*. International Organization for Standardization (1993).

[6] ISO 527-4:1997, edition 1, *Plastics – Determination of tensile properties – Part 4: Test conditions for isotropic and orthotropic fibre-reinforced plastic composites*. International Organization for Standardization (1997).

[7] J.D. Helm, S.R. McNeill and M.A. Sutton, "Improved three-dimensional image correlation for surface displacement measurement", *Optical Engineering*, 35(7), 1911-1920 (1996).

[8] ISO 1922:2001, edition 3, *Rigid cellular plastics -- Determination of shear strength*. International Organization for Standardization (2001).

[9] B. Hayman and A.T. Echtermeyer, "European Research on Composites in High Speed Vessels", *Fifth International Conference on Fast Sea Transportation (FAST'99)*, Seattle, USA, 1999.

[10] K. Branner, *Capacity and Lifetime of Foam Core Sandwich Structures*, PhD Thesis, Department of Naval Architecture and Offshore Engineering, Technical University of Denmark, Kongens Lyngby, Denmark (1995).

[11] ISO 844:2007, edition 5, *Rigid cellular plastics -- Determination of compression properties*, International Organization for Standardization (2007).

SHEAR STRENGTH CHARACTERIZATION OF PUR-FOAM CORE BY MODIFIED 4-POINT BENDING TESTS

Jörg Feldhusen, Sivakumara K. Krishnamoorthy and Martin J. Benders

Chair and Institute for Engineering Design (IKT)
RWTH Aachen University
Steinbachstr. 54 B, D-52074 Aachen
e-mail: feldhusen@ikt.rwth-aachen.de, krishnamoorthy@ikt.rwth-aachen.de,
benders@ikt.rwth-aachen.de, web page : http://www.ikt.rwth-aachen.de

Key words: Failure modes, Experimental methods, Shear strength, FEM, Sandwich beam

Summary: *This research show, how 3D FE-Tools can be effectively used in forcing conventional test specimen to fail predominantly under shear. Changing the dimension of the test specimen by attaching simple geometrical shapes is one way to achieve this. Guidelines for the determination of shear strength of PUR-Foam core by using standard 4-Point bending tests are given. These guidelines are based on numerical prediction using finite element analysis and experimental verification. The approach provided here can be carried out for both static and dynamic characterization of shear strength of sandwich materials.*

1   INTRODUCTION

Typically, cores are the weakest part of sandwich structures and they fail due to shear. Therefore, understanding the shear strength properties of sandwich core plays an important role in the design of sandwich structures subjected to flexural loading. Bending tests are often performed in understanding the flexural behavior of sandwich structures. In theory, this testing procedure could also be employed to determine the shear strength of the core material. But in practice, failure modes such as face wrinkling, local indentation or a combination of both occurs beforehand especially for low density PUR-foam materials. Zones prone to such a failure in a four point bending test bench are shown in Fig. 1. Because of these unwanted premature failure modes, core shear failure may not be realized easily in practice.
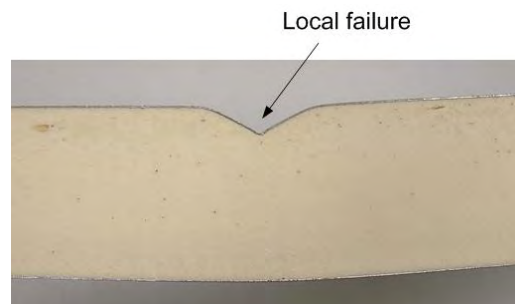

Figure 1: Local failure

The aim of this paper is to provide a guideline with the help of which, sandwich beams with low density foam core materials can be forced to fail predominantly under shear stresses. Hence shear strength of the sandwich core can be determined. Some advantages of determining shear strength using four point bending test by avoiding conventional shear testing standards such as DIN 53 294 [1] or ASTM 273 00 [2] include:

- No additional acquisition or production costs and reduced time consumption in preparing additional test specimens.
- The specimens undergo rather in-service testing conditions.
- The determined strength value strongly considers uncertainties in manufacturing, for instance the material in-homogeneity within the core. During testing, the sandwich beam undertakes shear loadings along two different regions that lie between the inner and outer support of the test bench. With similar testing conditions, the weaker region is the one to fail first under shear. Hence overestimating the shear strength of sandwich core can be effectively avoided.

The failure mode of sandwich structure depends on the loading configuration of the structure, its material properties and the geometry of the structure [3]. Hence by modifying the geometry of the structure, the desired failure mode (core shear failure) could be achieved. Fig. 2a shows the core shear failure of the sandwich beam with PUR-foam core under a 4-point bending test done at the institute. In this case, the geometry of the beam is modified by gluing thin metal plates with a thickness of about 1.5 mm to the sandwich beam. These plates are placed above the lines of force transmission of the sandwich beam to overcome the face wrinkling failure mode of the structure. The region in between outer and inner roller supports of the sandwich beam (Fig. 2b) is defined in this paper as *shear zone*.
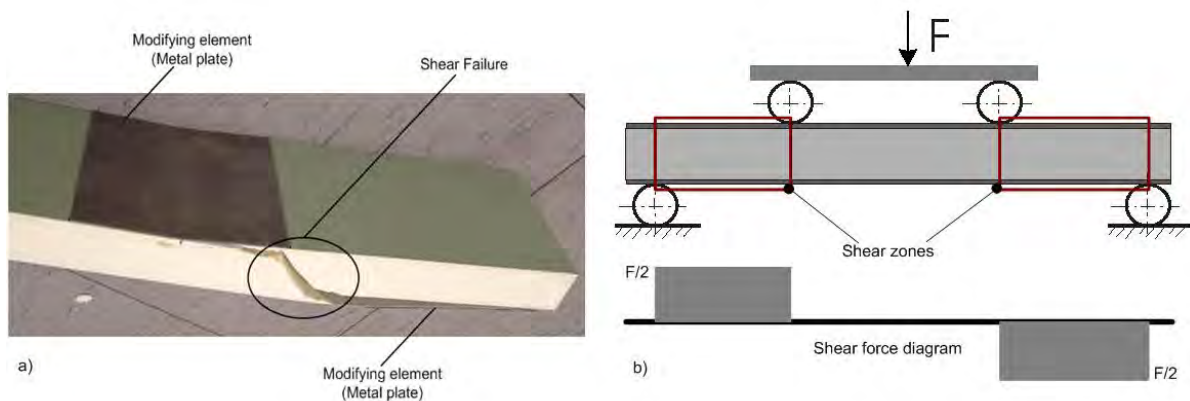

Figure 2: a) core shear failure; b) shear zones

Although pure shear conditions cannot be achieved in a 4-point bending test bench, the dimensions and the shape of the modifying element can be varied in such a way that the secondary stresses i.e., compressive and tensile stresses at the failure region are negligible. Analytical calculations to determine local stress distribution or failure modes for such a

Jörg Feldhusen, Sivakumara K. Krishnamoorthy and Martin J. Benders

geometrically modified beam are quite difficult to obtain. Therefore, 3D finite-element analysis is used to understand the mechanical behavior of modified beam structures. The shape and the dimensions of the modifying element are varied systematically using FEM until the structure fails predominantly under shear.

2 MODIFYING ELEMENT- A SYSTEMATIC APPROACH

The modifying element shall enable smooth force transmission from the bending text fixture to the sandwich beam by maximizing shear stresses and minimizing localized compressive stresses at the shear zones. Hence the dimensions are to be carefully chosen so that important parameters are not neglected. Systematic variation of working surfaces of the modifying element is one way to avoid the negligence of important parameters. In the Table 1, few possible variants are shown. Finding the appropriate shape and topology of the variants 2 and 3 in Table 1 by using commercial topology or shape optimization software's could be useful in an academic point. But in a practice, this idea could not be quite satisfactory because it incorporates additional manufacturing effort, cost and time. Hence in this work, the shape variants 2 and 3 are not investigated using numerical simulation.
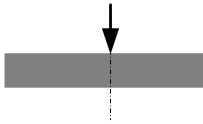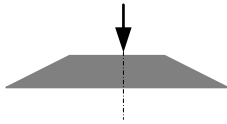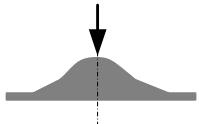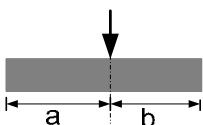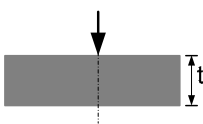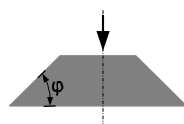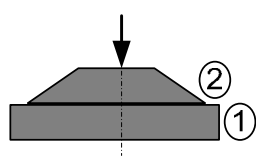
Variants	1	2	3
Shape and Topology			
Position		Variables: a, b	
Size	Variable thickness t	Variable angle φ	
Number			

Table 1 : Variants of the modifying elements

3 NUMERICAL SIMULATION AND THEORY

The FEM-Software ALGOR^{TM} is used for the simulation of sandwich structures. The structure is appropriately modeled and discretized to achieve solution convergence. Detailed approach of 3D-modeling and simulation of sandwich structures using commercial FE-Softwares is provided in literature [4]. The results obtained from simulations are used to understand the distribution of 3-dimensional tensor stress components $\sigma_{XX}, \sigma_{YY}, \sigma_{ZZ}, \sigma_{XY}, \sigma_{YZ},$ and σ_{XZ} of sandwich core. The coordinate system and the beam dimensions are shown in Figure 3. These dimensions are chosen in accordance with DIN 53293 [5]. Previous investigations with simple modifying elements have shown that the consideration of the stress components $\sigma_{XX}, \sigma_{ZZ}, \sigma_{XZ}$ and σ_{XY} at the shear zones is trivial, because the magnitudes of these components are negligible in comparison with the magnitudes of the compressive (σ_{YY}) and shear (σ_{YZ}) components. Hence the aim of numerical simulation is to provide guidelines with which σ_{YZ} components are maximized and σ_{YY} components are minimized, resulting in an almost pure shear failure at the shear zones. The shape of the modifying elements is kept as simple as possible, but its influence in minimizing σ_{YY} components by variation of its position, size and number is investigated further.
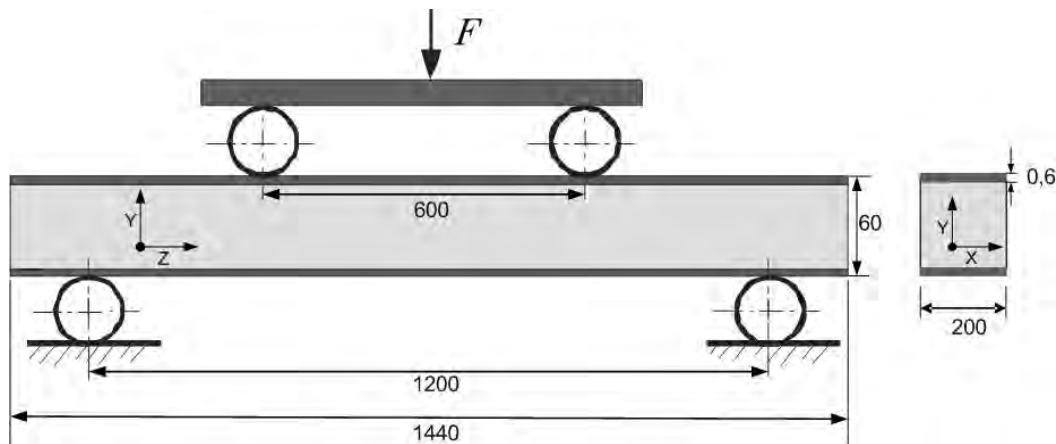

Figure 3: Beam dimensions in millimeters

The material parameters Young's modulus (*E*), Shear modulus (*G*) and the density (ρ) of the sandwich beam considered here is presented in Table 2.

Sandwich material	*E* [MPa]	*G* [MPa]	ρ [kg/m^3]
Face (Steel)	200,000	75,500	7,800
Core (PUR)	14	5.93	75

Table 2 : Material Properties

3.1 Position study

The aim of this study is to generalize the influence of position of simple modifying elements (metals plates) in reducing compressive stresses in shear zone. The variables *a* and *b* specified here are defined in Table 1. Four metal plates with a thickness of 10 mm are attached along the line of transmission of forces. Three different scenarios are simulated in which the variable *a* is kept constant as 50 mm and the variable *b* is varied as follows; i) 70 mm, ii) 130 mm and iii) 220 mm. Where the variable *a* lis positioned outside shear zones and hence its variation is considered trivial. The beam is loaded with a force of 4 kN in a four-point bending simulation. Results of the simulations at shear zones can be seen in Figure 5. Here, only the tensor stress components σ_{YY} that cause unwanted compressive stresses are shown. It can be clearly seen that the variant iii) allows smooth transmission of compressive forces, whereas variants i) and ii) have strong stiffness incompatibilities. Hence for sandwich beams having relatively thin face sheets, following conclusion can be met. The variable b of the modifying element shall be so chosen, that they overlap each along the shear zones to minimize compressive stress components.

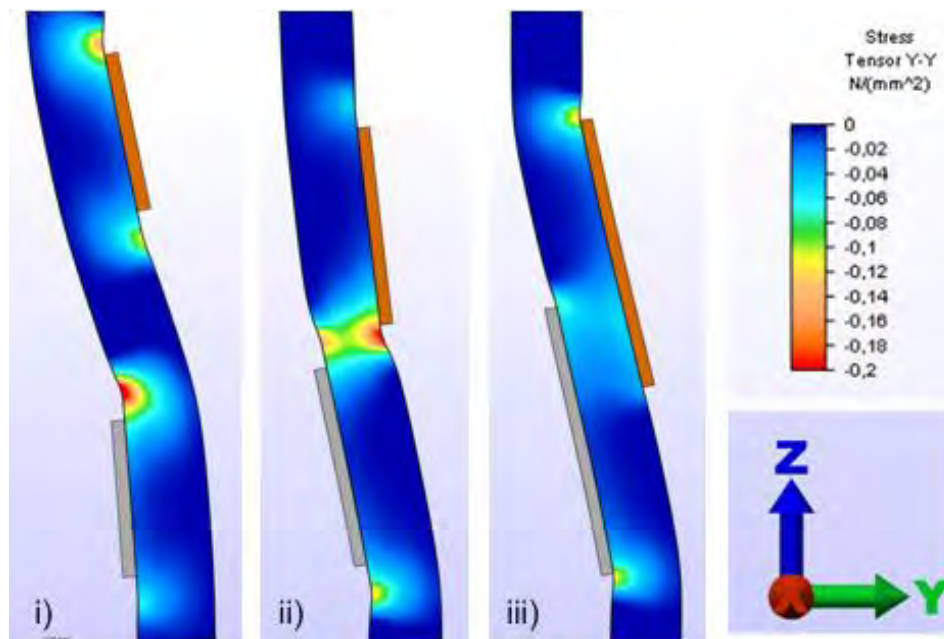Figure 4: Compressive tensor stress components

3.2 Thickness study

To understand the influence of thickness of the modifying elements, several simulations have been carried out with varying thicknesses. The dimensions *a* and *b* are chosen based on the previous study i.e. variant iii, where stiffness incompatibilities are relatively low. Table 3

shows the influence of thickness in determining the maximum compressive and shear stresses at shear zones for a load of 6 kN. These values are normalized stress components that are taken directly from the results of simulations. For illustration, the distribution of compressive stresses (σ_{YY}) and shear stresses (σ_{YZ}) in the core with modifying plates having a thickness of 1 mm is shown in figure 5. Here, attention shall be paid to the maximum values in the respective stress tensor scales.

Plate thickness (mm)	σ_{YZ} [MPa]	σ_{YY} [MPa]
1	0.29	0.37
2	0.27	0.25
4	0.24	0.13
10	0.125	0.08

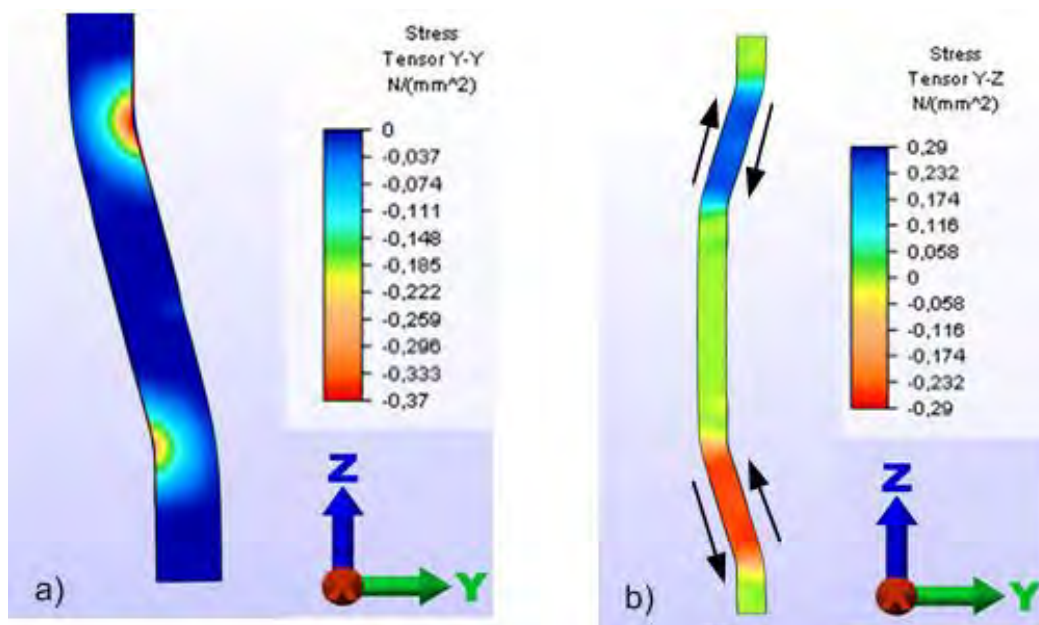Table 3 : Maximal shear and compressive tensor components in shear zones

Figure 5: a) compressive stresses at a shear zone; b) shear stresses at shear zones

Based on these results, three important conclusions can be met:

3.2.1 Firstly, both compressive and shear stresses in the shear zone reduces as the thickness of modifying plates increases. This idea can be used to improve the load carrying capacity of sandwich structures in practical applications.

3.2.2 Secondly, shear failure may not be realized at all by using modifying elements having thickness that are over-dimensioned due to probable occurrence of other failure modes outside shear zones. Hence thickness of the modifying plate shall be

carefully chosen by understanding the bending behavior of sandwich beam by considering its material and geometric properties.

3.2.3 Thirdly, it is obvious from the Table 3, that the thickness of the plate should be large enough at the line of transmission of forces to minimize compressive stresses and small enough at the shear critical zones to maximize shear stresses. This can be achieved by adding additional plate elements along the line of transmission of forces. For illustration, a simulation is carried out by changing the model shown in Figure 5, by adding additional plate elements with a thickness of 1 mm and a length 30 mm (Figure 6a). With this simple dimensional change, the maximum compressive stresses occurring at shear zones can be reduced approximately by 78% (Figure 6b). Here the maximum obtained values of the tensor components σ_{YZ} and σ_{YY} are 0.28 MPa and 0.08 MPa respectively. But unfortunately in this case, it can also be seen that the compressive stresses, in close vicinity to the shear zones is getting significant. This may lead to shear and local failure, if the compressive strength is weaker at this region. Hence in such situations the length of the additional plate element can be adjusted or the thickness of the modifying element can be enlarged (say 1.5 mm) to allow smooth transmission of forces.
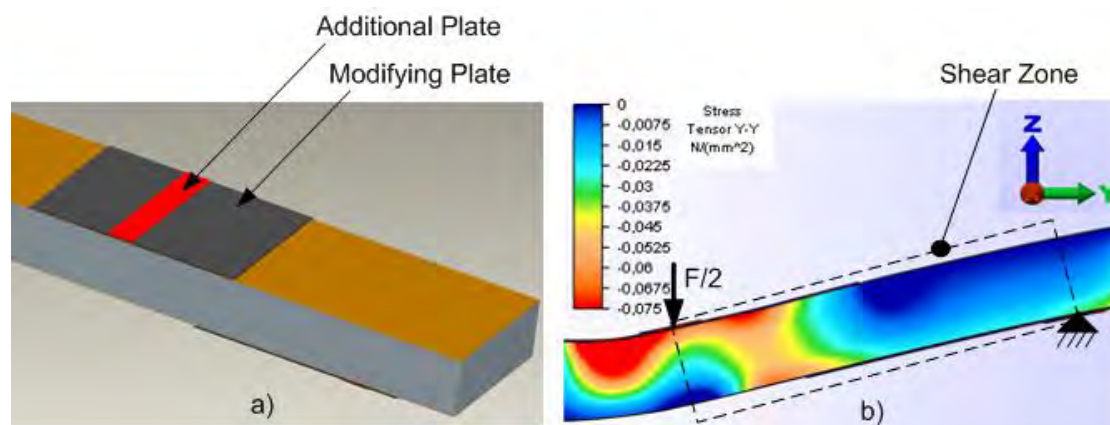

Figure 6: a) CAD Model; b) Compressive stresses with additional plate elements

3.3 Theoretical predictions – a comparison

Though for complex geometries, one cannot directly compare the maximum stress components of FEM-Simulations with simple sandwich beam theories, there are few advantages in doing so:

- Under circumstances where FE-Programs are not available, such comparisons would allow to choose an appropriate theory with which the shear strength of sandwich structures can be analytically determined.
- In all the above mentioned FE-Simulations, it is assumed that the properties of the core material are homogeneous throughout the structure. But in practice, due to the inconsistency in manufacturing, the strength properties of sandwich core materials

often vary from region to region. This may lead to strong deviations in experimental results. Here, it would be difficult to say if the deviation occurs due to modeling error or due to the manufacturing inconsistency. In such cases, the comparison of FEM-results with established theories would ensure the correctness of the FE-Modeling to a certain extent.

In this part of this paper, the shear stress calculation based on DIN 53293 [5] and Zenkert [3] in a bending test is compared with FE-simulations. According to DIN 53293, the shear stress (σ_{shear1}) of a sandwich beam in a four-point bending is given by;

$$\sigma_{shear1} = \frac{F}{2bd} \tag{1}$$

Where, b and d are respectively the breadth and thickness of the sandwich beam. In this formula, the material properties of the neither the core nor the face sheet is taken in to account. On contrary, the sandwich theory proposed in Zenkert considers both geometrical as well as material properties in calculating maximum shear stress (σ_{shear2}) in sandwich core and can be written as follows:

$$\sigma_{shear2} = \frac{F}{2bD}\left(\frac{E_f t_f (d - t_f)}{2} + \frac{E_c t_c^2}{8}\right) \tag{2}$$

$$D = \frac{E_c t_c^3}{12} + \frac{E_f t_f (d - t_f)^2}{2} + \frac{E_f t_f^3}{6} \tag{3}$$

Where, E_f and E_c are the elastic moduli of the face and core materials respectively. The thicknesses of the face and core materials are given as t_f and t_c respectively. The variable D represents the flexural rigidity of the sandwich beam. It shall be noted that the Formula 2 and 3 slightly differs from the one mentioned in Zenkert because of differences in the definition of variables in this paper. In Table 4, FE-Results are compared with theoretical predictions. The thickness d for these calculations is taken from the cross-section that results in maximum shear stresses. FE-Results have a very good correlation with theoretical predictions according to Zenkert for modifying plates having relatively small thickness, in this case up to say 4 mm.

Plate thickness (mm)	Max. σ_{YZ} [MPa]	Max. σ_{shear2} [MPa]	Max. σ_{shear1} [MPa]
1	0.29	0.29	0.248
2	0.27	0.27	0.244
4	0.24	0.25	0.236
10	0.125	0.22	0.216

Table 4 : Comparison of maximum shear stresses

4 EXPERIMENTAL VERIFICATION

4.1 Influence of thickness

Experimental results agree excellent with the numerical simulations. As suggested before, the load carrying capacity of the sandwich structure increases with the increasing thickness of modifying plates. Three different experiments have been carried out with modifying plates having thicknesses of 2 mm, 1.5 mm and 1 mm and the load at which the failure occurs is approx. 6.4 kN, 5.5 kN and 5.2 kN respectively. To reduce local compressive stresses by using 1 mm plate (see Fig. 5 a), additional plate elements are bonded as exactly as suggested in section 3.2.3. As predicted in this section, shear crack starts to propagate in the weaker shear zone (Fig 7a), but the failure occurs due to local compressive stresses at the vicinity of the shear zone. For the other two cases; plates with 2 mm and 1.5 mm thicknesses, the structure has failed predominatly under shear. Figure 7b shows shear failure with plate elements of 2 mm thickness.
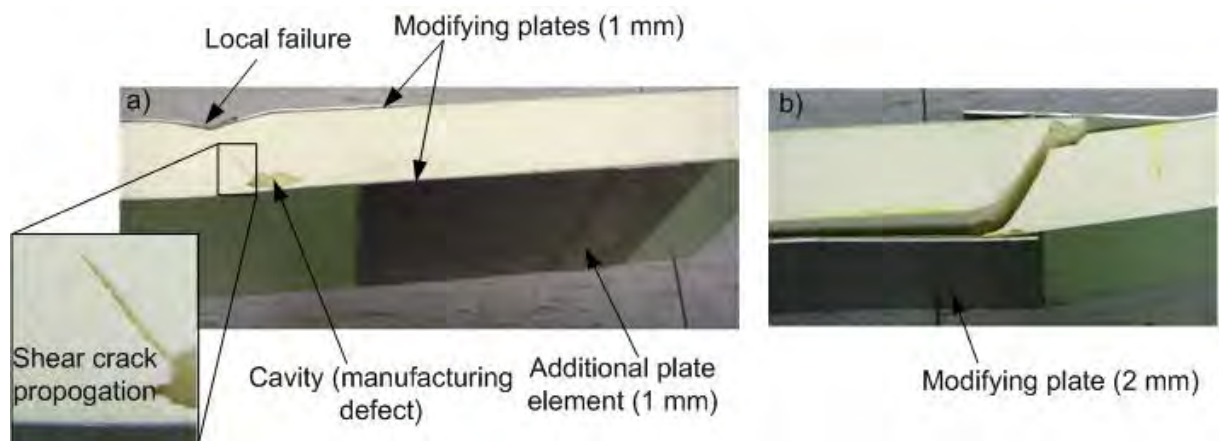

Figure 7: a) Local failure with shear crack propagation b) Predominant Shear failure

4.2 Influence of position

Three different experiments are carried out by varying the position of modifying elements as suggested in section 3.1, with plates having a thickness of 2 mm. The predominant mode of failure in all of these experiments is shear failure. However, the results are not consistent with the predictions using numerical simulation. It is expected that the plates that overlap each other at shear zones are the ones to have the largest load carrying capacity due to smooth transmission of compressive forces. But experiments show that the load carrying capacity varies randomly from ca. 6.4 kN up to ca. 6.7 kN without conforming to the predicted pattern. This non-conformity is only marginal and can be attributed to the manufacturing defects such as cavities in the core material (Figure 7a and Figure 8).
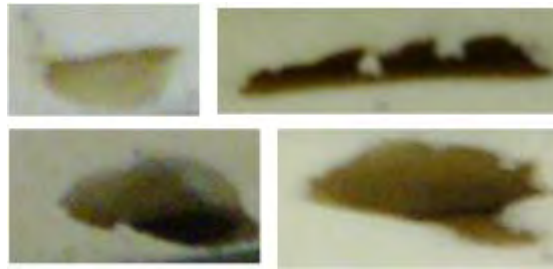
Figure 8: Inherent manufacturing defects in the core material

5 CONCLUSION

The thickness of plate elements has a determining role in finding the shear strength of sandwich core materials. Experimental results agree very well with FE- Simulations in this aspect. An almost pure shear failure can be obtained by using plates that have a varying thickness along the shear zone. One way to realize this in practice is by gluing additional plate elements. The length of such elements shall be determined beforehand using FE-Analysis to avoid stiffness discontinuities. Here the knowledge of the compressive strength of the core material would be helpful to avoid compressive failure in the vicinity of shear zones. Though the effect of the position of the plate element cannot be experimentally verified due to inherent manufacturing defects in the core material, the deviations of the failure loads are only marginal.

Based on this research, a guideline is given below to determine the shear strength of weak core materials. Although a predominant shear failure cannot be always guaranteed due to uncertainties in testing conditions, manufacturing etc., this guideline can still be used as a foundation based on which shear strength can be characterized in a 4-point bending test.

- The necessary linear-elastic parameters for numerical simulation shall be obtained from 4-point bending tests and compressive tests, if the test data are not available. The four-point bending test shall be performed until failure to understand the mode of failure. Furthermore, the compressive strength of the sandwich material shall be determined to avoid pre-mature failures outside shear zones.

- FE-Modeling and simulation of a four-point bending test shall be carried out to identify hotspots that cause failure in the above test. In case of low density foam core materials, these hotspots are typically the compressive stresses at the line of transmission of forces.

- Based on these results, the dimensions of the modifying elements have to be chosen (thickness, number and position) so that compressive stresses are minimized and shear stresses are maximized at shear zones. Performing hand calculations at first, as given in section 3.3 would give a rough estimate about the dimensions, rather than directly performing time-consuming simulations. Then FE-Simulations can be performed to quantify the dimensions of modifying elements.

- Sandwich beam with modifying elements and additional elements shall be tested in

a 4-point bending. If there is no predominant shear failure, FE-Modeling shall be revisited to identify the possible cause.

- In case of shear failure, few more specimens have to be tested to avoid over-estimations. All the load-values at which the structures fail shall be noted.
- Of all the measured failure loads, the least load-value shall be used for the estimation of shear strength of the sandwich core. In case of FE-Calculations, the shear value σ_{YZ} at the failure load can be taken as the shear strength of the core material. In case of hand calculations the least of σ_{shear1} and σ_{shear2} at the failure load shall be taken.

REFERENCES

[1] DIN 53294, Prüfung von Kernverbunden: Schubversuch, Feb 1982.

[2] ASTM C 273-00, Standard test method for shear properties of sandwich core materials, July 2000.

[3] D. Zenkert (Ed.), *The handbook of sandwich construction*, Cradley Heath, West Midlands, EMAS 1997.

[4] J. Feldhusen, S. Torsakul, A. N. Brezing and S. K. Krishnamoorthy, "An Approach to Numerical Modeling and Simulation of Cellular Foam Sandwich Structures in Commercial FE-Softwares", *Submitted to J. of Sandwich Structures and Materials,* 2007.

[5] DIN 53293, Prüfung von Kernverbunden: Biegeversuch, Feb 1982.

STUDY ON INDENTATION TEST METHODOLOGY OF AIRCRAFT FLOOR HONEYCOMB CORE SANDWICH COMPOSITE PANELS

H. Talebi Mazraehshahi[*], A. Vahedi[†], B. Hamidi Qalehjigh[†] and M.A. Vaziri Zanjani[†]

[*] Aerospace Engineering Department, Sharif University of Technology
Tehran, Iran
e-mail: h_talebi@alum.sharif.edu

† Aerospace Engineering Department, Amirkabir University of Technology
Tehran, Iran
e-mail: b_hamidi_g@yahoo.com
e-mail: av_vahedi@yahoo.com
e-mail: vaziry@hesaco.com

Key words: Floor composite Sandwich panel, Experimental test, Indentation.

Summary

The indentation behavior of aircraft floor panel (honeycomb sandwich structures) was investigated from the viewpoints of test methodology, effects of panel layout, and failure mechanisms. The aim was to achieve a design procedure for aircraft floor panels. Due to their high stiffness and strength to weight ratios, composite sandwich structures have proven their usefulness in a large number of applications in various technical fields, especially in aeronautics, automotive and civil engineering. One of the main drawbacks of sandwich structures is the loss of load carrying capacity due to indentation damages.

An indentation test method using a simply-supported plate was developed which can more accurately replicate observed in-use failure modes. The localization and type of damage induced with this test method correlated well with damage present in panels returned from airline. Such damages in real conditions are mainly due to highly concentrated loads from heels.

Indentation tests using various skin and core constructions demonstrated the influence of changing core density, core material, and skin construction on indentation damage resistance.

This paper presents the results of experimental investigation on civil Aircraft floor panels with sandwich composite construction. First, the BOEING Company procedure for indentation testing of floor panels is explained. Next, a new procedure will be presented, and the obtained results will be compared with those reported by Boeing procedure. The effects of varying parameters such as core material and density, and skin layer quantity on indentation test results were also investigated.

H. Talebi Mazraehshahi, A. Vahedi, B. Hamidi Qalehjigh and M.A. Vaziri Zanjani

1 Introduction

Aircraft flooring applications use honeycomb sandwich panels such that the primary loading is normal to the panel top surface such as from passengers, beverage carts, or other equipment. Gross behavior of the panels (bending and shear) as a result of such loading can be usually accounted for based on known design principles. However, localized deformation and damage in the panels resulting from surface loads in or around the immediate load contact areas have not been well understood. Several test methods exist for measuring properties related to localize loading of this nature, such as stabilized core compression, roller-cart testing and impact strength. These tests in one way or another often do not accurately represent the loading conditions of the panels in the aircraft.

Aircraft floor panels are often subjected to loading conditions close to static loads in addition to impact [1]. For example, passenger foot traffic alone could introduce substantial damage to the floor panels during service, especially in the under seat areas that usually have panels of lower core density than the aisleway area. Such damage is especially likely to be the result of concentrated loads such as from high-heel loadings that have a small contact area and thus impart large normal indentation pressures to the panel. The resistance of floor panel to this kind of damage and its accumulation often determines the usable life, or durability of the panels. Therefore, for panel performance assessment as well as for product development, damage resistance from concentrated loads on the upper panel surface is a crucial parameter to consider.

Figure 1 shows a general description of the damaged location in honeycomb sandwich flooring as it occurs due to in-service usage in aircraft [2]. Two types of panels are depicted. At the top of Figure 1 "dual-density" panel is shown. This panel is made of one skin, but with different cores; low density core for the underseat area, and higher density for the aisleways.The figures at the bottom of Figure 1 show low-density underseat panels in which the damage is created either directly in front of a seat in a narrow through (as shown on the left) or randomly distributed (as shown on the right). In general, where passenger movement on airplanes is restricted such as between seat rows or aisleways, damage tends to concentrate in areas as can be seen in Figure 1. Since passengers walk and stand up between the seat rows and because these areas are of lower density than the aisleways, these areas develop damage first when viewed visually, these damaged areas appear as dents or, when large, as depressions in the surface of panel.
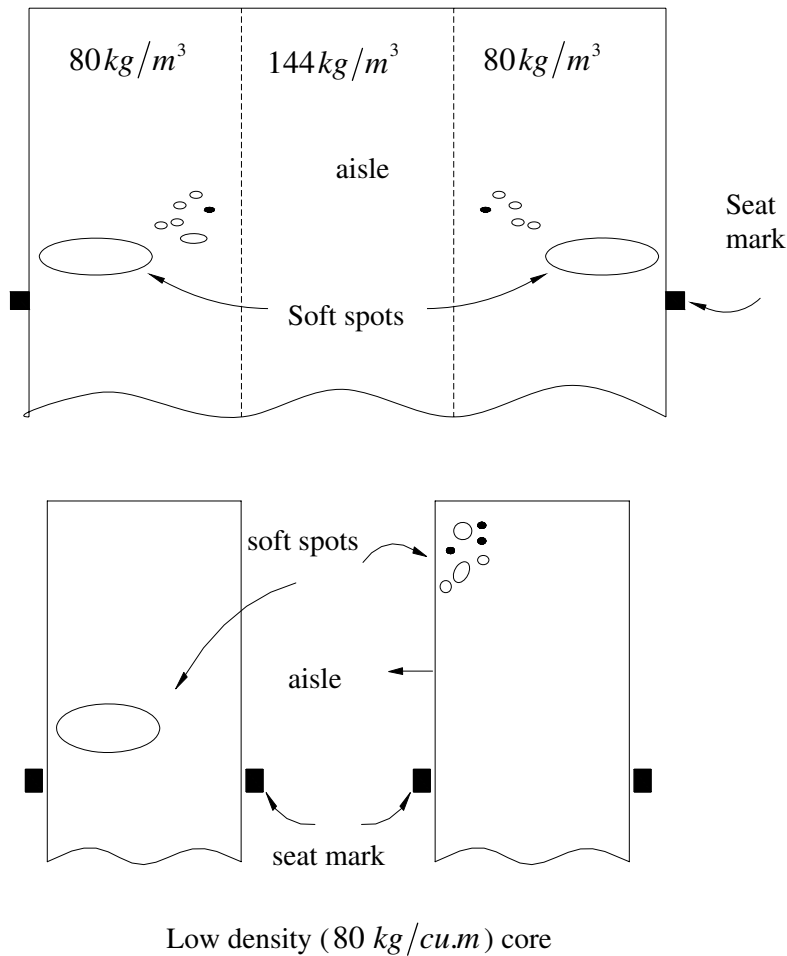
H. Talebi Mazraehshahi, A. Vahedi, B. Hamidi Qalehjigh and M.A. Vaziri Zanjani

Figure 1: Depiction of damage patterns observed in unidirectional cross-ply fiberglass-skinned,aramid core

(80 kg/m3) floor panels after removal from servic from an aircraft.

Previous usage of indentation testing to characterize aircraft floor panels has defined failure as being the existence of skin, adhesive, or core damage. Typically, the definitions have been related to visible damage phenomena such as a deformation, skin cracks, delimitation, and skin puncture. For example, permanent deformation may be used as a failure criterion by defining the first point at which a large increase in deflection occurs without a correspondingly large increase in load to be the failure load [2].

This paper reports a study on the indentation behavior of floor panels from the viewpoints of tests methodology, effects of panel constructions, and failure mechanisms. An indentation test method using a simply-supported plate is described to replicate observed in-use failure modes. Differences in the influence of varying panel constructions such as changing core density or skin weight are presented for stabilized core compression versus indentation. Additionally, the effects of changing indentation tup diameter have also been investigated.

2 INDENTATION TEST

In this section, two test procedures were compared with each other, namely the Boeing procedure with our proposed procedure.

2.1 Indentation test according to Boeing procedure

Indentation tests performed in Boeing procedure used a cylindrical steel indenter with a flat bottom face and chamfered edges with a diameter of either 6.35 mm(1/4 inch) or 12.7 mm(1/2inch). The indenter was used atop a 3.18-mm (1/8-in.) thick piece silicone rubber (to simulate aircraft carpeting) to compress the top surface of the panel. Test panels measuring 305 by 305 mm (12 by 12 in.) were simply supported along the edges (Figure 2).
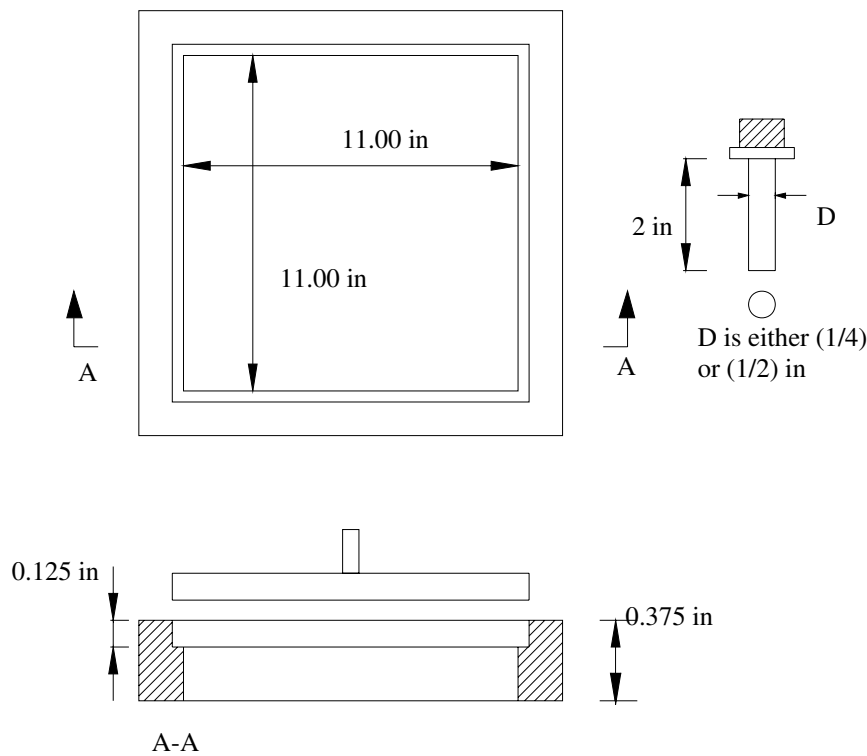
Figure 2: Schematic of indentation test fixture and indentation tup according to Boeing procedure [2]

2.2 Indentation test according to our proposed procedure

Indentation tests performed in our study used a cylindrical steel indenter with a flat bottom face and chamfered edges with a diameter of 12mm .The indenter was used atop a 2mm (0.08-in.) silicone rubber (to simulate aircraft carpeting) to compress the top surface of the panel. Test panels measuring 150 by 150 mm were simply supported along the edges (Figure 3).
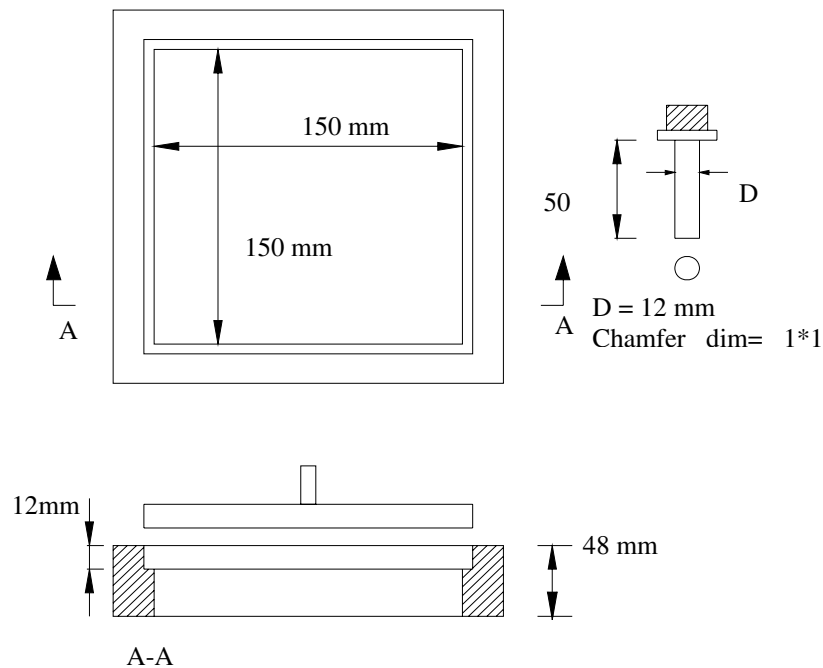
Figure 3: Schematic of indentation test fixture and indentation tup according to our proposed procedure

Damage determined by monitoring load versus displacement and noting points at which a distinct load drop or slop changed occurred. Figure 4 shows schematic of load-displacement responses observed in indentation testing shown in Figure 3.
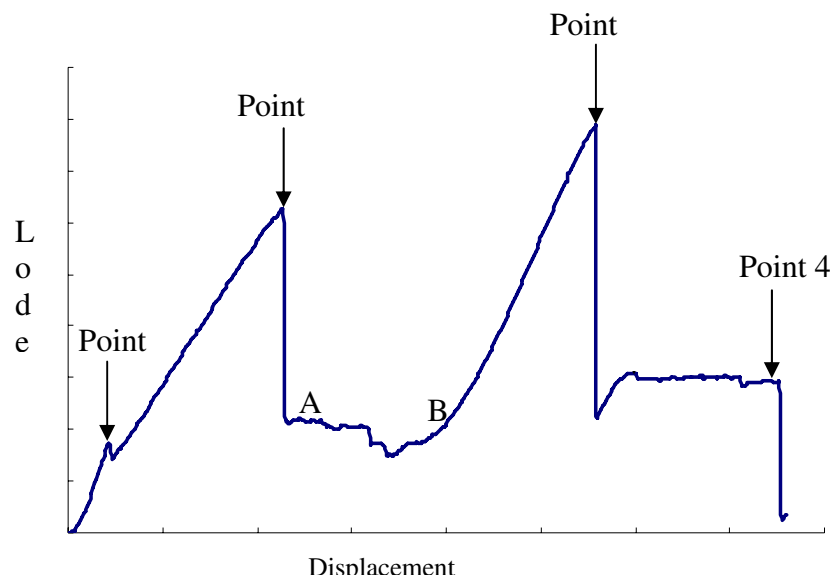

Figure 4: Schematic of indentation test fixture and indentation tup

From the figure, the four distinguishable points are:

Point 1: This point indicates the onset of damage (primary mode of damage) and corresponds to formation of resin cracks in the core, adhesive fillet, or skin.

Point 2: This point corresponds to breaking of top skin (top skin failure). In this point, the load drops suddenly and then increases again. From point 2 to point A, the top skin destroys completely and afterwards the load will be tolerated by the core. From A to B the core crashing occurred and was completed at point B. From this point as the load applies on the bottom skin and there will be an increase in load-displacement curve.

Point 3: This point corresponds to crack in bottom skin (bottom skin failure). However, the panel can still tolerate extra displacement because of presences of residual strength of structure.

Point 4: This point corresponds to failure of panel (bottom skin puncture) which in this point indenter runs through the panel without any resistance.

Since core damage is the primary mode of failure observed (point 1) as shown in Figure 4, the use of the flat indenter allowed the observation of load drops or slope changes indicative of (point 1) incipient core damage. In the case of nonflat indenters, damage onset cannot be observed because the continuously increasing contact area and corresponding load increase smear damage onset in the load-displacement response top skin failure (point 2). This gross damage is not indicative of in-service damage modes. The damage modes produced by the flat indenter match those observed on panels damaged in-service (point 1).

The current indentation test differs from other tests due to fully-supported panels. The latter test will tend to give artificially high values for indentation strength by preventing panel bending. A flat indenter was used in the current test method because it provided a constant contact area during loading. This is due to the panels fail (are as defined in this paper) at loads far below these to cause large overall bending of the panel that would cause uneven contact between the indenter and panel. This is in contrast to hemispherical indenters in which the contact area continuously changes as the panel surface begins to deflect. With a hemispherical tup, onset loads cannot be meaningfully compared between different panels because of the different deformation characteristics of varying panel constructions.

3 RESULTS AND DISCUSSION

Several different panel construction types were tested and studied as follow:

- Panel were manufactured from glass fabric 7781/epoxy skins with nomex core with density 48, 96,123 kg/m^3 (HRH 10-3-48, HRH 10-3-96, HRH 10-3-123) [4, 5].
- Ready-panel Fibrelam grade1were from HEXCEL Company manufactured from 2 cross ply of unidirectional S-glass/epoxy skins with nomex core density 144 kg/m^3 (HRH 10-3-144) [6].

- Ready-panel Fibrelam 2100 grade 2 were from HEXCEL Company manufactured from 2 cross ply of undirectional glass/carbon skins with nomex core density 64 kg/m^3 [7].
- Ready-panel Fibrelam 2100 grade 3 were from HEXCEL Company manufactured from 2 cross ply of undirectional glass/carbon skins with nomex core density $123\,kg/m^3$ [7].
- Panel was manufactured from kevlar/glass fabric T-42-1-76 and core PSP-1-2.5-100 (this core material was manufactured from BFSK paper in Russia which has 5mm cell size) with $100\,kg/m^3$ density [8, 9].

Boeing procedure only measures point 1 which is the onset of damage and then uses this as a criterion for design of the panel (Figure 4). But, our test procedure performs the measurement on peak loads at points 1, 2, 3 (Figure 4) and then applied our design procedure on indentation load at these points for each panel. Our design criteria for the proper panel at different places in the aircraft were base on the maximum loading in points 2 and 3. These maximum loadings are listed in table 1 below.

Load	Point 2 kgf	Point 3 kgf
Aisle panel	180	300
Under seat	120	-----

Table 1 : maximum loading in points 2 and 3

3.1 Effect of skin layer quantity

Figures 5, 6 and 7 depict the effect of number of layers on panels with different core density. It can be seen from the figures that changes in skin layer quantity (two, three or four layers), do not have a large effect on the onset of damage (point 1).

It is noteworthy that adding an extra layer to the panel will increase the panel weight per square meter. For example, for preprag 7781, by adding one layer to the panel (due to symmetry one layer to the top skin and one layer to the bottom skin) an additional weight of ($2 \times 0.55 = 1.1\,Kg/m^2$) adds up to the panel specific weight. Since the weight is a very important factor in aircraft industry, it can be concluded that effect of adding a layer is small in compare to changing the core density. This is presented in more details in the next section.

3.2 Effect of core density

By comparing Figures 5, 6 and 7, one can see that the indentation strength is almost completely dependent on the core density. For example, by changing the core density from 48 kg/m^3 to 96 kg/m^3 with similar skin lay-up, the required force for onset of the damage will be increased approximately by 400 N.
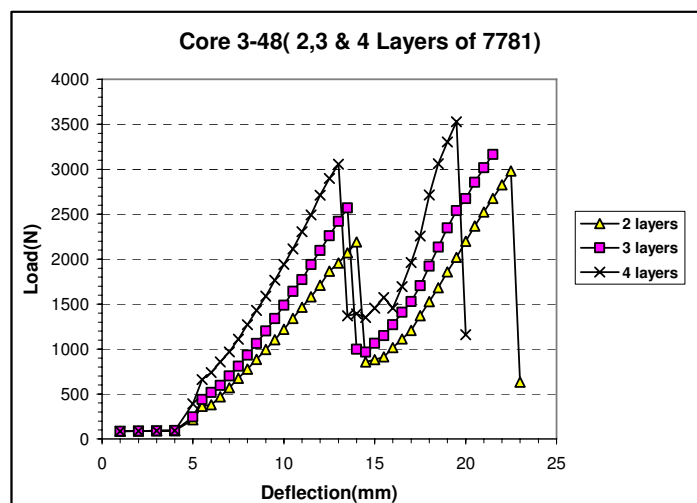
Figure 5:Effect of layers quantity on panel with core density $48 \, kg/m^3$

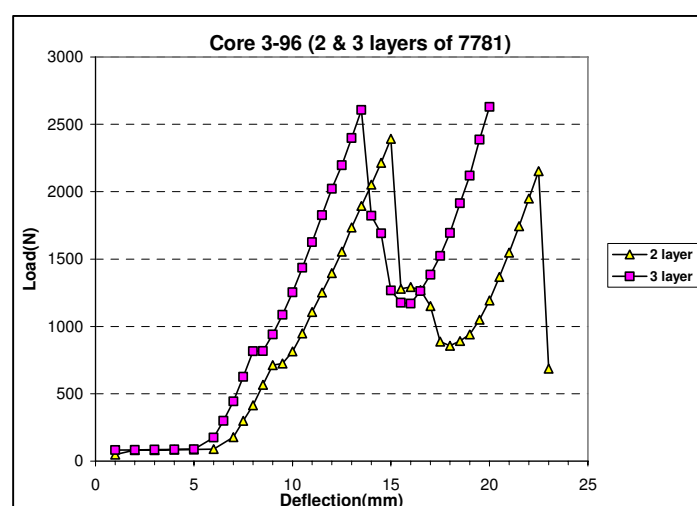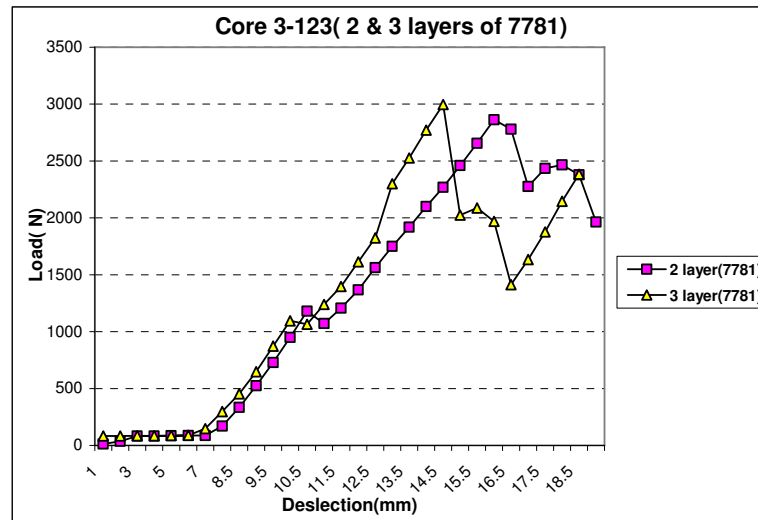Figure 6: Effect of layers quantity on panel with core density $96 \, kg/m^3$

Figure 7: Effect of layers quantity on panel with core density 123 kg/m^3

Table 2 tabulates the measured loads at points 1, 2 and 3 for different types of panels.

panel	Load (N) point 1	Load (N) point 2	Load (N) point 3	Core Compression Strength (Mpa)
HRH10- 3-48 (2 Layers of 7781)	360	2150	2980	2.4
HRH10- 3-48 (3 Layers of 7781)	410	2550	3150	2.4
HRH10- 3-48 (4 Layers of 7781)	700	3050	3500	2.4
HRH10- 3-96 (2 Layers of 7781)	715	2390	2130	7.7
HRH10- 3-96 (3 Layers of 7781)	810	2590	2610	7.7
HRH10-3-123 (2 Layers of 7781)	1150	2860	2350	11.5
HRH10- 3-123 (3 Layers of 7781)	1200	2990	2490	11.5
Fiberlam Grade 1	1350	2100	2700	15
Fiberlam 2100 Grade 2	420	1590	1780	3.9
Fiberlam 2100 Grade 3	1200	1780	2400	11.5
PSP 1-2.5-100 (3 Layers of T42-1-76)	1357	3635	3405	5

Table 2 : Measured load at points 1, 2 and 3 fof load-displacement curve for diffferent panel types

3.3 Effect of rubber

By using rubber seal under the indenter, it was observed that it does not have great influence on the onset of damage load. However, it influences the behavior of the panel after primary damage and causes increasing the load at points2 and 3 (Figure 8). This figure is for panel Fibrelam Grade 1. Similar results were obtained for other types of panels which are not reported here for the sake of brevity.
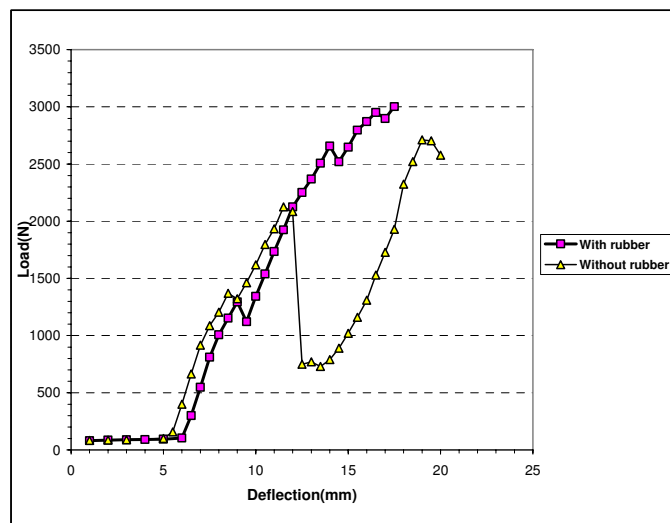

Figure 8:Effect of rubber seal on load-deflection curve (Fibrelam Grade 1)

3.4 Effect of indenter diameter

Because the test was performed on panels with different core density and skins, it was not possible to compare all our results with the Boeing tests, and therefore only the results for panel made of Fiberlam Grad 1 has been compared. But influence of indenter diameter compared based on Boeing test on Figures 9 and 10.

From the results shown in Figure 9, it can be seen that, despite a fourfold increase in indenter area, indentation loads for the 12.7-mm indenter are only about twice those for the 6.35-mm indenter. The principal reasons for this are: (1) the non continuous contact surface presented by the honeycomb geometry; and (2) the indenter contact areas are slightly different from the actual indenter size due to the presence of silicone rubber. Of these two, the former plays a larger role.
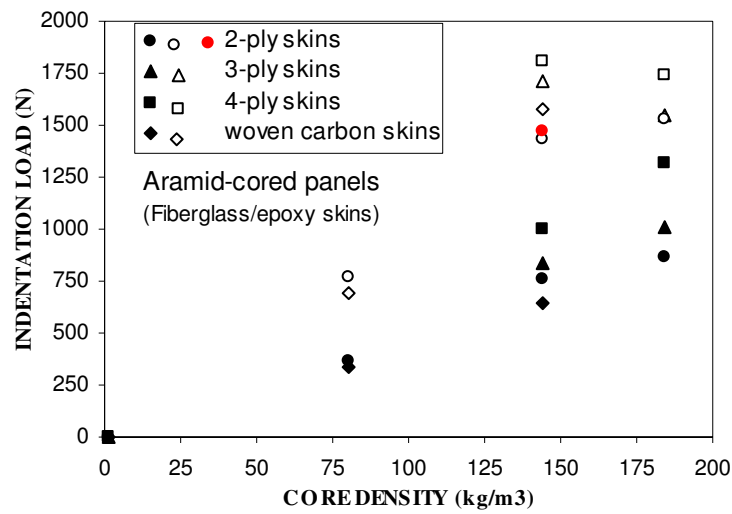
Figure 9:Identation failure load versus core density

Open symbols (identor dia. 12.7mm)[2], Dark symbols (identor dia. 6.35mm)[2], Red symbols (identor dia. 12
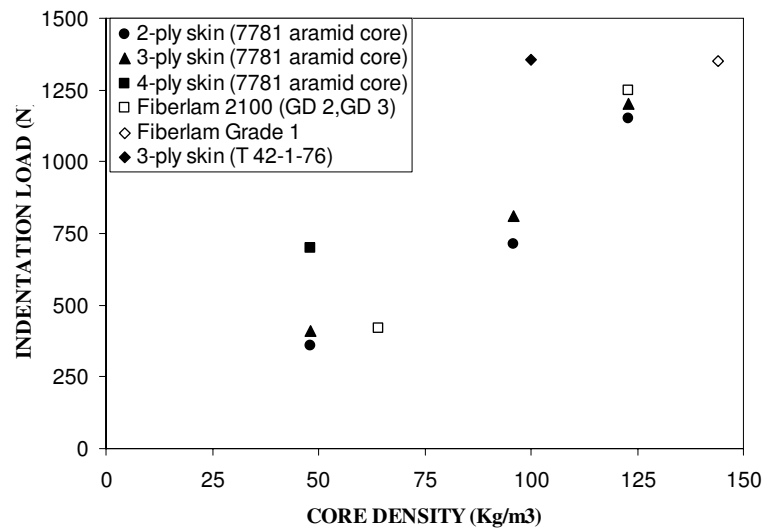
mm)

Figure 10: Identation failure load versus core density (Identor dia. 12 mm)

4 CONCLUSIONS

In this study, the indentation behavior of floor panels was investigated from the viewpoint of test methodology, effects of panel construction, and failure mechanisms. An indentation test method using a simply-supported plate is described that replicates observed in-use failure modes. Tests show that primary failures occurred just below the resin fillet on the top skin.

Furthermore, damage growth appears to be due to accumulation of multiple indentation events more so that due to the propagation of individual indentation damages.

Indentation tests on panels with various combinations of skin and core construction showed indentation strengths to be highly dependent on the core density, as expected. Additionally, an increase in the number of plies in the top (loaded) skin also gave rise to a marked increase in indention resistance. These results strongly indicate that the near-surface properties dominate indentation behavior in contrast to the core-dominated stabilized core compression test.

REFERENCES

[1] Jack R.Vinson, *The Behavior of Sandwich Structures of Isotropic and Composite Materials*, Technomic Publishing Co.INC, 1999.

[2] Thomas K.Tsotsis and Shaw M.Lee, *Characterization of Localized Failure Modes in Honeycomb Sandwich Panels Using Indentation*, Composite Materials Testing and Design (Twelfth Volume).

[3] J.E. Williamson And P.A. Lagace ,*Response Mechanism in the Impact of Graphite/Epoxy Honeycombe Sandwich Panels*, Proceeding, American Society for Composites-Eighth Technical Conference, Cleveland, OH, 18-21 Oct. 1993, Technomic, Lancaster, PA, PP.287-297

[4] Glass Fabric 7781, *Data Sheet*, Hexcel Composites, F.R.

[5] HRH 10, *Data Sheet*, Hexcel Composites, F.R.

[6] Fiberlam GD-1, *Data Sheet*, Hexcel Composites, F.R.

[7] Fiberlam 2100, *Data Sheet*, Hexcel Composites, F.R.

[8] R.E.Shalin, *Polymer Matrix Composites*, Published by Chmpman and Hall, 1995.

[9] A.G.Bratukhin And V.S.Bogolgabov, *Composites Manufacturing Technology*, Published by Chmpman and Hall, 1995.

TESTING OF SANDWICH STRUCTURES WITH CORK AGGLOMERATE CORES

B. Soares, L. Reis and A. Silva[†]

[†]Instituto Superior Técnico (IST)
Universidade Técnica de Lisboa
Avenida Rovisco Pais, 1049-001 Lisboa, Portugal
e-mail: pcasilva@mail.ist.utl.pt
e-mail: lreis@ist.utl.pt
web page: http://www.ist.utl.pt

Key words: Sandwich structures, Cork core, Cork agglomerates, 3PB, 4PB, Experimental mechanics.

Summary. *Cork is a material of great value to the Portuguese economy. Unfortunately, its application is still restricted to the traditional areas, having yet to achieve its full potential field of application, especially in the agglomerate form. It is the purpose of this project the viability study of applying cork based material in aeronautical and aerospace applications as core materials in sandwich structures. It is intended to introduce such materials for its isolation properties (both thermal and acoustic), without significant performance loss when compared to the current used materials (namely Rohacell® and honeycomb). It presents other advantages as well, such as, less energy waste in manufacturing and a better environmental integration, both in the transformation stage and in the end of life recycling stage. The objective of this study is to test different kinds of sandwich specimens, with carbon/epoxy faces, and cores of different kinds of cork agglomerates, in 3 and 4 point bending tests, using the standard test method ASTM C393, and its comparison with the results obtained with similar specimens using current material cores, for the same application. The results obtained show that there still exists significant room for improvement, in order for the cork agglomerates are able to compete with the leading materials. Calculations are presented to support these claims as well as a main avenue of investigation show by the failure modes of the cores, in order to improve the cork based cores competitiveness with the current core materials.*

1 INTRODUCTION

Although of great value to the Portuguese economy, cork is still restricted to the traditional clusters having yet to achieve its full potential field of applications, especially in the agglomerate form. The purpose of this work is to study the applicability of cork based cores in sandwich structures, since sandwich structures, with its high stiffness and strength to

weight ratio, are quickly becoming the main structural components in many state of the art constructions, and require high performance cork materials. The cork agglomerate cores are studied using the standard test method ASTM C 393-00, in 3 and 4 point bending, and compared to Rohacell® and Honeycomb based cores, in regards to maximum applied load to failure, maximum beam deflection, core shear stress and core shear modulus. The results show that cork based cores in sandwich application still have significant room for improvement, if the cork based cores are to compete with leading materials. The failure occurs in the material used to bind the cork grains in the cork agglomerates, which signifies that it is possible, by developing new bonding techniques and materials, to improve the cork based cores behavior under flexural loads.

2 SPECIMENS, EQUIPMENT AND TEST PROCEDURE

All of the specimens tested were sandwich structures with carbon fiber-epoxy multiaxial 0º/90º laminate Vicotex 6376/40%/G803 faces and five core materials, three cork agglomerates references 8303, 8123 and 8810, presented in Fig. 1, Rohacell® and Honeycomb, presented in Fig. 2.

Figure 1: Cork agglomerate specimens

Figure 2: Rohacell and Honeycomb specimens